Fracture scale fluid flow models for the simulation of poroelasticity

Tim Hageman

A thesis submitted in partial fulfilment of the requirements
for the degree of Doctor of Philosophy

The University of Sheffield
Faculty of Engineering
Department of Civil and Structural Engineering

December 2021

ABSTRACT

Fractures are a common occurrence in poroelastic materials: They are created to aid in underground resource recovery, or are unwanted during failure and collapse of materials. One of the main challenges for simulating these fractures is their small opening height compared to their length, making direct simulation of the interior of the fracture computationally expensive. In this thesis, models which reduce the two-dimensional fluid flow in the interior of the fracture to the in and outflow at a one-dimensional discontinuity are extended to include the complex fluid rheology of non-Newtonian power-law and Carreau fluids. One of the main advantages of the obtained sub-grid models is their ability to reconstruct the fluid behaviour through post-processing the obtained results, allowing a detailed description of the fluid within the fracture to be re-obtained. In addition, these sub-grid models are also applied to multiphase flows, allowing the interactions between the fluid phases within the fracture to be included. Finally, a numerical two-scale model is presented, coupling numerically resolved velocity profiles within the fracture to the mass balance at the discontinuity. This allows for velocity profiles for which an analytic solution is not available to be included, such as fluids displaying inertial effects.

These sub-grid models are implemented using finite element methods based on standard Lagrangian elements, non-uniform rational basis splines, and T-splines. While the Lagrangian elements are convenient and commonly used, it is shown that the increased inter-element continuity of Non-Uniform Rational B-Splines (NURBS) and T-splines is required to obtain continuous fracture outflows. It is furthermore shown that this increased continuity is beneficial for the convergence rate of the non-linear solver. The benefits of using lumped integration for the fracture inflow term are demonstrated, suppressing fluid velocity oscillations, and a special fracture tip integration scheme is presented which prevents non-physical fracture inflows for NURBS. Finally, a method to generate unequal order T-spline meshes is presented, allowing for interface elements to solely be inserted for fractured elements, and making mesh refinement near the discontinuity possible.

The fracture scale models and discretisation methods are used to investigate the interactions between the fluid and fracture propagation. It is shown that including a non-Newtonian fluid rheology can significantly alter the propagation velocity of the fracture, and the velocity of the fluid within the fracture. For multiphase flows, the fracture scale models show the importance of including inter-phase interactions within the fracture, providing significantly different results depending on the assumed flow model, either bubbly flow or separated flow. By comparing the fracture flow model to results obtained through direct simulation of the fracture flow the validity and accuracy of the fracture scale models are confirmed. Finally, simulations including inertial effects in the porous material show the interstitial fluid is capable of causing "stick-slip" like behaviour, and simulations using a numerical two-scale approach give an indication of the possible pressure oscillations resulting from stepwise propagation.

STATEMENT OF ORIGINALITY

Unless otherwise stated in the text, the work described in this thesis was carried out by the candidate. None of this work has already been accepted for any degree, nor is it concurrently submitted in candidature for any degree.

Name: Tim Hageman

Signature:

Date: Sunday 19th December, 2021

CONTENTS

LIST OF FIGURES

List of Symbols

$\square^+$	Related to the top of the discontinuity
$\square^-$	Related to the bottom of the discontinuity
$\square^{cp}$	Related to the control points
$\square^{t+\Delta t}$	Taken at time step $t+\Delta t$
$\square_\pi$	Related to phase π
$\square_d$	Related to the discontinuity
$\square_f$	Related to the fluid
$\square_n$	Related to the non-wetting fluid phase
$\square_s$	Related to solid material
$\square_w$	Related to the wetting fluid phase
$\square_{ext}$	Related to the external forces/fluxes
$\square_{int}$	Related to the internal forces/fluxes
$\dot{\square}$	Time derivative
$\ddot{\square}$	Second time derivative
$[\![\square]\!]$	Jump in $\square$ across the discontinuity
$\mathrm{d}\square$	Iterative increment
$\overline{\square}$	Externally applied forces/fluxes

α	Biot coefficient
β	Time integration parameter
Γ	Domain boundary
Γ_d	Discontinuity
γ	Time integration parameter
Δt	Time increment
Δt	Time-step size
ϵ_j	Energy based residual after step j
ζ	Fluid test function
η	Line-search factor
η	Solid test function
Θ	Rotational inertia
θ	Time integration parameter
μ	Dynamic viscosity
μ_0	Base viscosity
μ_∞	Carreau fluid viscosity limit
$\overline{\mu}$	Volume averaged viscosity
ν	Poisson ratio
$\overline{\rho}$	Volume averaged density
ρ	Density
ξ	Fluid test function
Ω	Interior of the domain

$C_{\pi_1\pi_2}$	Lumped pressure capacity
c_v	Consolidation coefficient
E	Young's modulus
f	Plastic yield function
f_t	Tensile strength
G_c	Cosserat shear modulus
$\mathcal{G}_c$	Fracture energy
g	Plastic potential function
h	Fracture opening height
K_π	Bulk modulus of phase π
K_t	Total bulk modulus
k	Intrinsic permeability
k_f^*	Effective permeability
k_i	Interface permeability
k_n	Dummy stiffness
k_s	Dummy stiffness
$k_{d\pi}$	Cubic law relative permeability

$k_{i,d}$	Dummy interface permeability
$k_{r\pi}$	Relative permeability
ℓ_c	Cosserat length scale
M	Biot modulus
m_w	Confined compressibility
n	Non-Newtonian fluid index
n_f	Porosity
p	Interstitial fluid pressure
p_c	Capillary pressure
p_d	Discontinuity pressure
p_n	Non-wetting phase fluid pressure
p_w	Wetting phase fluid pressure
Q	Point-forced fluid inflow
$\overline{q}$	External fluid flux
q	Fluid flux within the fracture
S_π	Saturation of phase π
t	Time
(v, w)	Fluid velocity within the fracture
V_π	Volume contained by phase π
v_f	Fracture wall velocity

$\boldsymbol{B}$	Displacement to strain mapping matrix
$\boldsymbol{C}$	Damping matrix
$\boldsymbol{D}_d$	Discontinuity stiffness matrix
$\boldsymbol{D}_{el}$	Linear-elastic stiffness matrix
$\boldsymbol{\varepsilon}$	Strains
$\boldsymbol{\varepsilon}_p$	Plastic strains

$\boldsymbol{f}$	Force vector
$\boldsymbol{I}$	Identitiy matrix
$\boldsymbol{m}$	Direction of plastic strain
$\boldsymbol{m}$	Divergence mapping vector
$\boldsymbol{N}_\pi$	Interpolation/shape functions
$\boldsymbol{n}$	Normal vector
$\boldsymbol{n}_d$	Normal to the fracture wall
$\boldsymbol{n}_{\Gamma_d}$	Normal to the discontinuity
$\boldsymbol{q}$	Darcy fluid flux
$\boldsymbol{q}$	Flux vector
$\boldsymbol{R}$	Rotation matrix
$\boldsymbol{\sigma}$	Stress
$\boldsymbol{\sigma}_s$	Solid stress
$\boldsymbol{\tau}$	Traction
$\boldsymbol{\tau}_d$	Solid component of interface traction
$\boldsymbol{\tau}_{\Gamma_d}$	Total traction at interface
$\boldsymbol{t}_d$	Tangential to the fracture wall
$\overline{\boldsymbol{\tau}}$	External tractions
$\boldsymbol{u}$	Displacement
$\boldsymbol{v}$	Velocity

$error_j$	Normalised energy based residual after step j
$sgn(\cdot)$	Signum function
(x, y)	Cartesian coordinates
(x_d, y_d)	Local coordinate system at the discontinuity

1

INTRODUCTION

Fluid flow in porous media is a common phenomenon in many problems of engineering interest, for instance underground oil flow and recovery [11, 18, 26, 49, 240], and spreading of pollutants[26, 126]. Other applications include blood flow inside the human body [189, 215, 224], underground geothermal energy storage [249], and failure in porous materials [19, 110, 141]. In most of these applications, not only the fluid flow but also the deformation of the porous media caused by the fluid plays an important role. Due to these deformations, pre-existing fractures may open [125, 237, 249], or new fractures can be created [43, 49, 67, 142, 165].

The fluid flows slowly through the porous media while flowing faster through opened fractures. This creates additional challenges for simulating fluid flow through these materials [49, 67]: Whereas the fluid in the porous media reacts slowly to changes, the fluid inside the fracture reacts almost instantly, resulting in different timescales for the flow in the porous media and the fracture. Furthermore, these fractures are long, at least in the order of meters but they can stretch several kilometres for geological simulations [71, 150, 230], while the opening is at most a few millimetres. This creates a large difference between the relevant length scales of the problem, requiring the simulation of large domains to contain the complete fracture while being dominated by the fluid flow in the interior of the fracture which flows through a very small opening.

The combined fracture flow and poroelastic medium flow can be directly simulated as a combination of Darcy flow in the porous material and Stokes flow inside the fracture [13, 14, 25]. Alternatively, both these domains can be described using a single set of equations using Brinkman flow [50, 133, 159]. The main advantage of these methods is that they allow the fluid flow within fractures to be treated in the same manner as other voids that might be present, for instance boreholes [25] or tunnels [50]. While these methods allow for the flow inside the fracture to be accurately resolved, they require very fine meshes to properly discretise the fracture height. Furthermore, the mesh needs to adapt to changes in fracture opening, and propagate with the fracture. This makes directly simulating the fluid flow inside the fracture computationally costly and impractical.

1.1. FRACTURE FLOW SUB-GRID MODELS

A more efficient method to include the flow within the fracture is to reduce the dimension of the fracture, approximating a fracture in a two-dimensional domain as a one-dimensional discontinuity line. This approach was first taken by *Boone and Ingraffea* [32] to simulate the interior of the fracture using a one-dimensional finite difference scheme, coupled to a two-dimensional finite element method for the porous material. For the interior of the fracture, inertial effects were neglected and the fluid flow was described through Poiseuille flow, resulting in a relation between the pressure gradient and fracture opening height, and the total fluid transport within the fracture. This simple relation is referred to as the "cubic law" [27, 238].

The cubic law can be cast into an effective permeability term, allowing similar equations to be used for the porous domain and the fracture itself [113, 207]. Due to the ease of use of this formulation, it has been successfully applied to a large range of applications, for instance impermeable natural fractures [95] and pressurised fractures [43, 54, 84]. Another method to include the fracture flow based on the cubic law is to distribute the fluid transport inside the fracture over the element in which it is contained, removing the need to separately simulate the fracture [12, 79, 91, 142].

While using the cubic law allows fluid flows inside fractures to be included in a straightforward manner, it does not allow for an in-depth look at the fluid behaviour inside the fracture. In contrast, the continuous pressure model [39, 187] does allow the velocity profile inside the fracture to be obtained through post-processing. This model relates the pressure gradient and opening height to an analytically obtained expression for the fluid flux, with this expression based on the velocity profile inside the fracture. This velocity profile can then be reconstructed afterwards through post-processing of the interstitial fluid pressure and displacements, allowing the fracture fluid flow to be included in a sub-grid model while still retaining the information from within the fracture. This sub-grid model can be extended to use a discontinuous pressure along the fracture [41, 185], allowing the inclusion of an entry resistance to the fluid flow. This interface permeability is also used to include boundary layers between a pressurised fracture and the porous material, without explicitly resolving these boundary layers [185].

1.2. DISCRETISATION METHODS

Independent of the used sub-grid model, most poroelastic simulations are discretised using finite element methods, with the fractures included through either interface elements [42, 49, 162, 173], the extended finite element method [41, 90, 145, 154, 155, 187], or phase field methods [70, 75, 120, 123]. Mixed approaches are also sometimes utilised, with the interstitial fluid pressure discretised using a finite element scheme, while the solid displacements are modelled using central force/lattice [46, 147, 148] or peridynamics methods [163, 166]. However, the disadvantage of all these methods is that they use Lagrangian polynomials as interpolants, and thereby only obtain a C^0 inter-element continuity. This results in continuous but non-smooth pressures and displacements, and discontinuous stresses and fluid fluxes at the element boundaries [100].

An increased inter-element continuity can be obtained using non-uniform rational basis splines (NURBS) [33, 63, 97, 174] or T-splines [21, 203, 204]. While originally aimed at using the same mesh for modelling and simulating objects (referred to as "isogeometric analysis", IGA) [97], the higher-order continuity obtained through the spline-based interpolants is advantageous for simulations. Using these interpolants not only results in continuous fluid fluxes in the porous material but also increases the accuracy of the simulation results with a reduced number of control points [100]. An added advantage of IGA is its ability to create unequal-order meshes [232]. These unequal order meshes, with the solid displacements discretised with interpolants one order higher than the interstitial fluid pressure, fulfil the inf-sup condition [53] and thereby prevent non-physical pressure oscillations [24, 223].

1.3. RELEVANT PHYSICS

Even though some important fluids relevant for fluid flow in porous media are non-Newtonian, for instance crude oil [9, 11], the above-described sub-grid models have so far focused on Newtonian fluids. However, the limited number of results available for non-Newtonian fluids inside fractures indicate the importance of including realistic fluid rheology, with shear-thinning fluids flowing faster in fractures compared to Newtonian fluids [58, 118, 192]. Similar behaviour is also observed in the porous material itself, with shear-thinning fluids flowing faster through the porous medium [191].

Another important area is multiphase flows, for instance water/air in unsaturated materials or water/oil in underground reservoirs. Currently, these fluid flows within fractures are often modelled through empirical correction factors for the cubic law [44, 153, 155, 196, 241, 246]. Another option is to describe the fluid flow inside the fracture as a single-phase flow, while still considering the porous material to contain multiple phases [17, 96, 137]. These models allow for easy integration of fractures into the description of the porous material, and extending them to include more phenomena like heat transfer is straightforward [111, 226]. However, since they are based on an empirical correction factor for the cubic law, no insight is provided into the actual fluid behaviour in the fracture. Some attempts have been made to cast this multiphase cubic law formulation into a continuous pressure sub-grid model [188], but they still retained the dependence on the empirical factor and did not gain the additional insight into the fluid velocity profiles usually associated with sub-grid models.

Finally, there is the interaction between the fluid inside the fracture and the fracture propagation itself. While the effects of a pressurised fluid on fracture propagation are well studied, both through analytic solutions [76, 86] and simulations, it has been recently argued that fractures in a porous material propagate stepwise instead of in a continuous fashion [45, 172]. Experimentally, this stepwise propagation has been observed as pressure oscillations at the inlet of pressurised fractures [82, 127]. However, most continuum models such as the finite element method have been unable to reproduce these pressure oscillations, and have only obtained stepwise propagation due to the limited size of the elements used [155, 173, 184]. The exception to these results is the results from *Cao et al.* [45, 46], who by separating time steps (in which the fluid inside the fracture is allowed to flow) and fracture propagation steps (no fluid flow allowed) were able to obtain stepwise propagation and the suggested accompanying pressure oscillations. However, due to their combination of mesh and time step size, their discontinuity propagates in every propagation step, suggesting that the claimed step wise propagation is artificially induced by the distinction between time and propagation steps. Methods not based on a continuum approach, such as the lattice method [171] or an approach based on peridynamics [163], have been able to obtain some stepwise propagation. However, no convincing explanation has been given on the source of this propagation behaviour, and why it should create large pressure oscillations inside the fracture.

1.4. AIMS

The main aims of this research were as follows:

- Extend the sub-grid formulation for fluid flows in fractured porous materials to include additional physically relevant behaviour, such as non-Newtonian fluid rheologies, inertial effects, and multiphase flows, while still retaining the ability to reproduce the velocity profiles within the fracture through post-processing.

- Analyse the effect of using standard Lagrangian finite elements compared to spline-based elements when simulating fractured porous materials, mainly focusing on the flows inside the fracture. This involves both how the obtained results are improved through the higher order continuity from spline-based elements, as well as analysing any improvements in the convergence rate of the non-linear solver.

- Investigate the effects of using a more physically correct representation for the fluid in the porous material and fracture, with the main focus on the interaction of these added physics with the fracture propagation.

1.5. THESIS STRUCTURE

The introduction of this chapter summarised the importance and current developments for the simulation of fluid flows in porous materials. To further supplement this with in-depth and relevant literature, each chapter will start of with a more detailed description of the literature relevant to that chapter.

Chapter 2 will focus on non-Newtonian fluid flows: Detailing the equations for fluid flow in porous materials, and extending these to include a non-Newtonian rheology using a power-law fluid. This chapter will focus on non-propagating fractures and will use a continuous pressure model to approximate the fluid transport inside the fracture. It will show the effect of including this non-linear fluid behaviour on the fluid transported through the porous material, and inside the fracture. A standard Lagrangian finite element discretisation will be compared with a discretisation using splines, and the results will be compared to demonstrate the advantages of the spline-based elements.

In Chapter 3, the convergence rate of the non-linear solver used in the scheme of chapter 2 will be analysed. The main focus of this analysis is on the terms added by the fracture flow, adding these terms one-by-one to preserve a constant and symmetric system matrix as long as possible. The effect of omitting some terms will be shown, both for Newtonian and non-Newtonian fluids. Furthermore, the effect on the convergence of either discretising the domain using standard Lagrangian elements or using spline based elements is investigated.

Next, the continuous pressure fracture flow model will be applied to two fluid phases in Chapter 4. An explanation on how to couple the fluid velocity profiles inside the fracture with the surrounding porous material will be given, and applied to well-mixed bubbly flow and separated flow types. These flow types will be compared to the commonly used cubic law by simulating a simplified problem and two cases more representative of actual applications. This will show the ability of the sub-grid models to include complicated physical interactions within the fracture, without a need to actually simulate the interior of these fractures.

The non-Newtonian fracture flow model is extended to allow pressurised fractures in Chapter 5. Special integration schemes will be detailed to prevent non-physical and oscillatory fracture inflows. Furthermore, a comparison between Newtonian and non-Newtonian fluids and their effect on the propagation velocity will be undertaken.

One of the main issues arising from Chapter 5 is the need of a separate integration scheme around the fracture tip. A discretisation based on T-splines able to circumvent this issue will be detailed in Chapter 6. Mesh generation of unequal order T-spline meshes will be explained, and simulations using these meshes will be compared to results from the previous chapter.

These T-splines will be used in Chapter 7 to simulate propagating fractures using a discontinuous pressure model, and using directly simulated Stokes flow inside the fracture. This will confirm the accuracy of the discontinuous pressure model, and provide a comparison between the velocity profiles within the fracture.

Chapter 8 combines the previously detailed discontinuous pressure fracture flow model with more complex behaviour of the solid. This chapter will combine plastic deformation of the porous materials, with acceleration driven fluid flows and shear-based fracture propagation. This will result in a formulation more representative of real-world application, for instance earthquake-like processes. Attention will be given to the effects of including acceleration driven fluid flows and fluid inertia, and the effect of simulating the fluid flow itself instead of assuming no fluid flow on the propagation will be investigated.

Finally, Chapter 9 details a subgrid scheme which uses a numerically obtained velocity profile within the discontinuous pressure model. This will allow for inertial effects inside the fracture to be included, as well as making previously derived subgrid models applicable to fluids for which an analytic velocity profile is no longer obtainable, such as non-Newtonian Carreau fluids.

The thesis will conclude with a conclusions chapter, highlighting and reflecting on the main advances and findings obtained during the previous chapters.

2

NON-NEWTONIAN FLUIDS USING THE CONTINUOUS PRESSURE MODEL

Several models exist to describe non-Newtonian fluids. One of the simplest and most commonly used models to describe the shear-dependent viscosity of these non-Newtonian fluids is the power-law model. This simplicity allows the derivation of an explicit expression for the fluid flow inside the porous material for one-dimensional cases [59, 78, 169], with this expression able to be extended to yield-stress fluids. Simulations using the pore-scale network method [216] and direct simulation of the fluid inside the pores [157] have shown the accuracy of the power-law fluid term. However, these simulations also indicated the inability of these simple one dimensional formulations to properly capture the yield-stress dependence due to the pore-size distribution allowing for flow in the smaller pores, whereas macro scale formulations do not include this gradual increase in fluid flow. The one-dimensional formulation for power-law fluids has been extended to multi-dimensional flows [212] and successfully used in simulations of non-deformable porous materials [68], although this resulted in an implicit expression for the fluid flux.

Fractures filled with non-Newtonian power-law fluids have been simulated using the finite volume method [118, 119]. These simulations showed that shear-thinning power law fluids flow faster through the fractures compared to Newtonian fluids, but that shear-thickening fluids flow considerably slower. However, this method only used the pressure gradient normal to the cell faces, thereby not including the coupling between the flow directions present for power-law fluids. Semi-analytical solutions for a simplified one dimensional fracture produced similar findings, with shear-thinning fluids flowing faster than Newtonian fluids [144, 219]. The combination of a non-deformable porous material with fractures with a pre-determined opening height have been simulated using a MATLAB reservoir engineering toolbox [18, 131], removing the need to discretise the used equations, but also obfuscating the actual implementational aspects of the described method.

This chapter first describes the governing equations for Newtonian and power-law fluids inside the porous material. The continuous pressure model will be used to derive the fluid flow inside the fracture for these fluids. Next, in Section 2.2, the finite element discretisation methods using Lagrangian polynomials and splines are explained, after which the governing equations are discretised. These discretised equations are used in Section 2.3 to show the effects of including the non-Newtonian rheology compared to linearising the non-Newtonian fluids to a Newtonian fluid. Finally, the spline based and Lagrangian based discretisations will be compared in Section 2.4. All the results and methods presented in this chapter have been previously published in [4].

2.1. NON-NEWTONIAN POROELASTICITY

The fractured porous material is represented by the domain Ω, shown in Figure 2.1. On the outside of this domain, interstitial fluid pressures and displacements are prescribed on Γ_p and Γ_u respectively, while tractions and fluid fluxes are prescribed on Γ_t and Γ_q. The domain is split by the discontinuity Γ_d which represents both the fracture and the still intact material in the extend of the fracture. The fracture itself is described using its opening height h normal to Γ_d, and uses a local (x_d, y_d) coordinate system.

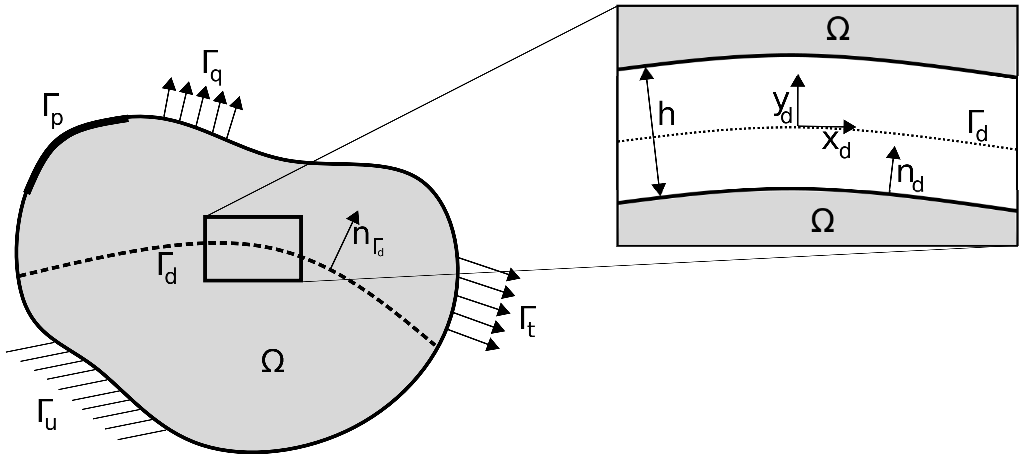

Figure 2.1: Schematic overview of the considered domain, including local coordinate system for the fracture.

2.1.1. Interior

Momentum balance

In the model described here, no mass transfer between the solid and fluid phase is presumed, and no reactions between the fluid and solid phase occur. By furthermore neglecting the momentum transfer due to convection, the momentum balance of the fluid and solid phases $\pi = s, f$ is given by [38, 247]:

$$\nabla \cdot \boldsymbol{\sigma}_\pi + \boldsymbol{T}_\pi - \rho_\pi \ddot{\boldsymbol{u}}_\pi = \boldsymbol{0} \tag{2.1}$$

with $\boldsymbol{\sigma}_\pi$ the stress tensor, ρ_π the apparent density, and $\ddot{\boldsymbol{u}}_\pi$ the acceleration of phase π. The interaction between the phases is represented by $\boldsymbol{T}_\pi$, the transfer of momentum between the phase π and the other phase. Since the only transfer of momentum due to this interaction is between the phases, $\boldsymbol{T}_s = -\boldsymbol{T}_f$.

Summing the momentum balance of the two phases results in:

$$\nabla \cdot \boldsymbol{\sigma} - \left(n_f \rho_f \ddot{\boldsymbol{u}}_f + (1 - n_f)\rho_s \ddot{\boldsymbol{u}}_s\right) = \boldsymbol{0} \tag{2.2}$$

with n_f the porosity, and the total stress $\boldsymbol{\sigma}$ related to the stresses in the solid $\boldsymbol{\sigma}_s$ and the interstitial fluid pressure p through:

$$\boldsymbol{\sigma} = \boldsymbol{\sigma}_s - \alpha p \boldsymbol{I} \tag{2.3}$$

with $\boldsymbol{I}$ the identity tensor, and α the Biot coefficient [28]. This Biot coefficient is related to the bulk modulus of the solid material, K_s, and the bulk modulus of the total skeleton (porous solid material without fluid), K_t, by:

$$\alpha = 1 - \frac{K_t}{K_s} \tag{2.4}$$

The bulk modulus of the solid is often large compared to that of the skeleton, and in these cases the Biot coefficient is usually taken as $\alpha = 1$. This corresponds to the case of a nearly incompressible solid material, while the porous material is still deformable.

One final simplification is made by assuming the solid and fluid accelerations to be equal, $\ddot{\boldsymbol{u}}_s = \ddot{\boldsymbol{u}}_f$. This is an often made assumption, both for problems in which dynamical effects are negligible [110, 152, 171, 199], as well as for problems which are dominated by acceleration effects, e.g. earthquake dynamics [66, 245, 247]. This allows Eq. 2.2 to be simplified to:

$$\boldsymbol{\nabla}\cdot\boldsymbol{\sigma}-\overline{\rho}\ddot{\boldsymbol{u}}=\mathbf{0} \tag{2.5}$$

with $\overline{\rho} = n_f\rho_f + (1-n_f)\rho_s$ the volume-averaged density of the poroelastic medium. The second term, $\overline{\rho}\ddot{\boldsymbol{u}}$ can be neglected if the system is assumed to be quasi-static, with the fluid flow being time-dependent, whereas the solid is assumed to always be in equilibrium. This is often the case in poroelastic problems, and will also be assumed here.

MASS BALANCE

The mass balance for each phase is given by:

$$\frac{\partial\rho_\pi}{\partial t}+\boldsymbol{\nabla}\cdot(\rho_\pi\dot{\boldsymbol{u}}_\pi)=0 \tag{2.6}$$

Assuming negligible effects of phase density gradients and a constant porosity, summing the mass balances of the two phases results in:

$$\frac{1}{\rho_f}\frac{\partial\rho_f}{\partial t}+\frac{1}{\rho_s}\frac{\partial\rho_s}{\partial t}+\boldsymbol{\nabla}\cdot\dot{\boldsymbol{u}}_s+n_f\boldsymbol{\nabla}\cdot\left(\dot{\boldsymbol{u}}_f-\dot{\boldsymbol{u}}_s\right)=0 \tag{2.7}$$

Finally, the relative fluid velocity is replaced by the Darcy fluid flux $\boldsymbol{q} = n_f(\dot{\boldsymbol{u}}_f - \dot{\boldsymbol{u}}_s)$, the Biot coefficient is used to rewrite the solid density derivative as $\dot{\rho}_s/\rho_s = (\alpha-1)\boldsymbol{\nabla}\cdot\dot{\boldsymbol{u}}$, and the fluid density derivative is rewritten by using the Biot modulus $\dot{\rho}_f/\rho_f = 1/M\,\dot{p}$, resulting in:

$$\frac{1}{M}\dot{p}+\alpha\boldsymbol{\nabla}\cdot\dot{\boldsymbol{u}}+\boldsymbol{\nabla}\cdot\boldsymbol{q}=0 \tag{2.8}$$

The Biot modulus is related to the bulk moduli of the solid and fluid, and the porosity of the porous material, n_f, by:

$$\frac{1}{M}=\frac{\alpha-n_f}{K_s}+\frac{n_f}{K_f} \tag{2.9}$$

If the fluid modelled is a Newtonian fluid, Darcy's law is used to relate the fluid flux $\boldsymbol{q}$ to the pressure gradient by:

$$\boldsymbol{q}=-\frac{k}{\mu}\boldsymbol{\nabla}p \tag{2.10}$$

with k the intrinsic permeability and μ the dynamic viscosity of the fluid.

NON-NEWTONIAN FLUIDS

The non-Newtonian fluid is represented through the power-law fluid model. For these fluids, the shear-stress τ inside the fluid is related to the velocity shear rate dv/dy through:

$$\tau=\mu_0\left|\frac{dv}{dy}\right|^{n-1}\frac{dv}{dy} \tag{2.11}$$

with μ_0 the consistency factor or base viscosity, and n the power-law index. A power-law index $n < 1$ represents shear-thinning fluids, such as oils [11] and suspensions of large molecules [29, 132]. An index $n > 1$ represents shear-thickening fluids, which is sometimes used to describe dense particle suspensions [124]. If $n = 1$, Eq. 2.11 reduces to the expression for a Newtonian fluid.

A one-dimensional expression for power-law fluids inside a porous material is given by [59, 78, 169]:

$$q=-k_f^*\left(\frac{\Delta p}{\Delta L}\right)^{\frac{1}{n}} \tag{2.12}$$

This expression relates the fluid flux q flowing through the porous material to the pressure gradient $\Delta p/\Delta L$. It assumes the flow is solely driven by this pressure gradient, and effects of inertia are negligible. The effective permeability k_f^* is defined as:

$$k_f^* = \frac{n}{3n+1}\left(\frac{50}{3}k\right)^{\frac{1+n}{2n}} \left(2C\mu_0\right)^{-\frac{1}{n}} n_f^{\frac{n-1}{2n}} \tag{2.13}$$

with k the intrinsic permeability and C a constant, normally taken as $\frac{50}{24}$ to correspond to a Newtonian fluid for $n = 1$. Since k_f^* only depends on material properties, it is a constant throughout the porous medium as long as the porosity and permeability are uniform. An implicit form, able to be used for multidimensional cases, has been formulated and used in [68, 157, 212]:

$$\nabla p = -\frac{\mu_0}{k^*}\left|\boldsymbol{q}\right|^{n-1}\boldsymbol{q} \tag{2.14}$$

with the constant k^* given by:

$$k^* = \frac{1}{2C}\left(\frac{50k}{3n_f}\right)^{\frac{n+1}{2}}\left(\frac{n\,n_f}{3n+1}\right)^{n} \tag{2.15}$$

This equation can be cast into an explicit form by continuously substituting the definition of $\boldsymbol{q}$:

$$\begin{aligned}
\boldsymbol{q} &= -\left|\boldsymbol{q}\right|^{1-n}\frac{k^*}{\mu_0}\nabla p_f \\
&= -\left|\boldsymbol{q}\right|^{(1-n)^2}\left|\nabla p_f\right|^{1-n}\left(\frac{k^*}{\mu_0}\right)^{1+(1-n)}\nabla p_f \\
&= -\left|\boldsymbol{q}\right|^{(1-n)^3}\left|\nabla p_f\right|^{(1-n)+(1-n)^2}\left(\frac{k^*}{\mu_0}\right)^{1+(1-n)+(1-n)^2}\nabla p_f \\
&= \ldots..
\end{aligned}$$

resulting in:

$$\boldsymbol{q} = -k_f^*\left|\nabla p\right|^{\sum_{i=1}^{\infty}(1-n)^i}\nabla p \tag{2.16}$$

with the definition of the effective permeability corresponding to the expression from the one-dimensional case, Eq. 2.13. The infinite series of Eq. 2.16 converges if n is between zero and two [236]. Since most power-law fluids of interest have fluid indices between zero and two, Eq. 2.16 can be simplified to:

$$\boldsymbol{q} = -k_f^*\left|\nabla p\right|^{\frac{1}{n}-1}\nabla p \tag{2.17}$$

which can be used in combination with the conservation of mass, Eq. 2.8, to fully describe the pressure changes for a poroelastic material for power-law fluids as:

$$\frac{1}{M}\dot{p} + \alpha\nabla\cdot\dot{\boldsymbol{u}} - k_f^*\nabla\cdot\left(\left|\nabla p\right|^{\frac{1}{n}-1}\nabla p\right) = 0 \tag{2.18}$$

2.1.2. FRACTURE

The fracture is represented by part of the discontinuity Γ_d, with the other part of the discontinuity representing still intact material. The displacement across the fracture has a C^{-1} continuity, to allow for jumps in normal and tangential displacements across the fracture. For the continuity of the pressure, several different models exist. Using a C^{-1} pressure continuity results in a jump in pressures across the fracture, thereby representing a discontinuous pressure model [173, 185]. In contrast, when a C^0 pressure continuity is used, the pressures are continuous across the discontinuity, but the fluid fluxes are discontinuous. This corresponds to the continuous pressure model [39, 187], which will be used in this chapter.

INTERFACIAL STRESSES

Similar to the stresses in the interior of the domain, the traction at the discontinuity, $\boldsymbol{\tau}_{\Gamma_d}$, is decomposed in contributions due to the solid deformations and the fluid pressure within the fracture:

$$\boldsymbol{\tau}_{\Gamma_d} = \boldsymbol{\tau}_d - p\boldsymbol{n}_d \tag{2.19}$$

with $\boldsymbol{n}_d$ the normal vector to the fracture (see Fig. 2.1), and p the pressure within the fracture, equal to the interstitial fluid pressure inside the porous material. By imposing this fluid pressure on the fracture walls, the interstitial fluid pressure just inside the porous material is counteracted, and the fracture is able to open. The solid traction $\boldsymbol{\tau}_d$ represents the tractions caused by the behaviour of the solid material, including phenomena such as traction-separation behaviour or dummy stiffness terms to enforce a continuous material.

For the intact part of the discontinuity, the solid part of the traction is given by:

$$\boldsymbol{\tau}_d = \boldsymbol{D}_d^* [\![\boldsymbol{u}]\!] \tag{2.20}$$

with $[\![\boldsymbol{u}]\!]$ the jump in displacement across the interface, and $\boldsymbol{D}_d^*$ the dummy stiffness matrix in the global coordinate system. This dummy stiffness matrix is obtained from the local dummy stiffness matrix $\boldsymbol{D}_d$ by using the rotation matrix $\boldsymbol{R}$:

$$\boldsymbol{D}_d^* = \boldsymbol{R}^T \boldsymbol{D}_d \boldsymbol{R} \tag{2.21}$$

The local dummy stiffness matrix is used to prevent non-physical compliance for the non-fractured part of the discontinuity by using a high dummy stiffness k_n, k_s, defining the local dummy stiffness matrix as:

$$\boldsymbol{D}_d = \begin{bmatrix} k_n & 0 \\ 0 & k_s \end{bmatrix} \tag{2.22}$$

For the part of the discontinuity representing the fracture, the solid traction can be defined through a cohesive zone model [242]. These cohesive zone models are used to more accurately represent the small-scale plastic deformations occurring close to the fracture tips, and remove stress singularities near the fracture tips. Since the fractures in this chapter are not allowed to propagate, no cohesive zone models are included for the fractured parts of the discontinuity and therefore $\boldsymbol{\tau}_d = \boldsymbol{0}$ for the cracked part of the discontinuity.

FRACTURE FLUID FLOW

The fluid flow within the fracture is simulated using a continuous pressure fracture inflow model [38, 39, 185]. These models implicitly include the fluid flow within the fracture by determining the fluid flowing into the fracture due to changes in flow profile within the fracture. The main advantage of this method is that the fluid velocity within the fracture can be included without needing to discretise the interior of the fracture.

The velocity of the fluid within the fracture is described in the local (x_d, y_d) coordinate system using the Stokes equation:

$$0 = -\frac{\partial p}{\partial x_d} + \frac{\partial \tau}{\partial y_d} \tag{2.23}$$

which combined with the constitutive relation for power-law fluids, Eq. 2.11, yields:

$$0 = -\frac{\partial p}{\partial x_d} + \frac{\partial}{\partial y_d}\left(\mu_0 \left(\frac{\partial v}{\partial y_d}\right)^n\right) \tag{2.24}$$

This assumes that inside the fracture the tangential fluid velocity is large compared to the normal fluid velocity. Furthermore, effects of inertia and density changes inside the fracture are neglected.

The tangential fluid velocity within the fracture should correspond to the fluid velocity inside the porous material at the fracture wall, thus $v(h/2) = v(-h/2) = v_f$ with the fluid wall velocity just inside the porous material approximated by:

$$v_f = -\frac{k_f^*}{n_f}\left|\frac{\partial p}{\partial x_d}\right|^{\frac{1}{n}-1}\frac{\partial p}{\partial x_d} + \dot{u}_s \tag{2.25}$$

Using this wall velocity boundary condition, an explicit expression for the fluid flow profile within the fracture is derived from Eq. 2.24:

$$v(y_d) = \frac{n}{n+1}\mu_0^{-\frac{1}{n}}\left|\frac{\partial p}{\partial x_d}\right|^{\frac{1}{n}-1}\frac{\partial p}{\partial x_d}\left(\left|y_d\right|^{\frac{1}{n}+1} - \left(\frac{h}{2}\right)^{\frac{1}{n}+1}\right) + v_f \quad \text{for } -\frac{h}{2} \leq y_d \leq \frac{h}{2} \tag{2.26}$$

The conservation of mass equation for the interior of the fracture is:

$$\frac{\partial \rho_f}{\partial t} + \boldsymbol{\nabla}\cdot\rho_f\boldsymbol{v} = 0 \tag{2.27}$$

For the interior of the fracture, it is assumed that the effects of the velocity are large compared to the density changes. This reduces the mass conservation to:

$$\frac{\partial v}{\partial x_d} + \frac{\partial w}{\partial y_d} = 0 \tag{2.28}$$

Integrating over the fracture height then results in the jump in fracture outflow:

$$\llbracket w \rrbracket_f = w\left(\frac{h}{2}\right) - w\left(-\frac{h}{2}\right) = -\int_{-h/2}^{h/2}\frac{\partial v}{\partial x_d}\mathrm{d}y_d \tag{2.29}$$

Using the velocity profile inside the fracture for a power-law fluid, Eq. 2.26, in Eq. 2.29 results in:

$$\llbracket w \rrbracket_f = \frac{2}{2n+1}\left(\frac{h}{2}\right)^{\frac{1}{n}+2}\mu_0^{-\frac{1}{n}}\left|\frac{\partial p}{\partial x_d}\right|^{\frac{1}{n}-1}\frac{\partial^2 p}{\partial x_d^2} + \left(\frac{h}{2}\right)^{\frac{1}{n}+1}\mu_0^{-\frac{1}{n}}\left|\frac{\partial p}{\partial x_d}\right|^{\frac{1}{n}-1}\frac{\partial h}{\partial x_d}\frac{\partial p}{\partial x_d} - h\frac{\partial v_f}{\partial x_d} \tag{2.30}$$

In order to link the expression for the fracture outflow to that of the fluid flow inside the porous medium, the definition of the fluid flux jump from the viewpoint of the porous medium is used:

$$\llbracket \boldsymbol{n}_{\Gamma_d}\cdot\boldsymbol{q} \rrbracket_{porous} = n_f \llbracket w_f - w_s \rrbracket_{porous} \tag{2.31}$$

The velocity jumps inside the porous medium are related to the velocity jumps inside the fracture through:

$$\llbracket w_f \rrbracket_{porous} = \frac{1}{n_f}\llbracket w_f \rrbracket_{fracture} \tag{2.32}$$

$$\llbracket w_s \rrbracket_{porous} = \frac{1}{n_f}\llbracket w_s \rrbracket_{fracture} \tag{2.33}$$

Substituting these definitions in Eq. 2.31 results in the total fracture outflow:

$$\llbracket \boldsymbol{n}_{\Gamma_d}\cdot\boldsymbol{q} \rrbracket = \llbracket w \rrbracket_f - \llbracket w \rrbracket_s \tag{2.34}$$

with the fracture outflow due to changes in fluid velocity profile given by Eq. 2.30, and the fracture inflow due to changes in fracture height given by:

$$\llbracket w \rrbracket_s = \frac{\partial h}{\partial t} = \boldsymbol{n}_{\Gamma_d}\cdot\llbracket \dot{\boldsymbol{u}} \rrbracket \tag{2.35}$$

Eq. 2.34 can be used to include the effects of the fracture on the fluid pressure without explicitly simulating the fluid within the fracture. Due to the continuous pressure model, no additional degrees of freedom are added by using this fracture outflow model. Aditionally, the fluid velocity profile inside the fracture, Eq. 2.26, can be re-obtained by post processing the interstitial pressure and displacements of the porous medium at the discontinuity.

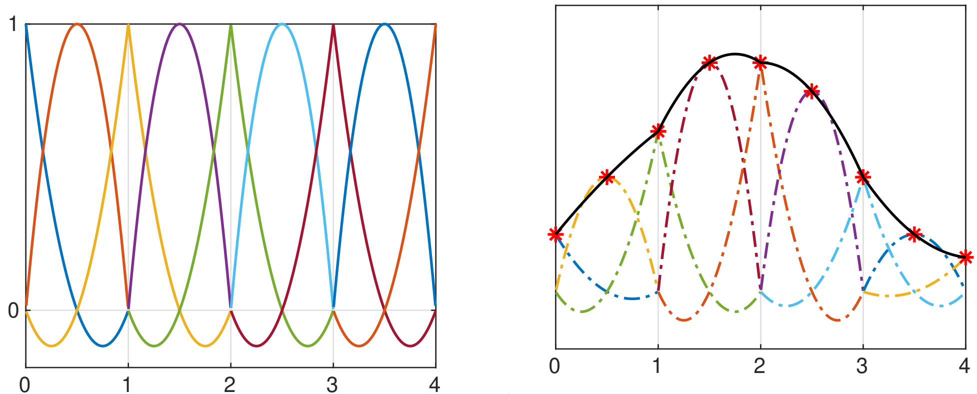

(a) Basis functions

(b) Example of possible solution, using the red markers as control points

Figure 2.2: Example of quadratic Lagrangian basis functions for four elements.

2.2. DISCRETISATION

The weak form of the momentum balance is obtained by multiplying Eq. 2.5 (neglecting the inertia term) with the test function $\boldsymbol{\eta}$ for the displacements and using the divergence theorem. This results in:

$$\int_{\Omega} \nabla\boldsymbol{\eta} : (\boldsymbol{\sigma}_s - \alpha p \boldsymbol{I})\,\mathrm{d}\Omega - \int_{\Gamma_d} \boldsymbol{\eta}\cdot(\boldsymbol{\tau}_d - p\boldsymbol{n}_d)\,\mathrm{d}\Gamma_d = \int_{\Gamma_t} \boldsymbol{\eta}\cdot\overline{\boldsymbol{\tau}}\,\mathrm{d}\Gamma_t \tag{2.36}$$

Similarly, Eq. 2.18 is transformed into a weak format by multiplying with the test function for the pressure, ζ, and performing integration by parts for the interstitial fluid flux term:

$$\int_{\Omega} \alpha\zeta\nabla\cdot\dot{\boldsymbol{u}}\,\mathrm{d}\Omega + \int_{\Omega} k_f^* \left|\nabla p\right|^{1/n-1} \nabla\zeta\cdot\nabla p\,\mathrm{d}\Omega + \int_{\Omega} \frac{1}{M}\zeta\dot{p}\,\mathrm{d}\Omega + \int_{\Gamma_d} \zeta\left(\llbracket w \rrbracket_f - \llbracket w \rrbracket_s\right)\mathrm{d}\Gamma_d = -\int_{\Gamma_q} \zeta\overline{q}\,\mathrm{d}\Gamma_q \tag{2.37}$$

2.2.1. INTERPOLATION FUNCTIONS

LAGRANGE POLYNOMIALS

To perform the spatial discretisation of Eq. 2.36 and 2.37 interpolation functions are needed to represent the interstitial fluid pressure and the solid displacements. Traditional finite element methods use Lagrangian polynomials to perform this discretisation. The main advantage of these Lagrangian polynomials, shown in Figure 2.2, is that they are only non-zero in the element in which their control point is located. This allows the internal force vector and tangential stiffness matrix required for finite element analyses to be constructed in an element-wise manner by summing the contributions of each individual element. Other advantages include the Lagrangian polynomials being the same for each element, and the values in the control-points corresponding to the values of the function at those points.

The main disadvantage of Lagrangian polynomials, however, is their lack of higher order inter-element continuity [63]. While increasing the order of the Lagrangian functions increases the continuity inside the elements, at their element boundaries the continuity is always C^0. This C^0 inter-element continuity is independent of the order of the functions used, and results in discontinuous gradients between elements, as shown in Figure 2.3.

The governing equations derived in Section 2.1 show that the stresses inside the porous material depend on the displacement gradients, and therefore are discontinuous when Lagrangian polynomials are used to discretise the displacements. Similarly, the fluid flux inside the porous medium depends on interstitial pressure gradients, and is therefore also discontinuous between elements [100]. While this discontinuous fluid flux at the element

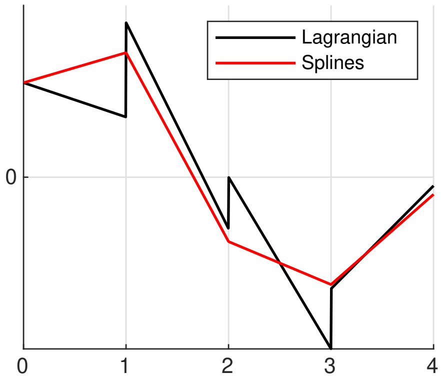

Figure 2.3: Example of gradients of quadratic interpolants resulting from the functions shown in 2.2b and 2.4b.

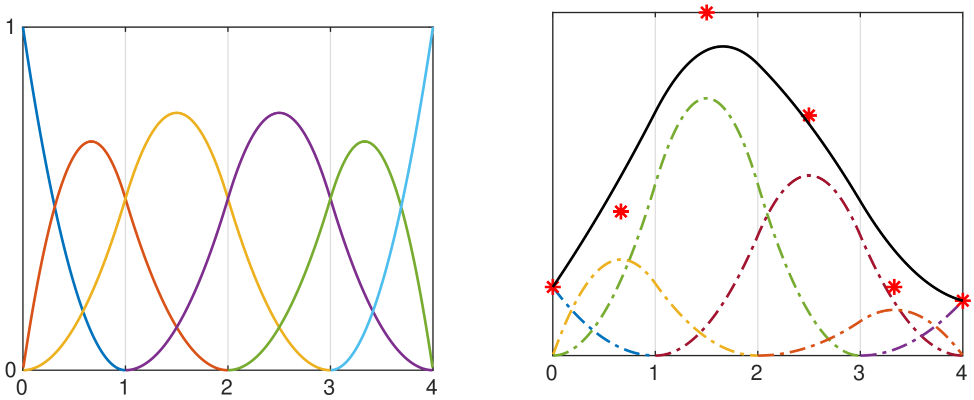

(a) Basis functions

(b) Example of possible solution, using the red markers as control points

Figure 2.4: Example of quadratic B-spline basis functions for four elements, using knot vector [0 0 0 1 2 3 4 4 4].

boundaries does not result in issues with global mass conservation, the resulting fluxes at the element boundaries are not locally mass-conserving.

The fracture outflow, Eq. 2.30, also depends on first derivatives of the displacements, and first and second derivatives of the interstitial fluid pressure. However, since this fracture outflow is directly based on changes in velocity profile, and does not explicitly keep track of the fluid entering and leaving the fracture, the discontinuous gradients between elements results in the fracture outflow term being slightly non-mass-conserving. Furthermore, post-processing to regain the fracture inflow and fluid velocity profiles within the fracture will result in discontinuous velocities.

NON-UNIFORM RATIONAL B-SPLINES

One way to obtain an increased inter-element continuity is by using Non-Uniform Rational Basis Splines (NURBS) [174]. Instead of defining elements, as is done for Lagrangian interpolants, NURBS are defined by using a knot vector which describes the splines in the complete domain, as shown in Figure 2.4. By using interpolation functions that span multiple elements, NURBS of order p are able to obtain an inter-element continuity of C^{p-1}. This inter-element continuity can be further altered by inserting additional knots at pre-existing knots, reducing the continuity to C^{p-k} at the location of the knot with multiplicity k. This knot insertion can be used to locally reduce the continuity to represent sharp changes in mesh direction, or discontinuities such as fractures [227, 234].

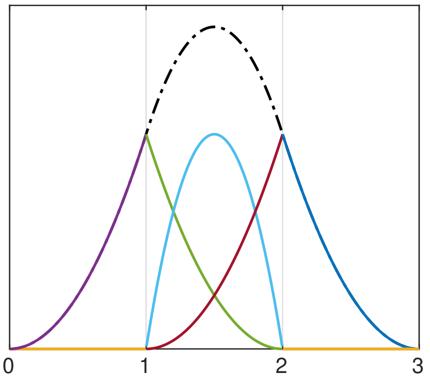

Figure 2.5: Example of Bézier extraction of the dotted B-spline into Bernstein polynomials.

NURBS are commonly used in isogeometric analysis (IGA), which aims to represent the geometry of the problem, and the finite element mesh using the same shape functions and discretisation [63, 97]. While this allows for an exact representation of the geometry, and results in smooth solutions without reduced continuity at the location of the knots, one of the main advantages of the Lagrangian interpolants is lost: NURBS are not only non-zero in the element their corresponding control-point is located in, but also in the neighbouring elements. Furthermore, the NURBS basis functions differ between elements, requiring different shape functions to be calculated for each element.

To negate these disadvantages, the NURBS can be written in terms of Bernstein polynomials through a process called Bézier extraction [33, 204]. This decomposes the non-zero NURBS $\boldsymbol{N}^e(\xi,\eta)$ at the parametric coordinates (ξ,η) into Bernstein polynomials $\mathscr{B}(\xi,\eta)$ as:

$$\boldsymbol{N}^e(\xi,\eta) = \boldsymbol{W}^e \boldsymbol{C}^e \mathscr{B}(\xi,\eta) \left(W^e(\xi,\eta)\right)^{-1} \tag{2.38}$$

with the weight functions being either one in the case of uniform weights, such as with simple rectangular domains, or in the case of non-uniform weights $\boldsymbol{w}^e$ defined through:

$$\begin{aligned} W^e(\xi,\eta) &= \left(\boldsymbol{w}^e\right)^T \boldsymbol{C}^e \mathscr{B}(\xi,\eta) \\ \boldsymbol{W}^e &= \boldsymbol{I}\boldsymbol{C}^e \boldsymbol{w}^e \end{aligned} \tag{2.39}$$

While the Bézier extraction operator $\boldsymbol{C}^e$ differs per elements, it only needs to be calculated once and can then be used throughout the simulation. An example of this Bézier extraction process is shown in Figure 2.5, where the yellow spline from Figure 2.4a is decomposed using the Bézier extraction operators (bold numbers relate to the shown decomposition):

$$\boldsymbol{C}^{e_1} = \begin{bmatrix} 1 & 0 & 0 \\ 0 & 1 & 0.5 \\ \mathbf{0} & \mathbf{0} & \mathbf{0.5} \end{bmatrix} \qquad \boldsymbol{C}^{e_2} = \begin{bmatrix} 0.5 & 0 & 0 \\ \mathbf{0.5} & \mathbf{1} & \mathbf{0.5} \\ 0 & 0 & 0.5 \end{bmatrix} \qquad \boldsymbol{C}^{e_3} = \begin{bmatrix} \mathbf{0.5} & \mathbf{0} & \mathbf{0} \\ 0.5 & 1 & 0.5 \\ 0 & 0 & 0.5 \end{bmatrix}$$

Using Bézier extraction, the interpolants can be evaluated on a per-element basis. This allows the forces and tangential stiffness matrices to be evaluated in a similar manner as in traditional finite element methods.

INTERPOLATION FUNCTION ORDER

The stresses in the solid material from the weak form of the momentum balance, Eq. 2.36, depend on first derivatives of the displacement. Therefore, at least linear functions are needed to evaluate this term, and the use of quadratic NURBS will ensure continuous stresses are obtained. Similarly for the fluid flux term in the mass balance, Eq. 2.37, which

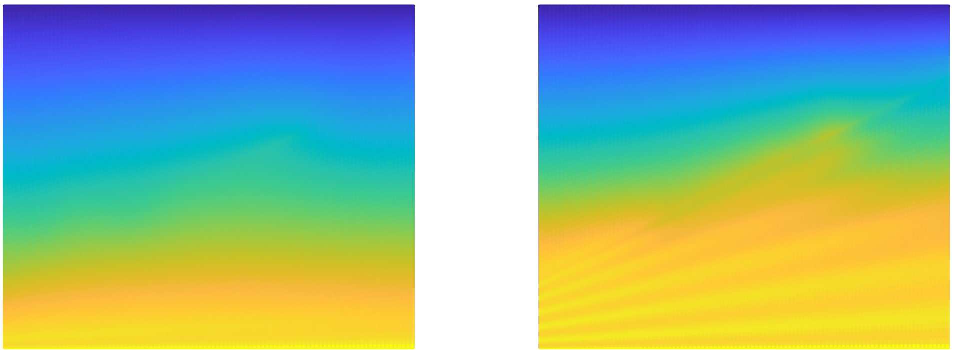

(a) Quartic for deformations, cubic for pressure (b) Cubic for deformations and pressure

Figure 2.6: Example of pressure oscillations due to interpolation function order, using the case from Section 2.3 and $n = 0.25$ (results shown after the first time-step).

depends on pressure gradients, and therefore also requires linear interpolants to be evaluated or quadratic NURBS to obtain a continuous fluid flux. Finally, the fracture outflow term depends on both first and second derivatives of the pressure, and first derivatives of the fracture opening height. To evaluate all the terms in the fracture outflow, Eq. 2.34, quadratic polynomials are needed for the interstitial fluid pressure, while cubic polynomials will result in a continuous fracture outflow velocity.

Another criterion for coupled systems to determine which order of interpolants to use is the inf-sup (or Ladyzhenskaya–Babuška–Brezzi) condition [53]. This criterion describes the requirement between the discretisation spaces in multi-field systems to retain a well-posed system of governing equations. It comes into effect for poroelasticity problems due to the interaction between the fluid pressure and displacement gradient in the momentum balance, and the solid velocity gradient and fluid pressure changes in the mass balance. One manner which is often considered to fulfil this condition is to use interpolation functions for the solid displacements which are one order higher compared to the fluid pressure [24, 100]. Using these unequal order discretisations will prevent spurious pressure oscillations from occurring. While it is not always the case, and dependent on problem specific parameters [190], the spurious oscillations that might occur when not fulfilling this condition often dominate the solution [117]. An example of these oscillations is shown in Figure 2.6 for the case described in Section 2.3 using a non-Newtonian fluid and 20 × 20 Bézier extracted elements.

When NURBS are used, unequal order meshes can be generated through p-refinement [97, 232]. First, the low order mesh is generated with the knots at the correct locations to obtain the required amount of elements. Next, this polynomial order of this mesh is increased by inserting an extra knot at the location of all knots of the original mesh, for example going from the quadratic knot vector [0 0 0 1 2 3 4 4 4] to the cubic knot vector [0 0 0 0 1 1 2 2 3 3 4 4 4 4]. By repeating every knot, the elements of the low order and high order meshes represent the exact same geometry, including the same inter-element continuity at the element boundaries.

To obtain a continuous fracture inflow velocity, it was chosen to use cubic NURBS to discretise the interstitial fluid pressure for the IGA simulations. To also fulfil the inf-sup condition, quartic NURBS are used for the solid displacement. When traditional finite elements are used, no continuous fracture inflow can be obtained independently of the used polynomial order, and therefore quadratic Lagrangian polynomials are used for the interstitial pressure and displacements for the FEM simulations. While these FEM simulations do not fulfil the inf-sup condition, no oscillations occurred.

2.2.2. Spatial and temporal discretisation

As described in the previous section, the spatial discretisation is performed using Lagrangian finite elements, and NURBS isogeometric elements. Using the interpolants for the solid displacement $\boldsymbol{N}_s$ and the interstitial fluid pressure $\boldsymbol{N}_f$, the pressure and displacement are discretised through a sum over all elements as:

$$\boldsymbol{u} = \sum_{el=1}^{n_{el}} \boldsymbol{N}_s^{el} \boldsymbol{u}^{el} \tag{2.40}$$

$$p = \sum_{el=1}^{n_{el}} \boldsymbol{N}_f^{el} \boldsymbol{p}^{el} \tag{2.41}$$

with $\boldsymbol{u}^{el}$ and $\boldsymbol{p}^{el}$ the values of the control points relevant to the element. Interface elements are used for the fractured and non-fractured parts of the discontinuity. Similar to the discretisation of the interior domain, both Lagrangian interpolants [200, 207] and NURBS [99, 234] were used for these interface elements. This allows the jump in displacement across the interface to be discretised as:

$$[\![\boldsymbol{u}]\!]^{el} = \boldsymbol{N}_d \boldsymbol{u}^{el} \tag{2.42}$$

Since a continuous pressure model is used, the discontinuity only contains a single degree of freedom for the pressure. Therefore, the pressure at the discontinuity is discretised using the same discretisation as the interstitial pressure.

The matrix $\boldsymbol{B}$ is defined to perform the mapping from displacements to strains as:

$$\boldsymbol{\varepsilon}^{el} = \boldsymbol{B}^{el} \boldsymbol{u}^{el} \qquad \boldsymbol{B}^{el} = \begin{bmatrix} \frac{\partial N_{s1}}{\partial x} & 0 & \frac{\partial N_{s2}}{\partial x} & 0 & \dots \\ 0 & \frac{\partial N_{s1}}{\partial y} & 0 & \frac{\partial N_{s2}}{\partial y} & \dots \\ \frac{\partial N_{s1}}{\partial y} & \frac{\partial N_{s1}}{\partial x} & \frac{\partial N_{s2}}{\partial y} & \frac{\partial N_{s2}}{\partial x} & \dots \end{bmatrix} \tag{2.43}$$

and a vector $\boldsymbol{m}$ is introduced to map these strains to the divergence of the displacement:

$$\nabla \cdot \boldsymbol{u} = \boldsymbol{m}^T \boldsymbol{B} \boldsymbol{u} \qquad \boldsymbol{m} = \begin{bmatrix} 1 & 1 & 0 \end{bmatrix}^T \tag{2.44}$$

The temporal discretisation is performed using a backward Euler scheme, with the first time derivative given through:

$$\dot{\square} = \frac{\square^{t+\Delta t} - \square^{t}}{\Delta t} \tag{2.45}$$

and requiring all internal forces and fluxes to be evaluated at time $t + \Delta t$.

Using the spatial discretisation from Eq. 2.40, the weak form for the momentum balance, Eq. 2.36 is discretised as:

$$\boldsymbol{f}_{ext} - \boldsymbol{f}_{int} - \boldsymbol{f}_d = \boldsymbol{0} \tag{2.46}$$

with the external force $\boldsymbol{f}_{ext}$ defined in a standard manner as:

$$\boldsymbol{f}_{ext} = \int_{\Gamma_t} \boldsymbol{N}_s^T \bar{\boldsymbol{\tau}} \, \mathrm{d}\Gamma_t \tag{2.47}$$

The forces resulting from the interior of the porous media are given by:

$$\boldsymbol{f}_{int} = \int_{\Omega} \boldsymbol{B}^T \boldsymbol{D}_{el} \boldsymbol{B} \boldsymbol{u}^{t+\Delta t} \, \mathrm{d}\Omega - \int_{\Omega} \alpha \boldsymbol{B}^T \boldsymbol{m} \boldsymbol{N}_f \boldsymbol{p}^{t+\Delta t} \, \mathrm{d}\Omega \tag{2.48}$$

using the linear-elastic stiffness matrix $\boldsymbol{D}_{el}$. Finally, the internal forces related to the discontinuity are determined using interface discretisation of Eq. 2.42, and given by:

$$\boldsymbol{f}_d = \int_{\Gamma_d} \boldsymbol{N}_d^T \boldsymbol{R}^T \boldsymbol{\tau}_d^{t+\Delta t} \, \mathrm{d}\Gamma_d - \int_{\Gamma_d} \boldsymbol{N}_d^T \boldsymbol{n}_{\Gamma_d} \boldsymbol{N}_f \boldsymbol{p}^{t+\Delta t} \, \mathrm{d}\Gamma_d \tag{2.49}$$

Since no propagating fractures are simulated, no cohesive zone model has been included. The tractions along the discontinuity are therefore given by:

$$\boldsymbol{\tau}_d^{t+\Delta} = \boldsymbol{D}_d \boldsymbol{R} \boldsymbol{N}_d \boldsymbol{u}^{t+\Delta t} \tag{2.50}$$

with the dummy stiffness matrix $\boldsymbol{D}_d$ containing large values for the intact part of the discontinuity, and being zero for the interface elements representing the fracture.

In a similar manner, the weak form of the mass conservation from Eq. 2.37 is discretised as:

$$\boldsymbol{q}_{ext} - \boldsymbol{q}_{int} - \boldsymbol{q}_{dh} - \boldsymbol{q}_{dp} = \boldsymbol{0} \tag{2.51}$$

with the external fluid flux given by:

$$\boldsymbol{q}_{ext} = -\Delta t \int_{\Gamma_q} \boldsymbol{N}_f^T \overline{q} \, \mathrm{d}\Gamma_q \tag{2.52}$$

and the internal fluid flux given by:

$$\begin{aligned} \boldsymbol{q}_{int} = -\int_\Omega \alpha \boldsymbol{N}_f^T \boldsymbol{m}^T \boldsymbol{B} \left(\boldsymbol{u}^{t+\Delta t} - \boldsymbol{u}^t\right) \mathrm{d}\Omega - \int_\Omega \frac{1}{M} \boldsymbol{N}_f^T \boldsymbol{N}_f \left(\boldsymbol{p}^{t+\Delta t} - \boldsymbol{p}^t\right) \mathrm{d}\Omega \\ - \Delta t \int_\Omega k_f^* \nabla \boldsymbol{N}_f^T \left|\nabla \boldsymbol{N}_f \boldsymbol{p}^{t+\Delta t}\right|^{\frac{1}{n}-1} \nabla \boldsymbol{N}_f \boldsymbol{p}^{t+\Delta t} \, \mathrm{d}\Omega \end{aligned} \tag{2.53}$$

The L^2 norm of the pressure gradient is given in a discrete format as:

$$\left|\nabla \boldsymbol{N}_f \boldsymbol{p}^{t+\Delta t}\right| = \left(\left(\nabla_1 \boldsymbol{N}_f \boldsymbol{p}^{t+\Delta t}\right)^2 + \left(\nabla_2 \boldsymbol{N}_f \boldsymbol{p}^{t+\Delta t}\right)^2\right)^{\frac{1}{2}} \tag{2.54}$$

with ∇_1 and ∇_2 the gradient operators in the Cartesian directions.

The fluid flux due to the discontinuity has been split into two contributions. The contribution related to the fracture inflow due to changes in opening height reads:

$$\boldsymbol{q}_{dh} = -\int_{\Gamma_d} \boldsymbol{N}_f^T \boldsymbol{n}_{\Gamma_d}^T \boldsymbol{N}_d \left(\boldsymbol{u}^{t+\Delta t} - \boldsymbol{u}^t\right) \mathrm{d}\Gamma_d \tag{2.55}$$

The second contribution accounting for the inflow due to changes in velocity profile caused by pressure and height gradients is given by:

$$\begin{aligned} \boldsymbol{q}_{dp} = \Delta t \int_{\Gamma_d} \boldsymbol{N}_f^T \Bigg(\frac{2}{2n+1} \mu_0^{-\frac{1}{n}} \left(\frac{1}{2} \boldsymbol{n}_{\Gamma_d}^T \boldsymbol{N}_d \boldsymbol{u}^{t+\Delta t}\right)^{\frac{1}{n}+2} \left|\nabla \boldsymbol{N}_f \boldsymbol{p}^{t+\Delta t}\right|^{\frac{1}{n}-1} \nabla^2 \boldsymbol{N}_f \boldsymbol{p}^{t+\Delta t} \\ + \mu_0^{-\frac{1}{n}} \left(\frac{1}{2} \boldsymbol{n}_{\Gamma_d}^T \boldsymbol{N}_d \boldsymbol{u}^{t+\Delta t}\right)^{\frac{1}{n}+1} \left|\nabla \boldsymbol{N}_f \boldsymbol{p}^{t+\Delta t}\right|^{\frac{1}{n}-1} \boldsymbol{n}_{\Gamma_d}^T \nabla \boldsymbol{N}_d \boldsymbol{u}^{t+\Delta t} \nabla \boldsymbol{N}_f \boldsymbol{p}^{t+\Delta t} \Bigg) \mathrm{d}\Gamma_d \end{aligned} \tag{2.56}$$

All the terms are integrated using a Gauss integration scheme. This allows the integrals over the domain to be substituted by sums over all elements and integration points:

$$\int_\Omega \square \, \mathrm{d}\Omega = \sum_{el=1}^{n_{el}} \sum_{ip=1}^{n_{ip}} w_{el,ip} \square \tag{2.57}$$

with the values of the shape functions determined in the integration points, and $w_{el,ip}$ the integration weight related to that integration point and element.

2.2.3. NON-LINEAR NEWTON-RAPHSON SOLVER

While most terms of Eq. 2.46 and 2.51 are linear, the terms related to the non-Newtonian fluid flux, Eq. 2.53, and the fracture inflow due to changes in flow profile, Eq. 2.56, are non-linear and depend on values at the new time. To solve this system of equations in a monolithic manner, a Newton-Raphson iterative algorithm is used. The solution is therefore obtained in an iterative manner as:

$$(\boldsymbol{K}_{int} + \boldsymbol{K}_d) \begin{bmatrix} \mathrm{d}\boldsymbol{u} \\ \mathrm{d}\boldsymbol{p} \end{bmatrix}_{j+1} = \begin{bmatrix} \boldsymbol{f}_{ext} \\ \boldsymbol{q}_{ext} \end{bmatrix} - \begin{bmatrix} \boldsymbol{f}_{int} + \boldsymbol{f}_d \\ \boldsymbol{q}_{int} + \boldsymbol{q}_{dp} + \boldsymbol{q}_{dh} \end{bmatrix}_j \tag{2.58}$$

with the tangential stiffness matrices $\boldsymbol{K}_{int}$ and $\boldsymbol{K}_d$ based on the values at the start of the iteration. The number of iterations required to obtain a converged solution depends on how well these tangential stiffness matrices approximate the Jacobian of the system.

The tangential stiffness matrix related to the internal forces and fluxes is given by:

$$\boldsymbol{K}_{int} = \begin{bmatrix} \boldsymbol{K} & \boldsymbol{Q} \\ \boldsymbol{Q}^T & \boldsymbol{C} + \boldsymbol{H} \end{bmatrix} \tag{2.59}$$

The submatrix related to the stresses caused by the displacement of the solid material is given by:

$$\boldsymbol{K} = \frac{\partial \boldsymbol{f}_{int}}{\partial \boldsymbol{u}} = \int_\Omega \boldsymbol{B}^T \boldsymbol{D}_{el} \boldsymbol{B} \, \mathrm{d}\Omega \tag{2.60}$$

The submatrix coupling the solid and fluid, including the interstitial pressure acting on the porous material and the compression of the porous material changing the pressure, is given by:

$$\boldsymbol{Q} = \frac{\partial \boldsymbol{f}_{int}}{\partial \boldsymbol{p}} = \left(\frac{\partial \boldsymbol{q}_{int}}{\partial \boldsymbol{u}} \right)^T = -\int_\Omega \alpha \boldsymbol{B}^T \boldsymbol{m} \boldsymbol{N}_f \, \mathrm{d}\Omega \tag{2.61}$$

The submatrix related to the pressure capacity term is given by:

$$\boldsymbol{C} = \frac{\partial \boldsymbol{q}_{c,int}}{\partial \boldsymbol{p}} = -\int_\Omega \frac{1}{M} \boldsymbol{N}_f^T \boldsymbol{N}_f \, \mathrm{d}\Omega \tag{2.62}$$

The final term related to the fluid diffusion in the interior is given by:

$$\begin{aligned} \boldsymbol{H} = \frac{\partial \boldsymbol{q}_{diff,int}}{\partial \boldsymbol{p}} &= -\Delta t \int_\Omega k_f^* \left| \nabla \boldsymbol{N}_f \boldsymbol{p} \right|^{\frac{1}{n}-1} \left(\nabla \boldsymbol{N}_f \right)^T \nabla \boldsymbol{N}_f \, \mathrm{d}\Omega \\ &- \Delta t \int_\Omega k_f^* \left(\frac{1}{n} - 1 \right) \left| \nabla \boldsymbol{N}_f \boldsymbol{p} \right|^{\frac{1}{n}-3} \left(\nabla \boldsymbol{N}_f \right)^T \left(\nabla \boldsymbol{N}_f \boldsymbol{p} \right) \Big(\left(\nabla_1 \boldsymbol{N}_f \boldsymbol{p} \right) \nabla_1 \boldsymbol{N}_f + \left(\nabla_2 \boldsymbol{N}_f \boldsymbol{p} \right) \nabla_2 \boldsymbol{N}_f \Big) \, \mathrm{d}\Omega \end{aligned} \tag{2.63}$$

which, in the case of a Newtonian fluid ($n = 1$) reduces to:

$$\boldsymbol{H} = -\Delta t \int_\Omega k_f^* \left(\nabla \boldsymbol{N}_f \right)^T \nabla \boldsymbol{N}_f \, \mathrm{d}\Omega \tag{2.64}$$

For the tangential stiffness matrix related to the discontinuity, only the term related to the dummy stiffness is included:

$$\boldsymbol{K}_d = \begin{bmatrix} \frac{\partial \boldsymbol{f}_d}{\partial \boldsymbol{u}} & \boldsymbol{0} \\ \boldsymbol{0} & \boldsymbol{0} \end{bmatrix} \tag{2.65}$$

with:

$$\frac{\partial \boldsymbol{f}_d}{\partial \boldsymbol{u}} = \int_{\Gamma_d} \boldsymbol{N}_d^T \boldsymbol{R}^T \boldsymbol{D}_d \boldsymbol{R} \boldsymbol{N}_d \, \mathrm{d}\Gamma_d \tag{2.66}$$

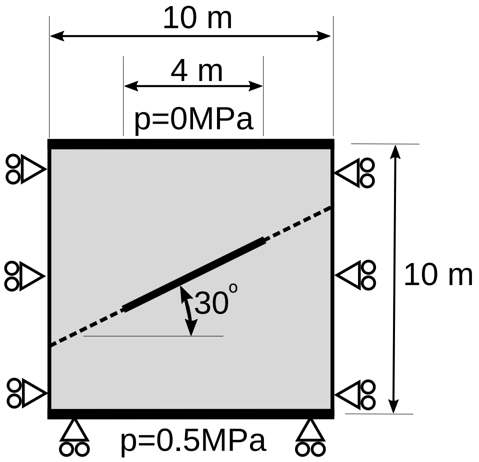

Figure 2.7: Overview of the geometry and boundary conditions

This follows the approach of [187, 232], and results in a symmetric matrix being retained. Furthermore, if a Newtonian fluid is simulated, the complete stiffness matrix will be constant, allowing for pre-conditioners or a LU-factorisation to only be calculated once. A more detailed look at the effects of neglecting the other terms will be taken in Chapter 3.

The convergence of the Newton-Raphson algorithm is checked based on an energy based criterion, with the error after step $j+1$ defined as:

$$\epsilon_{j+1} = \begin{bmatrix} \boldsymbol{f}_{int} + \boldsymbol{f}_d \\ \boldsymbol{q}_{int} + \boldsymbol{q}_{dh} + \boldsymbol{q}_{dp} \end{bmatrix}_{j+1} \cdot \begin{bmatrix} \mathrm{d}\boldsymbol{u} \\ \mathrm{d}\boldsymbol{p} \end{bmatrix}_{j+1} \tag{2.67}$$

which is normalised with the error of the first iteration:

$$error_{j+1} = \frac{\epsilon_{j+1}}{\epsilon_1} \tag{2.68}$$

This energy based convergence criterion has been chosen to give equal weight to the interstitial fluid pressure and the solid displacement. While the interstitial fluid pressure is in the order of MPa ($\mathcal{O}(10^6)$) and the deformations in the order of mm ($\mathcal{O}(10^{-3})$), they get multiplied by the fluid flux times time step (mm, $\mathcal{O}(10^{-3})$) and internal forces (MPa, $\mathcal{O}(10^6)$) respectively.

The discretised equations have been implemented in a C++ code using the JEM/JIVE finite element software library [73]. The code has been verified by comparing its results to solutions from literature. A full overview of the verifications performed is given in Appendix A.1 for Newtonian fluids, and A.2 for non-Newtonian fluids.

2.3. NON-NEWTONIAN FRACTURE FLOW

To show the effect of including the non-Newtonian fluid rheology, a typical boundary value problem has been used. The problem [232] consists of a square 10m × 10m plate, of which the middle 4 m is fractured at a 30° angle as shown in Figure 2.7. This fracture is stationary and not allowed to propagate. A constant pressure of $p = 0.5\,\mathrm{MPa}$ is imposed on the bottom, and a pressure of $p = 0\,\mathrm{MPa}$ is imposed at the top of the domain. The displacement is constrained in horizontal direction on the left and right edges, and in vertical direction on the bottom edge.

The porous material uses Young's modulus $E = 9.0\,\mathrm{GPa}$, Poisson ratio $\nu = 0.4$, Biot modulus $M = 10^{12}$ GPa, Biot coefficient $\alpha = 1.0$ and porosity $n_f = 0.3$. A dummy stiffness of

k [m^2]	n [−]	μ_0 [mPa s^n]	k [m^2]	n [−]	μ_0 [mPa s^n]	k [m^2]	n [−]	μ_0 [mPa s^n]
$1\cdot10^{-8}$	0.6	34.7096	$7\cdot10^{-10}$	0.6	20.3925	$1\cdot10^{-12}$	0.6	5.5011
	0.7	14.2732		0.7	9.5782		0.7	3.5853
	0.8	5.8782		0.8	4.5056		0.8	2.3402
	0.9	2.4235		0.9	2.1218		0.9	1.5291
	1.0	1.0		1.0	1.0		1.0	1.0
	1.1	0.4129		1.1	0.4716		1.1	0.6544
	1.2	0.1706		1.2	0.2225		1.2	0.4284
	1.3	0.0705		1.3	0.1050		1.3	0.2806
	1.4	0.0291		1.4	0.0496		1.4	0.1838

Table 2.1: Permeability, non-Newtonian fluid index, and base viscosity

$k_n = k_s = 10^2$ GPa has been used to prevent the non-fractured interface elements from opening.

Simulations were performed using permeability values of $k = 1.0\cdot10^{-12}$ m^2, $k = 7.0\cdot10^{-10}$ m^2, and $k = 1.0\cdot10^{-8}$ m^2. The viscosity for the Newtonian cases was taken as $\mu = 1.0\,\mathrm{mPa\,s}$. This combination of viscosity and permeabilities results in fluid fluxes through the porous domain of 0.05 mm/s, 35 mm/s, and 0.5 m/s for the low, medium and high permeability cases, respectively (assuming no influence of the fracture).

The power-law index n was varied between 0.6 and 1.4 for the non-Newtonian fluids. The base viscosity μ_0 corresponding to these power-law indices was chosen such that the fluid flux through the porous material in the absence of the fracture remained constant. This results in the ratio between non-Newtonian base viscosity and the Newtonian viscosity being given by:

$$\frac{\mu_0^{\frac{1}{n}}}{\mu} = \frac{n}{3n+1}\left(\frac{50}{3}\right)^{\frac{1+n}{2n}} k^{\frac{1-n}{2n}}\,(2C)^{-\frac{1}{n}}\, n_f^{\frac{n-1}{2n}}\left(\frac{\Delta p}{H}\right)^{\frac{1}{n}-1} \tag{2.69}$$

with Δp the pressure difference of 0.5 MPa being applied over the domain height $H =$ 10 m. By using this base viscosity, the Newtonian fluid is the linearised equivalent of all the non-Newtonian fluids when the linearisation is solely performed based on the porous material (neglecting the influence of the fracture). The resulting base viscosities are given in Table 2.1.

In this section, the simulations used a mesh composed of 80 × 40 Bézier extracted elements, using quartic NURBS for the solid displacement, and cubic NURBS for the interstitial fluid pressure. A time-step size of $\Delta t = 1\,\mathrm{s}$ was used for 50 time-steps, after which all simulations reached a steady-state. All results presented here are given at this steady state ($t = 50\,\mathrm{s}$).

The direction and magnitude of the fluid flux for the $k = 1\cdot10^{-12}$ case using a shear thinning fluid with $n = 0.6$ and a shear-thickening fluid with $n = 1.4$ are shown in Figure 2.8. To highlight the effect of the fracture, the fluid flux relative to the non-Fractured case is given in Figure 2.9. While the magnitude of the flux difference differs between the cases, the overall effect of the fracture is similar. The fracture increases the fluid flow from the bottom left corner towards the bottom fracture tip, and from the top fracture tip to the top right corner. Due to the fracture transporting fluid, less fluid is transported inside the porous material tangential to the fracture.

The fracture opening height for the $k = 10^{-8}$ case is shown in Figure 2.10. Due to the constant pressure boundary conditions used, the opening height is independent of the fluid

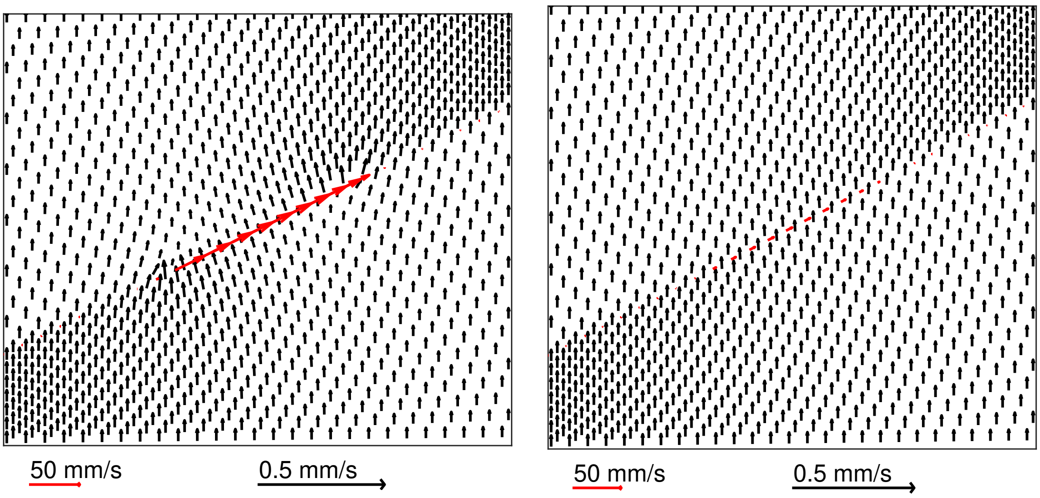

(a) Shear-thinning $n = 0.6$

(b) Shear-thickening $n = 1.4$

Figure 2.8: Fluid flux for the low permeability case. Black arrows represent the fluid flux inside the porous media and red arrows represent the fluid velocity in the centre of the fracture.

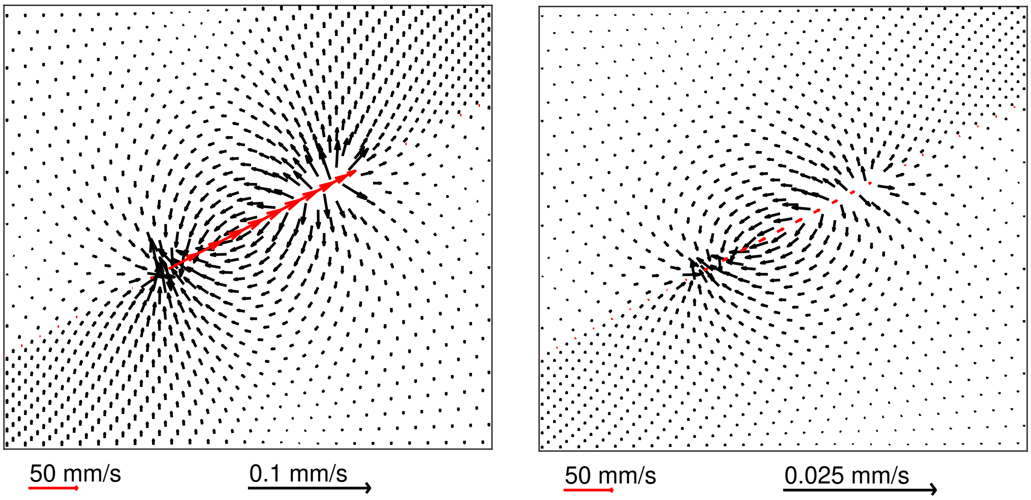

(a) Shear-thinning $n = 0.6$

(b) Shear-thickening $n = 1.4$

Figure 2.9: Difference in fluid flux relative to the non-fractured case for the low permeability case. Black arrows represent the fluid flux inside the porous media and red arrows represent the fluid velocity in the centre of the fracture.

index. The same fracture opening height was also obtained for the cases using the other permeabilities.

The fluid velocity for the high permeability case (Figure 2.11a) shows the shear-thickening fluids obtaining a higher velocity compared to the Newtonian fluid, and the shear-thinning fluids obtaining a lower velocity. Figure 2.11b, the fracture outflow velocity, also reflects this, with more fluid entering and leaving the fracture for the shear-thickening fluids. While the fluid velocity in the centre of the fracture is comparable to the velocity in the porous media (0.5 m/s), the small fracture opening height results in only a small fracture outflow. This fracture inflow is insufficient to alter the pressures in the surrounding porous material.

In contrast, the results for a lower permeability, $k = 7 \cdot 10^{-10}\text{m}^2$, show near to no influence of the fluid index in Figure 2.12. The shear-thinning fluids have slightly higher veloci-

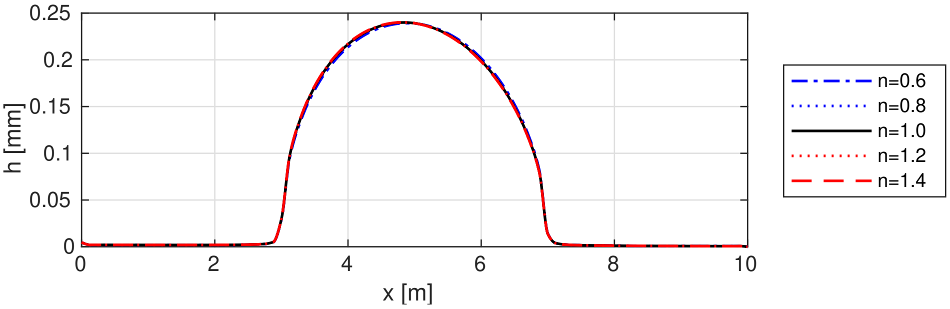

Figure 2.10: Fracture opening height for the $k = 10^{-8}$ m^2 case at steady state.

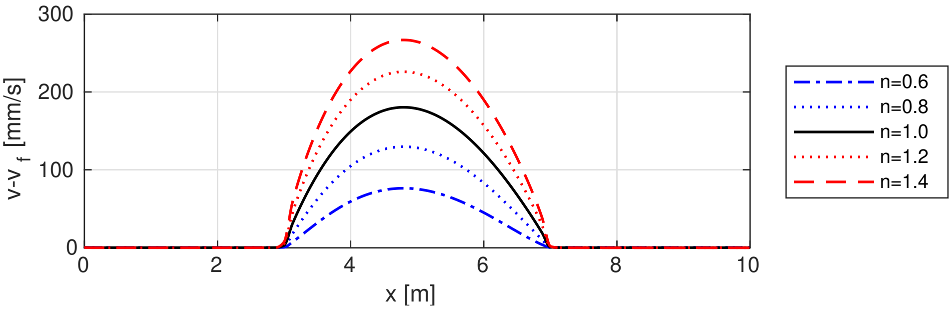

(a) Velocity in the centre of the fracture

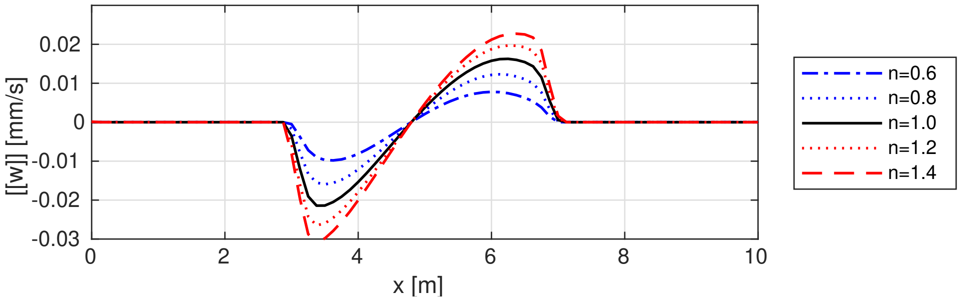

(b) Fracture outflow velocity

Figure 2.11: Results for the $k = 10^{-8}$ m^2 case at steady state.

ties in the middle of the fracture, whereas the shear-thickening fluids obtain higher velocities near the fracture tips. This velocity difference, combined with the different velocity profile shape, results in slight differences in the fracture outflow. Compared to the $k = 10^{-8}$ m^2 cases, the fracture outflow velocity is closer, although still small, relative to the fluid flux inside the porous medium with $q_y = 35$ mm/s. This results in the fracture having a slight influence on the pressure in the surrounding porous material, as shown in Figure 2.12c.

The low permeability cases, Figure 2.13, show the inverse behaviour compared to the high permeability cases. The shear-thinning fluids now have a significantly higher velocity compared to the Newtonian fluid, and the shear-thickening fluids obtain a lower velocity. This is also reflected in the tangential velocity jump, with the shear-thinning fluids having significantly higher inflow velocities. These fracture outflow velocities are comparable to the velocity inside the porous material ($q_y = 0.05$m/s), and therefore the fracture has a large influence on the interstitial fluid pressure, as shown in Figure 2.13d.

By integrating the vertical fluid flux over the top and bottom boundaries, the total fluid flux flowing through the complete domain is determined. This fluid flux is compared to the fluid flux for the non-fractured case to determine the added fluid transport due to the

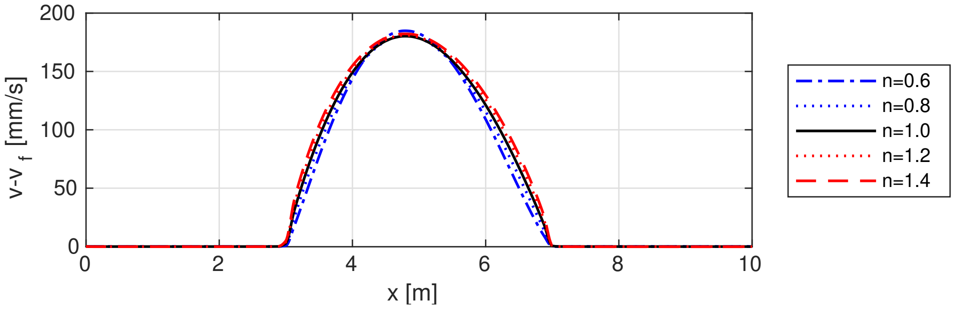

(a) Velocity in the centre of the fracture

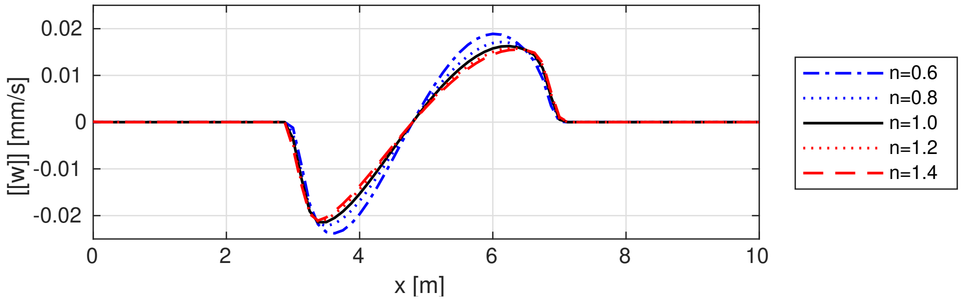

(b) Fracture outflow velocity

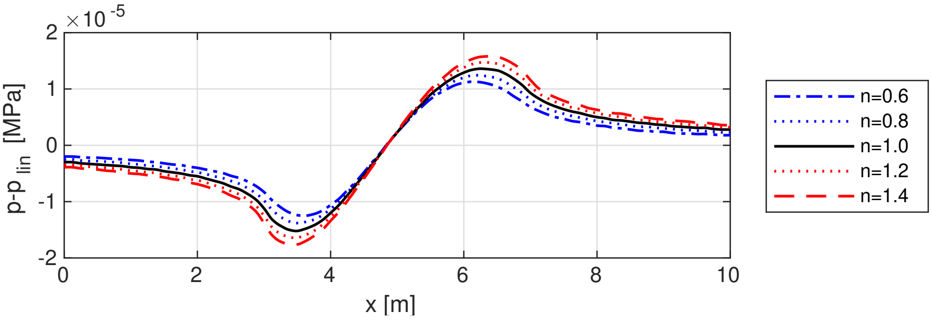

(c) Pressure difference along the discontinuity relative to the non-fractured case.

Figure 2.12: Results for the $k = 7 \cdot 10^{-10}$ m^2 case at steady state.

presence of the fracture:

$$q_{enh} = \frac{q_{frac} - q_0}{q_0} \cdot 100\% \tag{2.70}$$

with q_{frac} the total fluid flux for the fractured case and q_0 the fluid flux for the non-fractured case. The resulting influence of the fracture, normalised with the values for Newtonian fluids, are shown in Figure 2.14. This increase in fluid flux corresponds to the previous results: Dependent on the permeability of the porous material, either the shear-thinning or shear-thickening cases have an enhanced fluid transport compared to the Newtonian cases. For the low permeability cases, the difference between fluid indices is clearest, with the fracture increasing the total fluid transport by up to 2.8% for shear thinning fluids, whereas it is only increased by 0.3% for the shear-thickening $n = 1.4$ fluid.

It is finally noted that the fluid properties were chosen such that for a constant permeability all shear-thinning and shear-thickening fluids linearise to the same Newtonian fluids. The large differences between fluid velocities inside the fracture, and fracture outflow velocities, for varying flow indices indicate the importance of including the non-Newtonian rheology. Furthermore, these effects were mirrored for the low and high permeability cases, whereas near to no difference was observed for the medium permeability case.

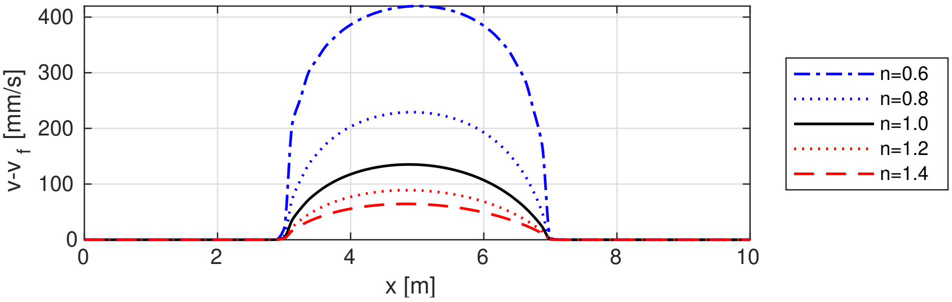

(a) Velocity in the centre of the fracture

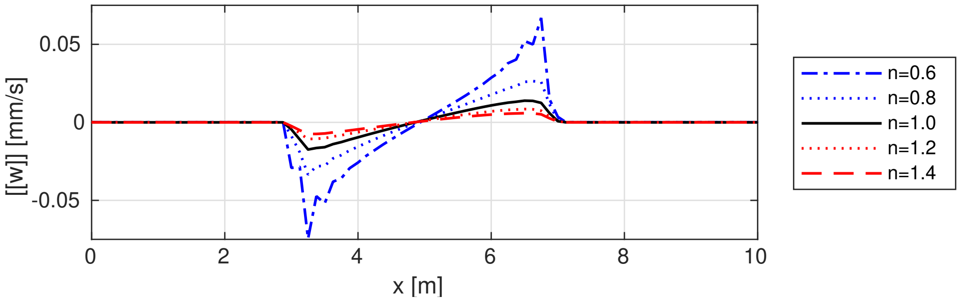

(b) Fracture outflow velocity

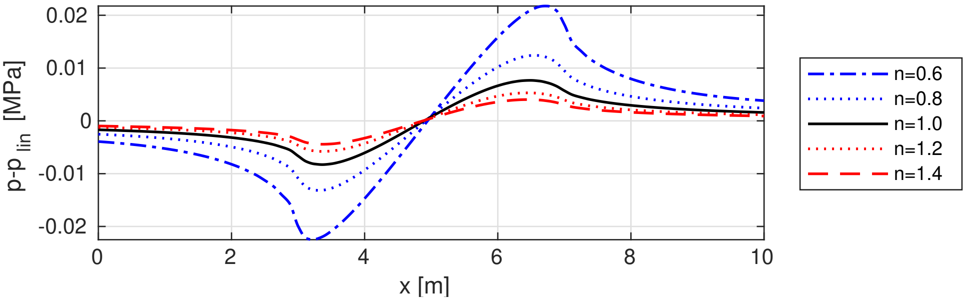

(c) Pressure difference along the discontinuity relative to the non-fractured case.

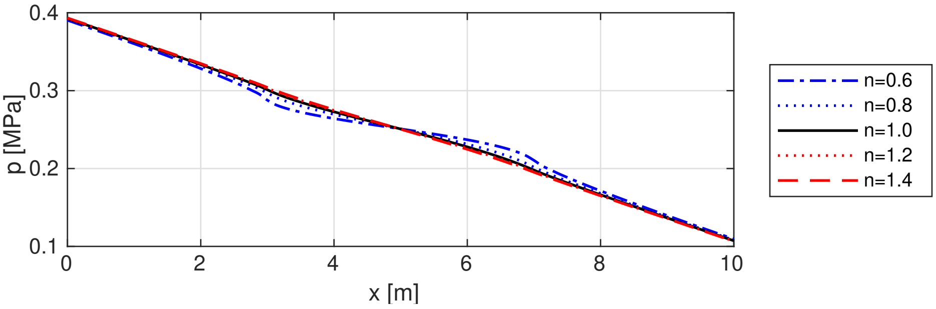

(d) Pressure along the discontinuity

Figure 2.13: Results for the $k = 10^{-12}$ m^2 case at steady state.

2.4. FEM vs IGA

In this section, simulations using meshes ranging from 20×10 to 160×50 elements were performed. After the 100×50 mesh, only the amount of horizontal (Bézier extracted) elements was varied. All simulations used a permeability $k = 10^{-12}$, and non-Newtonian fluid indices $n = 0.6$ and $n = 1.4$. This permeability was chosen since it resulted in the largest influence of the fracture on the interstitial fluid pressure.

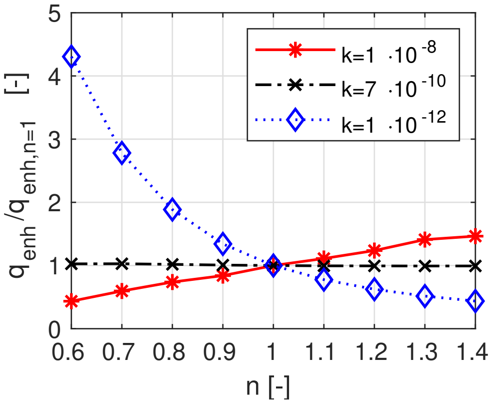

Figure 2.14: Relative increase in fluid transported through the complete domain relative to the Newtonian fluid case, $q_{enh,n=1} = 7.770\cdot10^{-5}$% for $k = 10^{-8}$ m^2, $q_{enh,n=1} = 1.139\cdot10^{-3}$% for $k = 7\cdot10^{-10}$ m^2 and $q_{enh,n=1} = 0.6486$% for $k = 10^{-12}$ m^2.

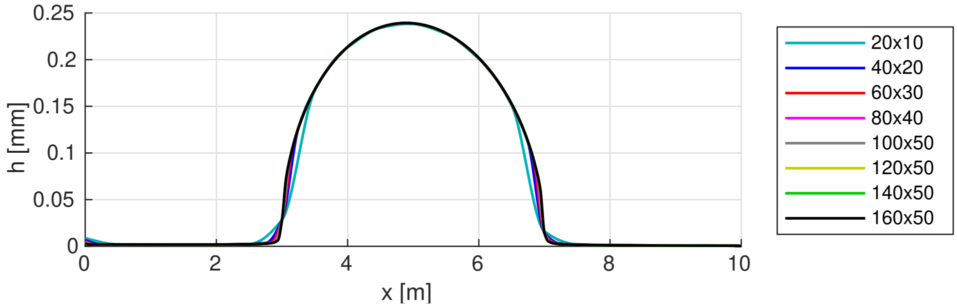

Figure 2.15: Fracture opening heights for $n = 0.6$ using IGA.

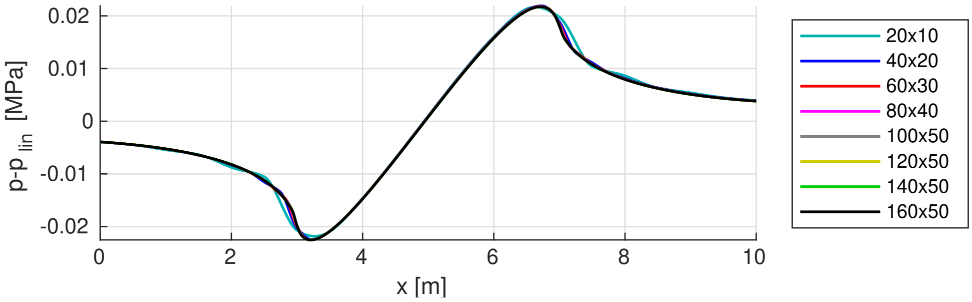

Figure 2.16: Difference in interstitial fluid pressure along the discontinuity compared to a non-fractured case for $n = 0.6$ using IGA.

2.4.1. MESH SENSITIVITY IGA

The fracture opening height using NURBS is shown in Figure 2.15. The centre of the fracture shows near to no difference between the coarsest meshes, whereas near the fracture tips some difference is visible for the 20 × 10 mesh. At the fracture tips, the results are more dependent on the discretisation. This is caused by the quartic NURBS not being able to represent a sharp fracture tip, and instead requiring approximately one element to represent a non-fractured discontinuity. While this results in differences near the fracture tip, these small differences do not seem to influence the centre of the fracture.

Similar to the opening height, the interstitial fluid pressure along the discontinuity, Figure 2.16, shows only minor differences between the coarsest meshes. Further refinement past the 40 × 20 mesh does not visibly alter the solution, indicating that a coarse mesh is

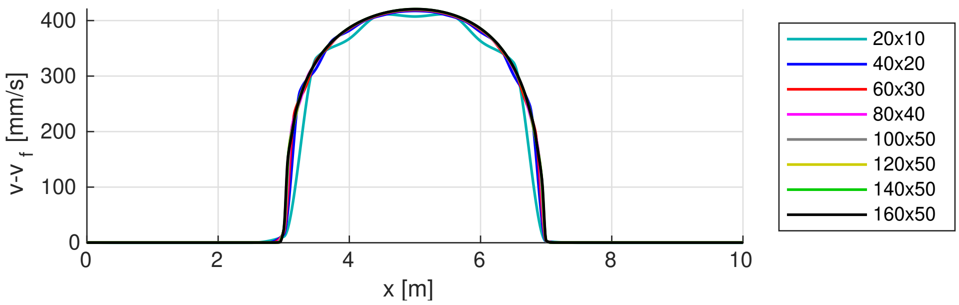

Figure 2.17: Velocity in the centre of the fracture for $n = 0.6$ using IGA.

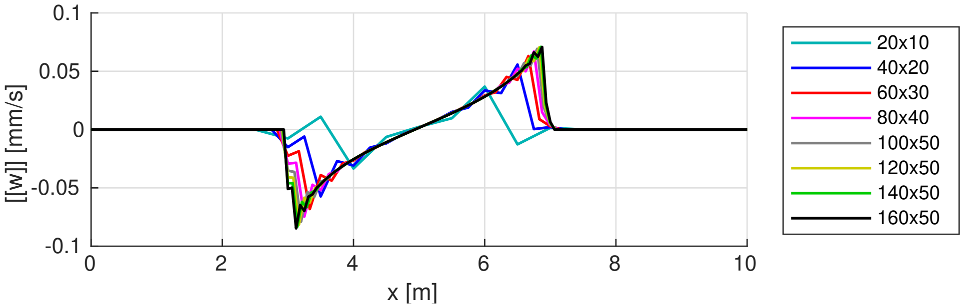

Figure 2.18: Jump in normal velocity for $n = 0.6$ using IGA.

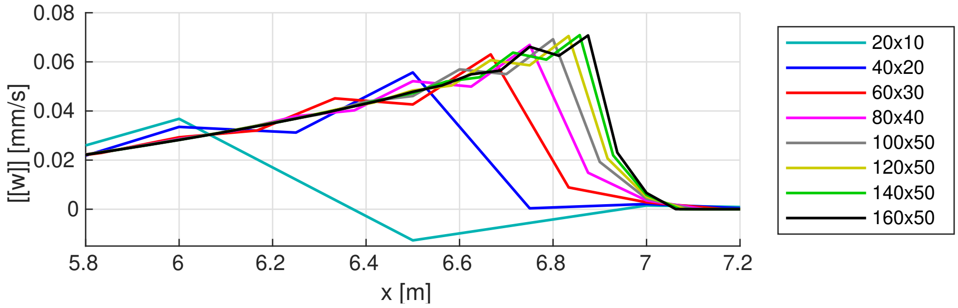

Figure 2.19: Jump in normal velocity around the right fracture tip for $n = 0.6$ using IGA.

sufficient to accurately include the effect of the fracture on the pressure inside the porous material.

The velocity in the centre of the fracture is shown in Figure 2.17. While the coarsest mesh shows oscillations in this velocity in the centre of the fracture, all other meshes obtain correct results. Since the velocity depends non-linearly on the fracture opening height, slight differences between the meshes are seen in the same locations as for the fracture opening height. At the fracture tip, these differences are decreased due to the non-linear dependence on the height, whereas closer to the middle of the fracture these differences become slightly more pronounced.

The fracture outflow, Figure 2.18 and 2.19, show the largest influence of the mesh. The 20×10 mesh shows large oscillations, even resulting in outflow velocities in the opposite direction compared to the finer meshes. While these oscillations lessen for finer meshes, they are still seen for the 160×50 mesh close to the fracture tips. These oscillations do not occur for smaller fracture inflows, as shown by the $n = 1.4$ case in Figures 2.20 and 2.21, and these results show smaller differences between the finest meshes.

From these results it can be concluded that a fairly coarse IGA based mesh is sufficient to model the effect of the fracture on the interstitial pressures and displacements of the porous

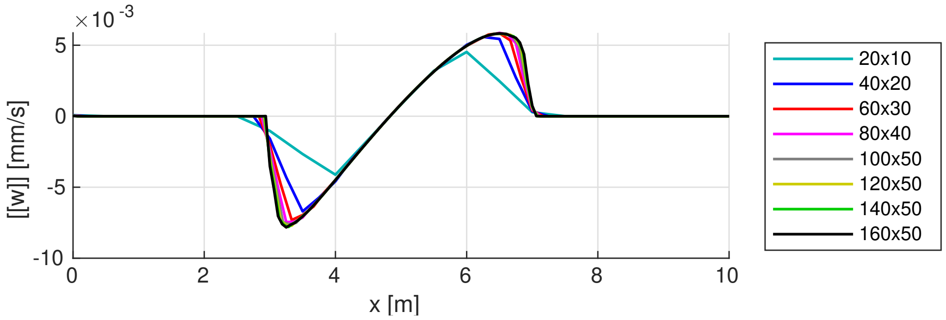

Figure 2.20: Jump in normal velocity for $n = 1.4$ using IGA.

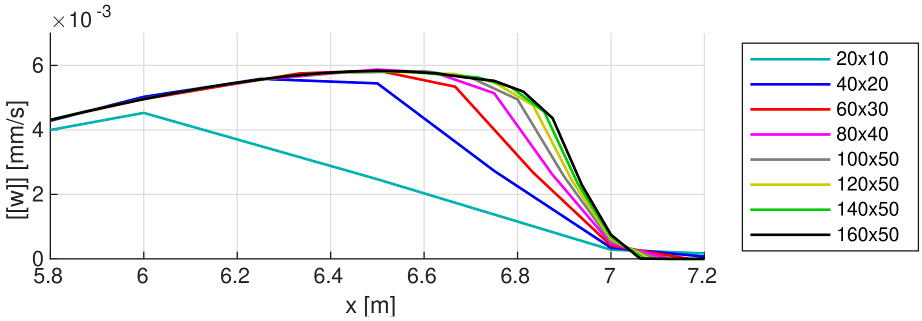

Figure 2.21: Jump in normal velocity around the right fracture tip for $n = 1.4$ using IGA.

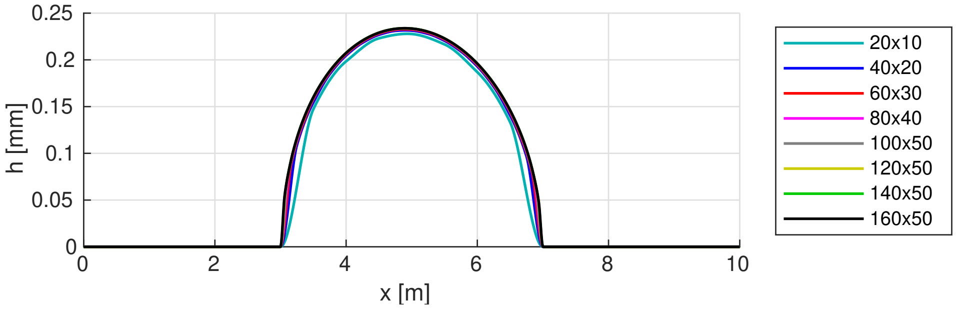

Figure 2.22: Fracture opening heights for $n = 0.6$ using the FEM.

material. When focussing on phenomena in or close to the fracture, however, finer meshes are needed to obtain accurate velocities inside the fracture. Due to the dependence on second derivatives, very fine meshes are needed to obtain accurate fracture outflow velocities, especially close to the fracture tips.

2.4.2. MESH SENSITIVITY FEM

the fracture opening height using quadratic Lagrangian polynomials is shown in Figure 2.22. In contrast to the IGA results, the opening height reaches zero at the fracture tips due to the C^0 inter-element continuity allowing for sharp fracture tips. While slightly larger differences are seen in the centre of the fracture for the FEM results compared to the IGA results, these differences disappear with finer meshes.

The interstitial fluid pressure along the discontinuity, Figure 2.23, shows a larger influence of the mesh. Clear differences are visible up to the 100 × 50 mesh. This is in contrast to the IGA results, for which coarse meshes sufficed to obtain accurate results, and corresponds to earlier results that NURBS are able to obtain more accurate results (for Newtonian fluids) compared to Lagrangian polynomials [99, 100].

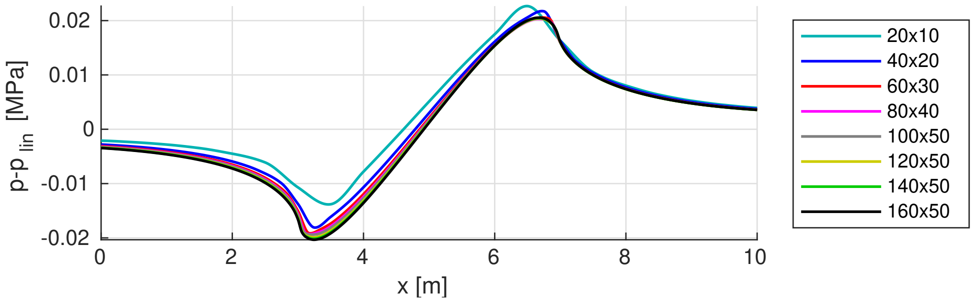

Figure 2.23: Difference in interstitial fluid pressure along the discontinuity compared to a non-fractured case for $n = 0.6$ using the FEM.

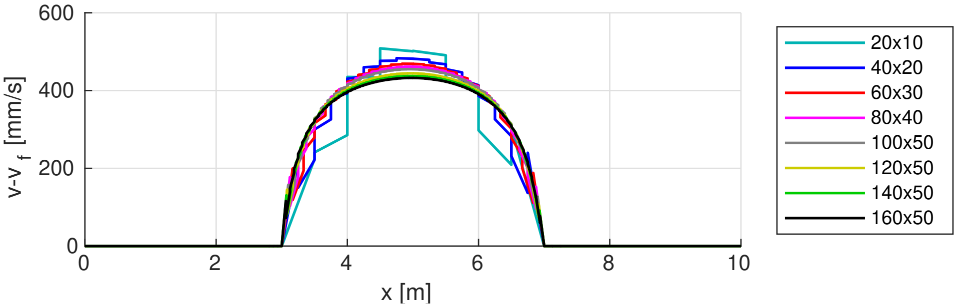

Figure 2.24: Velocity in the centre of the fracture for $n = 0.6$ using the FEM.

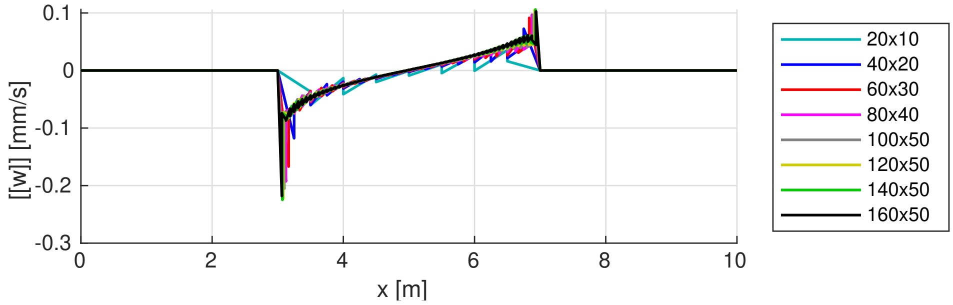

Figure 2.25: Jump in normal velocity for $n = 0.6$ using the FEM.

The velocity in the centre of the fracture is shown in Figure 2.24. Due to the C^0 continuity of the Lagrangian elements, jumps in the velocity occur between the elements. These jumps decrease with finer meshes, but still occur near the fracture tips for even the finest meshes. Furthermore, since the formulation for the fracture outflow is based on the velocity profile, having a discontinuous velocity inside the fracture will result in a small amount of fluid being lost between the elements, resulting in the fracture flow being slightly non-mass-conserving in the case of Lagrangian polynomials.

The jump in fluid velocity normal to the fracture, Figure 2.25 and 2.26, also show the effects of the C^0 inter-element continuity. For coarse meshes, large jumps occur throughout the discontinuity. While refining the mesh results in smaller jumps near the middle of the fracture, the jumps persist near the fracture tip. Furthermore, comparing the results of the finer meshes, these jumps seem to increase in magnitude when the mesh is refined, indicating that even using very fine meshes no accurate results can be obtained.

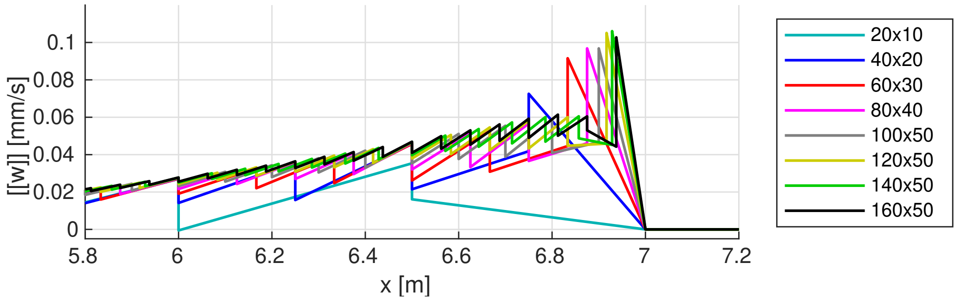

Figure 2.26: Jump in normal velocity around the right fracture tip for $n = 0.6$ using the FEM.

2.5. CONCLUSION

In this chapter, a fracture-scale sub-grid model for non-Newtonian fluid flows within fractures has been derived. This model, based on the continuous pressure model, allows the influence of the fracture on the surrounding porous material to be included by imposing the jump in velocity normal to the fracture. By post-processing the interstitial fluid pressure and displacements, the model furthermore allows for re-obtaining the velocity inside the fracture, without explicitly needing to simulate the interior of the fractures.

By simulating a typical boundary value problem, the influence of including the non-Newtonian rheology was shown. While for some values for the permeability of the porous material near to no effect of including the non-Newtonian behaviour was observed, results using a lower permeability showed significantly higher velocities inside the fracture for shear-thinning fluids, whereas increasing the permeability resulted in higher velocities for the shear-thickening fluids. These differences also resulted in differences in interstitial fluid pressure, and influenced the total fluid transport through the porous domain.

Finally, mesh sensitivity studies were performed using NURBS and standard Lagrangian finite elements. It was shown that a coarse mesh using NURBS was sufficient to obtain accurate solutions for the interior of the domain, while a finer mesh was needed to obtain accurate results for the fracture velocities. Using standard finite elements, correct results for the interstitial fluid pressure and displacements could also be obtained in the interior of the domain. However, standard finite elements were not able to obtain a continuous velocity in the middle of the fracture, and even when using fine meshes obtained incorrect results for the fracture inflow. This shows that while finite elements are sufficient to simulate the overall behaviour of the fractured porous material, NURBS are needed when a more detailed look into the velocities in and around the fracture is required.

3

CONVERGENCE OF THE CONTINUOUS PRESSURE MODEL

In the previous chapter, a monolithic scheme was used to solve the deformations and pressures inside the porous material at the same time as the fluid flow inside the fracture. While this is a commonly used method [49, 113, 155, 207, 232], it requires repetitively solving a large system of equations in which only a small part related to the discontinuity is non-linear. Because of this small non-linear part, pre-conditioners used to solve the system have to be recalculated every iteration, significantly increasing the computational cost to include fractures in the porous material. This can be (partly) negated by using a partially consistent stiffness matrix, for instance only including the linear and constant terms in the stiffness matrix [187]. However, it is unclear how deviating from a consistent tangential matrix influences the convergence of a Newton-Raphson solver when solving poroelasticity problems.

A different approach is to solve the system in a staggered manner. This method is often used to resolve the mass balance and momentum balance iteratively, allowing for pre-existing and optimized solvers to be used for each equation [114, 115, 209]. A similar approach is possible for hydraulic fractures, iterating between solving the linear poroelastic material, and the non-linear fracture flow [90, 122, 123, 168]. This splits the system into two, a constant part that only needs to be calculated (and possibly pre-conditioned) once, and a non-linear part which requires updating each iteration. While this reduces the size of the system matrices, and therefore the duration required to solve each iteration, convergence issues often arise due to the coupling between the two systems.

In this chapter, the effects of including terms related to the fracture in the tangential stiffness matrix will be analysed. While a monolithic scheme is used, it should be noted that in the absence of fracture flow related terms no difference exists between staggered and monolithic schemes. The terms required to obtain a consistent stiffness matrix will be detailed in Section 3.1, a short description of the role of these terms will be given, and a comparison is made with other pre-existing schemes (both monolithic and staggered). Next, a case containing a single fracture is simulated and the convergence of this case is studied, focusing on the effects of including the tangential stiffness terms, the order of the used interpolants, and whether Lagrangian or NURBS based interpolants are used. In section 3.3 these results will be extended to a case containing multiple fractures. Finally, in Section 3.4 a non-Newtonian power-law fluid is used and the effect of the added non-linearities is discussed. The results presented in this chapter have been previously published in [1].

3.1. CONSISTENT STIFFNESS MATRICES

The same model and discretisation as detailed in Section 2.1-2.2 are used in this chapter. Next to using the quadratic Lagrangian finite elements (hereafter referred to as 2×2 FEM) and NURBS using quartic polynomials for the displacement and cubic for the interstitial pressure (4×3 IGA), simulations have also been performed using equal order NURBS meshes, using cubic NURBS for the displacement and pressure (3×3) IGA and quadratic NURBS (2×2 IGA).

Also similar to the previous chapter, a Newton-Raphson iterative solver is used to obtain a converged solution in a monolithic manner. Therefore, the discretised equations are solved iteratively through Eq. 2.58:

$$(\boldsymbol{K}_{int}+\boldsymbol{K}_d)\begin{bmatrix}\mathrm{d}\boldsymbol{u}\\ \mathrm{d}\boldsymbol{p}\end{bmatrix}_{j+1}=\begin{bmatrix}\boldsymbol{f}_{ext}\\ \boldsymbol{q}_{ext}\end{bmatrix}-\begin{bmatrix}\boldsymbol{f}_{int}+\boldsymbol{f}_d\\ \boldsymbol{q}_{int}+\boldsymbol{q}_{dp}+\boldsymbol{q}_{dh}\end{bmatrix}_j \tag{3.1}$$

and the tangential stiffness matrix related to the interior given by Eq. 2.59.

In this chapter, the tangential stiffness terms related to the interface are added one-by-one, to investigate the influence of including or omitting these terms. The stiffness matrix related to the discontinuity is given by:

$$\boldsymbol{K}_d=\begin{bmatrix}\frac{\partial \boldsymbol{f}_d}{\partial \boldsymbol{u}} & \frac{\partial \boldsymbol{f}_d}{\partial \boldsymbol{p}}\\ \frac{\partial \boldsymbol{q}_{dh}}{\partial \boldsymbol{u}}+\frac{\partial \boldsymbol{q}_{dp}}{\partial \boldsymbol{u}} & \frac{\boldsymbol{q}_{dp}}{\partial \boldsymbol{p}}\end{bmatrix} \tag{3.2}$$

The first term, included for all cases, is the contribution due to the interface stiffness, given by Eq. 2.66:

$$\frac{\partial \boldsymbol{f}_d}{\partial \boldsymbol{u}}=\int_{\Gamma_d}\boldsymbol{N}_d^T\boldsymbol{R}^T\boldsymbol{D}_d\boldsymbol{R}\boldsymbol{N}_d\,\mathrm{d}\Gamma_d \tag{3.3}$$

This term has to be included to constrain the non-fractured elements from opening, thereby preventing free-body motion in part of the domain. Not including this term would result in an under-constrained system of equations, since no solid inertia terms have been included. Since this is the only complete term that can be included without rendering the tangential stiffness matrix non-symmetric, this was the only term included in earlier simulations using the continuous pressure model [187, 232].

The second term relates the changes in pressure acting on the fracture walls to the forces resulting from the discontinuity:

$$\frac{\partial \boldsymbol{f}_d}{\partial \boldsymbol{p}}=-\int_{\Gamma_d}\boldsymbol{N}_d^T\boldsymbol{n}_{\Gamma_d}\boldsymbol{N}_f\,\mathrm{d}\Gamma_d \tag{3.4}$$

Since this term and the previous term are both linear, including both terms will result in exact values for the displacement after each iteration, based on the updated pressure. This corresponds to an iterative scheme in which the fracture outflow is calculated based on old pressures and displacements, and then held constant while the updated displacements and pressures are calculated. This is similar to the $P \rightarrow W$/drained hydraulic fracture split which is used for impermeable fractures [90, 168].

The third sub-matrix added is related to the fluid absorbed into the fracture due to changes in the opening height of the fracture:

$$\frac{\partial \boldsymbol{q}_{dh}}{\partial \boldsymbol{u}}=-\int_{\Gamma_d}\boldsymbol{N}_f^T\boldsymbol{n}_{\Gamma_d}^T\boldsymbol{N}_d\,\mathrm{d}\boldsymbol{\Gamma}_d=\left(\frac{\partial \boldsymbol{f}_d}{\partial \boldsymbol{p}}\right)^T \tag{3.5}$$

By including both the submatrix from Eq. 3.4 and 3.5 a symmetric system is regained, which can be beneficial for computational efficiency and storage. Furthermore, if a Newtonian fluid is simulated all these terms and all terms relating to the interior of the porous medium are constant. This allows for the system matrices to only be constructed once, and allows more efficient use of preconditioners or direct LU solvers. Including all terms up to and including this term results in a similar scheme as the undrained split scheme for impermeable fractures, which has an improved convergence compared to the drained split [168].

The final two terms, related to changes in the fracture inflow due to changes in velocity profile inside the fracture are:

$$
\begin{aligned}
\frac{\partial \boldsymbol{q}_{dp}}{\partial \boldsymbol{p}} = &\int_{\Gamma_d} \frac{2\Delta t}{2n+1}\mu_0^{-\frac{1}{n}}\left(\frac{1}{2}\boldsymbol{n}_{\Gamma_d}^T\boldsymbol{N}_d\boldsymbol{u}\right)^{\frac{1}{n}+2}\left|\boldsymbol{\nabla}\boldsymbol{N}_f\boldsymbol{p}\right|^{\frac{1}{n}-1}\boldsymbol{N}_f^T\boldsymbol{\nabla}^2\boldsymbol{N}_f\,\mathrm{d}\Gamma_d \\
&+\int_{\Gamma_d} \frac{2\Delta t}{2n+1}\left(\frac{1}{n}-1\right)\mu_0^{-\frac{1}{n}}\left(\frac{1}{2}\boldsymbol{n}_{\Gamma_d}^T\boldsymbol{N}_d\boldsymbol{u}\right)^{\frac{1}{n}+2}\left|\boldsymbol{\nabla}\boldsymbol{N}_f\boldsymbol{p}\right|^{\frac{1}{n}-2}\boldsymbol{\nabla}^2\boldsymbol{N}_f\boldsymbol{p}\boldsymbol{N}_f^T\boldsymbol{\nabla}\boldsymbol{N}_f\cdot\mathrm{sgn}\left(\boldsymbol{\nabla}\boldsymbol{N}_f\boldsymbol{p}\right)\,\mathrm{d}\Gamma_d \\
&+\int_{\Gamma_d} \frac{\Delta t}{n}\mu_0^{-\frac{1}{n}}\left|\boldsymbol{\nabla}\boldsymbol{N}_f\boldsymbol{p}\right|^{\frac{1}{n}-1}\left(\frac{1}{2}\boldsymbol{n}_{\Gamma_d}^T\boldsymbol{N}_d\boldsymbol{u}\right)^{\frac{1}{n}+1}\left(\boldsymbol{n}_{\Gamma_d}^T\boldsymbol{\nabla}\boldsymbol{N}_d\boldsymbol{u}\right)\boldsymbol{N}_f^T\boldsymbol{\nabla}\boldsymbol{N}_f\,\mathrm{d}\Gamma_d
\end{aligned}
\tag{3.6}
$$

and

$$
\begin{aligned}
\frac{\partial \boldsymbol{q}_{dp}}{\partial \boldsymbol{u}} = &\int_{\Gamma_d} \frac{\Delta t}{n}\mu_0^{-\frac{1}{n}}\left|\boldsymbol{\nabla}\boldsymbol{N}_f\boldsymbol{p}\right|^{\frac{1}{n}-1}\boldsymbol{\nabla}^2\boldsymbol{N}_f\boldsymbol{p}\left(\frac{1}{2}\boldsymbol{n}_{\Gamma_d}^T\boldsymbol{N}_d\boldsymbol{u}\right)^{\frac{1}{n}+1}\boldsymbol{N}_f^T\boldsymbol{n}_{\Gamma_d}^T\boldsymbol{N}_d\,\mathrm{d}\Gamma_d \\
&+\int_{\Gamma_d} \Delta t\mu_0^{-\frac{1}{n}}\left|\boldsymbol{\nabla}\boldsymbol{N}_f\boldsymbol{p}\right|^{\frac{1}{n}-1}\boldsymbol{\nabla}\boldsymbol{N}_f\boldsymbol{p}\left(\frac{1}{2}\boldsymbol{n}_{\Gamma_d}^T\boldsymbol{N}_d\boldsymbol{u}\right)^{\frac{1}{n}+1}\boldsymbol{N}_f^T\boldsymbol{n}_{\Gamma_d}^T\boldsymbol{\nabla}\boldsymbol{N}_d\,\mathrm{d}\Gamma_d \\
&+\int_{\Gamma_d} \frac{\Delta t}{2}\left(\frac{1}{n}+1\right)\mu_0^{-\frac{1}{n}}\left|\boldsymbol{\nabla}\boldsymbol{N}_f\boldsymbol{p}\right|^{\frac{1}{n}-1}\boldsymbol{\nabla}\boldsymbol{N}_f\boldsymbol{p}\left(\frac{1}{2}\boldsymbol{n}_{\Gamma_d}^T\boldsymbol{N}_d\boldsymbol{u}\right)^{\frac{1}{n}}\left(\boldsymbol{n}_{\Gamma_d}\boldsymbol{\nabla}\boldsymbol{N}_d\boldsymbol{u}\right)\boldsymbol{N}_f^T\boldsymbol{n}_{\Gamma_d}^T\boldsymbol{N}_d\,\mathrm{d}\Gamma_d
\end{aligned}
\tag{3.7}
$$

with sgn(·) the signum function. Including both these terms results in a consistent tangential stiffness matrix. However, since these two terms are dependent on the displacement and pressure, they need to be re-calculated for each iteration. Furthermore, while the $\partial \boldsymbol{q}_{dp}/\partial \boldsymbol{p}$ term can be included without obtaining a non-symmetric matrix, adding the $\partial \boldsymbol{q}_{dp}/\partial \boldsymbol{u}$ term results in a non-symmetric matrix. For a Newtonian fluid, these last two sub-matrices are simplified to:

$$
\frac{\partial \boldsymbol{q}_{dp}}{\partial \boldsymbol{p}} = \int_{\Gamma_d} \frac{\Delta t}{12\mu}\left(\boldsymbol{n}_{\Gamma_d}^T\boldsymbol{N}_d\boldsymbol{u}\right)^3\boldsymbol{N}_f^T\boldsymbol{\nabla}^2\boldsymbol{N}_f\,\mathrm{d}\Gamma_d + \int_{\Gamma_d} \frac{\Delta t}{4\mu}\left(\boldsymbol{n}_{\Gamma_d}^T\boldsymbol{N}_d\boldsymbol{u}\right)^2\left(\boldsymbol{n}_{\Gamma_d}^T\boldsymbol{\nabla}\boldsymbol{N}_d\boldsymbol{u}\right)\boldsymbol{N}_f^T\boldsymbol{\nabla}\boldsymbol{N}_f\,\mathrm{d}\Gamma_d
\tag{3.8}
$$

$$
\begin{aligned}
\frac{\partial \boldsymbol{q}_{dp}}{\partial \boldsymbol{u}} = &\int_{\Gamma_d} \frac{\Delta t}{4\mu}\boldsymbol{\nabla}^2\boldsymbol{N}_f\boldsymbol{p}\left(\boldsymbol{n}_{\Gamma_d}^T\boldsymbol{N}_d\boldsymbol{u}\right)^2\boldsymbol{N}_f^T\boldsymbol{n}_{\Gamma_d}^T\boldsymbol{N}_d\,\mathrm{d}\Gamma_d + \int_{\Gamma_d} \frac{\Delta t}{4\mu}\boldsymbol{\nabla}\boldsymbol{N}_f\boldsymbol{p}\left(\boldsymbol{n}_{\Gamma_d}^T\boldsymbol{N}_d\boldsymbol{u}\right)^2\boldsymbol{N}_f^T\boldsymbol{n}_{\Gamma_d}^T\boldsymbol{\nabla}\boldsymbol{N}_d\,\mathrm{d}\Gamma_d \\
&+\int_{\Gamma_d} \frac{\Delta t}{2\mu}\boldsymbol{\nabla}\boldsymbol{N}_f\boldsymbol{p}\left(\boldsymbol{n}_{\Gamma_d}^T\boldsymbol{N}_d\boldsymbol{u}\right)\left(\boldsymbol{n}_{\Gamma_d}\boldsymbol{\nabla}\boldsymbol{N}_d\boldsymbol{u}\right)\boldsymbol{N}_f^T\boldsymbol{n}_{\Gamma_d}^T\boldsymbol{N}_d\,\mathrm{d}\Gamma_d
\end{aligned}
\tag{3.9}
$$

The order in which these terms are added has been chosen such that after adding the first two terms, Eq. 2.66 and 3.4, the solid is resolved exactly. Adding the third term, 3.5 results in a symmetric matrix, and adding the fourth sub-matrix preserves this.

Another possible way in which the convergence rate can be increased is by using a linear line search [64, 65]. By linearly interpolating between the internal forces and fluxes before and after the latest iteration, the factor η is determined:

$$
0 = (1-\eta)\begin{bmatrix}\boldsymbol{f}_{ext}-\boldsymbol{f}_{int}-\boldsymbol{f}_d \\ \boldsymbol{q}_{ext}-\boldsymbol{q}_{int}-\boldsymbol{q}_{dh}-\boldsymbol{q}_{dp}\end{bmatrix}_j\cdot\begin{bmatrix}\mathrm{d}\boldsymbol{u} \\ \mathrm{d}\boldsymbol{p}\end{bmatrix}_{j+1} + \eta\begin{bmatrix}\boldsymbol{f}_{ext}-\boldsymbol{f}_{int}-\boldsymbol{f}_d \\ \boldsymbol{q}_{ext}-\boldsymbol{q}_{int}-\boldsymbol{q}_{dh}-\boldsymbol{q}_{dp}\end{bmatrix}_{j+1}\cdot\begin{bmatrix}\mathrm{d}\boldsymbol{u} \\ \mathrm{d}\boldsymbol{p}\end{bmatrix}_{j+1}
\tag{3.10}
$$

This factor η is limited such that $0.05 < \eta < 1.0$. Once this factor is determined the increment of the current iteration gets multiplied by η and added to the state vector.

3.2. SINGLE FRACTURE

The first case simulated uses the geometry and parameters described in Section 2.3. The domain has been discretised using 40 × 40 Bézier extracted elements, and a time-step of $\Delta t = 1$s was used. As previously mentioned, the tangential stiffness sub-matrices related to

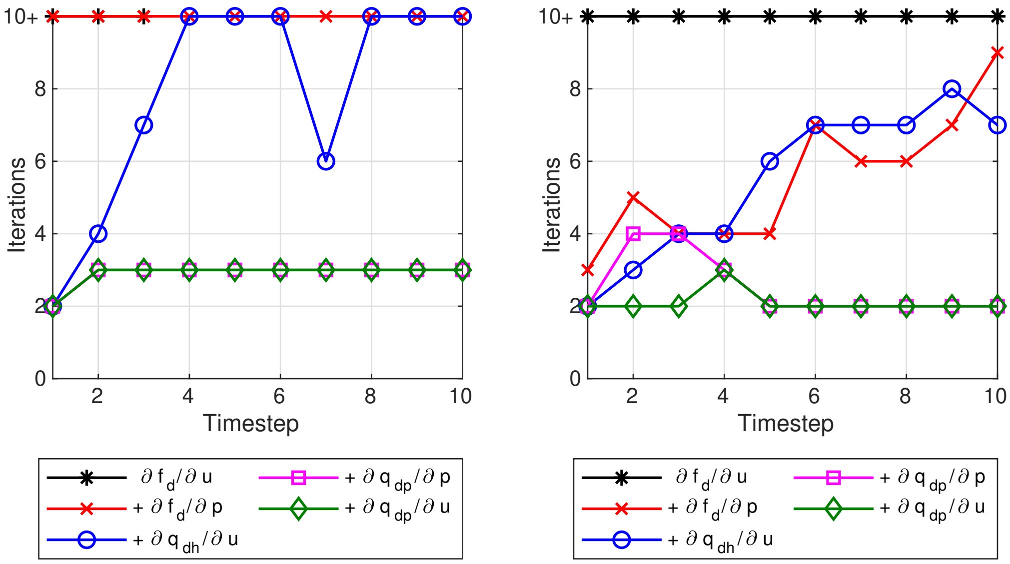

(a) Without line-search

(b) With line-search

Figure 3.1: Number of Newton-Raphson iterations per time-step for the single fracture case using 4×3 IGA.

the discontinuity are added one at a time, in the order they were introduced in the previous section.

The number of iterations required to obtain a converged solution ($error < 10^{-6}$) is shown in Figure 3.1a. With only the $\partial \boldsymbol{f}_d / \partial \boldsymbol{u}$ term added, the simulation diverges during the third timestep. Adding the $\partial \boldsymbol{f}_d / \partial \boldsymbol{p}$ term prevents this, and results in a converged solution while requiring 70-100 iterations. Adding the third term lowers this required amount of iterations. However, while with only two terms added all timesteps converged, by adding the third term the simulations diverge at the thirteenth timestep. Including the last two terms, only three iterations are needed per timestep.

The convergence behaviour during the third time-step is shown in Figure 3.2. When only the term related to the dummy stiffness is included, large oscillations occur. While the minimum reached decreases up to the 23^{rd} iteration, these oscillations eventually cause the Newton-Raphson solver to diverge. While adding the second term does not increase the convergence rate, it suppresses the oscillations and therefore prevents divergence. By adding the third term, the convergence is further improved. However, the convergence rate stagnates around the chosen convergence criteria. This stagnating convergence is also observed in literature for the iterative undrained split [168], and causes the simulation to diverge during the thirteenth timestep. Adding the final two terms results in a quardatic convergence rate. While for both cases only three iterations were required, including all terms results in a significantly faster decrease in the error.

3.2.1. LINE-SEARCH

When a linear line-search was used, all simulations converged, as shown in Figure 3.1b. With only the dummy stiffness term added, more than 100 iterations were needed to obtain a converged solution, whereas without line-search the simulation diverged. For the cases with two and three terms added, the use of line-search drastically reduces the required iterations, and prevents the divergence that occured during the thirteenth timestep for the non line-search case with three terms. For the cases with four and all terms added, the use of a line-search provides less benefits, with at most requiring one less iteration.

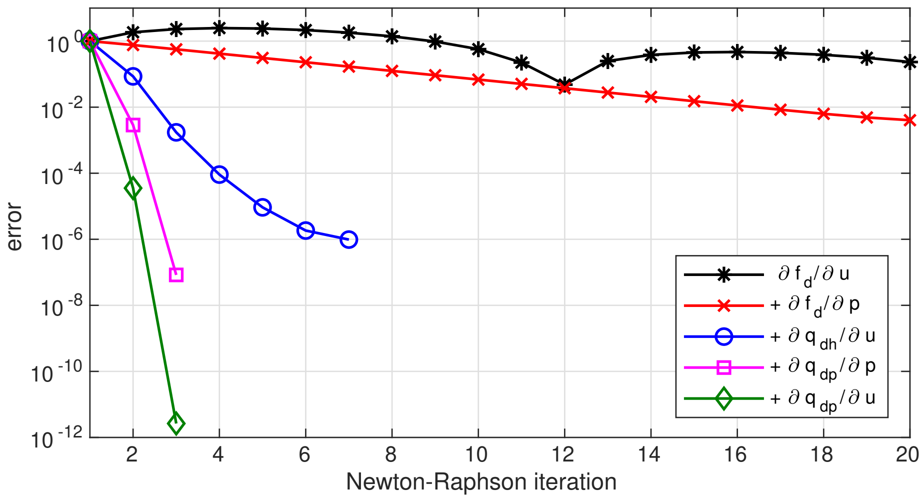

Figure 3.2: Convergence behaviour during the 3^{rd} time-step without line-search using 4 × 3 IGA.

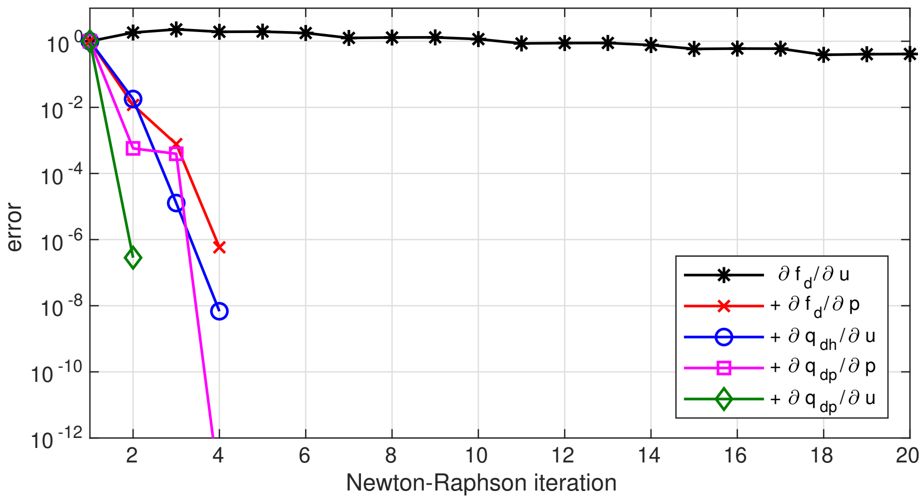

Figure 3.3: Convergence behaviour during the 3^{rd} time-step with line-search using 4 × 3 IGA.

The convergence behaviour, Figure 3.3, confirms these results. By comparing these results to the results without line-search, the improvements when only a partially complete tangential stiffness matrix is used are clear. However, when four or all five of the terms are included, the improvement in convergence is diminished, requiring one extra iteration to obtain converged results. This indicates that the use of a line-search is most beneficial when using a consistent tangential stiffness matrix is not feasible. Using a line-search is also beneficial when retaining a constant and symmetric tangential stiffness matrix is preferred.

3.2.2. FUNCTION ORDER

A comparison between the convergence behaviour when using 4 × 3 and 2 × 2 IGA is shown in Figure 3.4. Slight differences are seen between the high order and low order results when only one and two terms are added, with for both cases the low order simulation displaying a slightly faster convergence. In contrast, by adding the third term the high order simulation converges whereas the low order simulation diverges. It should be noted, however, that a similar divergence occurs for the high order results at a later time step, and presents itself in a similar manner: Initially showing a non-oscillatory and steadily decreasing error, which eventually stops decreasing and diverges. Negligible differences were seen between the two

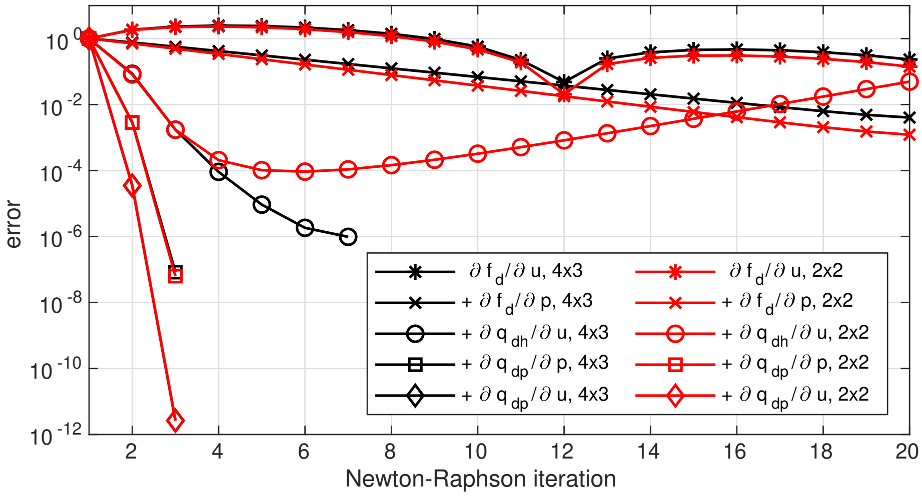

Figure 3.4: Comparison of the convergence behaviour between the 4×3 IGA and the 2×2 IGA during the 3^{rd} time-step without using line-search.

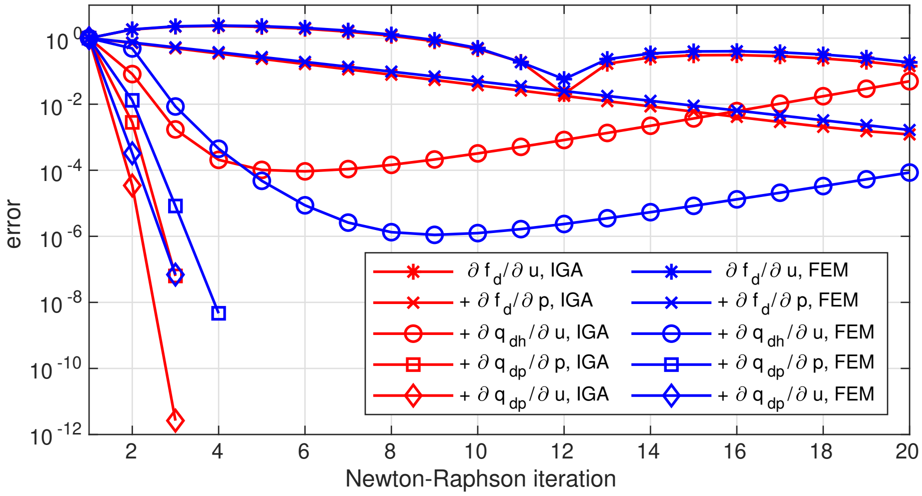

Figure 3.5: Comparison of the convergence behaviour between the 2×2 IGA and the 2×2 FEM during the 3^{rd} time-step without using line-search.

simulations when all the terms were added, indicating that the order of the NURBS meshes does not significantly alter the convergence. A similar conclusion was reached from the results using a linear line-search (not shown).

3.2.3. FEM VS IGA

A comparison between NURBS and traditional Lagrangian polynomials is given in Figure 3.5. When only the terms related to $\boldsymbol{f}_d$ are included, no significant difference in convergence occurs. Adding the third term, related to the fracture absorbing fluid by opening, results in divergence for both simulations. By adding the last two terms, a clear difference between the IGA and the FEM results can be seen. While the IGA results obtain a quadratic convergence rate, only a linear convergence is achieved for the Lagrangian polynomials. This is most likely caused by these terms containing higher-order derivatives, and therefore only being accurately evaluated when the C^1 inter-element continuity of the NURBS is used.

Similar results are obtained when using a linear line-search, as shown in Figure 3.6. Only using the first two terms does not result in any difference between the IGA and FEM sim-

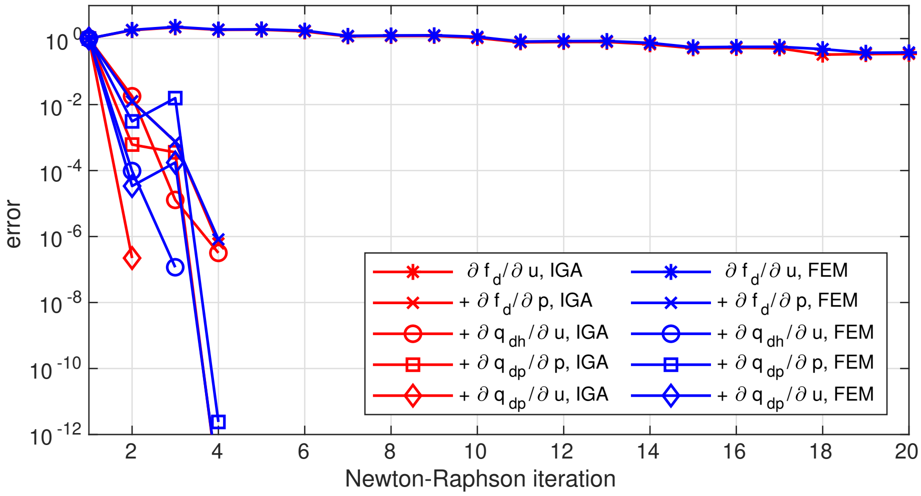

Figure 3.6: Comparison of the convergence behaviour between the 2 × 2 IGA and the 2 × 2 FEM during the 3^{rd} time-step with line-search.

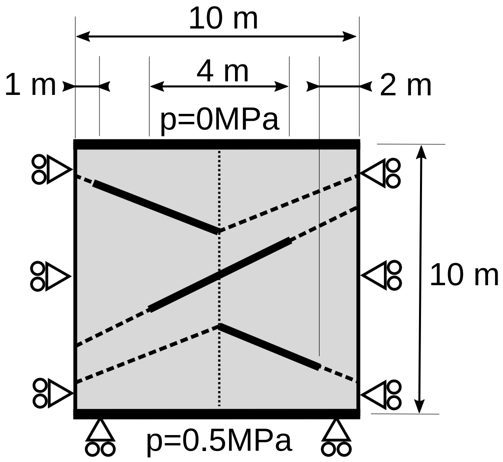

Figure 3.7: Geometry used for the multiple fracture cases

ulations. By adding the third term the convergence of both simulations is vastly improved, with the FEM simulations converging faster than the IGA simulations. By adding the last two terms, the IGA simulations converge faster again, further confirming the benefits of NURBS on the convergence behaviour.

3.3. MULTIPLE FRACTURE

Two additional fractures are added to investigate whether the conclusions from the previous section hold for multiple fractures. The geometry is shown in Figure 3.7, with both fractures being placed at a 15° angle. In order to allow for sharp changes in mesh line direction, a vertical C^0 continuity line is inserted through the middle. Two pressure differences between the top and bottom have been used, $\Delta p = 0.25$ MPa and $\Delta p = 0.5$ MPa. The remaining properties correspond to the values used in the previous section.

The required number of iterations using 4×3 IGA and $\Delta p = 0.25$ MPa is shown in Figure 3.8a for the cases without line-search, and in Figure 3.8b with line-search. Similar to the single fracture case, only including the terms relating to $\boldsymbol{f}_d$ results in a large amount of iterations being required to obtain converged solutions, for some cases even reaching 100+

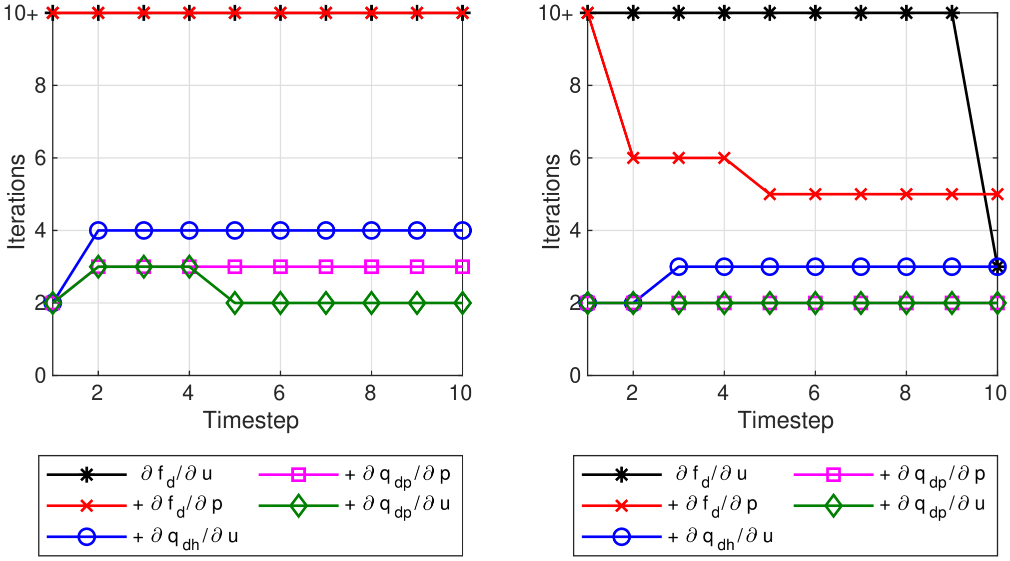

(a) Without line-search

(b) With line-search

Figure 3.8: Amount of iterations required per time-step using 4 × 3 IGA and $\Delta p = 0.25$ MPa for the three fracture case.

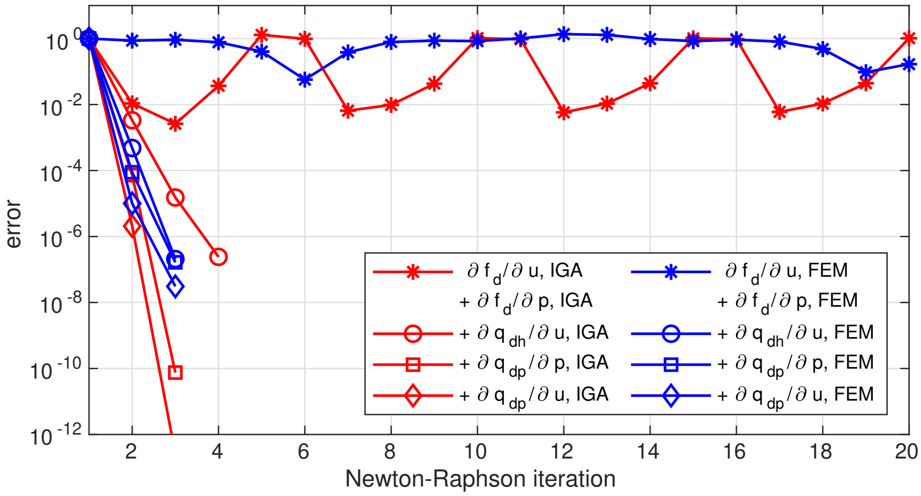

Figure 3.9: Comparison of the convergence behaviour between the 2×2 IGA and the 2×2 FEM during the 3^{rd} time-step without line-search for the three fracture case using $\Delta p = 0.25$ MPa

iterations. Adding the term related to $\boldsymbol{q}_{dh}$ vastly improves the convergence, and adding the final two terms results in only two to three iterations being required, similar to the single fracture case.

The convergence behaviour during the third timestep, Figure 3.9, shows these issues with the convergence when only the first term is included. Similar oscillations as obtained for the single fracture case occur with only the first term included, whereas these disappear when the second term is added (not shown). Also similar to the single fracture case, including all terms results in a quadratic convergence rate for the IGA simulations, whereas at most a linear convergence rate was obtained for the FEM simulations.

Results using a larger pressure difference, $\Delta p = 0.5$ MPa are shown in Figure 3.10. The IGA results show large oscillations when only a few terms are included,and the FEM simulations diverged before reaching the third time-step. Only by including the sub-matrices

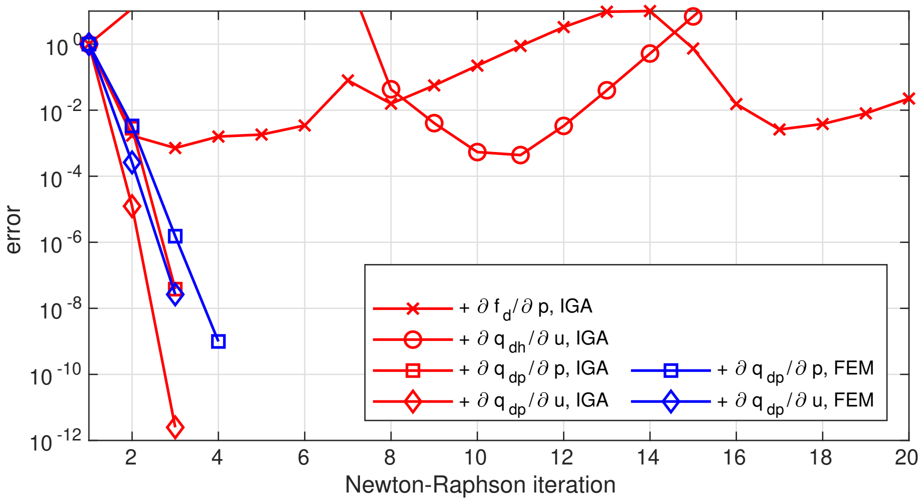

Figure 3.10: Comparison of the convergence behaviour between the 2 × 2 IGA and the 2 × 2 FEM during the 3^{rd} time-step without line-search for the three fracture case using $\Delta p = 0.5$ MPa

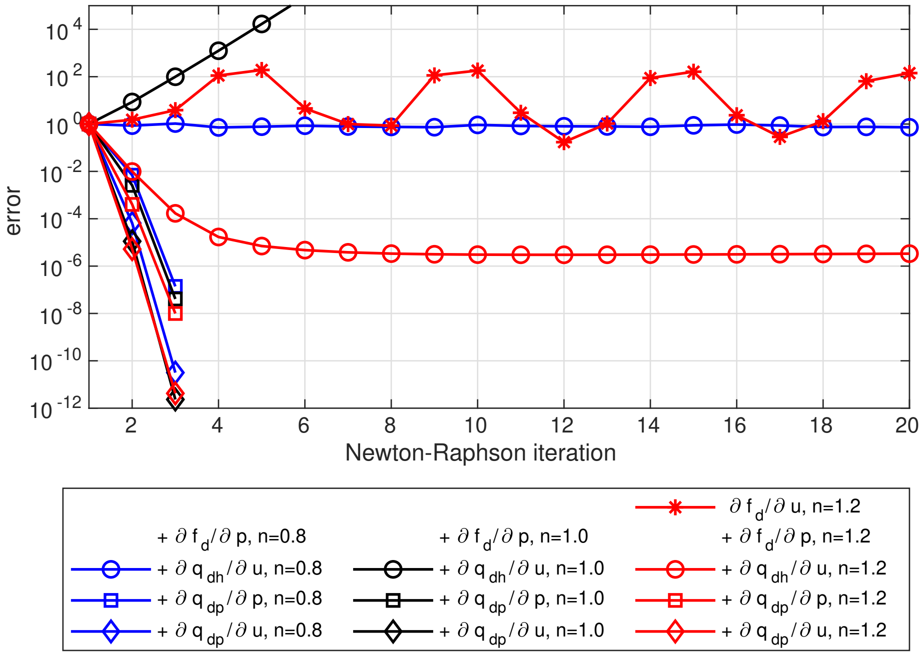

Figure 3.11: Convergence during the third time step for the non-Newtonian fluid cases without line-search

related to $\boldsymbol{q}_{dp}$ converged solutions could be obtained. Once these terms were included, quadratic convergence was re-obtained for the IGA simulations, and only three iterations were required to obtain converged solutions, similar to the case using the low pressure difference. This indicates that when the influence of the fracture is significant, using a consistent tangential stiffness matrix is required to obtain converged solutions, and even neglecting a few terms can result in a diverging Newton-Raphson algorithm for these cases. Furthermore, when all terms are included, the convergence rate is independent on the importance of the fracture, always obtaining a quadratic convergence rate.

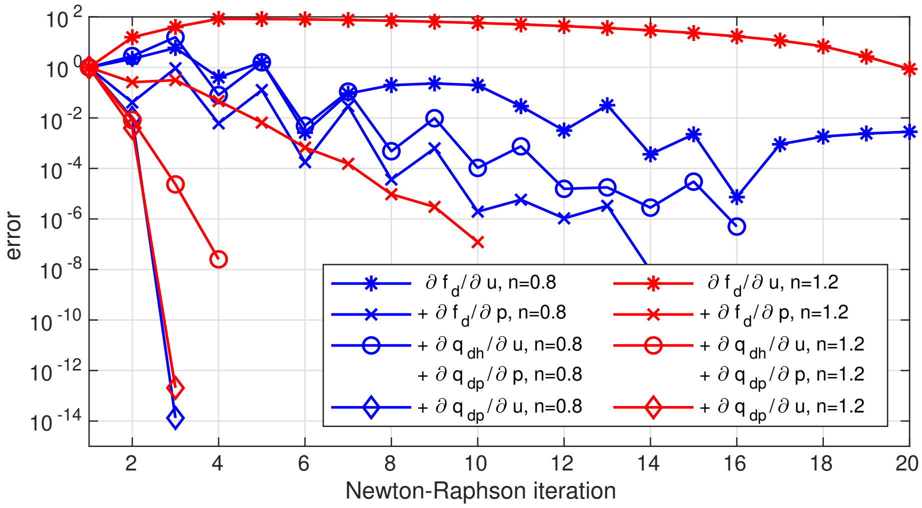

Figure 3.12: Convergence during the third time step for the non-Newtonian fluid cases with line-search

3.4. Non-Newtonian fluids

The case from Section 3.3 is repeated using a shear-thinning fluid ($n = 0.8$) and a shear-thickening fluid ($n = 1.2$) with the high pressure difference $\Delta p = 0.5$ MPa. A base viscosity $\mu_0 = 1$ mPa s^n has been used for both these fluids. By using a non-Newtonian fluid, the discretisation of not only the fractures but also the interior of the porous material becomes non-linear. A consistent tangential stiffness matrix for this interior, Eq. 2.63, has been used for all cases. Pressure oscillations were observed for the shear-thinning case when equal order interpolants were used, and therefore this section will only present results using quartic NURBS for the displacement and cubic NURBS for the interstitial fluid pressure.

The convergence behaviour during the third time step without line search is shown in Figure 3.11. While the shear-thinning and the Newtonian fluid diverged before the third step with only the first term added, the shear-thickening fluid only showed large oscillations. By adding the $\partial \boldsymbol{q}_{dh}/\partial \boldsymbol{u}$ term, all oscillations disappeared. However, similar to the cases presented in the previous sections, the convergence plateaued for the non-Newtonian fluids, and diverged during this time step for the Newtonian fluid. Finally, adding the last two terms resulted in a quadratic convergence rate, only requiring three iterations to converge with little difference between the Newtonian and non-Newtonian fluids.

When a linear line search is used, Figure 3.12, simulations using only the first term also converge. While a line search was sufficient to suppress oscillations when the $\partial \boldsymbol{f}_d/\partial \boldsymbol{p}$ was included for Newtonian fluids, these oscillations still occur for the shear-thinning fluid. Finally, similar to all other cases, by including all terms the simulations converge within three iterations again.

3.5. Conclusion

In this chapter, a consistent tangential stiffness matrix was derived for non-Newtonian fluid flows in fractures. The terms related to the dummy stiffness of the non-fractured elements, the pressure acting on the walls, fluid being absorbed due to the fracture opening, and due to changes in velocity profile were added one-by-one. This allowed the effect of these terms on the convergence of the Newton-Raphson algorithm to be analysed.

Including all terms, resulting in a consistent linearisation, resulted in a quadratic convergence rate, but due to the dependence of these terms on the pressure and displacement requires some terms to be recalculated for each iteration. In contrast, only including the term for the non-fractured interface elements allows the tangential stiffness matrix to be only calculated once, but results in diverging simulations.

When the influence of the fracture on the interstitial pressure is relatively small, it is sufficient to include the terms related to the force vector and the fracture opening. This allows the stiffness matrix to only be calculated once and used for the remainder of the simulations, and results in a symmetric matrix. In contrast, when the influence of the fracture is large, all terms need to be included and these benefits are removed. This requirement can be relaxed by using a linear line search, allowing a constant and symmetric matrix to be used even when the influence of the fracture is large.

A comparison between quartic NURBS for the displacement and cubic NURBS for the interstitial pressure, and quadratic NURBS for both the pressure and displacement showed near to no effect of the order of the shape function order on the convergence. In contrast, simulations using quadratic NURBS and Lagrangian polynomials showed that the increased inter-element continuity benefited the convergence of the simulations using NURBS, allowing a quadratic convergence rate to be obtained when using NURBS but not when using Lagrangian polynomials.

Finally, simulations were performed for non-Newtonian power-law fluids. It was shown that including all terms resulted in a quadratic convergence, whereas neglecting most terms resulted in diverging or ill-converging simulations. For non-Newtonian fluids, the discretised mass balance for the interior is non-linear, and therefore the tangential stiffness matrix needs to be recalculated for each iteration independent of the terms included. This allows the inclusion of updated terms related to the interface at near to no extra computational cost, and therefore it would be beneficial in all cases to include all terms when allowed by the linear solver, or all but the $\partial \boldsymbol{q}_{dp}/\partial \boldsymbol{u}$ term when a symmetric matrix is preferred.

4

MULTIPHASE FRACTURE FLOW MODELS

Inside porous materials, finite volume and finite element methods are often used to simulate multiphase fluid flows. When using finite volume methods, the focus is usually on including phenomena relevant to the fluid phases, such as including buoyancy and capillary forces, while not including the solid deformations and stresses [15, 128, 239]. Finite volume methods have also been employed in multi-scale schemes, in which the flow is resolved on a small scale and upscaled to make simulation of large domains feasible [135]. In contrast, finite element methods allow for an easy integration of solid deformations with the multiphase flow, either in a staggered [61, 101, 149] or monolithic scheme [110, 158, 201, 240]. These finite element methods have also included behaviour such as evaporation and heat transport inside the porous material [111, 183]. Finally, there are the pore-scale network methods which accurately capture the interactions between the fluid phases by direct numerical simulation of the flow within the pores [30, 31, 178, 241]. While this only allows small domains to be simulated, their results can be translated to relative permeability coefficients for larger simulations [107, 179, 225].

Multiphase flows within fractures are often included by combining the cubic law with an experimental correction factor, dependent on the saturation within the material surrounding the fracture [89, 108, 186, 198]. The fluid transport within the fracture has also been included through a continuous pressure sub-grid model [188]. However, this model for the fluid flow within the fracture was based on the cubic law, thereby retaining the dependence on an empirical factor. This dependence limits the information provided about the fluid flow within the fracture and does not allow the fluid phases to interact with each other except through the saturation. Therefore, these models do not allow the pressure gradients and velocities of the phases to impact the flow of the other phase. An alternative approach occasionally taken is to model the fracture flow as a single phase [121], or to spread the fluid transport over neighbouring elements through an effective permeability [102].

Experiments, however, have shown that the pressure gradient and velocity of one phase do influence the velocity of the other phase within the fracture [182]. Dependent on the velocity, the flow within the fracture ranges from a bubbly flow, in which both phases are well mixed, to a flow in which the two phases are fully separated [180, 181, 221]. As a result, the interactions between the two fluid phases also depend on the flow regime the fracture flow is in [26, 88]. These interactions and flow regimes are not included in the relative permeability used for the cubic law, and therefore the effect of the fluid phase interaction is not fully simulated.

In this chapter, fracture flow sub-grid models for multiphase flows will be derived which contain these interactions. This will result in a continuous pressure model for a well-mixed bubbly flow type, and a fully separated flow type, both of which allow the interactions and fluid distribution within the fracture to be simulated and viewed through post-processing. For this, the governing equations inside the porous material and the sub-grid models for the fracture will be derived in Section 4.1, and discretised in Section 4.2. A simplified case containing a single fracture is presented in Section 4.3, which is used to study the effects of the fracture flow models and compare these models to the cubic law. Finally, Section 4.4 presents two cases more representative of actual applications, showcasing the influence of including the phase interactions. The methods and results presented in this chapter are based on, and have been previously published in [6].

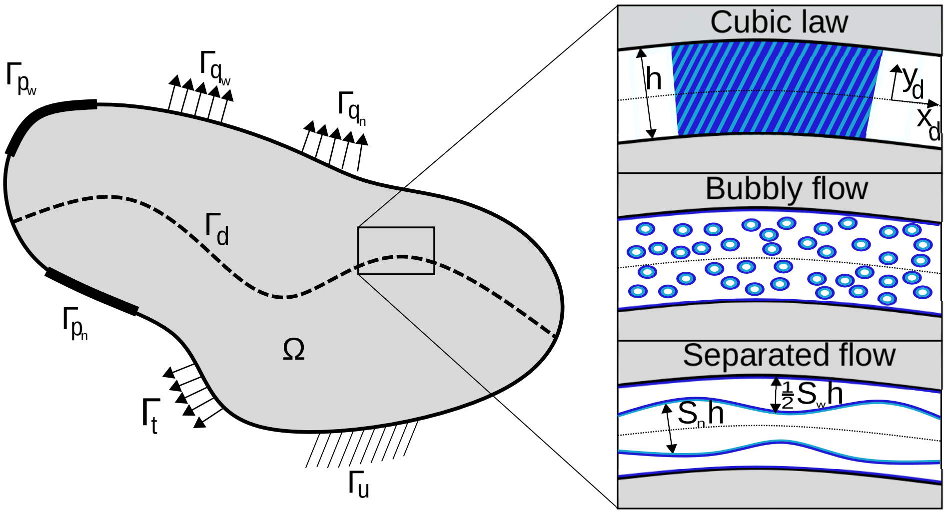

Figure 4.1: Overview of the domain, boundaries, fracture flow models and the local coordinate system used for the fracture.

4.1. GOVERNING EQUATIONS

Similar to the previous chapters, a domain Ω is considered, as shown in Figure 4.1. On this domain, inflow boundary conditions for the wetting phase are imposed on Γ_{q_w} and for the non-wetting phase on Γ_{q_n}. The interior of the domain is described by its displacement $\boldsymbol{u}$, the pressure of the wetting phase p_w, and the pressure of the non-wetting phase p_n.

At the micro-scale, when looking at the pores of the porous material, the two phases are considered immiscible. While the pores can contain both phases, each connection between these pores is usually considered to only transport either the wetting phase or the non-wetting phase [30, 225]. When this is up-scaled to the macro-scale, both fluids are allowed to coexist in the same location. The volume fraction taken up by the wetting and non-wetting phases are then described by the saturation:

$$S_w = \frac{V_w}{n_f V_{total}} = \frac{V_w}{V_w + V_n} \tag{4.1}$$

$$S_n = \frac{V_n}{n_f V_{total}} = 1 - S_w \tag{4.2}$$

with S_w and S_n the saturation of the wetting and non-wetting phases, V_π the volume taken up by phase $\pi = w, n$, and V_{total} the total volume taken up by both fluid phases and the solid material.

Inside the interior of the porous material, these saturations are related to the capillary pressure:

$$p_c = p_n - p_w \tag{4.3}$$

In this chapter, for the cases relating to an oil-water mixture, a saturation relation from [108] will be used:

$$S_w = e^{-p_c/B} \tag{4.4}$$

$$S_n = 1 - e^{-p_c/B} \tag{4.5}$$

with B an experimental constant taken as $B = 0.1$ MPa. For the cases relating to an air-water mixture, only used in Section 4.4.2, the Van Genuchten relation is used [87, 141]:

$$S_w = \left(1 - \left(\frac{p_c}{p_{ref}}\right)^{\frac{1}{1-m}}\right)^{-m} \tag{4.6}$$

with the reference pressure $p_{ref} = 18.6\,\mathrm{MPa}$ and the constant $m = 0.4369$.

4.1.1. INTERIOR

As was the case for the single phase flow from the previous chapters, it is assumed the solid deformations occur fast compared to the fluid flows. This allows the momentum balance to be described as:

$$\boldsymbol{\nabla}\cdot\left(\boldsymbol{\sigma}_s - \alpha\left(S_w p_w + S_n p_n\right)\boldsymbol{I}\right) = \boldsymbol{0} \tag{4.7}$$

For the mass balance of the wetting and non-wetting phases, several formulations are used in literature [38, 108, 110, 153, 188]. However, these formulations differ and little to none of the assumptions are given. Therefore, the mass balance has been derived in Appendix D, and a dimensional analysis has been performed to determine under which circumstances terms can be neglected. Assuming the wetting and non-wetting phases are nearly incompressible, and therefore the density gradients can be neglected, the mass balances for the wetting and non-wetting phases are given by:

$$\frac{1}{M_{ww}}\dot{p}_w + \frac{1}{M_{wn}}\dot{p}_n + \alpha S_w \boldsymbol{\nabla}\cdot\dot{\boldsymbol{u}} + \boldsymbol{\nabla}\cdot\boldsymbol{q}_w = 0 \tag{4.8}$$

$$\frac{1}{M_{nn}}\dot{p}_n + \frac{1}{M_{nw}}\dot{p}_w + \alpha S_n \boldsymbol{\nabla}\cdot\dot{\boldsymbol{u}} + \boldsymbol{\nabla}\cdot\boldsymbol{q}_n = 0 \tag{4.9}$$

with the local pressure capacities given by:

$$\frac{1}{M_{ww}} = S_w\frac{\alpha - n_f}{K_s}\left(S_w + p_c\frac{\partial S_w}{\partial p_c}\right) - n_f\frac{\partial S_w}{\partial p_c} + \frac{n_f S_w}{K_w} \tag{4.10a}$$

$$\frac{1}{M_{wn}} = S_w\frac{\alpha - n_f}{K_s}\left(S_n - p_c\frac{\partial S_w}{\partial p_c}\right) + n_f\frac{\partial S_w}{\partial p_c} \tag{4.10b}$$

$$\frac{1}{M_{nw}} = S_n\frac{\alpha - n_f}{K_s}\left(S_w + p_c\frac{\partial S_w}{\partial p_c}\right) + n_f\frac{\partial S_w}{\partial p_c} \tag{4.10c}$$

$$\frac{1}{M_{nn}} = S_n\frac{\alpha - n_f}{K_s}\left(S_n - p_c\frac{\partial S_w}{\partial p_c}\right) - n_f\frac{\partial S_w}{\partial p_c} + \frac{n_f S_n}{K_n} \tag{4.10d}$$

The fluid fluxes in the interior of the porous material are given through Darcy's law:

$$\boldsymbol{q}_w = S_w n_f\left(\boldsymbol{v}_w - \dot{\boldsymbol{u}}\right) = -k_w k_{rw}\boldsymbol{\nabla} p_w \tag{4.11}$$

$$\boldsymbol{q}_n = S_n n_f\left(\boldsymbol{v}_n - \dot{\boldsymbol{u}}\right) = -k_n k_{rn}\boldsymbol{\nabla} p_n \tag{4.12}$$

The relative permeabilities k_{rw} and k_{rn} are a function of the saturation. For the oil-water cases, the relation from [108] was used:

$$k_{rw} = S_w^5 \tag{4.13a}$$

$$k_{rn} = (1 - S_w)^5 \tag{4.13b}$$

whereas for the air-water case the relations corresponding to the Van Genuchten model were used [87, 141]:

$$k_{rw} = S_w^{1/2}\left(1 - \left(1 - S_w^{\frac{1}{m}}\right)^m\right)^2 \tag{4.14a}$$

$$k_{rn} = (1 - S_w)^{1/2}\left(1 - S_w^{\frac{1}{m}}\right)^{2m} \tag{4.14b}$$

4.1.2. FRACTURES

Similar to the previous chapters, the fracture is represented using interface elements. These elements were inserted for the fracture, and for the non-fractured elements along the remainder of the meshline containing the fracture. The tractions along this discontinuity are composed of the the volume-averaged pressures and the solid tractions:

$$\boldsymbol{\tau}_{\Gamma_d} = \boldsymbol{\tau}_d - \left(S_w p_w + S_n p_n\right) \boldsymbol{n}_d \tag{4.15}$$

with the solid traction equal to zero for the fractured elements (no cohesive zone model) and given by Eq. 2.20 for the non-fractured elements.

The wetting phase fracture inflow is obtained from the conservation of mass for the wetting phase:

$$\frac{\partial v_w}{\partial x_d} + \frac{\partial w_w}{\partial y_d} = 0 \tag{4.16}$$

with v_w the fluid velocity in x_d direction and w_w in y_d direction. Integrating this equation over the fracture height results in:

$$[\![w]\!]_w = w_w\left(\frac{h}{2}\right) - w_w\left(-\frac{h}{2}\right) = -\frac{\partial q_w}{\partial x_d} \tag{4.17}$$

with the total wetting phase flux inside the fracture defined by:

$$q_w = \int_{-h/2}^{h/2} v_w \,\mathrm{d}y_d \tag{4.18}$$

In a similar manner as done for single phase fracture flows in Eq. 2.34, the fracture outflow is given by:

$$[\![\boldsymbol{n}_{\Gamma_d} \cdot \boldsymbol{q}]\!]_w = [\![w]\!]_w - [\![w]\!]_{ws} \tag{4.19}$$

with the inflow due to changes in fracture height and saturation given by:

$$[\![w]\!]_{ws} = \frac{\partial S_w h}{\partial t} \tag{4.20}$$

Similarly, for the non-wetting phase:

$$[\![\boldsymbol{n}_{\Gamma_d} \cdot \boldsymbol{q}]\!]_n = [\![w]\!]_n - [\![w]\!]_{ns} \tag{4.21}$$

with:

$$[\![w]\!]_n = w_n\left(\frac{h}{2}\right) - w_n\left(-\frac{h}{2}\right) = -\frac{\partial q_n}{\partial x_d} \tag{4.22}$$

$$q_n = \int_{-h/2}^{h/2} v_n \,\mathrm{d}y_d \tag{4.23}$$

$$[\![w]\!]_{ns} = \frac{\partial S_n h}{\partial t} \tag{4.24}$$

Eqs. 4.17 and 4.22 can be used with different definitions for the fluid velocity profile in the fracture. Experiments using water and air in smooth, non-porous, channels indicate that a bubbly flow model is appropriate for slow-moving fluids [88, 164]. However, separated flow in fractures has been observed for gas/water and oil/water mixtures [26, 221], and has been used for the simulation of non-porous fractures [210, 211]. In the remainder of this section, velocity profiles for the bubbly flow and separated flow types will be derived. As a reference case, the cubic law will also be cast into the same formulation. While the cubic law does not provide any insight into the fluid velocity profiles within the fracture, it is an often used model to describe the fluid flow within fractures.

Cubic Law

The fluid flux inside the fracture is described by the cubic law as:

$$q_\pi = -\frac{k_{d\pi} h^3}{12\mu_\pi}\frac{\partial p_\pi}{\partial x_d} \tag{4.25}$$

with $k_{d\pi}$ the relative permeability of the wetting and non-wetting phases inside the fracture. The relative permeability is usually taken as a function of the saturation, for which the relation from [108] will be used here:

$$k_{dw} = S_w^3 \tag{4.26a}$$

$$k_{dn} = S_n^3 \tag{4.26b}$$

Substituting the fluid flux of Eq. 4.25 in Eq. 4.17 and combining with the definitions for the relative permeability with Eq. 4.19 and 4.20 results in the fracture outflow for the cubic law fracture flow model:

$$[\![\boldsymbol{n}_{\Gamma_d}\cdot\boldsymbol{q}]\!]_w = \frac{S_w^3 h^3}{12\mu_w}\frac{\partial^2 p_w}{\partial x_d^2} + \frac{h^2 S_w^3}{4\mu_w}\frac{\partial p_w}{\partial x_d}\frac{\partial h}{\partial x_d} + \frac{S_w^2 h^3}{4\mu_w}\frac{\partial S_w}{\partial p_c}\left(\frac{\partial p_n}{\partial x_d} - \frac{\partial p_w}{\partial x_d}\right)\frac{\partial p_w}{\partial x_d} - S_w\dot{h} - h\dot{S}_w \tag{4.27a}$$

$$[\![\boldsymbol{n}_{\Gamma_d}\cdot\boldsymbol{q}]\!]_n = \frac{S_n^3 h^3}{12\mu_n}\frac{\partial^2 p_n}{\partial x_d^2} + \frac{h^2 S_n^3}{4\mu_n}\frac{\partial p_n}{\partial x_d}\frac{\partial h}{\partial x_d} - \frac{S_n^2 h^3}{4\mu_n}\frac{\partial S_w}{\partial p_c}\left(\frac{\partial p_n}{\partial x_d} - \frac{\partial p_w}{\partial x_d}\right)\frac{\partial p_n}{\partial x_d} - S_n\dot{h} - h\dot{S}_n \tag{4.27b}$$

Bubbly Flow

For the bubbly flow model, it is assumed the two phases are well-mixed. This allows the volume-averaged viscosity to be obtained as:

$$\overline{\mu} = S_w\mu_w + S_n\mu_n \tag{4.28}$$

Based on this volume-averaged viscosity, the Stokes equation for the mixture is:

$$0 = -\left(S_w\frac{\partial p_w}{\partial x_d} + S_n\frac{\partial p_n}{\partial x_d}\right) + \frac{\partial}{\partial y_d}\left(\overline{\mu}\frac{\partial\overline{v}}{\partial y_d}\right) \tag{4.29}$$

with $\overline{v}$ the velocity of the two phases combined. This equation is combined with no slip boundary conditions:

$$\overline{v}(h/2) = \overline{v}(-h/2) = 0 \tag{4.30}$$

to obtain the velocity profile for the mixture. This profile is distributed based on the saturation of the wetting and non-wetting phases, resulting in:

$$v_w = S_w\overline{v} = \frac{1}{2}\frac{S_w}{S_w\mu_w + S_n\mu_n}\left(S_w\frac{\partial p_w}{\partial x_d} + S_n\frac{\partial p_n}{\partial x_d}\right)\left(y_d^2 - \left(\frac{h}{2}\right)^2\right) \quad \text{for } -\frac{h}{2} < y_d < \frac{h}{2} \tag{4.31a}$$

$$v_n = S_n\overline{v} = \frac{1}{2}\frac{S_n}{S_w\mu_w + S_n\mu_n}\left(S_w\frac{\partial p_w}{\partial x_d} + S_n\frac{\partial p_n}{\partial x_d}\right)\left(y_d^2 - \left(\frac{h}{2}\right)^2\right) \quad \text{for } -\frac{h}{2} < y_d < \frac{h}{2} \tag{4.31b}$$

These velocity profiles are used with Eq. 4.18 to obtain the fluid fluxes within the fracture as:

$$q_w = -\frac{S_w h^3}{12\left(S_w\mu_w + S_n\mu_n\right)}\left(S_w\frac{\partial p_w}{\partial x_d} + S_n\frac{\partial p_n}{\partial x_d}\right) \tag{4.32a}$$

$$q_n = -\frac{S_n h^3}{12\left(S_w\mu_w + S_n\mu_n\right)}\left(S_w\frac{\partial p_w}{\partial x_d} + S_n\frac{\partial p_n}{\partial x_d}\right) \tag{4.32b}$$

and combined with Eq. 4.19 to obtain the fracture inflow:

$$\begin{aligned}
[\![\boldsymbol{n}_{\Gamma_d}\cdot\boldsymbol{q}]\!]_w = {} & \frac{S_w h^3}{12\left(S_w\mu_w + S_n\mu_n\right)}\left(S_w\frac{\partial^2 p_w}{\partial x_d^2} + S_n\frac{\partial^2 p_w}{\partial x_d^2} + \left(\frac{\partial p_w}{\partial x_d} - \frac{\partial p_n}{\partial x_d}\right)\frac{\partial S_w}{\partial p_c}\left(\frac{\partial p_n}{\partial x_d} - \frac{\partial p_w}{\partial x_d}\right)\right) \\
& + \frac{h^3}{12}\left(S_w\frac{\partial p_w}{\partial x_d} + S_n\frac{\partial p_n}{\partial x_d}\right)\left(\left(S_w\mu_w + S_n\mu_n\right)^{-1} - S_w\left(S_w\mu_w + S_n\mu_n\right)^{-2}\left(\mu_w - \mu_n\right)\right)\frac{\partial S_w}{\partial p_c}\left(\frac{\partial p_n}{\partial x_d} - \frac{\partial p_w}{\partial x_d}\right) \\
& + \frac{S_w h^2}{4\left(S_w\mu_w + S_n\mu_n\right)}\left(S_w\frac{\partial p_w}{\partial x_d} + S_n\frac{\partial p_n}{\partial x_d}\right)\frac{\partial h}{\partial x_d} - S_w\dot{h} - h\dot{S}_w
\end{aligned} \tag{4.33a}$$

$$\begin{aligned}
[\![\boldsymbol{n}_{\Gamma_d}\cdot\boldsymbol{q}]\!]_n = {} & \frac{S_n h^3}{12\left(S_w\mu_w + S_n\mu_n\right)}\left(S_w\frac{\partial^2 p_w}{\partial x_d^2} + S_n\frac{\partial^2 p_w}{\partial x_d^2} + \left(\frac{\partial p_w}{\partial x_d} - \frac{\partial p_n}{\partial x_d}\right)\frac{\partial S_w}{\partial p_c}\left(\frac{\partial p_n}{\partial x_d} - \frac{\partial p_w}{\partial x_d}\right)\right) \\
& + \frac{h^3}{12}\left(S_w\frac{\partial p_w}{\partial x_d} + S_n\frac{\partial p_n}{\partial x_d}\right)\left(-\left(S_w\mu_w + S_n\mu_n\right)^{-1} - S_n\left(S_w\mu_w + S_n\mu_n\right)^{-2}\left(\mu_w - \mu_n\right)\right)\frac{\partial S_w}{\partial p_c}\left(\frac{\partial p_n}{\partial x_d} - \frac{\partial p_w}{\partial x_d}\right) \\
& + \frac{S_n h^2}{4\left(S_w\mu_w + S_n\mu_n\right)}\left(S_w\frac{\partial p_w}{\partial x_d} + S_n\frac{\partial p_n}{\partial x_d}\right)\frac{\partial h}{\partial x_d} - S_n\dot{h} - h\dot{S}_n
\end{aligned} \tag{4.33b}$$

Comparing the expressions for the fluid flux inside the fracture, Eq. 4.32 for bubbly flow and 4.25 for the cubic law, shows that in the case of bubbly flow this term not only depends on the pressure gradient of the phase itself, but also on the pressure gradient of the other phase. This allows for a high pressure gradient phase to drag the low gradient phase along, increasing the fluid flux of the low gradient phase while decreasing the flux of the high gradient phase.

If the non-wetting phase represents an easily flowing fluid, such as air, the pressure gradient of the wetting phase will be much larger than the pressure gradient of the non-wetting phase. This indicates that under these circumstances the velocity of the wetting phase and the gas phase are determined by the pressure gradient of the wetting phase. This also allows the wetting phase fracture flux for bubbly flow to be expressed in a similar manner as the cubic law. By neglecting the pressure gradient of the non-wetting phase, the relative permeability is given by:

$$k_{dw} = S_w^2\cdot\frac{\mu_w}{S_w\mu_w + S_n\mu_n} \tag{4.34}$$

For the case of an easily flowing gas, the non-wetting viscosity is small, reducing this expression to S_w, whereas if the non-wetting phase and wetting phase have similar viscosities, this expression can be simplified to S_w^2. Comparing this to the relative permeability used with the cubic law, the similarities are clear: For both these cases, the relative permeability only depends on the saturation, although the exponent differs. It is important to note that under these assumptions it is not possible to obtain a similar expression for the non-wetting phase, since the fluid flux for this phase depends on the wetting phase pressure gradient, whereas for the cubic law this only depends on the non-wetting phase pressure gradient.

Separated Flow

The separated flow profile described here presumes a non-wetting layer of height $S_n h$ in the centre of the fracture, surrounded on the top and bottom by layers of the wetting fluid, each having a height of $\frac{1}{2}S_w h$, as shown in Figure 4.1. The separate layers are considered to consist only of a single phase. The velocity within these layers is described through the Stokes' equation for each individual phase:

$$0 = -\frac{\partial p_w}{\partial x_d} + \frac{\partial}{\partial y_d}\left(\mu_w \frac{\partial v_w}{\partial y_d}\right) \quad \text{for} \quad \frac{S_n h}{2} < |y_d| < \frac{h}{2} \tag{4.35a}$$

$$0 = -\frac{\partial p_n}{\partial x_d} + \frac{\partial}{\partial y_d}\left(\mu_n \frac{\partial v_n}{\partial y_d}\right) \quad \text{for} \quad -\frac{S_n h}{2} < y_d < \frac{S_n h}{2} \tag{4.35b}$$

These equations are subject to no-slip boundary conditions at the fracture walls, and continuous fluid velocity and stresses at the interface between the phases. Additionally, since the boundary conditions and fluid layers are symmetric, the derivative of the non-wetting fluid velocity in the centre of the fracture should be zero, enforcing continuous and symmetric velocity profiles. These boundary conditions are given by:

$$v_w\left(-\frac{h}{2}\right) = v_w\left(\frac{h}{2}\right) = 0 \tag{4.36a}$$

$$v_w\left(\frac{S_n h}{2}\right) = v_n\left(\frac{S_n h}{2}\right) \tag{4.36b}$$

$$\mu_w \frac{\partial v_w}{\partial y_d}\bigg|_{\frac{S_n h}{2}} = \mu_n \frac{\partial v_n}{\partial y_d}\bigg|_{\frac{S_n h}{2}} \tag{4.36c}$$

$$\frac{\partial v_n}{\partial y_d}\bigg|_0 = 0 \tag{4.36d}$$

Using Eq. 4.35a-4.36d the velocity profiles for both phases are obtained:

$$v_w = \begin{cases} \frac{1}{2\mu_w}\frac{\partial p_w}{\partial x_d}\left(|y_d|^2 - \left(\frac{h}{2}\right)^2\right) + \frac{S_n h}{2\mu_w}\frac{\partial p_c}{\partial x_d}\left(|y_d| - \frac{h}{2}\right) & \text{for} \quad \frac{S_n h}{2} < |y_d| < \frac{h}{2} \\ 0 & \text{for} \quad -\frac{S_n h}{2} < y_d < \frac{S_n h}{2} \end{cases} \tag{4.37a}$$

$$v_n = \begin{cases} 0 & \text{for} \quad \frac{S_n h}{2} < |y_d| < \frac{h}{2} \\ \frac{1}{2\mu_n}\frac{\partial p_n}{\partial x_d}\left(|y_d|^2 - \left(\frac{Snh}{2}\right)^2\right) + \frac{1}{2\mu_w}\frac{\partial p_w}{\partial x_d}\left(\left(\frac{S_n h}{2}\right)^2 - \left(\frac{h}{2}\right)^2\right) & \\ \quad + \frac{1}{\mu_w}\frac{\partial p_c}{\partial x_d}\left(\left(\frac{S_n h}{2}\right)^2 - S_n\left(\frac{h}{2}\right)^2\right) & \text{for} \quad -\frac{S_n h}{2} < y_d < \frac{S_n h}{2} \end{cases} \tag{4.37b}$$

Through Eq. 4.19 these velocity profiles then result in the fracture fluid transport:

$$q_w = -\frac{h^3}{\mu_w}\frac{\partial p_w}{\partial x_d}\left(\frac{1}{12} - \frac{1}{8}S_n + \frac{1}{24}S_n^3\right) - \frac{h^3}{\mu_w}\frac{\partial p_c}{\partial x_d}\left(\frac{1}{8}S_n - \frac{1}{4}S_n^2 + \frac{1}{8}S_n^3\right) \tag{4.38a}$$

$$q_n = -\frac{S_n^3 h^3}{12\mu_n}\frac{\partial p_n}{\partial x_d} - \frac{h^3}{\mu_w}\frac{\partial p_w}{\partial x_d}\left(\frac{1}{8}S_n - \frac{1}{8}S_n^3\right) - \frac{h^3}{\mu_w}\frac{\partial p_c}{\partial x_d}\left(\frac{1}{4}S_n^2 - \frac{1}{4}S_n^3\right) \tag{4.38b}$$

Finally, substituting Eq. (4.38a) in the definition for the fracture inflow velocity, Eq. (4.19), results in:

$$\begin{aligned} [\![\boldsymbol{n}_{\Gamma_d} \cdot \boldsymbol{q}]\!]_w = {} & \frac{h^3}{\mu_w}\frac{\partial^2 p_w}{\partial x_d^2}\left(\frac{1}{12} - \frac{1}{8}S_n + \frac{1}{24}S_n^3\right) + \frac{h^2}{\mu_w}\frac{\partial p_w}{\partial x_d}\frac{\partial h}{\partial x_d}\left(\frac{1}{4}h^2 - \frac{3}{8}S_n h^2 + \frac{1}{8}S_n^3 h^2\right) \\ & + \frac{h^3}{\mu_w}\frac{\partial p_w}{\partial x_d}\frac{\partial S_w}{\partial p_c}\left(\frac{\partial p_n}{\partial x_d} - \frac{\partial p_w}{\partial x_d}\right)\left(\frac{1}{8} - \frac{1}{8}S_n^2\right) + \frac{h^3}{\mu_w}\left(\frac{\partial^2 p_n}{\partial x_d^2} - \frac{\partial^2 p_w}{\partial x_d^2}\right)\left(\frac{1}{8}S_n - \frac{1}{4}S_n^2 + \frac{1}{8}S_n^3\right) \\ & + \frac{h^2}{\mu_w}\frac{\partial p_c}{\partial x_d}\frac{\partial h}{\partial x_d}\left(\frac{3}{8}S_n - \frac{3}{4}S_n^2 + \frac{3}{8}S_n^3\right) + \frac{h^3}{\mu_w}\frac{\partial p_c}{\partial x_d}\frac{\partial p_n}{\partial x_d} - \frac{\partial p_w}{\partial x_d}\left(-\frac{1}{8} + \frac{1}{2}S_n - \frac{3}{8}S_n^2\right) - S_w\dot{h} - h\dot{S}_w \end{aligned} \tag{4.39}$$

and similarly for the non-wetting phase:

$$
\begin{aligned}
[\![\boldsymbol{n}_{\Gamma_d}\cdot\boldsymbol{q}]\!]_n = {} & \frac{S_n^3 h^3}{12\mu_n}\frac{\partial p_n^2}{\partial x_d^2} + \frac{h^2 S_n^3}{4\mu_n}\frac{\partial h}{\partial x_d}\frac{\partial p_n}{\partial x_d} - \frac{h^3 S_n^2}{4\mu_n}\frac{\partial p_n}{\partial x_d}\frac{\partial S_w}{\partial p_c}\left(\frac{\partial p_n}{\partial x_d}-\frac{\partial p_w}{\partial x_d}\right)\\
& + \frac{h^3}{\mu_w}\frac{\partial^2 p_w}{\partial x_d^2}\left(\frac{1}{8}S_n-\frac{1}{8}S_n^3\right) + \frac{h^2}{\mu_w}\frac{\partial p_w}{\partial x_d}\frac{\partial h}{\partial x_d}\left(\frac{3}{8}S_n-\frac{3}{8}S_n^3\right) + \frac{h^3}{\mu_w}\frac{\partial p_w}{\partial x_d}\frac{\partial S_w}{\partial p_c}\left(\frac{\partial p_n}{\partial x_d}-\frac{\partial p_w}{\partial x_d}\right)\left(-\frac{1}{8}+\frac{3}{8}S_n^2\right)\\
& + \frac{h^3}{\mu_w}\left(\frac{\partial^2 p_n}{\partial x_d^2}-\frac{\partial^2 p_w}{\partial x_d^2}\right)\left(\frac{1}{4}S_n^2-\frac{1}{4}S_n^3\right) + \frac{h^2}{\mu_w}\frac{\partial p_c}{\partial x_d}\frac{\partial h}{\partial x_d}\left(\frac{3}{4}S_n^2-\frac{3}{4}S_n^3\right)\\
& + \frac{h^3}{\mu_w}\frac{\partial p_c}{\partial x_d}\frac{\partial S_w}{\partial p_c}\left(\frac{\partial p_n}{\partial x_d}-\frac{\partial p_w}{\partial x_d}\right)\left(-\frac{1}{2}S_n+\frac{3}{4}S_n^2\right) - S_n\dot{h} - h\dot{S}_n
\end{aligned}
\tag{4.40}
$$

Similar to the bubbly fracture flow model, the fluid flux inside the fracture, Eq. 4.38a, depends on both the pressure gradient of the phase itself, and the pressure gradient of the other phase. This allows the wetting phase to be dragged along with the non-wetting phase, or be slowed down by it. Furthermore, due to the used separated flow model, one of the phases could flow against its own pressure gradient, or could be both flowing along with the pressure gradient in part of the fracture height, while flowing against it in the remainder of its flow profile.

Neglecting the non-wetting phase pressure gradient, the separated flow model can also be cast into the cubic law, resulting in a relative permeability for the wetting phase:

$$
k_{dw} = 1 - 3S_n + 3S_n^2 - S_n^3 = S_w^3 \tag{4.41}
$$

which corresponds to the expression used for the cubic law. It should be noted that this assumes negligible influence of the non-wetting phase pressure gradient, and therefore is only valid if the non-wetting phase represents a gas in a fairly high permeable porous material. Furthermore, the non-wetting phase can not be cast into an expression compatible with the cubic law, since using the separated flow model the non-wetting fluid flux depends on the wetting phase pressure gradient.

POST-PROCESSING

Eq. 4.27 for the cubic law flow type, Eq. 4.33 for bubbly flow, or Eq. 4.39-4.40 are used to directly describe the effect of the fracture on the surrounding porous material in terms of the degrees of freedom used to model the porous material. The main advantage is that this only requires these inflows to be integrated over the discontinuity, without having to simulate the fluid flow within the fracture. However, since the velocity profiles and fluid fluxes within the fracture are also detailed solely in terms of the degrees of freedom of the surrounding porous medium, these profiles can be re-obtained by post-processing the resulting pressures and displacements. By re-obtaining these velocity profiles, a detailed look into the interactions within the fracture is possible. This furthermore allows these models to be compared based on the fluid flow within the fracture, even though the models only prescribe the in/outflow on the discontinuity.

4.2. DISCRETISATION

In a similar manner as was done for the single phase flow in Section 2.2, the weak form of the momentum balance is obtained by multiplying with the test function $\boldsymbol{\eta}$:

$$
\int_\Omega \nabla\boldsymbol{\eta} : \left(\boldsymbol{\sigma}_s - \alpha S_w p_w \boldsymbol{I} - \alpha S_n p_n \boldsymbol{I}\right)\, \mathrm{d}\Omega - \int_{\Gamma_d} \boldsymbol{\eta}\cdot\left(\boldsymbol{\tau}_d - \boldsymbol{n}_d\left(S_w p_w + S_n p_n\right)\right)\, \mathrm{d}\Gamma_d = \int_{\Gamma_t} \boldsymbol{\eta}\cdot\bar{\boldsymbol{\tau}}\, \mathrm{d}\Gamma_t \tag{4.42}
$$

The mass balances, Eqs (4.8) and (4.9), are multiplied with the test functions ζ and ξ. The divergence theorem is used on the terms relating to the interior fluid flux and the fracture inflow, resulting in:

$$\begin{aligned}\int_\Omega \zeta \frac{1}{M_{ww}}\dot{p}_w + \zeta\frac{1}{M_{wn}}\dot{p}_n + \alpha S_w \zeta \boldsymbol{\nabla}\cdot\dot{\boldsymbol{u}} + k_w k_{rw}\boldsymbol{\nabla}\zeta\cdot\boldsymbol{\nabla} p_w \,\mathrm{d}\Omega - \int_{\Gamma_d} \frac{\partial\zeta}{\partial \bar{s}} q_w + \zeta\frac{\partial S_w h}{\partial t}\,\mathrm{d}\Gamma_d \\ = -\int_{\Gamma_q}\zeta\overline{q}_w\,\mathrm{d}\Gamma_q - \int_{\partial\Gamma_d}\zeta Q_w\,\mathrm{d}\partial\Gamma_d\end{aligned} \tag{4.43}$$

$$\begin{aligned}\int_\Omega \xi \frac{1}{M_{nw}}\dot{p}_w + \xi\frac{1}{M_{nn}}\dot{p}_n + \alpha S_n \xi \boldsymbol{\nabla}\cdot\dot{\boldsymbol{u}} + k_n k_{rn}\boldsymbol{\nabla}\xi\cdot\boldsymbol{\nabla} p_n \,\mathrm{d}\Omega - \int_{\Gamma_d} \frac{\partial\xi}{\partial \bar{s}} q_n + \xi\frac{\partial S_n h}{\partial t}\,\mathrm{d}\Gamma_d \\ = -\int_{\Gamma_q}\xi\overline{q}_n\,\mathrm{d}\Gamma_q - \int_{\partial\Gamma_d}\xi Q_n\,\mathrm{d}\partial\Gamma_d\end{aligned} \tag{4.44}$$

The fracture fluid fluxes q_w and q_n are dependent on the chosen model, and Q_w and Q_n are the fracture outflows imposed at the fracture tips, here assumed to be zero.

The fracture inflow for all models contain second spatial derivatives, similar to the single phase fracture flow formulation. Therefore, corresponding to the previous chapters, quartic NURBS are used to discretise the solid displacement and cubic NURBS are used for the wetting and non-wetting pressures. This allows the displacements and pressures to be discretised as:

$$\boldsymbol{u} = \sum_{el=1}^{n_{el}} \boldsymbol{N}_s \boldsymbol{u}^{el} \tag{4.45}$$

$$p_w = \sum_{el=1}^{n_{el}} \boldsymbol{N}_w \boldsymbol{p}_w^{el} \tag{4.46}$$

$$p_n = \sum_{el=1}^{n_{el}} \boldsymbol{N}_n \boldsymbol{p}_n^{el} \tag{4.47}$$

which allows the momentum balance to be discretised and split according to Eq. 2.46, with the external forces given by Eq. 2.47, the internal forces given by:

$$\boldsymbol{f}_{int} = \int_\Omega \boldsymbol{B}^T \boldsymbol{\sigma}_s^{t+\Delta t}\,\mathrm{d}\Omega - \int_\Omega \alpha S_w \boldsymbol{B}^T \boldsymbol{m}\boldsymbol{N}_w \boldsymbol{p}_w^{t+\Delta t}\,\mathrm{d}\Omega - \int_\Omega \alpha S_n \boldsymbol{B}^T \boldsymbol{m}\boldsymbol{N}_n \boldsymbol{p}_n^{t+\Delta t}\,\mathrm{d}\Omega \tag{4.48}$$

and the forces relating to the discontinuity by:

$$\boldsymbol{f}_d = \int_{\Gamma_d} \boldsymbol{N}_d^T \boldsymbol{R}^T \boldsymbol{D}_d \boldsymbol{R} \boldsymbol{N}_d \boldsymbol{u}^{t+\Delta t}\,\mathrm{d}\Gamma_d - \int_{\Gamma_d} S_w \boldsymbol{N}_d^T \boldsymbol{n}_{\Gamma_d} \boldsymbol{N}_w \boldsymbol{p}_w^{t+\Delta t}\,\mathrm{d}\Gamma_d - \int_{\Gamma_d} S_n \boldsymbol{N}_d^T \boldsymbol{n}_{\Gamma_d} \boldsymbol{N}_n \boldsymbol{p}_n^{t+\Delta t}\,\mathrm{d}\Gamma_d \tag{4.49}$$

The mass balances for the wetting and non-wetting phases are split into terms for the internal, external and discontinuity related fluid fluxes:

$$\boldsymbol{q}_{w,ext} - \boldsymbol{q}_{w,int} - \boldsymbol{q}_{w,d} = \boldsymbol{0} \tag{4.50}$$

$$\boldsymbol{q}_{n,ext} - \boldsymbol{q}_{n,int} - \boldsymbol{q}_{n,d} = \boldsymbol{0} \tag{4.51}$$

The external fluid fluxes are defined in a similar manner as for the single phase flow:

$$\boldsymbol{q}_{w,ext} = \Delta t \int_{\Gamma_q} \boldsymbol{N}_w^T \overline{q}_w\,\mathrm{d}\Gamma_q + \Delta t \int_{\partial\Gamma_d} \boldsymbol{N}_w^T Q_w\,\mathrm{d}\partial\Gamma_d \tag{4.52}$$

$$\boldsymbol{q}_{n,ext} = \Delta t \int_{\Gamma_q} \boldsymbol{N}_n^T \overline{q}_n\,\mathrm{d}\Gamma_q + \Delta t \int_{\partial\Gamma_d} \boldsymbol{N}_n^T Q_n\,\mathrm{d}\partial\Gamma_d \tag{4.53}$$

A backward Euler time discretisation scheme, see Eq. 2.45, is used to perform the temporal discretisation, resulting in the internal fluxes:

$$\begin{aligned}\boldsymbol{q}_{w,int} = &-\int_\Omega \alpha S_w \boldsymbol{N}_w^T \boldsymbol{m}^T \boldsymbol{B}\left(\boldsymbol{u}^{t+\Delta t} - \boldsymbol{u}^t\right)\,\mathrm{d}\Omega - \int_\Omega \Delta t k_w k_{rw} (\nabla \boldsymbol{N}_w)^T \nabla \boldsymbol{N}_w \boldsymbol{p}_w^{t+\Delta t}\,\mathrm{d}\Omega \\ &- \int_\Omega \frac{1}{M_{ww}} \boldsymbol{N}_w^T \boldsymbol{N}_w \left(\boldsymbol{p}_w^{t+\Delta t} - \boldsymbol{p}_w^t\right)\,\mathrm{d}\Omega - \int_\Omega \frac{1}{M_{wn}} \boldsymbol{N}_w^T \boldsymbol{N}_n \left(\boldsymbol{p}_n^{t+\Delta t} - \boldsymbol{p}_n^t\right)\,\mathrm{d}\Omega \end{aligned} \tag{4.54}$$

$$\begin{aligned}\boldsymbol{q}_{n,int} = &-\int_\Omega \alpha S_n \boldsymbol{N}_n^T \boldsymbol{m}^T \boldsymbol{B}\left(\boldsymbol{u}^{t+\Delta t} - \boldsymbol{u}^t\right)\,\mathrm{d}\Omega - \int_\Omega \Delta t k_n k_{rn} (\nabla \boldsymbol{N}_n)^T \nabla \boldsymbol{N}_n \boldsymbol{p}_n^{t+\Delta t}\,\mathrm{d}\Omega \\ &- \int_\Omega \frac{1}{M_{nw}} \boldsymbol{N}_n^T \boldsymbol{N}_w \left(\boldsymbol{p}_w^{t+\Delta t} - \boldsymbol{p}_w^t\right)\,\mathrm{d}\Omega - \int_\Omega \frac{1}{M_{nn}} \boldsymbol{N}_n^T \boldsymbol{N}_n \left(\boldsymbol{p}_n^{t+\Delta t} - \boldsymbol{p}_n^t\right)\,\mathrm{d}\Omega \end{aligned} \tag{4.55}$$

The fluid fluxes due to the discontinuity are split into two parts:

$$\boldsymbol{q}_{\pi,d} = \boldsymbol{q}_{\pi,dh} + \boldsymbol{q}_{\pi,dp} \tag{4.56}$$

The first term, $\boldsymbol{q}_{\pi,dh}$, is related to the fluid absorbed due to changes in fracture height and saturation. This term is the same for all fracture flow models, and given by:

$$\boldsymbol{q}_{w,dh} = -\int_{\Gamma_d} S_w \boldsymbol{N}_w^T \boldsymbol{n}_{\Gamma_d}^T \boldsymbol{N}_d \left(\boldsymbol{u}^{t+\Delta t} - \boldsymbol{u}^t\right) + \left(S_w^{t+\Delta t} - S_w^t\right) \boldsymbol{N}_w^T \boldsymbol{n}_{\Gamma_d}^T \boldsymbol{N}_d \boldsymbol{u}^{t+\Delta t}\,\mathrm{d}\Gamma_d \tag{4.57}$$

$$\boldsymbol{q}_{n,dh} = -\int_{\Gamma_d} S_n \boldsymbol{N}_n^T \boldsymbol{n}_{\Gamma_d}^T \boldsymbol{N}_d \left(\boldsymbol{u}^{t+\Delta t} - \boldsymbol{u}^t\right) + \left(S_n^{t+\Delta t} - S_n^t\right) \boldsymbol{N}_n^T \boldsymbol{n}_{\Gamma_d}^T \boldsymbol{N}_d \boldsymbol{u}^{t+\Delta t}\,\mathrm{d}\Gamma_d \tag{4.58}$$

The second term describes the fluid transported by the fracture. This term depends on the chosen fracture flow model. For the cases in which the cubic law is used to described the fracture flow, Eq. 4.25 with the relative permeabilities from Eq. 4.26, the fracture fluid flux is given by:

$$\boldsymbol{q}_{w,dp}^{cubic} = -\int_{\Gamma_d} \frac{\Delta t S_w^3}{12\mu_w} (\nabla \boldsymbol{N}_w)^T \left(\boldsymbol{n}_{\Gamma_d}^T \boldsymbol{N}_d \boldsymbol{u}^{t+\Delta t}\right)^3 \nabla \boldsymbol{N}_w \boldsymbol{P}_w^{t+\Delta t}\,\mathrm{d}\Gamma_d \tag{4.59}$$

$$\boldsymbol{q}_{n,dp}^{cubic} = -\int_{\Gamma_d} \frac{\Delta t S_n^3}{12\mu_n} (\nabla \boldsymbol{N}_n)^T \left(\boldsymbol{n}_{\Gamma_d}^T \boldsymbol{N}_d \boldsymbol{u}^{t+\Delta t}\right)^3 \nabla \boldsymbol{N}_n \boldsymbol{P}_n^{t+\Delta t}\,\mathrm{d}\Gamma_d \tag{4.60}$$

For the bubbly flow model, Eq. 4.33, these terms become:

$$\boldsymbol{q}_{w,dp}^{bubbly} = -\int_{\Gamma_d} \frac{\Delta t S_w}{12\left(S_w \mu_w + S_n \mu_n\right)} (\nabla \boldsymbol{N}_w)^T \left(\boldsymbol{n}_{\Gamma_d}^T \boldsymbol{N}_d \boldsymbol{u}^{t+\Delta t}\right)^3 \left(S_w \nabla \boldsymbol{N}_w \boldsymbol{p}_w^{t+\Delta t} + S_n \nabla \boldsymbol{N}_n \boldsymbol{p}_n^{t+\Delta t}\right)\,\mathrm{d}\Gamma_d \tag{4.61}$$

$$\boldsymbol{q}_{n,dp}^{bubbly} = -\int_{\Gamma_d} \frac{\Delta t S_n}{12\left(S_w \mu_w + S_n \mu_n\right)} (\nabla \boldsymbol{N}_w)^T \left(\boldsymbol{n}_{\Gamma_d}^T \boldsymbol{N}_d \boldsymbol{u}^{t+\Delta t}\right)^3 \left(S_w \nabla \boldsymbol{N}_w \boldsymbol{p}_w^{t+\Delta t} + S_n \nabla \boldsymbol{N}_n \boldsymbol{p}_n^{t+\Delta t}\right)\,\mathrm{d}\Gamma_d \tag{4.62}$$

and in the case of the separated flow model:

$$\begin{aligned}\boldsymbol{q}_{w,dp}^{separated} = &-\int_{\Gamma_d} \frac{\Delta t}{\mu_w} (\nabla \boldsymbol{N}_w)^T \left(\boldsymbol{n}_{\Gamma_d}^T \boldsymbol{N}_d \boldsymbol{u}^{t+\Delta t}\right)^3 \left(\nabla \boldsymbol{N}_w \boldsymbol{p}_w^{t+\Delta t} \left(\frac{1}{12} - \frac{1}{8} S_n + \frac{1}{24} S_n^3\right)\right. \\ &\left. + \left(\nabla \boldsymbol{N}_n \boldsymbol{p}_n^{t+\Delta t} - \nabla \boldsymbol{N}_w \boldsymbol{p}_w^{t+\Delta t}\right)\left(\frac{1}{8} S_n - \frac{1}{4} S_n^2 + \frac{1}{8} S_n^3\right)\right)\,\mathrm{d}\Gamma_d \end{aligned} \tag{4.63}$$

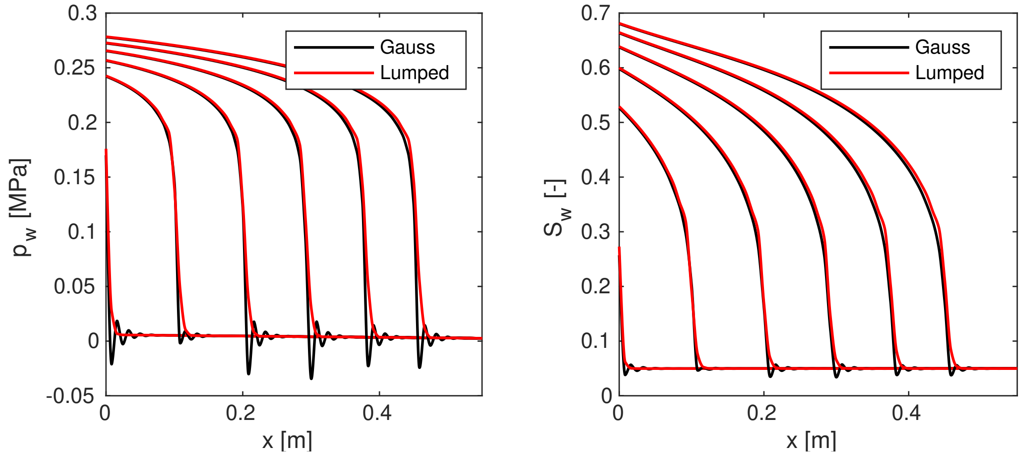

(a) Wetting phase pressure

(b) Wetting phase saturation

Figure 4.2: Comparison between a standard Gauss integration scheme and the lumped pressure capacity scheme for the case described in Section 4.3 and Figure 4.3 (excluding the fracture). Lines show results in 1000 s increments.

$$\begin{aligned}\boldsymbol{q}_{n,dp}^{separated} = -\int_{\Gamma_d} \Delta t \left(\boldsymbol{\nabla N}_n\right)^T \left(\boldsymbol{n}_{\Gamma_d}\boldsymbol{N}_d\boldsymbol{u}^{t+\Delta t}\right)^3 \Bigg(\frac{1}{12\mu_n} S_n^3 \boldsymbol{\nabla N}_n \boldsymbol{p}_n^{t+\Delta t} + \frac{1}{8\mu_w}\boldsymbol{\nabla N}_w \boldsymbol{p}_w^{t+\Delta t}\left(S_n - S_n^3\right) \\ + \frac{1}{4\mu_w}\left(\boldsymbol{\nabla N}_n \boldsymbol{p}_n^{t+\Delta t} - \boldsymbol{\nabla N}_w \boldsymbol{p}_w^{t+\Delta t}\right)\left(S_n^2 - S_n^3\right)\Bigg) \mathrm{d}\Gamma_d \qquad (4.64)\end{aligned}$$

The discretised equations have been solved using a Newton-Raphson scheme, similar to the scheme employed in the previous chapters. Following on from the conclusions of Chapter 3 a consistent tangential stiffness matrix was used, which resulted in a quadratic convergence rate. The system matrices are given in Appendix C.1

4.2.1. STABILISATION

When simulating the oil-water cases, sharp changes in saturation occurred. Near these phase interfaces, strong pressure oscillations were observed, as shown in Figure 4.2 for the parameters and geometry (excluding the discontinuity) that will be given in detail in the next section. Since the fracture inflow models depend on the first and second derivatives of the pressure, and the first derivative of the saturation, these oscillations resulted in large oscillations in the fracture inflow velocity with these oscillations large compared to the actual fracture inflow.

Several stabilisation schemes exist to prevent these oscillations. Multi-scale stabilisation [98] has been shown to be able to suppress pressure oscillations throughout the interior of the domain in non-deformable porous media [104, 105]. The Galerkin least squares method has also been shown to suppress these oscillations [222], and has been used to circumvent the inf-sup condition in deformable porous materials [233]. Another scheme also capable of circumventing the inf-sup condition, and suppressing non-physical pressure oscillations, was derived by [130] based on a pressure-projecting technique. In their paper, they derive optimal stabilisation parameters for their scheme. One of their observations is that the optimal stabilisation parameter reduces their scheme to only alter the pressure capacity matrix, and corresponds to using a lumped pressure capacity matrix.

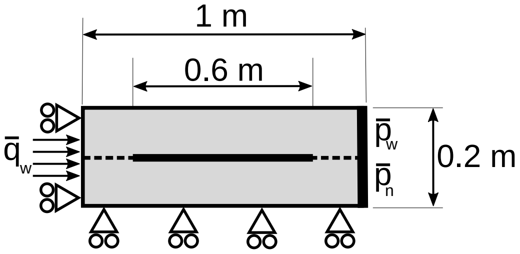

Figure 4.3: Geometry and boundary conditions used for the single fracture case.

Using the lumped pressure capacity matrix as stabilisation method, the terms relating to the pressure capacity in Eq. 4.54-4.55 are integrated through a sum over all control points:

$$\int_\Omega \frac{1}{M_{ww}} \boldsymbol{N}_w^T \boldsymbol{N}_w \left(\boldsymbol{p}_w^{t+\Delta t} - \boldsymbol{p}_w^t\right) \mathrm{d}\Omega = \sum_{cp=1}^{n_{cps}} C_{ww} \left(\boldsymbol{p}_{w,cp}^{t+\Delta t} - \boldsymbol{p}_{w,cp}^t\right) \tag{4.65}$$

with the representative pressure capacities determined by integrating over the complete element , using a standard Gauss integration scheme:

$$C_{ww} = \int_\Omega \frac{1}{M_{ww}} \boldsymbol{N}_{cp} \, \mathrm{d}\Omega \tag{4.66}$$

with M_{ww} determined at the integration points and $\boldsymbol{N}_{cp}$ the interpolant corresponding to the control point. It should be noted that if Lagrangian polynomials were used for the interpolation functions, a Newton-Cotes integration scheme would result in a similar lumped matrix [234]. This indicates that while using traditional finite elements the pressure oscillations can be suppressed by locating the integration points to correspond with the control points of the mesh, this does not suffice when isogeometric elements are used, thereby requiring the described lumped integration scheme.

The effect of this stabilisation is shown in Figure 4.2, showing that the lumped integration suppresses all the non-physical pressure oscillations. Away from the interface, the scheme does not significantly alter the obtained pressure.

The implementation of the multiphase fluid flow within the porous material, and the cubic law for the fluid flow within the fracture have been verified by simulating a case from [108], which is detailed in Appendix A.4.

4.3. COMPARISON OF FRACTURE FLOW MODELS

A boundary value problem containing a single fracture has been simulated to compare the effects of the fracture flow model on the resulting pressures and saturation. This case, shown in Figure 4.3, consists of a 1m × 0.2m rectangular domain, with a 0.6 m horizontal fracture in the centre. A wetting phase fluid inflow of $\overline{q}_w = 10^{-5}$ m/s is imposed on the left boundary, while a constant pressures of $\overline{p}_w = 0$ MPa and $\overline{p}_n = 0.3$ MPa are imposed on the right edge, resulting in a constant saturation on the right boundary of $S_w = 0.05$. Displacements are constrained in vertical direction on the bottom boundary, and in horizontal direction on the left boundary. Initial pressures of $p_w = 0$ MPa and $p_n = 0.3$ MPa have been used at the start of the simulation, resulting in an initial saturation $S_w = 0.05$.

For the wetting phase, a water like fluid has been used ($\mu_w = 1$ mPa s, $K_w = 2.15$ GPa) and for the non-wetting phase an oil-like fluid ($\mu_n = 0.45$ mPa s, $K_n = 1.5$ GPa). The porous material used a porosity $n_f = 0.2$, Poisson ratio $\nu = 0.2$, bulk modulus $K_s = 36$ GPa, Biot coefficient $\alpha = 1.0$, and intrinsic permeability $k = 10^{-12}$ m^2. Section 4.3.1 and 4.3.2 use a

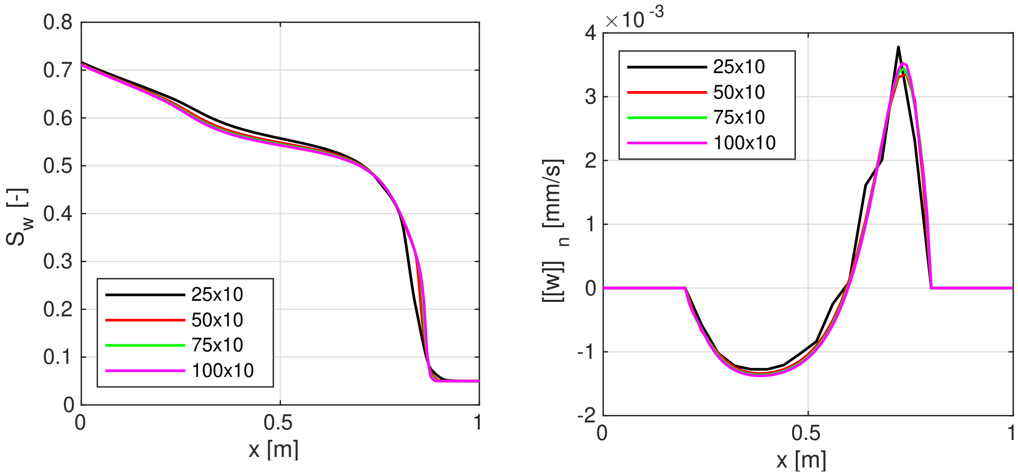

(a) Saturation

(b) Jump in non-wetting fracture inflow velocity

Figure 4.4: Effect of mesh refinement using the cubic law fracture flow model. Results shown for $t = 2.5$ hours.

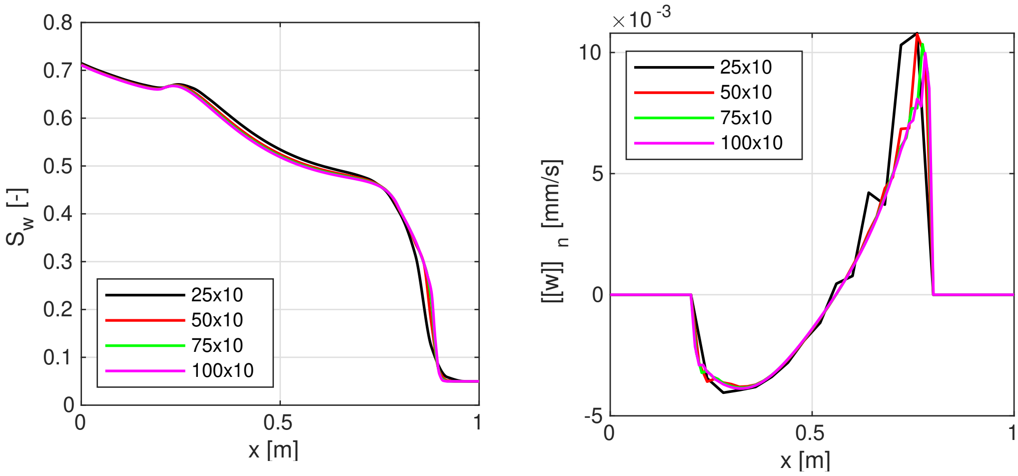

(a) Saturation

(b) Jump in non-wetting fracture inflow velocity

Figure 4.5: Effect of mesh refinement using the bubbly fracture flow model. Results shown for $t = 2.5$ hours.

Young's modulus $E = 20$ GPa, whereas the Young's modulus is varied between $E = 1$ GPa and $E = 1000$ GPa in Section 4.3.3.

The domain has been discretised using quartic NURBS for the solid displacement and cubic NURBS for the wetting and non-wetting pressures. In Section 4.3.1 the number of Bézier extracted elements is varied between 25×10 and 100×10, whereas for the remainder of this case 100×10 are used. A constant time-step $\Delta t = 25$ s has been used.

4.3.1. MESH REFINEMENT STUDY

A mesh refinement study has been performed to determine if the conclusions for single phase flows, Section 2.4.1, also hold for the multiphase fracture flow models. The results are shown in Figure 4.4 for the cubic law, Figure 4.5 for the bubbly flow, and Figure 4.6 for the separated fracture flow. Looking at the degree of saturation, differences are seen between the 25×10 mesh and the finer meshes. These differences are most notable near the sharp drop in saturation, with the coarse meshes combined with the NURBS being unable to rep-

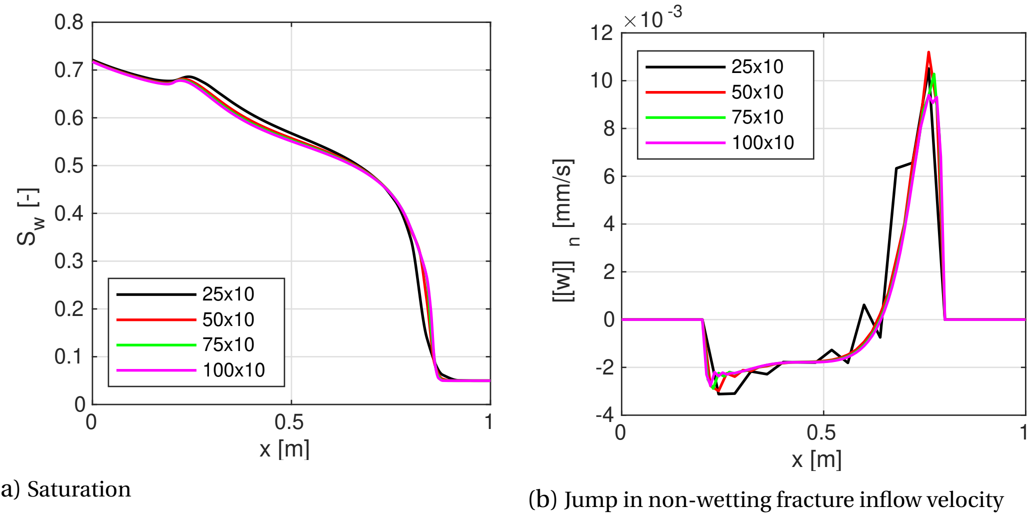

(a) Saturation

(b) Jump in non-wetting fracture inflow velocity

Figure 4.6: Effect of mesh refinement using the separated fracture flow model. Results shown for $t = 2.5$ hours.

resent sharp changes in pressure result in the coarse mesh being insufficient to accurately represent the interface. Starting from the 50 × 10 mesh, the sharp drop in saturation is represented better, and the pressures near the fracture tips also become more accurate. This results in near to no visible difference between the 50 × 10 and the 100 × 10 meshes.

The fracture outflow fluxes show similar oscillations as were seen for the single phase cases for the coarse mesh. Refining the mesh reduces these oscillations in the centre of the fracture, and limits the oscillations to near the fracture tips. Even though no difference between the two finest meshes is seen in the centre of the fracture, at the fracture tips these differences do still occur, and are most visible for the right fracture tip where the sharp drop in saturation occurs together with the sharp changes in outflow.

Most of these results correspond to the single phase conclusions. A coarse mesh is sufficient to represent the effect of the fracture on the pressure (and saturation) in the surrounding porous medium, whereas a finer mesh is needed to suppress the oscillations in fracture outflow. The main difference between the single phase and multiphase cases is the sharp drop in saturation, which requires a finer mesh to accurately represent this interface correctly. This results in a somewhat finer mesh being needed for the multiphase case compared to the single phase cases if only the behaviour of the porous material is analysed, while similar fine meshes are needed to obtain accurate results for the fracture, independent of the simulations representing single phase or multiphase fluid flows.

4.3.2. FLUID FLOW WITHIN THE FRACTURE

The saturation resulting from the simulations using the separated flow model are shown in Figure 4.7. The wetting phase flows from the left boundary into the fracture. From the fracture it diffuses both to the outflow, and to the impermeable top and bottom of the domain, pushing the non-wetting phase towards the outflow in the process. The small height of the domain results in the fluid flow mostly flowing in horizontal direction, as shown in Figure 4.8.

The saturation along the discontinuity is given in Figure 4.9b for the different fracture flow models. The bubbly and separated flow fracture flow models resulted in a higher saturation near the left fracture tip, whereas the saturation is slightly higher near the right frac-

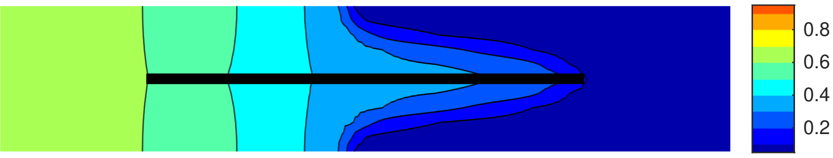

(a) $t = 1.5$ hours

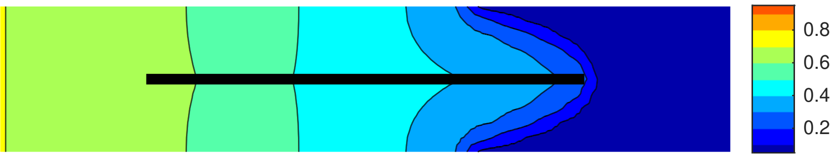

(b) $t = 2$ hours

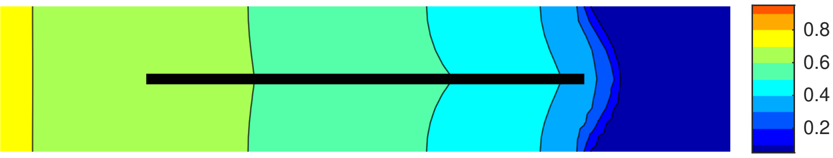

(c) $t = 2.5$ hours

Figure 4.7: Wetting phase saturation using the separated fracture flow model.

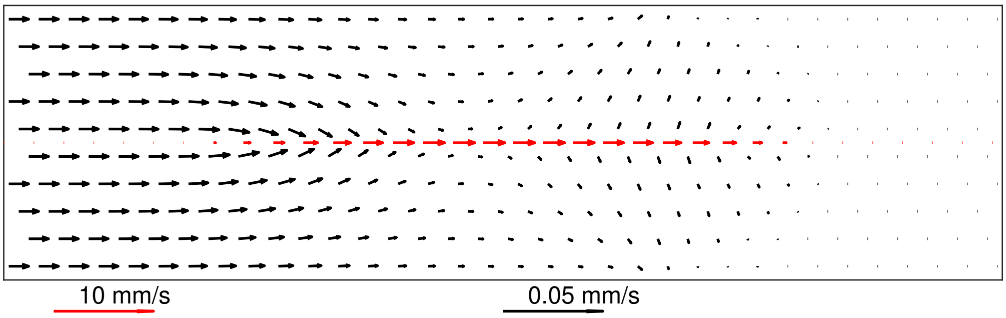

(a) Wetting phase

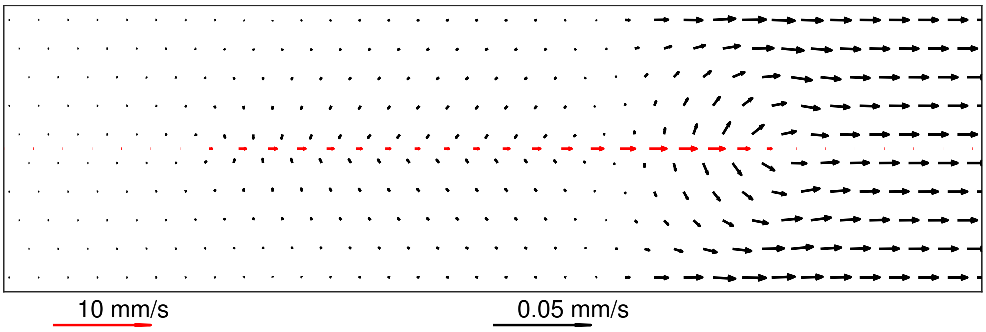

(b) Non-wetting phase

Figure 4.8: Fluid flux inside the porous medium (black) and maximum fluid velocity inside the fracture (red) at $t = 2$ hours using the separated fracture flow model.

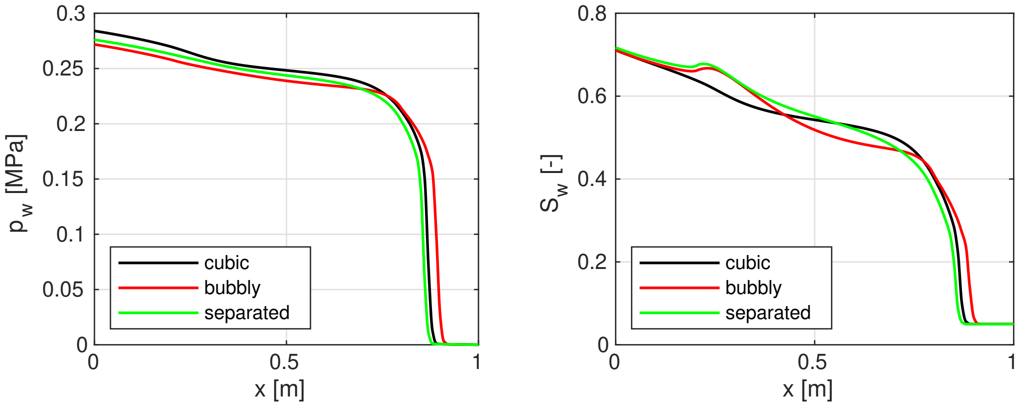

(a) Wetting phase pressure

(b) Saturation

Figure 4.9: Wetting phase pressure and saturation along the discontinuity at $t = 2.5$ hours.

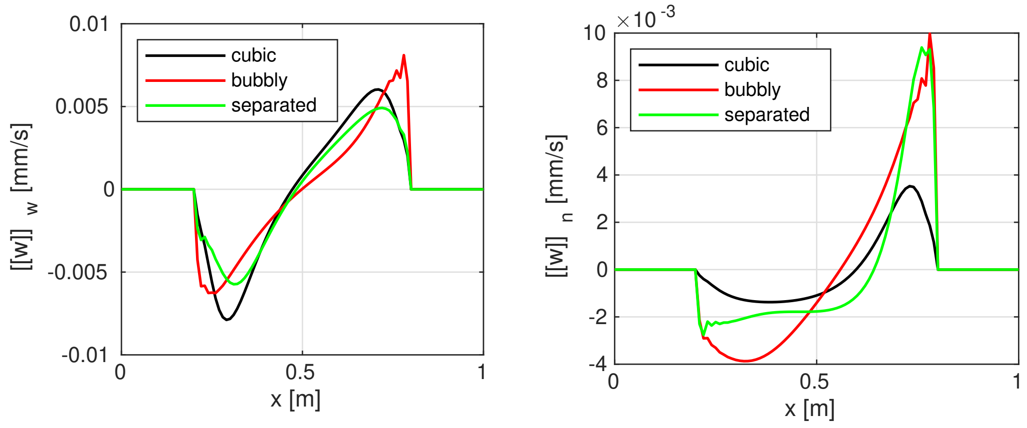

(a) Wetting phase

(b) Non-wetting phase

Figure 4.10: Jump in fluid velocity normal to the fracture along the discontinuity at $t = 2.5$ hours.

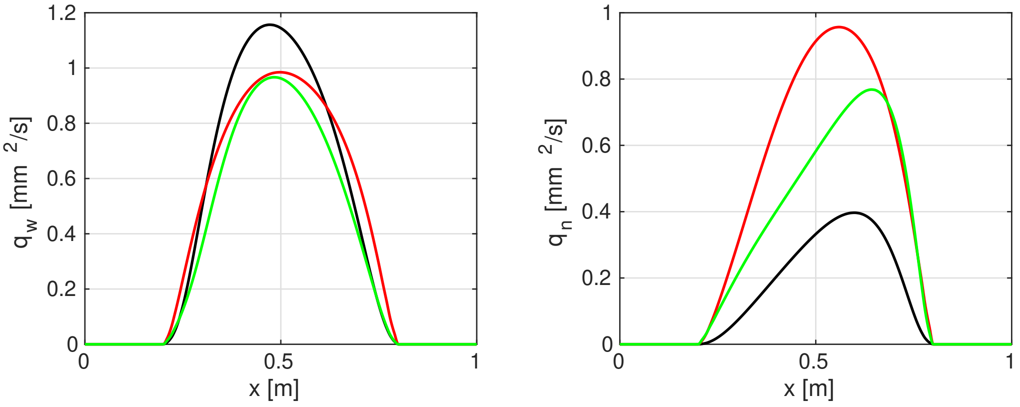

(a) Wetting phase

(b) Non-wetting phase

Figure 4.11: Fluid flux in tangential direction inside the fracture at $t = 2.5$ hours

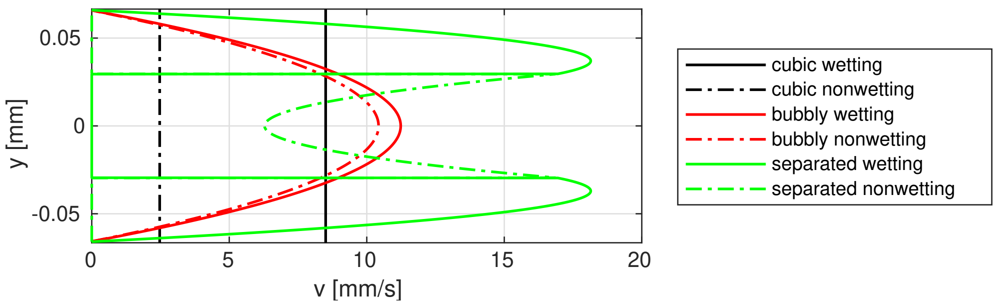

Figure 4.12: Velocity profiles inside the fracture at $x = 0.5$ m, $t = 2.5$ hours.

ture tip for the cubic law. The bubbly flow model also resulted in a slightly further penetration of the wetting phase. The wetting phase pressure, Figure 4.9a, shows similar results.

The jump in fluid flux normal to the fracture, the fracture outflow, after 2.5 hours is given in Figure 4.10. Using the bubbly flow model, the wetting phase has higher in and outflows near the fracture tips, whereas the separated flow model has higher inflows near the centre of the fracture. However, the wetting phase fluid inflow is fairly similar between all models. In contrast, the non-wetting phase shows large differences in fracture inflow depending on the chosen model. These differences are caused by the non-wetting phase, which has a low pressure gradient, being drag along by the higher pressure gradient of the wetting phase. This causes a slight decrease in the wetting phase fracture outflow, due to the decreased velocity of this phase, while increasing the non-wetting phase outflow. This is also confirmed by looking at the fluid flux in tangential direction inside the fracture, Figure 4.11, showing a significantly higher non-wetting fluid flux for the bubbly and separated flow models compared to the cubic law, while slightly lower wetting phase fluid fluxes are obtained for these models.

By post processing the saturations and pressures the velocity profiles inside the fracture can be obtained. The velocity profiles in the middle of the fracture, at $x = 0.5$ m, are shown in Figure 4.12. In this figure, the cubic law is shown as a constant velocity throughout the fracture height, since the cubic law only describes the total fluid flux, and not the velocity profiles. By looking at the profiles of the separated flow model, the interaction between the phases is clearly visible. The wetting phase drags along the non-wetting phase, resulting in a decreased velocity of the wetting phase near the interface, while significantly increasing the velocity of the non-wetting phase near the phase interface compared to the centre of the fracture. The bubbly flow also has the wetting phase dragging the non-wetting phase along. Due to the volume averaging and the saturation the wetting phase obtains slightly faster velocities compared to the non-wetting phase.

4.3.3. EFFECT OF MODEL CHOICE

The effect of the fracture and the chosen fracture flow model on the surrounding porous medium has been investigated by varying the Young's modulus, with variations in Young's modulus scaling approximately inverse linearly with the fracture opening height. These changes in opening height result in changes in the fluid flux inside the fracture, allowing the influence of the fracture to be varied between dominating the fluid flow for low Young's moduli to the fracture having near to no influence on the fluid flow inside the porous medium for high Young's moduli.

To compare the fluid flux within the fracture, the wetting and non-wetting fluid fluxes are calculated in the vertices of the interface elements and summed, resulting in Figure 4.13. When the Young's modulus is increased, the fluid flux inside the fracture decreases until the

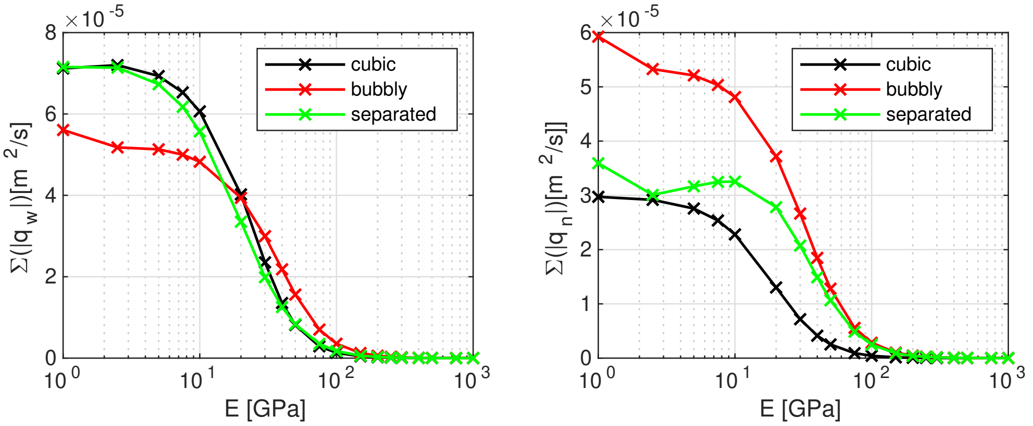

(a) Wetting phase

(b) Non-wetting phase

Figure 4.13: Sum of the fluid flux inside the fracture for varying Young's moduli at $t = 2.5$ hours

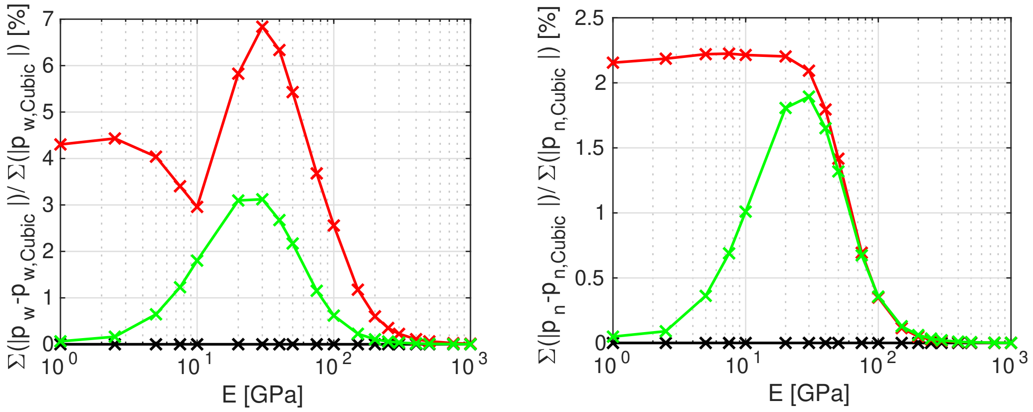

(a) Wetting phase

(b) Non-wetting phase

Figure 4.14: Relative difference in pressure along the discontinuity for varying Young's moduli at $t = 2.5$ hours.

fracture opening height is negligible and no fluid flows within the fracture. This limit is approached in a similar manner for the cubic law and separated flow when looking at the wetting fluid flux, whereas for the non-wetting phase the separated flow and cubic law approach in a similar manner. When the Young's modulus is decreased, the fluid transported inside the fracture increases, and the differences between the models become more pronounced. While for the wetting fluid flux the difference between the cubic law and separated flow model are small, large differences occur for the non-wetting fluid flux. For all low Young's moduli, the bubbly flow model results in significantly different fluid fluxes compared to the other models.

The difference in pressure between the cubic law and the other models is shown in Figure 4.14. Due to the negligible difference in fluid flux between the cubic law and separated flow model for low and high Young's moduli, the difference in pressure approaches zero for the separated flow model. The same behaviour is seen for the saturations, shown in Figure 4.15, with the maximum difference in saturation corresponding to $E = 20$ GPa, corresponding to the differences shown in Figures 4.9-4.12.

For all Young's moduli the difference between the cubic law and bubbly flow is larger than between the cubic law and separated flow. Furthermore, while the difference disap-

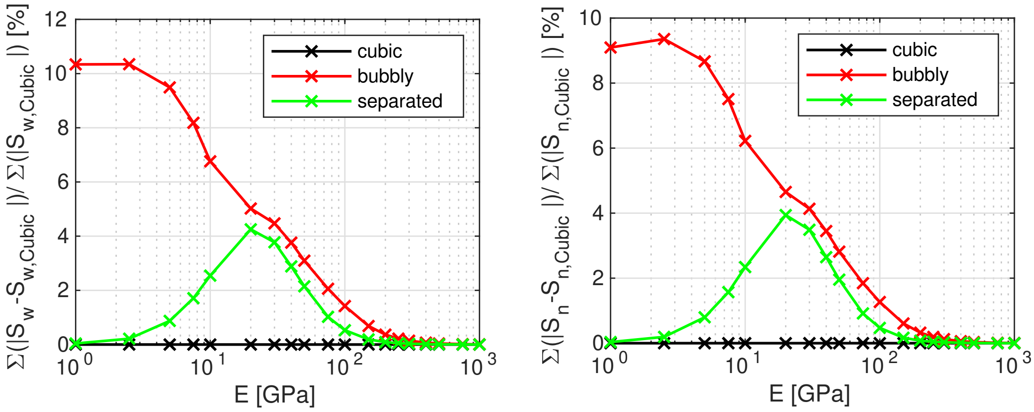

(a) Wetting phase

(b) Non-wetting phase

Figure 4.15: Relative difference in wetting phase saturation along the discontinuity at $t = 2.5$ hours.

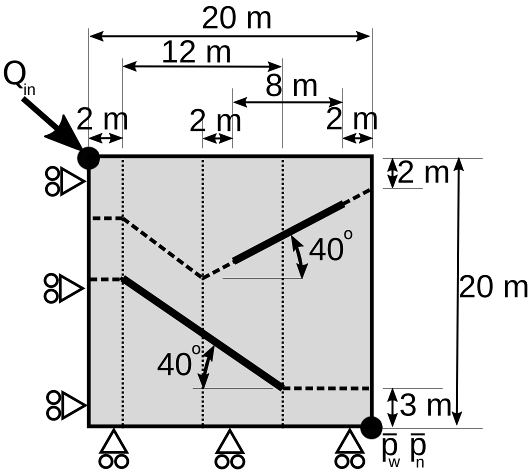

Figure 4.16: Geometry used for the complex multiphase flow cases. The dashed lines represent the interface elements, and the dotted lines are C^0 continuity lines.

peared for low Young's moduli for the separated flow model, this difference does not disappear for the bubbly flow model. For higher values of the Young's modulus, the difference between the bubbly flow and separated flow becomes more similar, most notably for the saturations and non-wetting fluid flux. This indicates that for both cases, the coupling has a similar effect for high Young's modulus cases: The wetting phase drags along the non-wetting phase, resulting in a decrease in non-wetting phase pressure around the right fracture tip (not shown here). Due to the volume averaging used for the bubbly flow, this effect persists for high fracture opening heights, and therefore the differences between the cubic law and the bubbly flow model do not reduce to zero in the low Young's modulus limit.

4.4. COMPLEX CASES

To further illustrate the effect of including the interactions within the fracture in the fracture flow model, two cases representative of more real-world applications were simulated: Oil recovery by injecting water, and underground gas/CO_2 storage.

The geometry used for both these cases is shown in Figure 4.16, and consists of a square domain containing two fractures. Reduced continuity lines were inserted to allow for sharp changes in mesh-line direction to accommodate the angles of the fracture. A constant time-

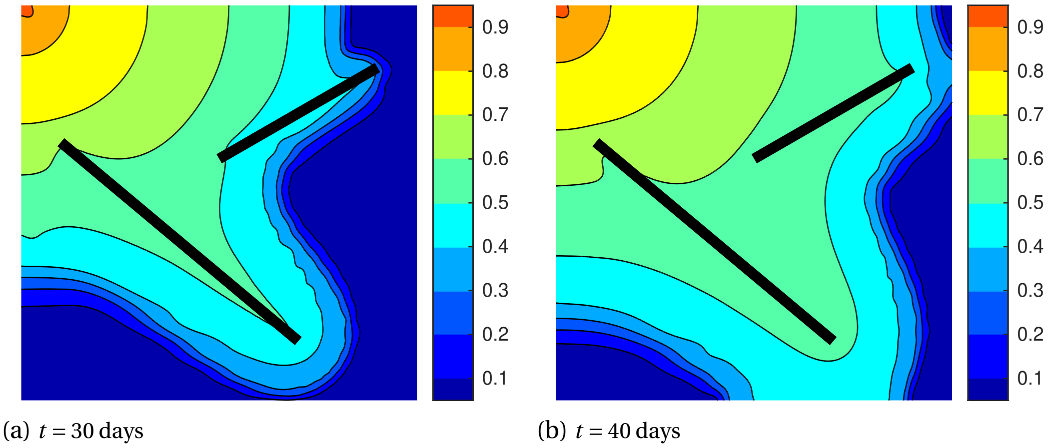

(a) $t = 30$ days (b) $t = 40$ days

Figure 4.17: Saturation for the complex oil-water case using the cubic law.

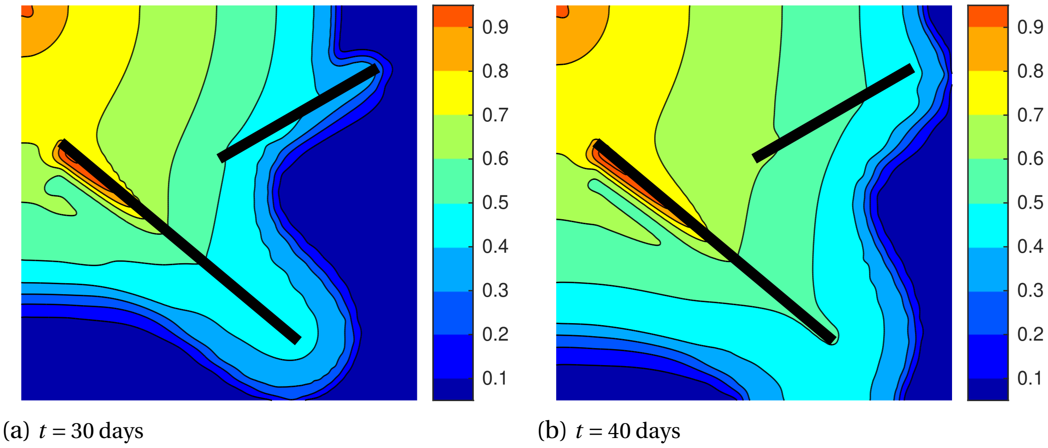

(a) $t = 30$ days (b) $t = 40$ days

Figure 4.18: Saturation for the complex oil-water case using the bubbly flow fracture model.

step $\Delta t = 1000$ s was used for both cases, and similar to the previous sections, the fractures were stationary and not allowed to propagate.

4.4.1. OIL-WATER

The first case uses the same properties as described in Section 4.3. A water inflow of $Q_{in} = 10^{-5}$ m^3/s is imposed on the top left corner, and a constant pressure of $\overline{p}_w = 0$ MPa and $\overline{p}_n = 0.3$ MPa is applied to the bottom right corner. The initial pressures are set equal to the prescribed pressure boundary condition, resulting in an initial water saturation of $S_w = 0.05$.

The saturation after $t = 30$ days and $t = 40$ days using are shown in Figure 4.17 using the cubic law. The bottom fracture enhances the fluid transport from the top left to the bottom right, but also result in a pocket of oil being isolated from the outlet in the bottom left corner. The top fracture equalises the saturation near to itself, by transporting both oil and water. This prevents the oil in the top right corner from being isolated from the outlet, as was the case for the bottom left corner.

Using the volume averaged bubbly flow model results in the water in the bottom fracture dragging the oil along, creating a local increase in saturation near the fracture tip as shown in Figure 4.18. The saturation is higher near the bottom of the fracture compared to the top due to the inlet pushing more oil towards the top of the fracture, thereby limiting the saturation. The top-right fracture shows a similar effect as the cubic law case, equalising the

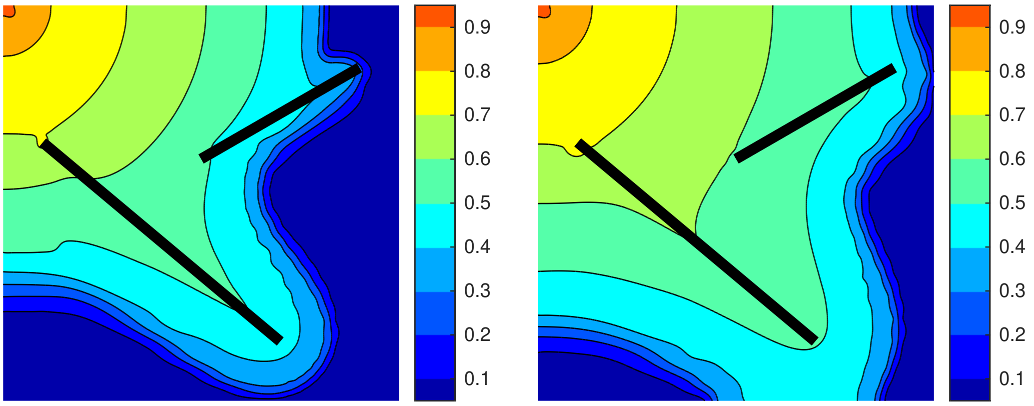

(a) $t = 30$ days

(b) $t = 40$ days

Figure 4.19: Saturation for the complex oil-water case using the separated flow fracture model.

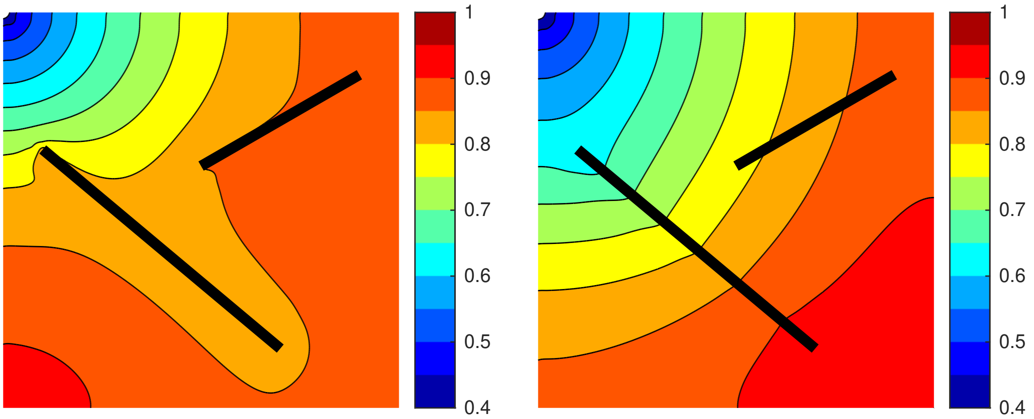

(a) Separated flow model and cubic law

(b) Volume-avaraged bubbly flow

Figure 4.20: Saturation for the air-water case after $t = 15.5$ hours.

saturation along its length. However, due to the volume averaging employed, slightly larger saturation gradients persist along the fracture, compared to the cubic law.

The separated fracture flow model, Figure 4.19, shows a balance between the results of the cubic law and bubbly flow models. The coupling between the fluid phases inside the fracture still results in an increase in saturation at the fracture tip of the bottom fracture, but this effect is less pronounced compared to the bubbly flow since the water and oil are still allowed to flow in opposite directions depending on their respective pressure gradients. The water flowing at the walls of the fracture is also less slowed down by the oil in the centre of the fracture, resulting in a higher saturation near the bottom compared to the cubic fracture flow model.

4.4.2. AIR-WATER

For the second case, the domain has an initial water saturation of $S_w = 0.9$ ($p_w = -0.9$ MPa, $p_n = 8.1$ MPa). In the top left corner air ($\mu_n = 2 \cdot 10^{-5}$ Pas, $K_n = 0.1$ MPa) is injected with an inflow of $Q_{in} = 5 \cdot 10^{-2}$ m^2/s. Similar to the previous case, constant pressures equal to the initial pressure are imposed on the bottom right corner for it to function as an outlet. The porous material is assumed to be sandstone like, using $k = 10^{-13}$ m^2 and all other properties equal to those of the previous sections. To correctly model the air-water interactions in the

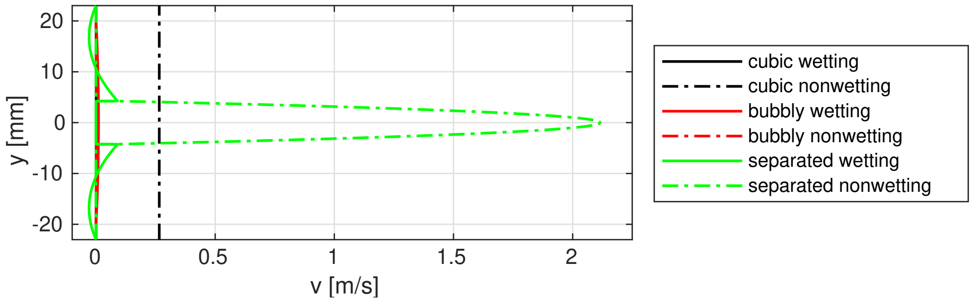

Figure 4.21: Velocity profile in the bottom fracture at $x = 10$ m, $t = 15.5$ hours.

porous material the Van Genuchten relations were used, Eq. 4.6 for the saturation and Eq. 4.14 for the relative permeabilities.

For both the cubic law and the separated flow model, the fractures equalised the saturation along the fracture, as shown in Figure 4.20a. Due to the large fluid velocity inside the fracture compared to in the surrounding porous material, no visible difference between these two cases occurred. In contrast, the volume averaged bubbly flow model, Figure 4.20b, shows a large saturation gradient along the fracture. Due to the volume averaging and the high water saturation, the effective viscosity of the mixture is much higher than the viscosity of the air itself, resulting in a low air velocity inside the fracture.

The velocity profiles inside the fracture are obtained through post-processing the pressures and saturation, and shown in Figure 4.21. The air velocity using the separated flow model is very high, and manages to drag along water with it. This causes a pressure gradient for the water phase, resulting in a water backflow near the fracture walls. The air dragging along causes a large fluid flux for the separated flow compared to the bubbly flow, even though the bubbly flow has a relatively lower effective viscosity.

4.5. CONCLUSION

In this chapter, fracture scale sub-grid models were derived for volume-averaged bubbly flow and separated flow types. By using the continuous pressure assumption, these models are able to describe the fluid flow and interactions between the phases inside the fracture, without explicitly having to simulate the fluid flow in the interior of the fracture. By post-processing the saturation and pressures, these models allow the velocity profiles within the fracture to be re-obtained, allowing for a detailed look into the fluid flows within the fracture.

A boundary value problem containing a single fracture was simulated to show the effect of using these flow models compared to the commonly used cubic law. Both the bubbly flow model and the separated flow model allow the high pressure gradient phase to drag along the low pressure gradient phase, increasing the fluid flux inside the fracture for one phase while limiting the other phase its fluid flux. This effect is strongest for the bubbly flow, while the separated flow provides results more similar to the cubic law. It should be noted, however, that the choice of models should be motivated by the actual flow type predicted to occur within the fracture, and this choice can significantly alter the results obtained depending on the fracture opening height.

Finally, two cases more representative of real-world applications were simulated. These simulations showed that the interactions within the fracture, and the fluid dragging the other phase along, could result in local increases in saturation. Furthermore, large differences between the cubic law, and the fracture flow models derived in this chapter highlight the importance of including the fluid flows and their interactions within the fracture. Results for an air-water mixture also showed that a water backflow can occur inside the fracture due to high air velocities when using the separated flow model, whereas the use of volume averaging in the bubbly flow model strongly limits the velocity of the low viscosity air phase.

5

PRESSURISED FRACTURES

The previous chapters have assumed that the fluid is easily able to flow into and out of the fracture, and thereby retain a continuous pressure between the fracture and porous material. However, this is not always the case. Small-scale plastic deformations resulting from the high stresses near fracture tips and shear motion at the fracture walls can reduce the permeability of the fracture walls, creating a resistance to the fluid flow [19, 207, 208]. This resistance allows the fracture to sustain a different pressure compared to the surrounding porous material, introducing a pressure jump at the fracture walls.

This pressure jump between the fracture and the porous material is included in the discontinuous pressure model [49, 185], introducing an interface permeability term which restricts the fluid flow entering the fracture. A time-dependent interface permeability can be used to represent small-scale boundary layers [185], whereas a constant value is more representative of permanent changes in permeability close to the fracture due to the fracturing process. Furthermore, by using a high interface permeability the pressure jump between the fracture and porous material is reduced, approximating the continuous pressure model [173]. While the discontinuous pressure model is commonly used to simulate propagating fractures [162, 185], it can also be used for closed fractures to describe fluid-blocking barriers [16, 41, 139].

This chapter will extend the previously derived relations for a non-Newtonian power-law fluid to the discontinuous pressure model, allowing for pressurised fractures with an entry resistance to be simulated. The governing equations and discretisation will be detailed in Sections 5.1-5.2, with special attention paid to the integration scheme for the interface permeability terms required to obtain a non-oscillatory solution and prevent non-physical fracture inflows. The effects of this scheme are shown in Section 5.3. Finally, the effect of including a non-Newtonian rheology on propagating fractures will be demonstrated through a typical fracture propagation case in Section 5.4. The results presented in this chapter have been previously published in [7], and the code used for the fracture propagation and traction-separation law are derived from the Lagrangian finite element code from [173].

5.1. DISCONTINUOUS PRESSURE MODEL

To simulate fractures containing a pressurised fluid, an additional pressure is introduced representing the pressure inside the fracture p_d. Similar to the continuous pressure models, this pressure is assumed to only vary in tangential direction, and has a constant value for the complete fracture height. Different from the continuous pressure model, the fluid flux normal to the fracture is now described through [38]:

$$-\boldsymbol{n}_d \cdot \boldsymbol{q}_d^+ = k_i \left(p_d - p^+\right) \tag{5.1}$$

$$-\boldsymbol{n}_d \cdot \boldsymbol{q}_d^- = k_i \left(p_d - p^-\right) \tag{5.2}$$

with p^+ and p^- the interstitial fluid pressures inside the porous material at the top and bottom of the fracture. The interface permeability k_i represents the resistance to the fluid to leave the fracture.

The velocity profile for the fluid flow inside the fracture, Eq. 2.26 for the continuous pressure model, is now based on the discontinuity pressure:

$$v(y_d) = \frac{n}{n+1}\mu_0^{-\frac{1}{n}}\left|\frac{\partial p_d}{\partial x_d}\right|^{\frac{1}{n}-1}\frac{\partial p_d}{\partial x_d}\left(|y_d|^{\frac{1}{n}+1}-\left(\frac{h}{2}\right)^{\frac{1}{n}+1}\right)+v_f \quad \text{for } -\frac{h}{2}\leq y_d \leq \frac{h}{2} \tag{5.3}$$

and the mass conservation for the interior of the fracture, integrated over the fracture height and combined with Eq. 5.1-5.2, now becomes:

$$k_i\left(2p_d-p^+-p^-\right)+\frac{\partial h}{\partial t}=\int_{-\frac{h}{2}}^{\frac{h}{2}}\frac{\partial v}{\partial x_d}\,\mathrm{d}y_d \tag{5.4}$$

Finally, substituting the velocity profile from Eq. 5.3 into this mass balance results in:

$$k_i\left(2p_d-p^+-p^-\right)+\frac{\partial h}{\partial t}-\frac{\partial}{\partial x_d}\left(\frac{-2n}{2n+1}\mu_0^{\frac{1}{n}-1}\left|\frac{\partial p_d}{\partial x_d}\right|^{\frac{1}{n}-1}\frac{\partial p_d}{\partial x_d}\left(\frac{h}{2}\right)^{\frac{1}{n}+2}\right)=0 \tag{5.5}$$

In contrast to the continuous pressure model, this equation can not be directly imposed as boundary conditions for the interstitial pressure and instead has to be resolved together with the mass balance and momentum balance for the interior of the porous material, Eq. 2.5 and 2.18. The introduction of a separate pressure inside the discontinuity also introduces two additional boundary conditions, a prescribed discontinuity pressure and a prescribed inflow at the fracture tips:

$$p_d=\overline{p}_d \quad \text{on} \quad \boldsymbol{x}\in\partial\Gamma_{p_d} \tag{5.6}$$

$$q_d=Q_{tip} \quad \text{on} \quad \boldsymbol{x}\in\partial\Gamma_Q \tag{5.7}$$

The coupling between the fluid pressure inside the fracture and the interstitial pressure is provided through the discontinuity fluid flux, Eq. 5.1-5.2, which are imposed as boundary conditions on the mass balance of the porous material. The discontinuity pressure is also included in the momentum balance, similar to Eq. 2.19 , through:

$$\boldsymbol{\tau}_{\Gamma_d}=\boldsymbol{\tau}_d-p_d\boldsymbol{n}_d \tag{5.8}$$

Since the fracture is allowed to propagate for the cases simulated, a cohesive zone model is included for the fractured elements:

$$\boldsymbol{\tau}_d=\begin{cases} k_d[\![\boldsymbol{u}]\!] & \text{for non-fractured elements}\\ \boldsymbol{n}_d f_t e^{\left(-\frac{f_t}{G_{Ic}}[\![u]\!]_n\right)} & \text{for fractured elements}\end{cases} \tag{5.9}$$

where $[\![u]\!]_n$ is either the jump in normal displacement or the maximum jump in normal displacement obtained during the simulation, whichever is the highest. The normal displacement is calculated after each time-step is converged, and the maximum displacement jump is updated based on these converged values.

5.2. DISCRETISATION

Replacing the tractions at the interface with Eq. 5.8 in Equation 2.36, the weak form of the momentum balance becomes:

$$\int_\Omega \nabla\boldsymbol{\eta}:(\boldsymbol{\sigma}_s-\alpha p\boldsymbol{I})\,\mathrm{d}\Omega-\int_{\Gamma_d}\boldsymbol{\eta}\cdot(\boldsymbol{\tau}_d-p_d\boldsymbol{n}_d)\,\mathrm{d}\Gamma_d=\int_{\Gamma_t}\boldsymbol{\eta}\cdot\overline{\boldsymbol{\tau}}\,\mathrm{d}\Gamma_t \tag{5.10}$$

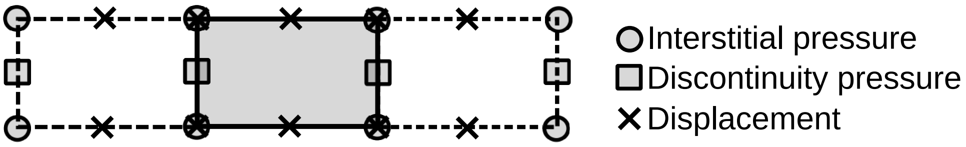

Figure 5.1: Interface element and the control points relevant to this element. The vertical height is added for clarity, whereas for the actual interface elements the top and bottom are located at the some location.

and by substituting Eq. 5.1-5.2, the mass balance for the porous material becomes:

$$\int_\Omega \alpha\zeta\boldsymbol{\nabla}\cdot\dot{\boldsymbol{u}}\,\mathrm{d}\Omega+\int_\Omega k_f^*\left|\boldsymbol{\nabla}p\right|^{1/n-1}\boldsymbol{\nabla}\zeta\cdot\boldsymbol{\nabla}p\,\mathrm{d}\Omega+\int_\Omega\frac{1}{M}\zeta\dot{p}\,\mathrm{d}\Omega+\int_{\Gamma_d}\zeta k_i\left(p-p_d\right)\,\mathrm{d}\Gamma_d=-\int_{\Gamma_q}\zeta\overline{q}\,\mathrm{d}\Gamma_q \tag{5.11}$$

Finally, the weak form for the mass balance inside the fracture is obtained by multiplying Eq. 5.5 with the test function ξ, and using the divergence theorem on the fluid flow term:

$$\int_{\Gamma_d} k_i\xi\left(p^+ + p^- - 2p_d\right)-\xi\frac{\partial h}{\partial t}\,\mathrm{d}\Gamma_d+\int_{\Gamma_d}-\frac{2n}{2n+1}\mu_0^{-\frac{1}{n}}\frac{\partial\xi}{\partial\overline{s}}\left|\frac{\partial p_d}{\partial\overline{s}}\right|^{\frac{1}{n}-1}\left(\frac{\partial p_d}{\partial\overline{s}}\right)\left(\frac{h}{2}\right)^{\frac{1}{n}+2}\mathrm{d}\Gamma_d = \int_{\partial\Gamma_d}\xi Q_d\,\mathrm{d}\partial\Gamma_d \tag{5.12}$$

Similar to the discretisation used in the previous chapters, cubic NURBS are used to discretise the interstitial fluid pressure, whereas quartic NURBS are used for the solid displacement. Since the interstitial fluid pressure at the interface is now discontinuous, both the displacement and the interstitial pressure have a C^{-1} continuity at the discontinuity. The pressure inside the discontinuity is also discretised using cubic NURBS. It should be noted that in contrast to the interstitial pressure, the discontinuity pressure is discretised on a line at the discontinuity instead of on the complete mesh. The resulting locations of the control points are shown in Figure 5.1, in which an interface element is shown with the control points associated with that element.

Using the Bézier extracted NURBS, the displacement, interstitial pressure and discontinuity pressure are discretised as:

$$\boldsymbol{u}=\sum_{el=1}^{n_{el}}\boldsymbol{N}_s^{el}\boldsymbol{u}^{el} \tag{5.13}$$

$$p=\sum_{el=1}^{n_{el}}N_f^{el}\boldsymbol{p}^{el} \tag{5.14}$$

$$p_d=\sum_{el_i=1}^{n_{el_i}}N_{pd}^{el}\boldsymbol{p}_d^{el_i} \tag{5.15}$$

with the displacements and pressures determined by a sum over all elements el, whereas the discontinuity pressure is determined by a sum over all interface elements el_i.

5.2.1. DISCRETISED EQUATIONS

The momentum balance is discretised by:

$$\boldsymbol{f}_{ext}-\boldsymbol{f}_{int}-\boldsymbol{f}_d=\boldsymbol{0} \tag{2.46}$$

with the internal forces given by Eq. 2.48 and the external forces by Eq. 2.47. The forces due to the discontinuity are given by:

$$\boldsymbol{f}_d=\int_{\Gamma_d}\boldsymbol{N}_d^T\boldsymbol{R}^T\boldsymbol{\tau}_d^{t+\Delta t}\mathrm{d}\Gamma_d-\int_{\Gamma_d}\boldsymbol{N}_d^T\boldsymbol{n}_{\Gamma_d}\boldsymbol{N}_{pd}\boldsymbol{p}_d^{t+\Delta t}\mathrm{d}\Gamma_d \tag{5.16}$$

The discretised mass conservation for the porous material is:

$$\boldsymbol{q}_{ext} - \boldsymbol{q}_{int} - \boldsymbol{q}_d = \mathbf{0} \tag{5.17}$$

with $\boldsymbol{q}_{ext}$ and $\boldsymbol{q}_{int}$ given by Eq. 2.52 and 2.53. The fluid fluxes due to the discontinuity are given by:

$$\boldsymbol{q}_d = \int_{\Gamma_d^{\pm}} k_i^{el} \Delta t\, \boldsymbol{N}_f^T \left(\boldsymbol{N}_{pd} \boldsymbol{p}_d^{t+\Delta t} - \boldsymbol{N}_f \boldsymbol{p}^{t+\Delta t} \right) \mathrm{d}\Gamma_d \tag{5.18}$$

with $\int_{\Gamma_d^{\pm}}$ indicating that the integration is performed twice: Once for the top of the fracture using p^+ (the interstitial pressure at the top of the discontinuity) and p_d, and once for the bottom with p^- and p_d. The interface permeability of the element k_i^{el} is taken as the interface permeability k_i for fractured elements, while a dummy permeability $k_{i,d}$ is used for non-fractured elements to enforce a continuous pressure over the non-fractured interface elements.

The weak form for mass conservation inside the fracture, Eq 5.12, is discretised as:

$$\boldsymbol{q}_{d,ext} - \boldsymbol{q}_{d,int} - \boldsymbol{q}_{d,d} = 0 \tag{5.19}$$

with the external flux defined as:

$$\boldsymbol{q}_{d,ext} = \Delta t \int_{\partial \Gamma_Q} \boldsymbol{N}_{pd}^T Q_{tip}\, \mathrm{d}\partial\Gamma_d \tag{5.20}$$

The internal fluid flux caused by the fluid flow within the fracture is:

$$\boldsymbol{q}_{d,int} = -\Delta t \int_{\Gamma_d} \frac{2n}{2n+1} \mu_0^{-\frac{1}{n}} \nabla \boldsymbol{N}_{pd}^T \left| \nabla \boldsymbol{N}_{pd} \boldsymbol{p}_d^{t+\Delta t} \right|^{\frac{1}{n}-1} \left(\frac{\boldsymbol{n}_{\Gamma_d}^T \boldsymbol{N}_d \boldsymbol{u}^{t+\Delta t}}{2} \right)^{\frac{1}{n}+2} \nabla \boldsymbol{N}_{pd} \boldsymbol{p}_d^{t+\Delta t}\, \mathrm{d}\Gamma_d \tag{5.21}$$

and the fluxes due to the coupling between the porous material and fracture are given by:

$$\begin{aligned} \boldsymbol{q}_{d,d} = \Delta t \int_{\Gamma_d} k_i^{el} \boldsymbol{N}_{pd}^T \left(\boldsymbol{N}_f \boldsymbol{p}^{+\,t+\Delta t} + \boldsymbol{N}_f \boldsymbol{p}^{-\,t+\Delta t} - 2 \boldsymbol{N}_{pd} \boldsymbol{p}_d^{t+\Delta t} \right) \mathrm{d}\Gamma_d \\ - \int_{\Gamma_d} \boldsymbol{N}_{pd}^T \boldsymbol{n}_{\Gamma_d}^T \boldsymbol{N}_d \left(\boldsymbol{u}^{t+\Delta t} - \boldsymbol{u}^t \right) \mathrm{d}\Gamma_d \end{aligned} \tag{5.22}$$

These discretised equations have been implemented using a monolithic Newton-Raphson scheme, similar to the previous chapters. A consistent tangential stiffness matrix is used, and quadratic convergence was obtained. The tangential stiffness sub-matrices are given in Appendix C.2, and a short verification for the correct implementation is given in Appendix A.3.

5.2.2. FRACTURE INTEGRATION SCHEME

Oscillations were observed in the fracture inflow velocity near the fracture tips. These type of oscillations are commonly seen for non-fractured interface elements when a dummy stiffness is used [200]. For standard Lagrangian elements, these oscillations can be supressed by using a standard Newton-Cotes integration scheme [200], while due to the higher continuity of NURBS a special lumped integration scheme is needed [99, 234]. For the tractions at the non-fractured interface elements, the integration using this lumped scheme is performed as:

$$\boldsymbol{f}_d^{non-frac} = \int_{\Gamma_d} \boldsymbol{N}_{ds}^T \boldsymbol{R}^T \boldsymbol{D}_d \boldsymbol{R} \boldsymbol{N}_{ds} \boldsymbol{u}^{el}\, \mathrm{d}\Gamma_d = \sum_{cp=1}^{n_{cp}} \boldsymbol{M}_l^T \boldsymbol{R}^T \boldsymbol{D}_d \boldsymbol{R} \boldsymbol{M}_l \boldsymbol{u}^{cp} A_{cp} \tag{5.23}$$

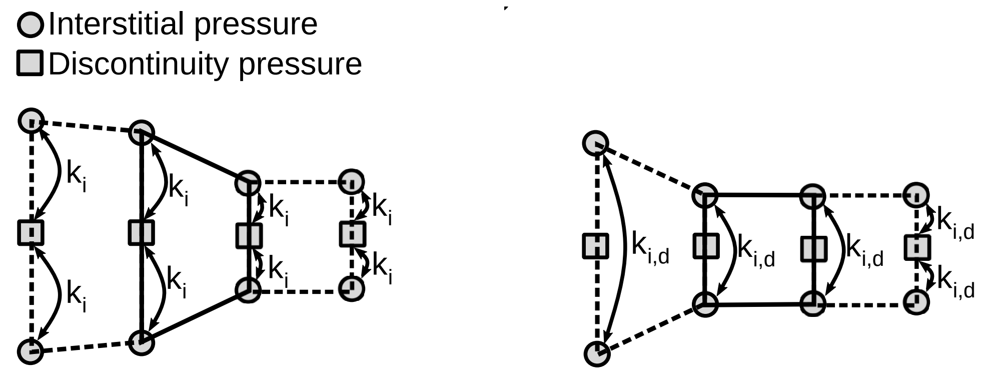

(a) Fractured element

(b) Non-fractured element

Figure 5.2: Fracture tip integration scheme for a fractured element at the fracture tip and a neighbouring non-fractured element.

with n_{cp} the number of control-point sets for the interface element, and $\boldsymbol{u}^{cp}$ the displacements of the control-point set. The lumped integration matrix $\boldsymbol{M}_l$ is used to construct the jump in displacement of the control point set:

$$[\![\boldsymbol{u}]\!]_{cp} = \begin{bmatrix} -1 & 1 & 0 & 0 \\ 0 & 0 & -1 & 1 \end{bmatrix} \begin{bmatrix} u_x^- \\ u_x^+ \\ u_y^- \\ u_y^+ \end{bmatrix} = \boldsymbol{M}_l \boldsymbol{u}_{cp} \tag{5.24}$$

The weighting factor A_{cp} corresponding to the control-point set is obtained through integrating the interpolation function over the domain using a Gauss integration scheme:

$$A_{cp} = \int_{\Gamma_d} \boldsymbol{N}_s^{cp} \, \mathrm{d}\Gamma_d \tag{5.25}$$

A similar lumped integration scheme is employed to suppress oscillations in the fluid flux normal to the fracture:

$$\boldsymbol{q}_d = \int_{\Gamma_d^\pm} k_i^{el} \Delta t \, \boldsymbol{N}_f^T \left(\boldsymbol{N}_{pd} \boldsymbol{p}_d^{t+\Delta t} - \boldsymbol{N}_f \boldsymbol{p}^{t+\Delta t} \right) \mathrm{d}\Gamma_d = \sum_{cp=1}^{n_{cp}} A_{cp,d} k_i^{el} \boldsymbol{N}_l^T \left(\boldsymbol{N}_l \boldsymbol{p}_{\boldsymbol{d}}^{cp} - \boldsymbol{N}_l \boldsymbol{p}^{cp} \right) \tag{5.26}$$

with $\boldsymbol{N}_l$ used to select the degrees of freedom corresponding to the control point set, and the weighting factor for the fluid determined through:

$$A_{cp,d} = \int_{\Gamma_d} \boldsymbol{N}_f^{cp} \, \mathrm{d}\Gamma_d = \int_{\Gamma_d} \boldsymbol{N}_{pd}^{cp} \, \mathrm{d}\Gamma_d \tag{5.27}$$

Since a large interface permeability can be used for fractured elements to approximate the continuous pressure model, this scheme is used for both the fractured and non-fractured elements.

A side effect of using NURBS to discretise the pressure at the discontinuity is that the interpolation functions are not limited to only fractured or non-fractured elements. This results in control points both being linked to the interstitial pressure through the dummy permeability, and being used for the fluid flow within the fracture. The fluid is allowed to enter the fracture at the fracture tips without the resistance of the interface permeability, and then transported within the fracture, resulting in extra and non-physical amounts of fluid entering and leaving the fracture. To prevent this, a special integration scheme is used

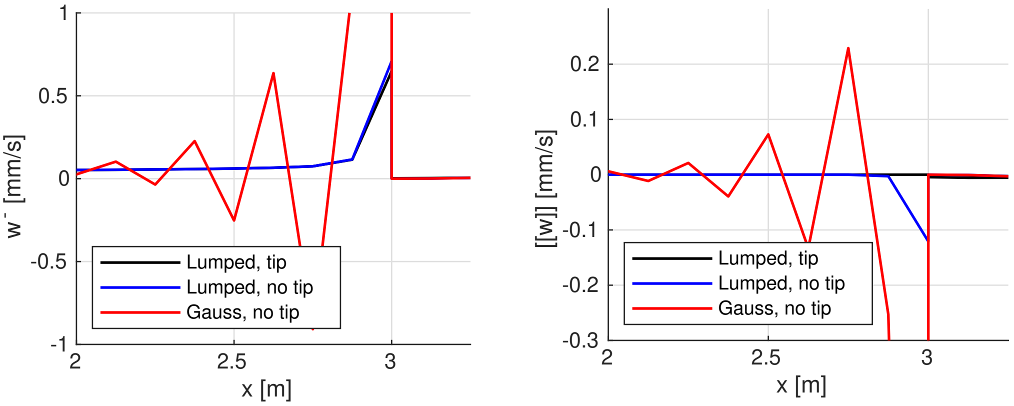

(a) Velocity through the bottom of the interface

(b) Velocity jump over the interface

Figure 5.3: Fluid velocity and jump in fluid velocity at the discontinuity, zoomed on the left fracture tip.

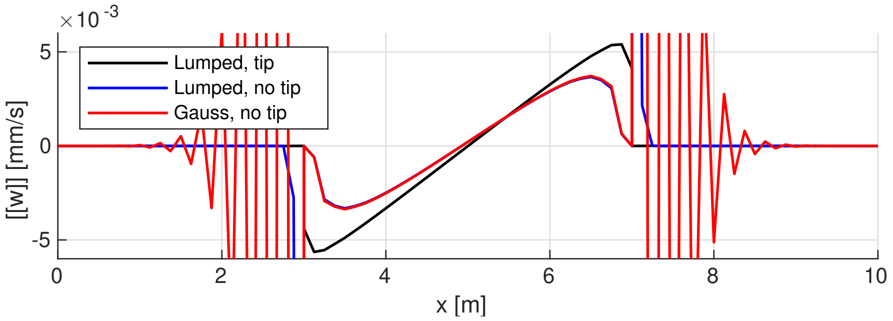

Figure 5.4: Fluid velocity jump at the discontinuity

around the fracture tips to separate the control points in the interior of the discontinuity from the dummy permeability. For the non-fractured elements, if a control point set includes a degree of freedom that is also integrated through a fractured element, the discontinuity pressure is skipped and the fluid flux at the interface is integrated as:

$$\boldsymbol{q}_d = \mp \int_{\Gamma_d^\pm} \frac{1}{2} k_{i,d} \Delta t \boldsymbol{N}_f^T \left(\boldsymbol{N}_f \boldsymbol{p}^+ - \boldsymbol{N}_f \boldsymbol{p}^-\right) \mathrm{d}\Gamma_d \tag{5.28}$$

This fracture tip integration scheme is schematically shown in Figure 5.2. Control point sets for the fractured elements, and control point sets for non-fractured elements away from the fracture tip are integrated through the lumped integration scheme, Eq. 5.26. Only the control point sets for non-fractured elements that are located near the fracture tip are calculated by Eq. 5.28.

5.3. EFFECT OF INTEGRATION SCHEMES

To demonstrate the effect of the lumped integration and the fracture tip integration scheme a typical boundary value problem is simulated. This problem uses the geometry and parameters from Figure 2.7 and Section 2.3. A newtonian fluid ($n = 1.0$, $\mu = 1$ mPa s) is used, and the fracture has an interface permeability of $k_i = 10^{-10}$ m/Pa s. The non-fractured elements used a dummy permeability $k_{i,d} = 0.5 \cdot 10^{-3}$ m/Pa s.

The fluid velocity normal to the discontinuity is shown in Figure 5.3a. With the Gauss integration scheme, large oscillations occur, and these oscillations do not cancel out with the velocity at the top at the discontinuity (Figure 5.3b). These oscillations not cancelling out

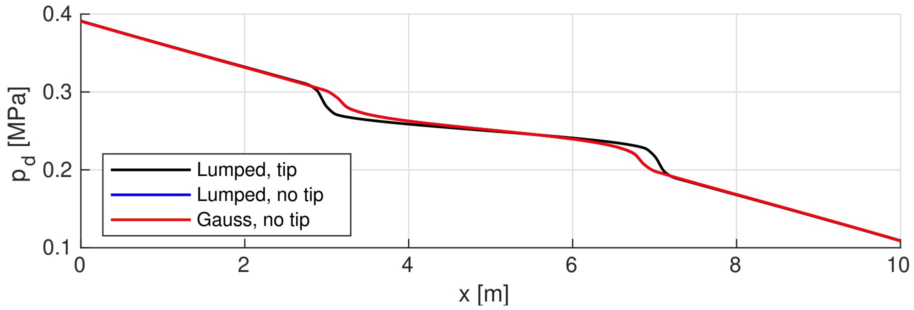

Figure 5.5: Discontinuity pressure along the discontinuity line at steady state for the single fracture case.

indicates that fluid is disappearing around the discontinuity, and therefore the simulation is not mass conserving. Using the lumped integration scheme these oscillations disappear, both in the velocity at the individual top and bottom of the discontinuity, as well as in the velocity jump.

Looking at the velocity jump around the fracture tip, Figure 5.3b, a jump in fluid velocity is seen when the lumped integration without fracture tip integration scheme is used. This peak in fracture inflow is significantly higher than the fracture inflow in the fractured elements, and indicates that fluid flows into the fracture using the much higher dummy permeability instead of the interface permeability. When the lumped integration and the fracture tip scheme are both used, this high inflow around the fracture tips disappears.

The fracture outflow velocity for the complete discontinuity is shown in Figure 5.4. While the large oscillations occur at the non-fractured elements with a Gauss integration scheme, no such oscillations occur in the fractured part of the discontinuity due to the lower interface permeability. Using lumped integration, the large peak in fracture outflow is visible near the fracture tips, having a peak around $[\![w]\!] \approx \pm 100 \cdot 10^{-3}$mm/s. The lumped and fracture tip schemes their results have a higher fracture in and outflow in the fractured part of the discontinuity. Looking at the pressure gradient in Figure 5.5, however, it can be seen that the cases without tip integration scheme obtain a higher pressure gradient inside the fracture. This indicates that even though the use of the fracture tip scheme results in a higher inflow for the fractured elements, higher fluid velocities inside the fracture are obtained for the cases without tip integration, and therefore more fluid is transported for these cases despite the lower inflow in the fractured part of the domain. From this, it can be concluded that the non-physical fracture inflow at the tips due to the dummy permeability can significantly alter the obtained results, thereby confirming that the fracture tip integration scheme is needed to obtain correct results when combining NURBS with the discontinuity pressure fracture model.

5.4. HYDRAULIC FRACTURING WITH NON-NEWTONIAN FLUIDS

A typical fracture propagation problem has been simulated to show the influence of including the non-Newtonian rheology. The case exists of a 0.25 × 0.25 m square domain with an initial fracture of 5 mm at the left edge. A fluid inflow $Q_{in} = 10^{-5}$ m^2/s is imposed on the left fracture tip (located at the domain boundary), and constant interstitial fluid pressure boundary conditions are imposed on the top, right and bottom boundaries. The solid displacement is also constrained in horizontal and vertical direction on these boundaries, while the left edge is constrained only in horizontal direction. An overview of the geometry and boundary conditions is given in Figure 5.6.

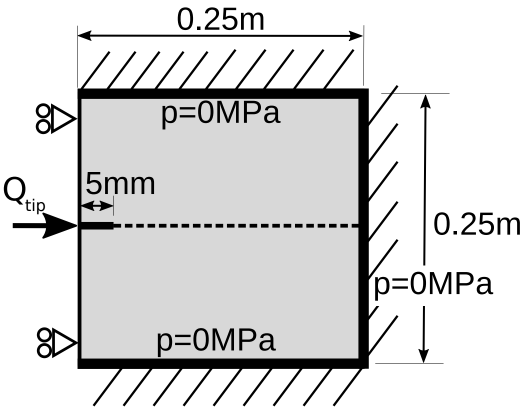

Figure 5.6: Overview of the geometry and boundary conditions for the pressurised fracture case.

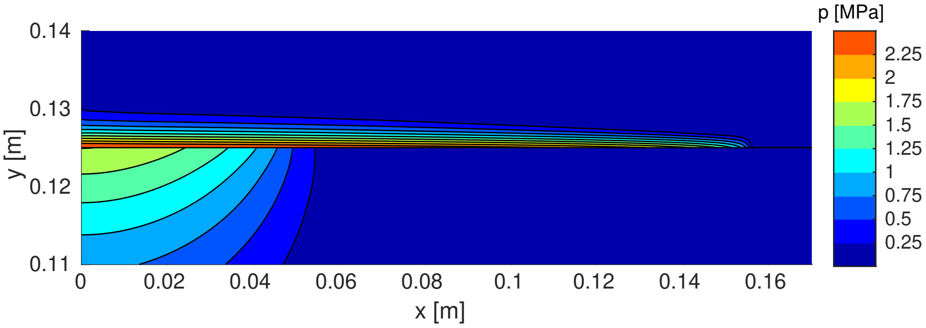

(a) Shear-thinning ($n = 0.8$)

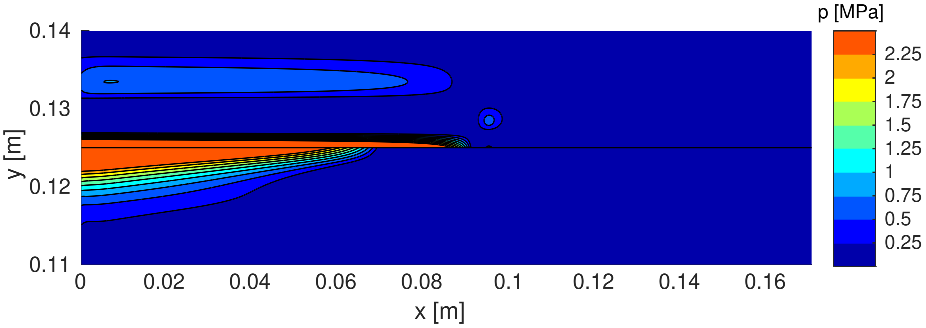

(b) Shear-thickening ($n = 1.2$)

Figure 5.7: Interstitial fluid pressure around the discontinuity at $t = 0.25$ s using $k = 10^{-16}$ m^2 (lower parts of each figure) and $k = 10^{-18}$ m^2 (upper parts of each figure)

The simulations were performed using the following material properties: Young's modulus $E = 25.85$ GPa, bulk modulus $K_s = 13.46$ GPa, Poisson ratio $\nu = 0.18$, fluid bulk modulus $K_f = 0.2$ GPa, Biot coefficient $\alpha = 1$, tensile strength $f_t = 1.7$ MPa, fracture energy $\mathcal{G}_c = 0.2$ kN/m, and porosity $n_f = 0.2$. Non-Newtonian fluids using fluid indices from $n = 0.8$ up to $n = 1.2$ have been simulated, and a base viscosity of $\mu_0 = 0.5$ mPa s^n has been used for all fluids. The fracture used an interface permeability $k_i = 10^{-10}$ m/Pa s, and the non-fractured interface elements used dummy permeability $k_{i,d} = 10^{-3}$ m/Pa s and dummy stiffness $k_s = k_n = 5 \cdot 10^3$ GPa.

To vary the amount of fluid leaking from the fracture to the surrounding porous material the permeability has been varied, using $k = 10^{-16}$ m^2, $k = 10^{-17}$ m^2, and $k = 10^{-18}$ m^2. It was chosen to vary the leak-off by altering the permeability of the porous material instead of

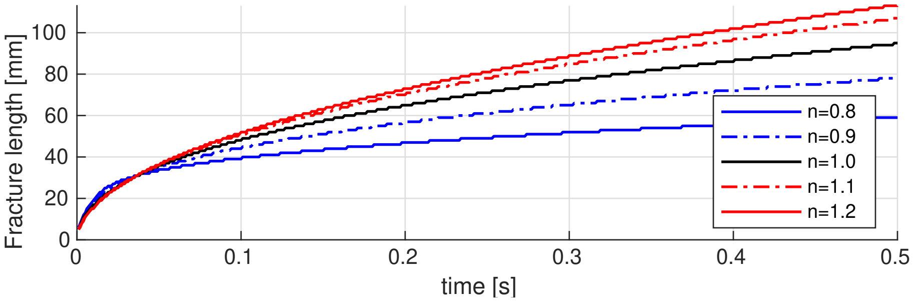

(a) $k = 10^{-16}$ m^2

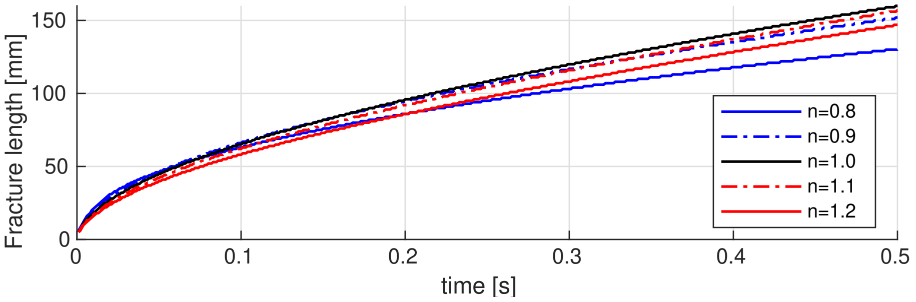

(b) $k = 10^{-17}$ m^2

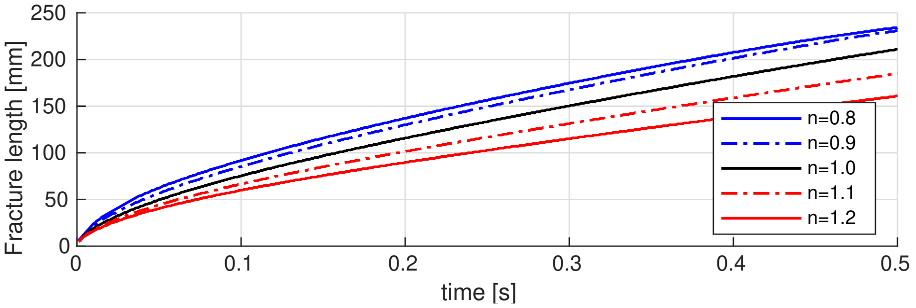

(c) $k = 10^{-18}$ m^2

Figure 5.8: Fracture length for the pressurised fracture cases.

the interface permeability since a relation between the effective permeability and the non-Newtonian fluid index was available for this bulk permeability, whereas no such relation exists for the interface permeability.

The domain is discretised using 250 × 20 Bézier extracted elements. The horizontal element size is constant over the complete domain, using $dx = 1$ mm, while the vertical element size is varied between $dy = 3$ mm close to the discontinuity up to $dy = 55$ mm near the top and bottom of the domain. A constant time step $\Delta t = 1$ ms has been used, for a total duration of the simulations of 0.5 s.

The interstitial fluid pressure for a shear-thinning and shear-thickening fluid is shown in Figure 5.7. The differences in the pressure contours between the low and high permeability cases are bigger for the shear-thinning fluid, indicating that changes in permeability alter the leak-off from the fracture more for shear-thinning fluids. Furthermore, the pressure near the fracture is higher for the shear-thickening fluid, resulting in a higher pressure within the fracture compared to the shear-thinning fluid cases.

The fracture length for the high permeability case, $k = 10^{-16}$ m^2, is shown in Figure 5.8a. The larger leak-off for shear-thinning fluids result in a significantly slower fracture propa-

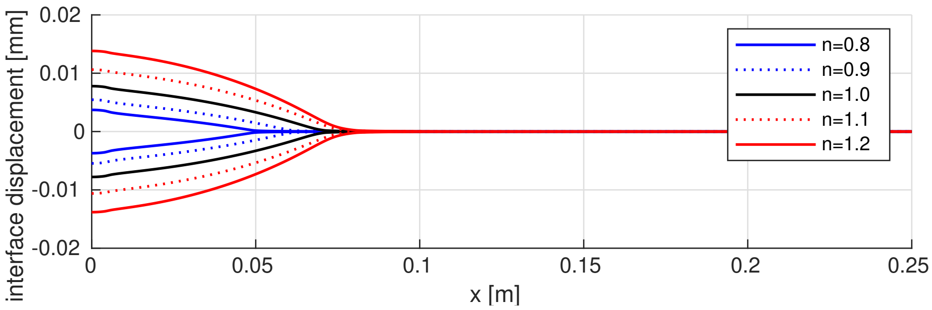

(a) Interface displacement, $\frac{1}{2}h$

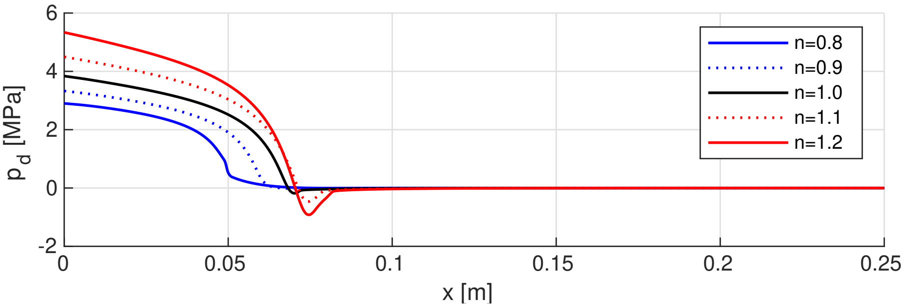

(b) Pressure inside the discontinuity, p_d

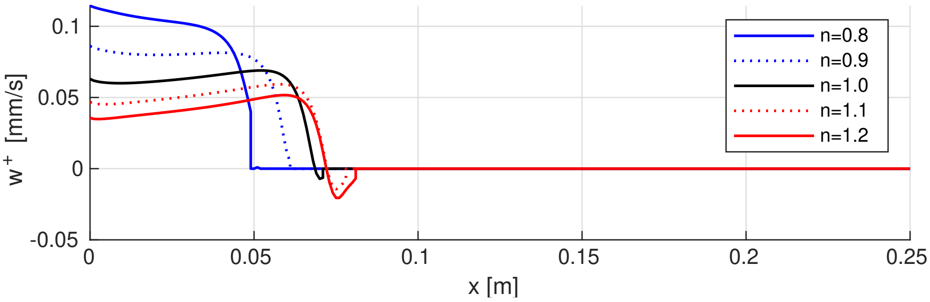

(c) Fracture outflow velocity at the top of the discontinuity, w^+

Figure 5.9: Results for the $k = 10^{-16}$ m^2 case, at $t = 0.25$ s.

gation compared to Newtonian and shear-thickening fluids. This large leak-off is also confirmed by Figure 5.9c, showing a higher fracture outflow velocity for shear-thinning fluids. As a result of the lower leak-off from the fracture, the pressure inside the discontinuity (Figure 5.9b) is higher for shear-thickening fluids. This results in both a higher fracture opening, Figure 5.9a, and a faster fracture propagation. Due to the still relatively small fracture opening height, the shear-thinning fluid flows faster through the fracture compared to the shear-thickening fluid. As a result, the discontinuity pressure is positive for the complete fracture length for the shear-thinning fluids, whereas this pressure becomes negative near the fracture tip.

For the cases using a permeability of $k = 10^{-18}$ m^2, the discontinuity pressure around the fracture tip is negative for the shear-thickening fluids, and much lower compared to the high permeability cases, as shown in Figure 5.11b. In contrast, the shear-thinning fluids still retain a positive discontinuity pressure throughout the fracture. Similar to the higher permeability case, the shear-thickening fluid has a lower leak-off from the fracture to the surrounding porous material compared to the shear-thinning fluid, Figure 5.11c. Due to the negative discontinuity pressure, the fluid flows from the surrounding porous material into

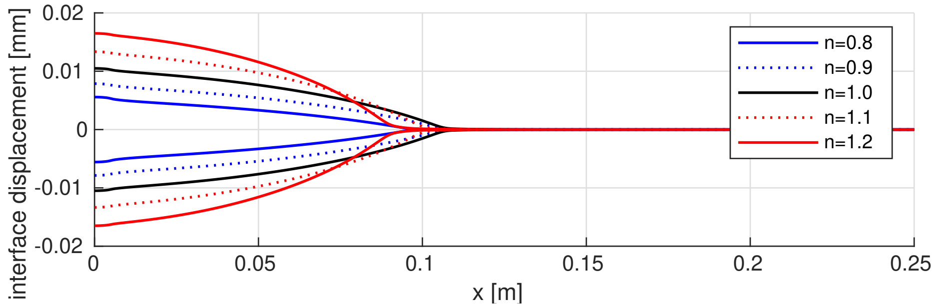

(a) Interface displacement, $\frac{1}{2}h$

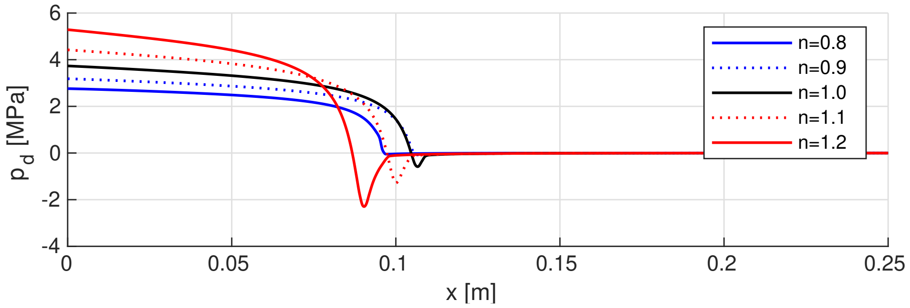

(b) Pressure inside the discontinuity, p_d

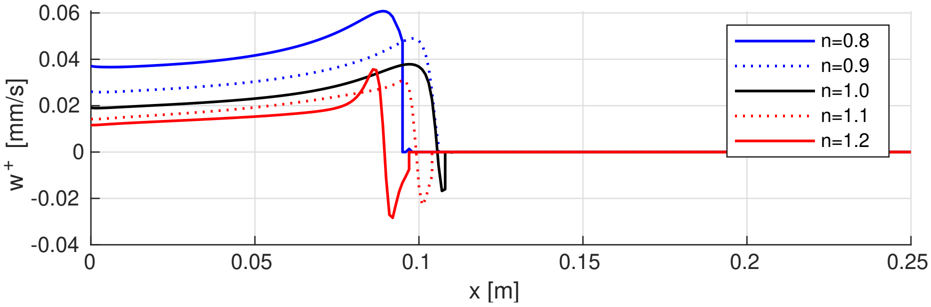

(c) Fracture outflow velocity at the top of the discontinuity, w^+

Figure 5.10: Results for the $k = 10^{-17}$ m^2 case, at $t = 0.25$ s.

the fracture near to the fracture tip. Looking at the fracture propagation length, Figure 5.8c, the effect of the negative pressure around the fracture, and negative discontinuity pressure at the fracture tip for shear-thickening fluids is clear. While the fracture propagated faster for the shear-thickening fluids for the high permeability case, it propagates slower compared to the shear-thinning fluids for the lower permeability due to this negative pressure.

For the $k = 10^{-17}$ m^2 cases, the simulation using a Newtonian fluid appear to have the fastest fracture propagation, as shown in Figure 5.8b. The shear-thickening cases suffer from a more negative discontinuity pressure near to the fracture tip, shown in Figure 5.10b, resulting in a slower fracture propagation compared to the Newtonian case. The shear-thinning fluids obtain a higher fracture outflow compared to the Newtonian fluid, and therefore also obtain a slower fracture propagation. This indicates that both the higher leak-off associated with the shear-thinning fluids, and the slower fluid flow and resulting negative pressure resulting from shear-thickening fluids have an important influence on the fracture propagation speed.

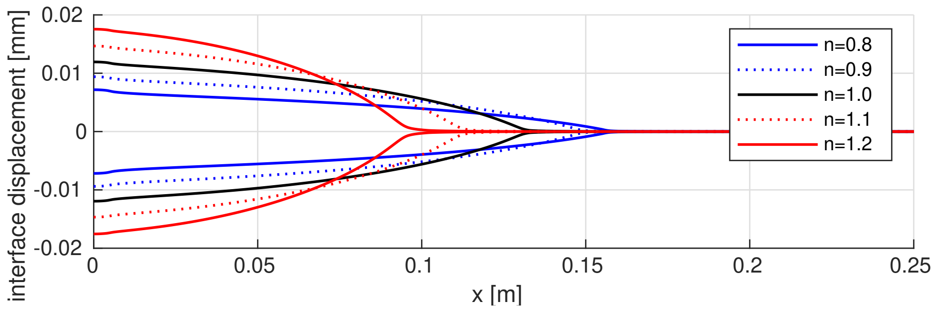

(a) Interface displacement, $\frac{1}{2}h$

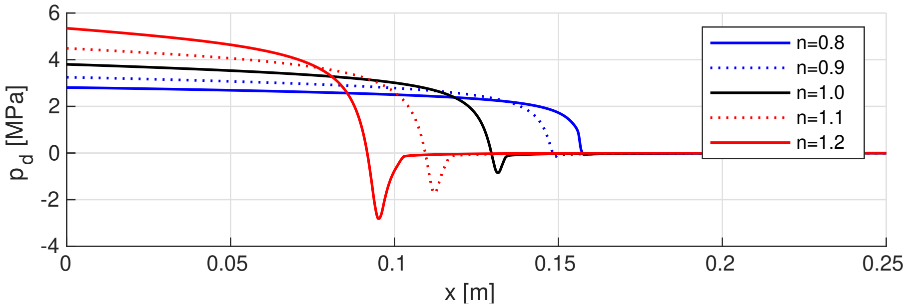

(b) Pressure inside the discontinuity, p_d

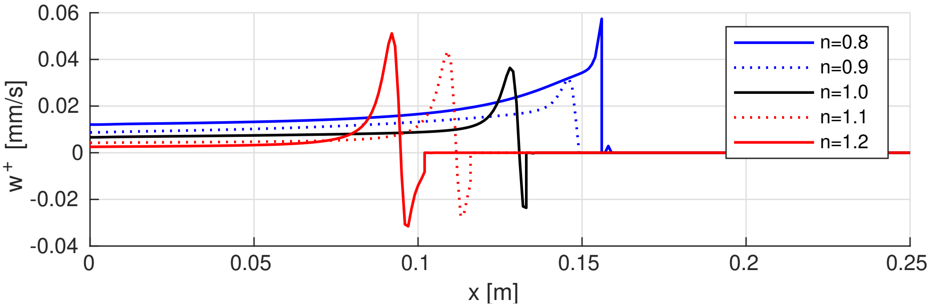

(c) Fracture outflow velocity at the top of the discontinuity, w^+

Figure 5.11: Results for the $k = 10^{-18}$ m^2 case, at $t = 0.25$ s.

5.5. CONCLUSION

In this chapter, the non-Newtonian fluid flow formulation was extended to pressurised fractures. To prevent oscillations in the fracture inflow velocity, it was shown that a lumped integration scheme was needed for these inflow velocities. Furthermore, to prevent non-physical amount of fluid entering the fracture, a special fracture tip integration scheme was detailed. By simulating a typical boundary value problem, the effects of these integration schemes on the resulting discontinuity pressure and fracture inflow was shown.

To show the effect of including the non-Newtonian fluid rheology, a pressurised and propagating fracture was simulated. Shear-thinning fluids were shown to have a higher leak-off compared to Newtonian and shear-thickening fluids, while shear-thickening fluids flowed through the fracture slower which resulted in a negative pressure at the fracture tip. Both of these effects slowed the fracture propagation velocity, with the magnitude of the slow-down depending on the properties of the problem. This indicates that including the non-Newtonian fluid behaviour can lead to significantly different results compared to approximating the fluid as a Newtonian fluid.

6

UNEQUAL ORDER T-SPLINE MESHES

While the increased continuity of NURBS enables continuous fluid velocity profiles to be obtained for the fracture, and is required to obtain accurate fracture inflow profiles, the use of NURBS also has disadvantages. In the previous chapter it was shown that a special integration scheme is needed at the fracture tip to prevent non-physical fluid flow into the fracture. Furthermore, since NURBS only allow a C^{-1} discontinuity to be inserted along a line passing through the complete domain, creating fractured and non-fractured interface elements, dummy stiffness and permeability values are needed. One final disadvantage of NURBS is their inability to refine the mesh at some regions, while still maintaining a coarse discretisation in other regions.

All these disadvantages can be removed by using T-splines [21, 204]. Similar to NURBS, T-splines allow higher order inter-element continuity, and enable the continuity to be locally reduced when required. However, unlike NURBS, T-splines are not defined through a domain-wide knot vector, instead using a T-mesh to define local knot vectors for each control point individually. This allows a fine mesh to be used locally, while using coarser elements in other parts of the domain, greatly reducing the number of control points required to discretise the complete domain [21, 140, 203]. Similar refined meshes can also be achieved by using hierarchically refined NURBS [34, 57, 92, 116]. However, T-splines meshes are simpler to generate, and allow more flexibility with inserting locally reduced continuity lines compared to these hierarchically refined NURBS.

Using T-splines also allows for interface elements to only be inserted for fractured elements [56, 227]. By locally reducing the inter-element continuity to C^{-1} a fracture can be represented, while still maintaining a higher order inter-element continuity in front of the fracture tip. This removes the need for lumped integration schemes ahead of the fracture to prevent oscillations resulting from the dummy stiffness.

T-splines have been shown able to simulate advection-diffusion and reaction-diffusion problems [21]. By refining the T-spline meshes near strong gradients, accurate solutions were obtained with fairly coarse meshes. Other cases that have demonstrated this ability of T-splines to locally refine the mesh include contact problems [69], strongly refining the mesh near the contact point, and fluid-structure interaction problem of a wind turbine [22], refining the mesh near the tips of the rotor blades to obtain an increased accuracy. The geometry of a large, geological domain has also been succesfully discretised (although not simulated) with T-splines [244], showing the capabilities of T-splines to discretise domains relevant to poroelasticity.

Propagating fractures have been successfully simulated using T-splines [55, 56]. By using a re-meshing technique to reduce the inter-element continuity from C^1 to C^{-1}, new interface elements are inserted to propagate the fracture. This method can be further refined by altering the locations of the control points to allow the fracture to propagate in an arbitrary direction [56]. To obtain sharp fracture tips, C^0 continuity lines are commonly inserted tangential to the fracture during this remeshing process. While this isolates the domain ahead of the fracture from the influence of the fracture, this also leaves a trail of C^0 continuity lines behind after each fracture propagation step. Since these papers only simulate linear-elastic deformations, and therefore are solely interested in the stresses ahead of the fracture, this does not pose any issues.

In this chapter, the generation of unequal-order T-spline meshes will be detailed. These unequal order meshes are needed to fulfil the inf-sup condition, and prevent non-physical

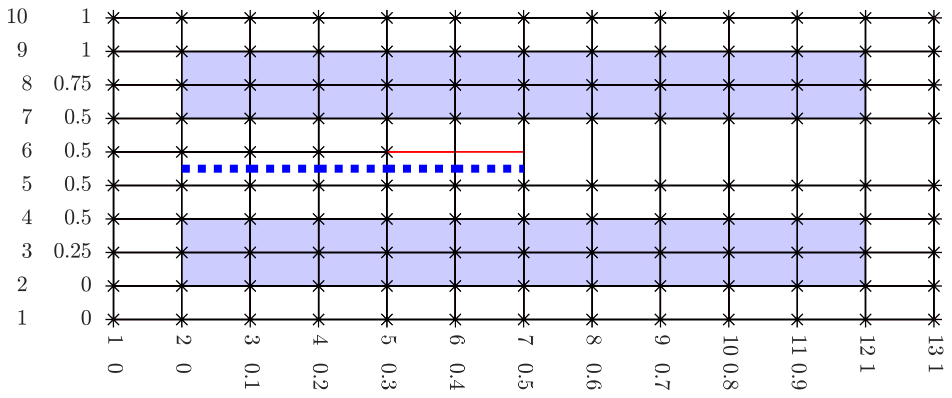

(a) Cubic mesh with reduced continuity lines at the fracture tip

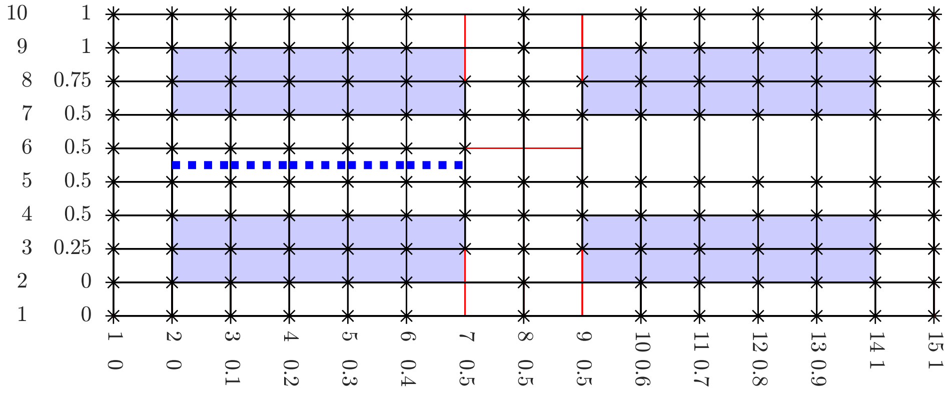

(b) Cubic mesh with C^0 continuity line tangential to the fracture tip (not used anywhere else in this chapter)

Figure 6.1: Interface elements and elements around the interface for a cubic mesh in parametric (inner coordinates) and index space (outer coordinates). Black lines represent the meshlines, red lines the reduced continuity lines, blue squares the interior elements, and blue dotted lines the interface elements.

pressure oscillations. Interface elements will be used to represent the fracture, and a remeshing and fracture propagation scheme retaining the higher order inter-element continuity along the fracture will be presented. This scheme offers several possible meshes, which will be described with their advantages. Finally, the T-spline meshes will be used to simulate the pressurised fracture case from the previous chapter, and the results will be compared to show the capabilities of T-splines to simulate fracture propagation in poroelastic media.

6.1. MESH GENERATION

T-spline meshes are defined through a T-mesh, given in an index/parametric space [21]. On this mesh, the anchors correspond to control points in the physical space. These anchors each have their own local knot vector, which are defined through the meshlines. An example of a T-mesh in index space is given in figure 6.1a. For instance, the anchor that is located at $(3,3)$ is defined through the knot vectors $\Xi_x = [0\ 0\ 0.1\ 0.2\ 0.3]$ and $\Xi_y = [0\ 0\ 0.25\ 0.5\ 0.5]$. These knot vectors are based on the meshlines directly horizontal and vertical of the anchors, and differ for each anchor.

By having multiple meshlines in the index space correspond to the same value in the parametric space, knots are repeated and the continuity is reduced at the location of the repeated knots [227]. Since the meshlines for T-meshes are allowed to start and stop at each perpendicular meshline, C^{-1} continuity can be inserted to represent the fracture without creating extra C^{-1} continuity elements that do not represent the fracture (in contrast to NURBS).

The shape functions created through the knot vectors occupy a square spanned by these knot vectors. This introduces a reduced continuity at the edge of the space occupied by the shape function. For most cases, this reduced continuity collides with a meshline, which were purposely inserted there to create this reduced continuity. However, when meshlines are stopped, the shape functions using those meshlines will create additional reduced continuity lines, as shown in Figure 6.1a at the discontinuity, and in Figure 6.1b both at the discontinuity and inside the domain itself.

To use T-splines in a similar manner as NURBS and standard Lagrangian finite elements, elements are defined on the T-mesh. These elements are enclosed by the combination of meshlines and reduced continuity lines, creating an element when a non-zero area is covered in the parametric space [203]. This results in the elements shown in Figure 6.1, where the blue squares represent the elements that cover a non-zero area in the parametric space, and will thus persist into the physical space. Due to the repeated meshlines around the discontinuity, "zero-area elements" are present, which do not carry over into the physical space, and are therefore not considered as elements. Similarly for interface and boundary elements, which are created when a non-zero length is covered by either a meshline or a reduced continuity line [227]. Once the elements are determined, the Bézier extraction process can be used in the same manner as for NURBS to describe the T-splines as a combination of Bernstein polynomials [204].

6.1.1. UNEQUAL ORDER T-SPLINE MESHES

Next to the cubic mesh for the interstitial fluid pressure, a quartic mesh for the solid displacement is needed. This quartic mesh needs to represent the exact same geometry and elements as the cubic mesh to enable the coupling between the solid and fluid to be easily included. Therefore, the quartic mesh requires the same inter-element continuity as the cubic mesh, and thus requires additional every meshline and reduced continuity line to be repeated once.

Since reduced continuity lines for both quartic and cubic meshes have the same length in the index space, and every meshline is repeated for the quartic mesh, the reduced continuity lines have different lengths in the parametric (and therefore physical) space. Cubic meshes obtain two additional interface elements due to these reduced continuity lines, as shown in Figure 6.1a, whereas only a single additional interface element is created for the quartic mesh, Figure 6.2a. This is resolved by inserting additional meshlines at the discontinuity, resulting in equal discontinuity length for the quartic and cubic meshes.

Similar issues arise near mesh refinement steps, as seen by comparing Figure 6.8 with Figure 6.9. Here, additional meshlines need to be inserted tangential with the refinement layer to match the elements and inter-element continuity between the meshes. The repeated meshlines in parametric space offer a choice on this point, allowing for an extra layer of anchors/meshlines to be inserted while still corresponding to the cubic mesh its discretisation. It was chosen here to use the minimal required number of anchors instead of using the additional layer, mainly to limit the number of degrees of freedom associated with the solid displacement (which due to the repeated meshlines already has many more anchors/control points).

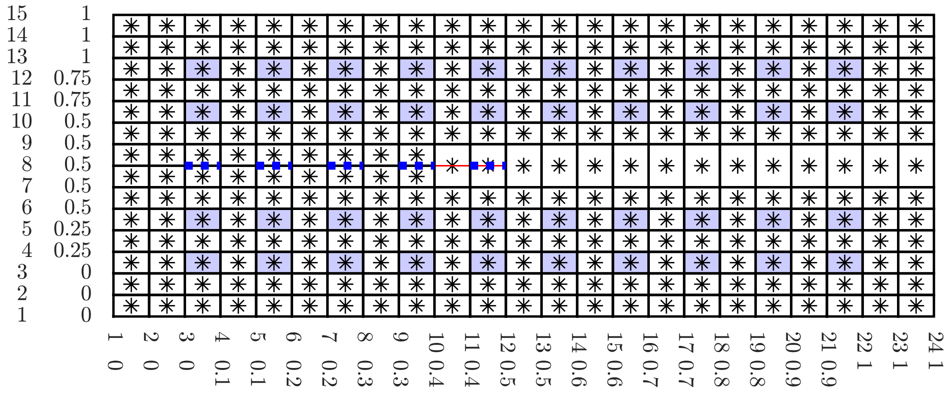

(a) Minimum amount of discontinuity lines

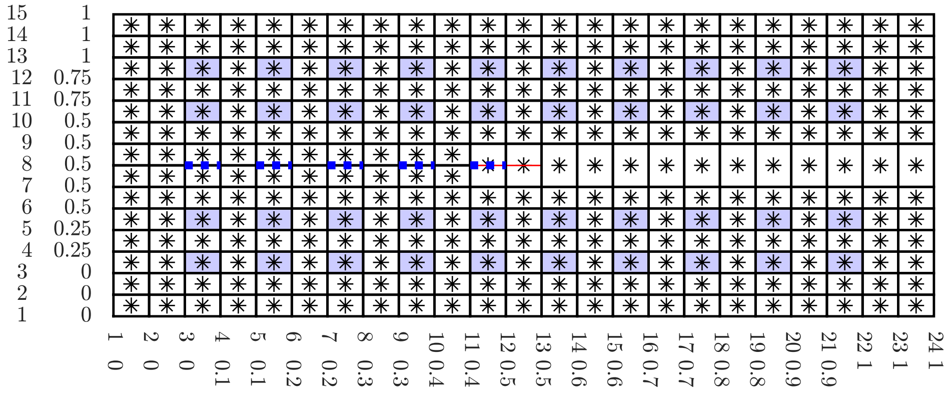

(b) Maximum amount of discontinuity lines

Figure 6.2: Interface elements and elements around the interface for a quartic mesh in parametric and index space, corresponding to the cubic mesh from Figure 6.1a. Black lines represent the meshlines, red lines the reduced continuity lines, blue squares the interior elements, and blue dotted lines the interface elements.

6.1.2. INTERFACE ELEMENTS USING T-SPLINES FOR PRESSURISED FRACTURES

Interface elements are inserted at the C^{-1} discontinuity to represent the fluid filled fracture. Similar to the mesh refinement steps, there are several options for how to insert the interface elements. The approach taken by [55, 56, 227] is to isolate the fractured from the still-to-be fractured part by inserting a C^0 continuity line perpendicular to the fracture, as shown in Figure 6.1b. Interface elements only correspond to the meshlines, while the reduced continuity lines are contained by the C^0 continuity line. When the fracture is propagated, the reduced continuity is left in place, resulting in a reduced continuity in between the interface elements.

A different approach is to insert interface elements at the meshlines and reduced continuity lines, as shown in Figure 6.1a. This has as main advantage that the higher order continuity is preserved, both around the fracture tip in the porous material and between the interface elements at the fracture. However, this limits the number of shape functions near the fracture tip, slightly limiting the interstitial pressure jumps that can be represented close to the fracture tip. This is shown in Figure 6.3, comparing the actual pressure jump obtained with the available interpolants when a $-1, 1$ pressure jump is imposed on the control points. Since this disadvantage is diminished when finer meshes are used, whereas the reduced continuity resulting from the first approach remains, this approach will be used here.

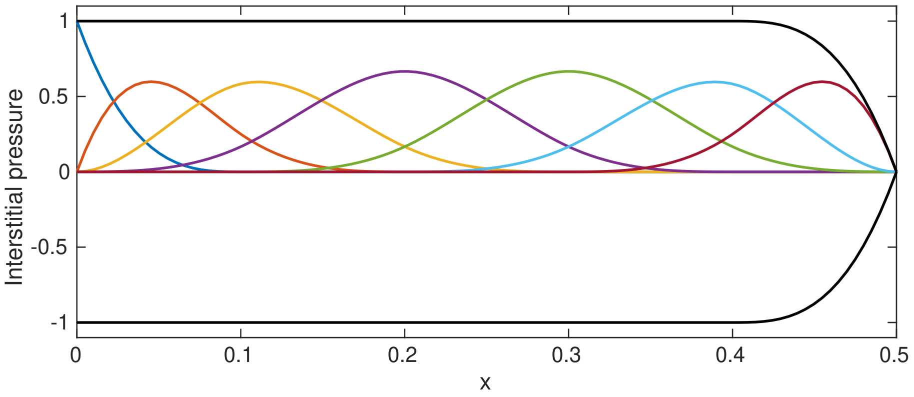

(a) C^0 continuity line perpendicular to the fracture tip.

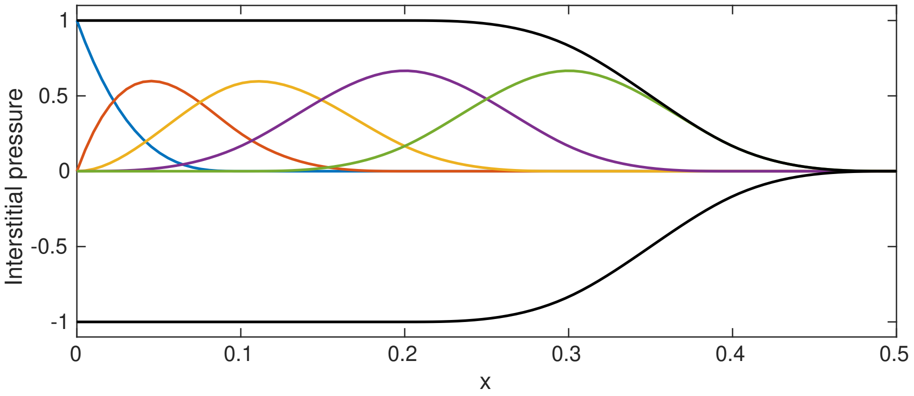

(b) Meshlines and reduced continuity lines as interface elements.

Figure 6.3: Interpolation functions corresponding to the discontinuity (coloured), and the interstitial pressure by imposing a pressure jump between -1 and 1.

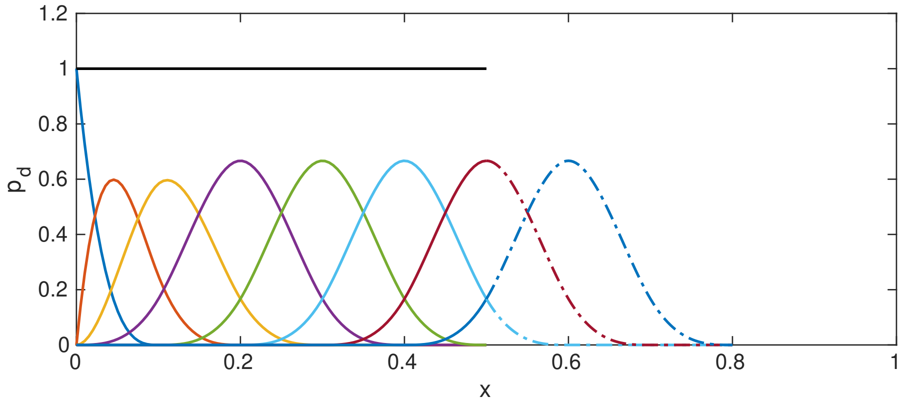

Figure 6.4: Interpolation functions used for the discontinuity pressure (solid lines) and remaining parts outside the interface elements not used (dotted lines).

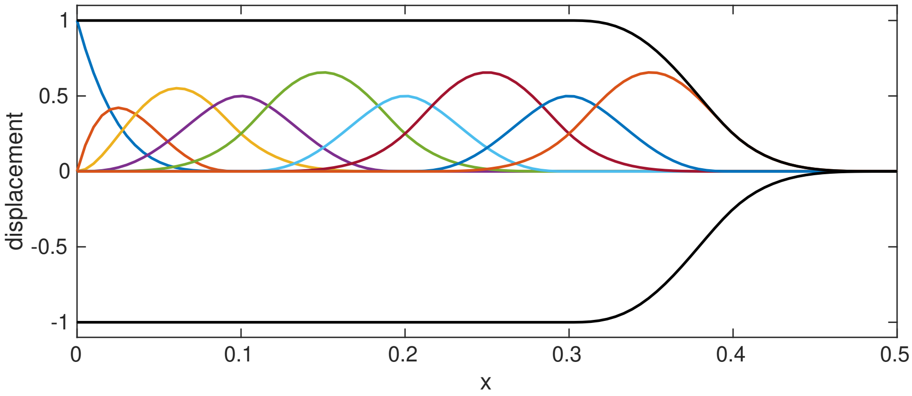

(a) Minimum amount of discontinuity lines

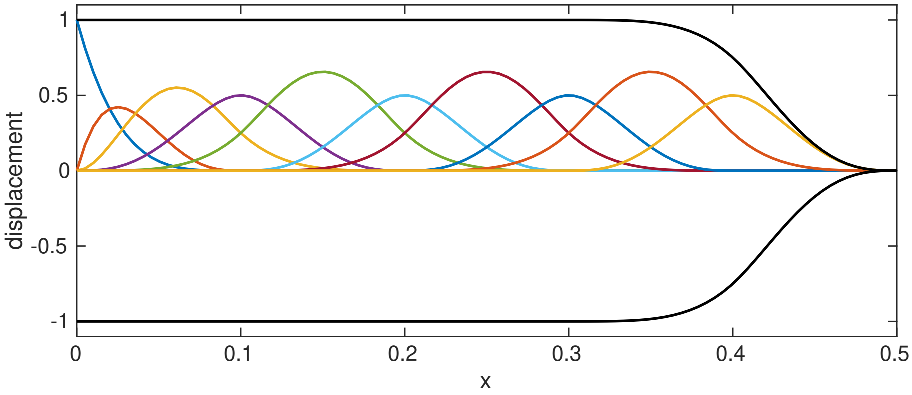

(b) Maximum amount of discontinuity lines

Figure 6.5: Interpolation functions corresponding to the discontinuity (coloured), and the interface displacement by imposing a displacement jump between -1 and 1.

Degrees of freedom related to the pressure inside the discontinuity also need to be added to the interface elements. If these degrees of freedom were solely added to the discontinuous control points, the pressure at the fracture tip would be forced to be equal to zero. To allow the fracture pressure at the fracture tip to be non-zero, discontinuity pressure degrees of freedom are added to all control points located at the bottom of the interface elements, independent whether they are duplicated with a top node to create a C^{-1} discontinuity or are still C^0 continuous. The parts of the interpolation functions that are not contained within any interface element are disregarded, and only get included when the fracture propagates to create new interface elements covering their length. The resulting interpolation functions, and the ignored parts of these functions, are shown in Figure 6.4.

As was the case for the mesh refinement for the quartic mesh, the discontinuity near the fracture tip is allowed to contain an extra meshline, as shown in Figure 6.2. While this extra meshline does not add an extra interface element due to the repeated knot, it does add an extra control point near the quartic mesh. This introduces an extra interpolation function, as shown in Figure 6.5, and allows for a sharper fracture tip. Both these meshes result in the same mesh and interface elements in the physical space. In the next section, the effect of this choice on the resulting fracture opening will be analysed.

6.1.3. FRACTURE PROPAGATION

The fracture is propagated by creating new interface elements through meshline insertion. To limit the remeshing required, a C^0 continuity line is inserted at the future fracture path

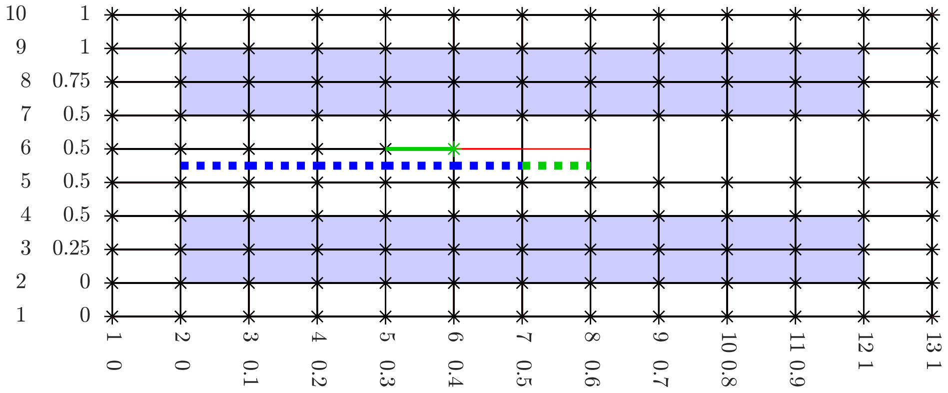

(a) Cubic mesh

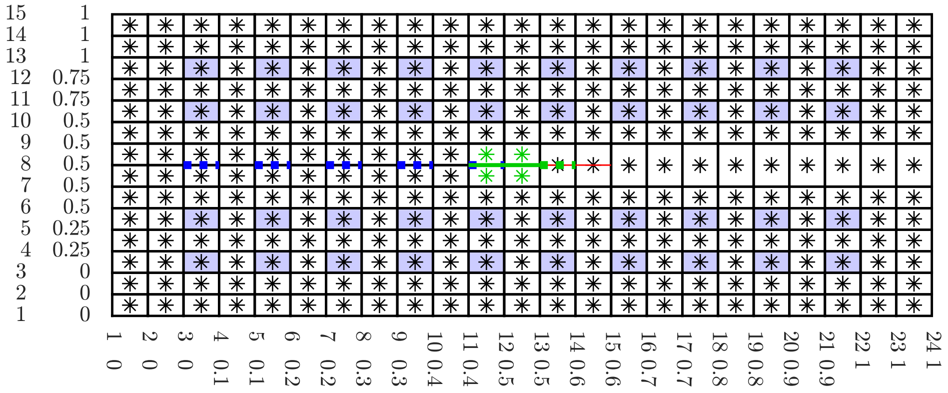

(b) Quartic mesh

Figure 6.6: Meshline insertion to propagate the discontinuity one interface element length. Green lines represent the inserted meshlines, green markers the inserted or altered anchors, and the green dotted line the newly created interface element.

when the mesh is generated. This simplifies the meshline insertion, by only altering the location of the anchors in the parametric space, while no control points change location in physical space. Furthermore, the Bézier extraction operators for the interior elements are not changed by propagating the fracture along the pre-inserted C^0 continuity line.

The discontinuity inside the cubic mesh is propagated by inserting a single meshline one interface element behind the fracture tip, as shown in Figure 6.6a. This creates a new anchor at the end of this meshline, and creates a new interface element to propagate the fracture. The control point corresponding to this newly created anchor is initialised by setting the displacements and interstitial fluid pressure equal to the pre-existing control point at the same location now belonging to the bottom of the discontinuity. Similar for the cubic meshes, which by inserting two meshlines and two anchors create a single new interface element and two new control points, as shown in Figure 6.6b for the quartic mesh using the maximum number of discontinuity lines.

Because the interface elements are only inserted for fractured elements, there is no need for dummy stiffness and dummy permeability values. For the tractions on the fracture walls, this removes the need for a lumped integration scheme, and these tractions are integrated using a standard Gauss integration scheme. The terms containing the interface permeability are still integrated using the interface permeability since this permeability can be high enough to create oscillations for cases in which a continuous pressure model is approximated. However, the need for the fracture tip integration scheme described in the previous chapter is removed, since no dummy permeability is needed.

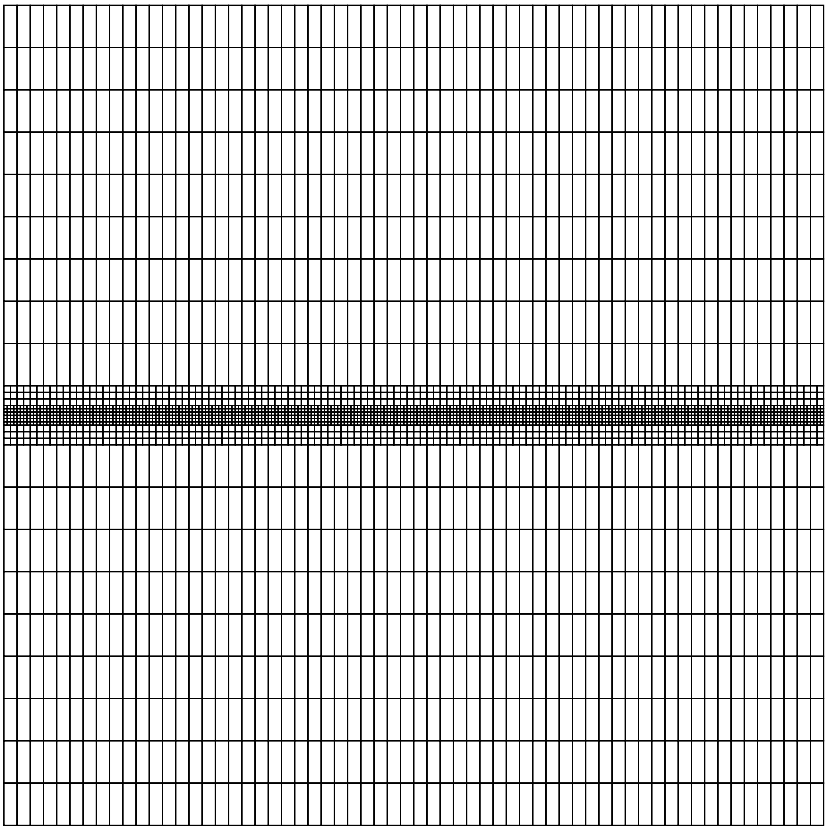

Figure 6.7: Mesh in physical space.

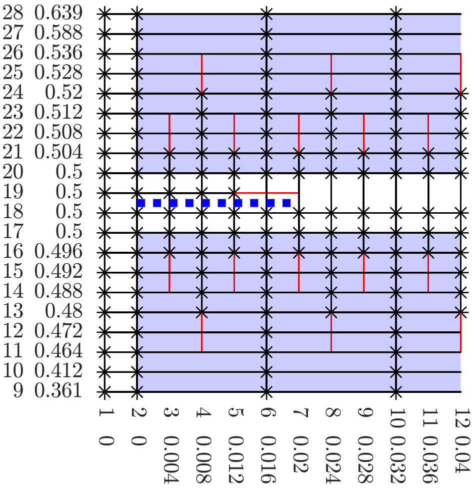

Figure 6.8: Cubic mesh in parametric/index space. Black lines represent the meshlines, red lines the reduced continuity lines, blue squares the interior elements, and blue dotted lines the interface elements.

6.2. COMPARISON T-SPLINES AND NURBS

To compare the effects of using T-splines with NURBS, and to investigate the influence of using the minimum amount of discontinuity lines at the fracture tip, the case from the previous chapter (Section 5.4) is repeated using T-splines. The simulations were performed using a Newtonian fluid ($n = 1$), and all properties correspond to those of the previous simulations (except that no dummy stiffness and permeability values were needed). Since T-

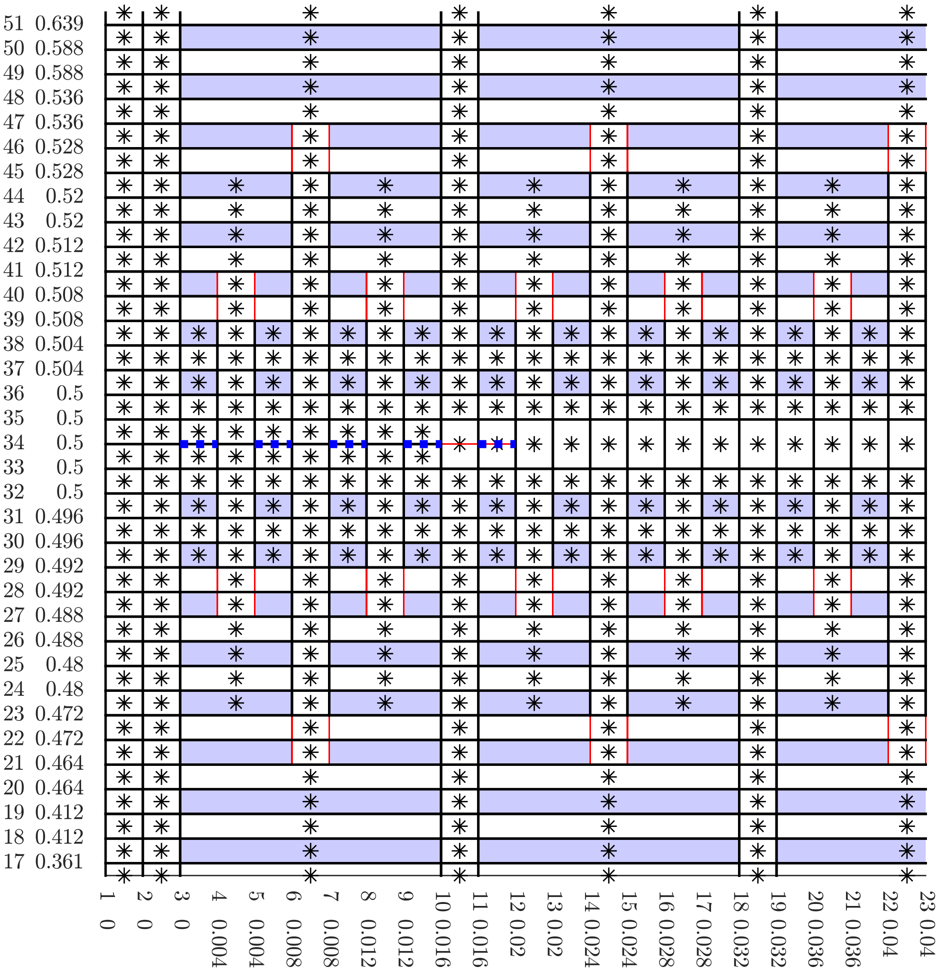

Figure 6.9: Quartic mesh with the minimum amount of discontinuity lines at the fracture tip. Black lines represent the meshlines, red lines the reduced continuity lines, blue squares the interior elements, and blue dotted lines the interface elements.

splines allow mesh refinement in parts of the domain, 248 × 6 small elements are used near the interface, surrounded by a layer of 124 × 3 elements on each side, and the remainder of the domain filled on the top and bottom by 62 × 9 elements. This mesh is shown in Figure 6.7 in the physical domain. To allow for an equal length of the initial fracture, the size of the first 5 horizontal elements are slightly altered, such that the total length of these elements is 5 mm.

The cubic mesh used for the fluid is shown in the parametric space in Figure 6.8. As mentioned before, a C^0 continuity is used in the path of the fracture, both to make the fracture propagation along this line easier, and to keep the Bézier extraction matrices of the interior elements constant, even when the fracture is propagated. The mesh refinement near the interface is mainly caused by the reduced continuity lines extending from the control points, and not the mesh lines themselves. As a side effect, at least 3 elements for the finest refinement layer are needed to prevent the coarser elements introducing additional reduced continuity lines at the interface, and thereby introducing extra interface elements.

The two quartic meshes used for the displacement are shown in Figure 6.9 and 6.10. The first mesh uses the minimum amount of meshlines and anchors to create the required interface elements, whereas for the second mesh an extra control point is added to allow for a sharper fracture opening near the fracture tip. The cubic mesh combined with either of

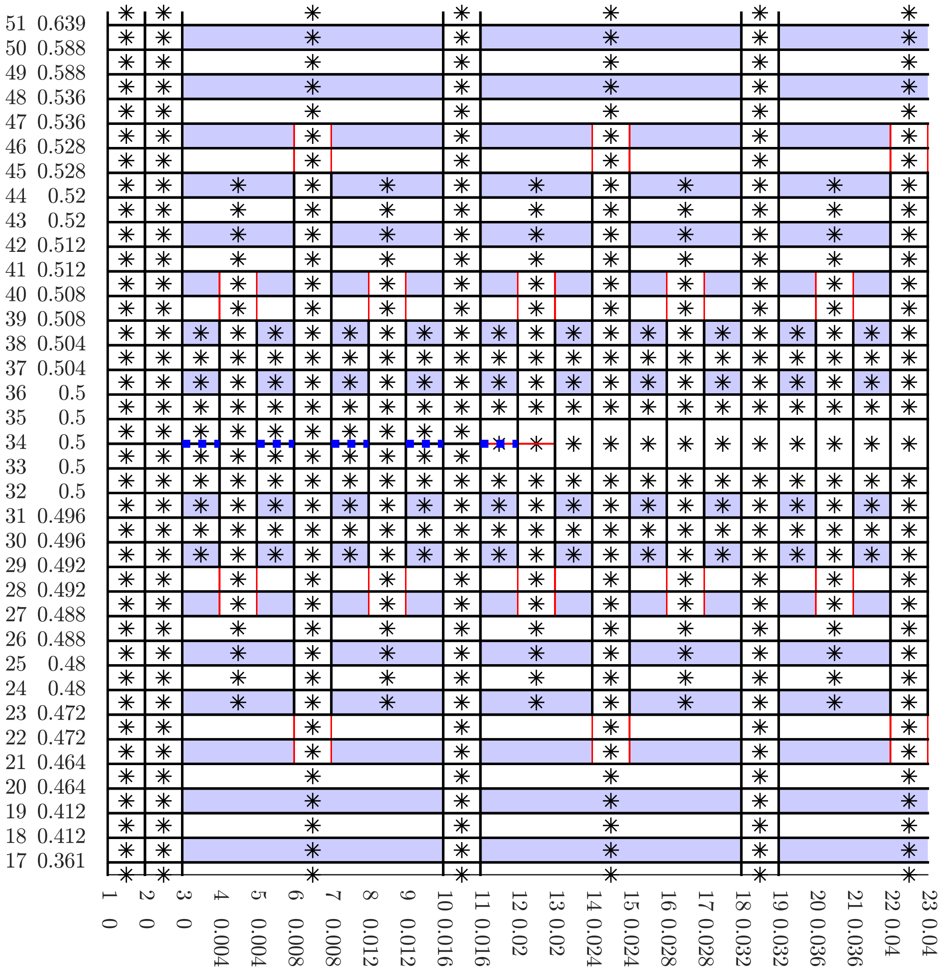

Figure 6.10: Quartic mesh with the additional discontinuity line at the fracture tip. Black lines represent the meshlines, red lines the reduced continuity lines, blue squares the interior elements, and blue dotted lines the interface elements.

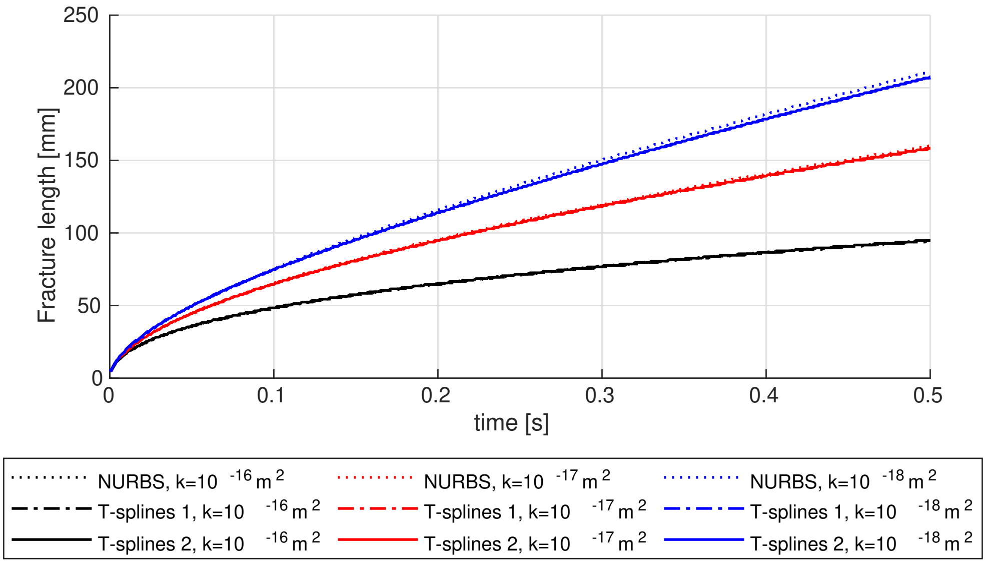

Figure 6.11: Comparison between the fracture length as obtained using NURBS and T-splines with the minimal (T-splines 1) and maximum (T-splines 2) number of inserted discontinuity lines around the fracture tip.

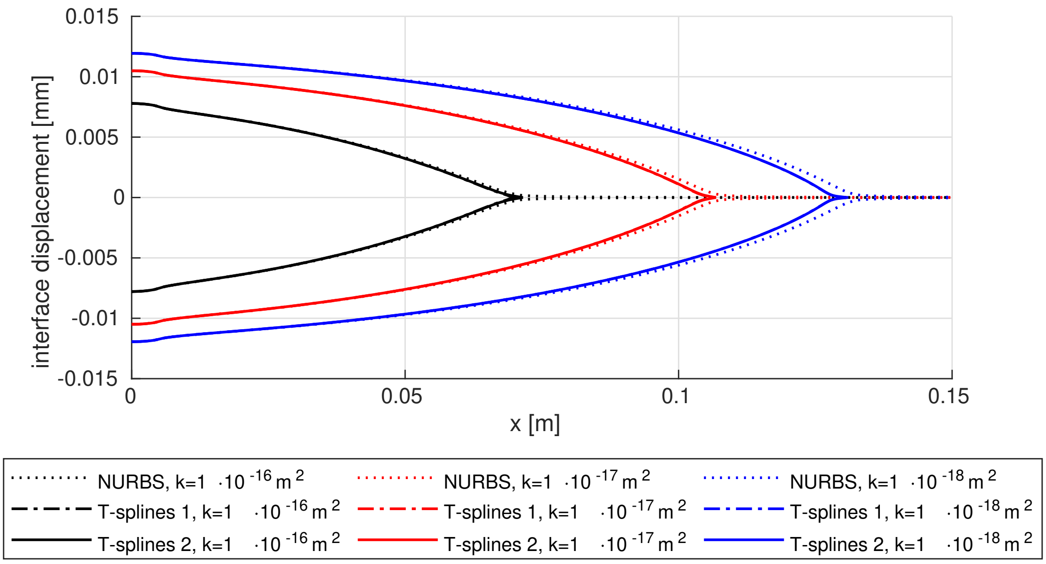

Figure 6.12: Fracture opening height h at $t = 0.25$s using NURBS and T-splines with the minimal (T-splines 1) and maximum (T-splines 2) number of inserted discontinuity lines around the fracture tip.

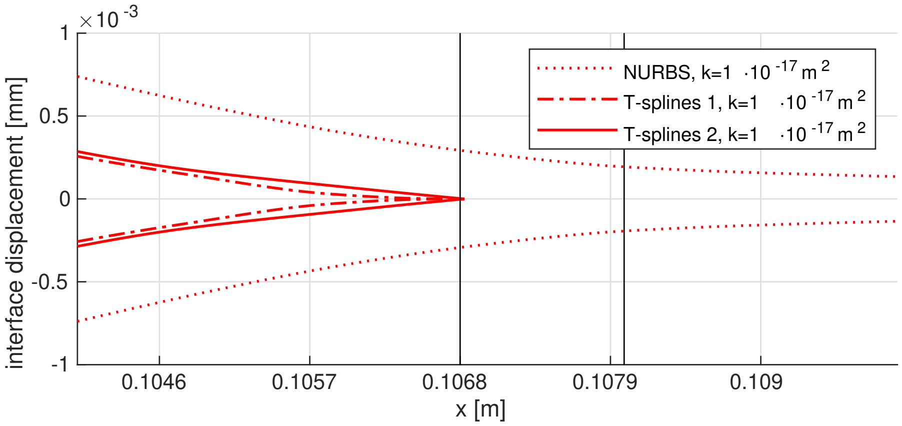

Figure 6.13: Fracture opening height h at $t = 0.25$s using NURBS and T-splines with the minimal (T-splines 1) and maximum (T-splines 2) number of inserted discontinuity lines around the fracture tip, zoomed in at the fracture tips. Black vertical lines indicate the total fractured length.

these meshes are hereafter referred to as "T-splines 1" (cubic with minimum discontinuity line quartic) and "T-splines 2" (cubic with extra anchor quartic meshes). All results are compared to the NURBS mesh from the previous chapter, which used 250 × 20 elements.

A comparison between fracture lengths using NURBS and T-splines is given in Figure 6.11. For the $k = 10^{-16}\text{m}^2$ results, no difference is seen between the different meshes. For the $k = 10^{-17}\text{m}^2$ simulations, at most 2 element lengths difference between the NURBS and T-splines occurs, with the NURBS propagating slightly faster. Similar results are seen for the lowest permeability, with at most 3-4 elements difference.

The fracture opening height halfway through the simulation, Figure 6.12, also shows fairly small differences between T-splines and NURBS. While the T-splines result in a discrete fracture tip, the NURBS obtain a smoother fracture tip. This is clearly shown by zooming in on the fracture tip, Figure 6.13. The dummy stiffness used with the NURBS does not enforce no fracture opening, but only applies a large force to limit the opening height as

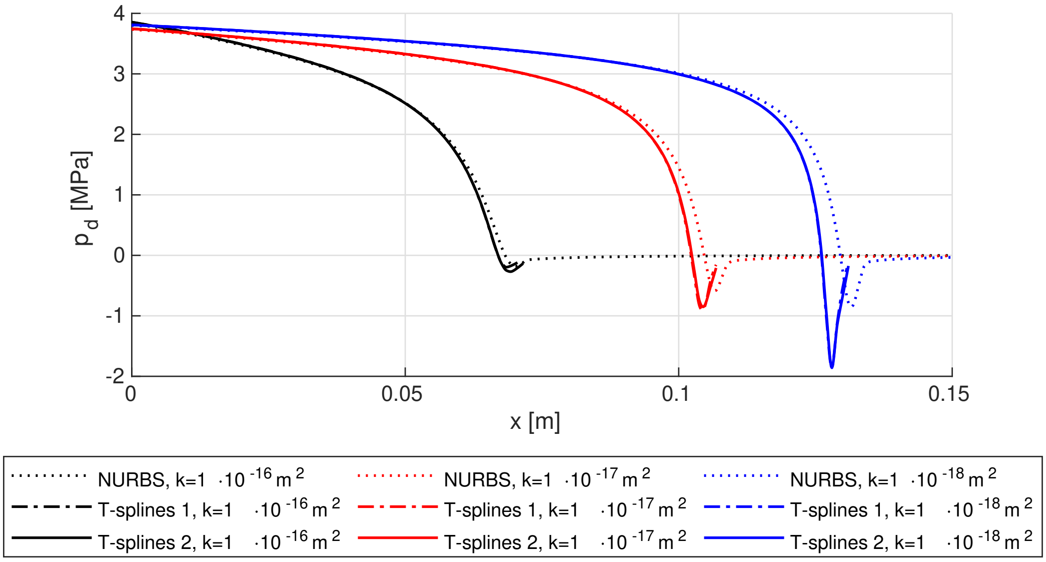

Figure 6.14: Pressure inside the discontinuity,p_d, at $t = 0.25$s, using NURBS and T-splines with the minimal (T-splines 1) and maximum (T-splines 2) number of inserted discontinuity lines around the fracture tip.

much as possible. This results in a larger opening height, and a slightly non-zero opening even at the fracture tip. In contrast, the T-splines obtain a fracture without opening height at the fracture tip. The results with the additional anchor added to the "T-spline 2" mesh allow for a slightly sharper fracture tip and a larger opening height, although the differences between the two T-spline meshes disappears after 2 elements.

The differences in fracture opening height near the tip also influence the pressure inside the discontinuity, Figure 6.14. For NURBS, the discontinuity pressure is defined for the complete discontinuity (both fractured and non-fractured), while for the T-splines the discontinuity pressure is limited to the fracture. Due to the lower opening height of T-splines, less fluid flows near the fracture tip inside the fracture. This results in a lower pressure near the fracture tip, explaining the slightly slower fracture propagation for T-splines compared to NURBS. Since no difference in fracture height occurred away from the fracture tip, the NURBS and T-spline simulations obtain the same discontinuity pressure.

6.3. CONCLUSION

In this chapter, the mesh generation for unequal order T-spline meshes has been detailed. By combining a cubic mesh for the interstitial fluid pressure with a quartic mesh for the solid displacement, the inf-sup condition can be fulfilled and non-physical pressure oscillations are prevented. To retain higher order inter-element continuity for the interface elements, these interface elements are created by a combination of meshlines and reduced continuity lines. Finally, a fracture propagation scheme was detailed, propagating the discontinuity along a C^0 continuity line by inserting meshlines in both the cubic and quartic meshes.

The unequal order meshes allow for several choices for the quartic mesh near the discontinuity: Either using a minimum amount of meshlines to match the discontinuity between the two meshes, or adding an extra meshline to increase the degrees of freedom near the fracture tip. These two choices have been compared, showing near to no difference on the overall results and only slight differences in the fracture opening height close to the fracture tip.

Comparing the T-spline meshes to a mesh generated with NURBS, the advantages of T-splines are clear: The T-spline meshes allowed for smaller elements to be used near the discontinuity, while using larger elements for the remainder of the domain. In contrast, the NURBS mesh required mesh refinements to be performed for the complete domain. Furthermore, T-spline meshes allow for only using interface elements for the fracture, which removed the need for a lumped integration scheme for the tractions at the interface and the fracture tip integration scheme for the pressure inside the discontinuity.

Finally, simulation results comparing NURBS to T-splines showed that T-splines obtained a completely closed fracture at the fracture tip, whereas the dummy stiffness used with NURBS allowed for a slightly opened fracture, even at the fracture tip. While this difference in fracture opening height altered the discontinuity pressure near the fracture tip, it did not significantly change the fracture propagation velocity.

7

DIRECT SIMULATION OF FRACTURE FLOW

Using the cubic law to model the fluid transport within a fracture under continuous pressure conditions has long been known to accurately represent the influence of the fluid filled fracture on the surrounding porous material [238]. However, the accuracy of discontinuous pressure models to represent fractures with an entry resistance has not been shown, with most uses of the interface permeability term being solely numerical. Comparisons between the discontinuous pressure model and continuous pressure model have shown its accuracy in the near continuous pressure limit [173], and simulations using a variety of discretisation methods have shown its independence of the used discretisation method [79].

Direct simulations of the Stokes flow in the interior of the fracture, coupled to the surrounding porous material through an interface permeability term, have shown the feasibility of fully simulating the fluid inside the fracture [25]. This approach is commonly taken when large voids are present [13, 14, 50], allowing for simulations which do not adhere to the assumptions taken during the derivation of subgrid models: A small fracture opening compared to its length. However, these simulations have been limited to non-propagating fractures and pre-determined voids. An alternative approach is to assume the fracture to be filled with highly permeable porous material, allowing both the fracture and the surrounding material to be described using the same set of equations [70, 133, 143]. A downside of this approach is that it does not give velocity profiles within the fracture. Furthermore, including entry resistance for the fluid is solely accomplished using a smeared approach, approximating the pressure jump across the fracture wall as a steep pressure gradient.

In this chapter, a scheme for the simulation of Stokes flow within the fracture will be described, allowing for fully simulating the fluid flow within propagating fractures coupled to a poroelastic material. The porous material is discretised using T-splines, as described in the previous chapter. To resolve both the fracture flow and poroelastic material, an iterative approach will be adopted, alternating between solving the interior of the fracture and solving the porous domain. This allows the fluid inside the fracture to be fully simulated, with a comparison between the direct simulation and subgrid model approaches given in Section 7.2. The methods and results presented in thic chapter have been previously published in [3].

7.1. GOVERNING EQUATIONS

The interior of the fracture is described using the Stokes equations, given in the fracture-local coordinate system for a Newtonian fluid as:

$$-\frac{\partial p_d}{\partial x_d}+\mu\left(\frac{\partial^2 v}{\partial x_d^2}+\frac{\partial^2 v}{\partial y_d^2}\right)=0 \tag{7.1}$$

$$-\frac{\partial p_d}{\partial y_d}+\mu\left(\frac{\partial^2 w}{\partial x_d^2}+\frac{\partial^2 w}{\partial y_d^2}\right)=0 \tag{7.2}$$

$$\frac{\partial v}{\partial x_d}+\frac{\partial w}{\partial y_d}=0 \tag{7.3}$$

subject to no-slip boundary conditions at the top and bottom fracture wall:

$$\boldsymbol{t}_d\cdot\begin{pmatrix}v\\w\end{pmatrix}=0\quad\text{on}\quad\Gamma_d^{\pm} \tag{7.4}$$

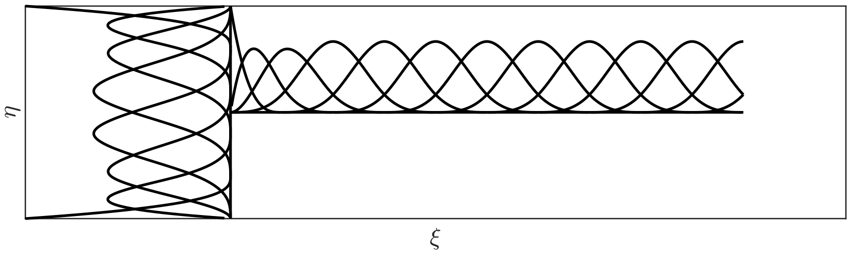

(a) Input meshes: Two one-dimensional B-splines in the parametric domain

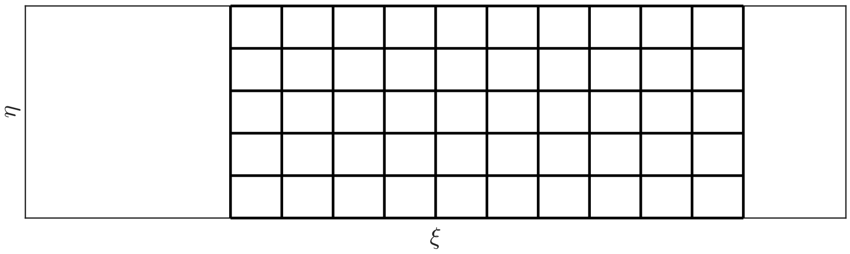

(b) Generated mesh in the parametric domain

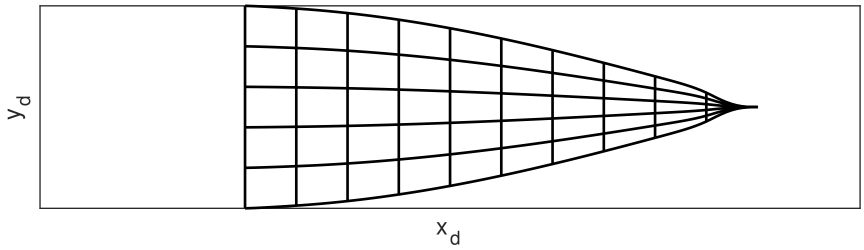

(c) Generated mesh mapped to physical domain

Figure 7.1: Mesh generation procedure for the interior of the fracture

and a mass conservation condition across the fracture walls:

$$\boldsymbol{n}_d \cdot \begin{pmatrix} v \\ w \end{pmatrix} + \frac{1}{2}\dot{h} + k_i \left(p_d - p\right) = 0 \quad \text{on} \quad \Gamma_d^{\pm} \tag{7.5}$$

using the velocity (v, w) in the interior of the fracture and the normal and tangential vectors to the fracture walls, $\boldsymbol{n}_d$ and $\boldsymbol{t}_d$ respectively. At the inlet of the fracture, a parabolic inflow profile is used:

$$v = Q_{in}\left(\frac{3}{2h} - \frac{6y_d^2}{h^3}\right) \quad \text{on} \quad \Gamma_{in} \tag{7.6}$$

allowing a total fluid flux Q_{in} to be imposed at the fracture inlet. Finally, the tractions across the interface are given in a similar manner as for the discontinuous pressure model as:

$$\boldsymbol{\tau}_{\Gamma_d} = \boldsymbol{\tau}_d(\llbracket \boldsymbol{u} \rrbracket) - p_d \boldsymbol{n}_d \quad \text{on} \quad \Gamma_d^{\pm} \tag{7.7}$$

It should be noted that the boundary conditions used here are those commonly used in fracture flow models. It was chosen to use these boundary conditions for both the discontinuous pressure model and the direct simulation of the flow inside the fracture for consistency and to allow the results to be directly compared. However, the formulation for the direct simulation of the fracture is formulated such that other boundary conditions can easily be substituted, for instance the Beavers-Joseph-Saffman condition [23, 197] which is commonly used for Stokes flow over porous objects.

7.1.1. DISCRETISATION

To discretise the interior of the fracture, a set of B-splines for the fracture height are defined in a parametric space, as shown in Figure 7.1a. This set of B-splines is combined with the pre-existing set of T-splines that define the discontinuity in the porous material, discretising the complete fracture in the parametric (ξ, η) space. Finally, this space is mapped to the physical space through $x_d = \xi$, $y_d = h/2\ \eta$ for the horizontal fractures used in this chapter. This mapping allows the discretisation of the fracture to automatically deform when the opening height changes. To aid in the implementation of the boundary conditions between the porous and fracture domains, the velocity components are split in an interior and boundary part, discretising the interior of the fracture as:

$$p_d = \sum \left(\boldsymbol{N}_f \otimes \boldsymbol{N}_3\right) \boldsymbol{p}_d = \sum \boldsymbol{N}_{pd} \boldsymbol{p}_d \tag{7.8}$$

$$\begin{aligned} v &= \sum \left(\boldsymbol{N}_s \otimes \boldsymbol{N}_{4b}\right) \boldsymbol{v}_b + \sum \left(\boldsymbol{N}_s^{2+} \otimes \boldsymbol{N}_{4i}\right) \boldsymbol{v}_i + \sum \left(\boldsymbol{N}_s^{1} \otimes \boldsymbol{N}_{4i}\right) \boldsymbol{v}_{in} \\ &= \sum \boldsymbol{N}_{vb} \boldsymbol{v}_b + \sum \boldsymbol{N}_{vi} \boldsymbol{v}_i + \sum \boldsymbol{N}_{in} \boldsymbol{v}_{in} \end{aligned} \tag{7.9}$$

$$w = \sum \left(\boldsymbol{N}_s \otimes \boldsymbol{N}_{4b}\right) \boldsymbol{w}_b + \sum \left(\boldsymbol{N}_s \otimes \boldsymbol{N}_{4i}\right) \boldsymbol{w}_i = \sum \boldsymbol{N}_{wb} \boldsymbol{w}_b + \sum \boldsymbol{N}_{wi} \boldsymbol{w}_i \tag{7.10}$$

with $\boldsymbol{N}_3$ and $\boldsymbol{N}_{4i}$ the sets of cubic and quartic splines used for the height discretisation of the fracture, with $\boldsymbol{N}_{4i}$ only including the splines that are zero at the fracture walls. $\boldsymbol{N}_{4b}$ includes the non-zero splines at the walls, which are used for the boundary conditions. $\boldsymbol{N}_s^1$ indicates that only the first spline is used for the inlet velocity discretisation, and the other splines $\boldsymbol{N}_s^{2+}$ for the interior discretisation. The set of splines $\boldsymbol{N}_s^{2+}$ directly implements the no flow boundary condition at the fracture tip by using only the discontinuous splines, whereas $\boldsymbol{N}_{pp}$ and $\boldsymbol{N}_s$ use all splines along the discontinuity, thereby allowing for non-zero vertical velocities and pressures at the fracture tip. Since these discretisations are directly dependent on the splines defining the discontinuity, they are easily adapted to a new fracture length upon fracture propagation. Furthermore, by performing the construction of the force vectors in a parametric space the fracture does not need to be remeshed when the fracture opening height changes.

Using this discretisation, the momentum balances (Eq. 7.1 and 7.2) and mass balance (Eq. 7.3) are discretised by integrating over the paramtric domain Ω_f as:

$$\begin{aligned} \int_{\Omega_f} \mu \left(\frac{\partial \boldsymbol{N}_{wi}}{\partial x_d}\right)^T \left(\frac{\partial \boldsymbol{N}_{wi}}{\partial x_d} \boldsymbol{w}_i + \frac{\partial \boldsymbol{N}_{wb}}{\partial x_d} \boldsymbol{w}_b\right) + \mu \left(\frac{\partial \boldsymbol{N}_{wi}}{\partial y_d}\right)^T \left(\frac{\partial \boldsymbol{N}_{wi}}{\partial y_d} \boldsymbol{w}_i + \frac{\partial \boldsymbol{N}_{wb}}{\partial y_d} \boldsymbol{w}_b\right) \\ + \boldsymbol{N}_{wi}^T \frac{\partial \boldsymbol{N}_{pd}}{\partial y_d} \boldsymbol{p}_d \, \mathrm{d}\Omega_f = \boldsymbol{0} \end{aligned} \tag{7.11}$$

$$\begin{aligned} \int_{\Omega_f} \mu \left(\frac{\partial \boldsymbol{N}_{vi}}{\partial x_d}\right)^T \left(\frac{\partial \boldsymbol{N}_{vi}}{\partial x_d} \boldsymbol{v}_i + \frac{\partial \boldsymbol{N}_{vb}}{\partial x_d} \boldsymbol{v}_b\right) + \mu \left(\frac{\partial \boldsymbol{N}_{vi}}{\partial y_d}\right)^T \left(\frac{\partial \boldsymbol{N}_{vi}}{\partial y_d} \boldsymbol{v}_i + \frac{\partial \boldsymbol{N}_{vb}}{\partial y_d} \boldsymbol{v}_b\right) \\ + \boldsymbol{N}_{vi}^T \frac{\partial \boldsymbol{N}_{pd}}{\partial y_d} \boldsymbol{p}_d \, \mathrm{d}\Omega_f = -\int_{\Omega_f} \mu \left(\frac{\partial \boldsymbol{N}_{vi}}{\partial x_d}\right)^T \frac{\partial \boldsymbol{N}_{in}}{\partial x_d} \boldsymbol{v}_{in} + \left(\frac{\partial \boldsymbol{N}_{vi}}{\partial y_d}\right)^T \frac{\partial \boldsymbol{N}_{in}}{\partial y_d} \boldsymbol{v}_{in} \, \mathrm{d}\Omega_f \end{aligned} \tag{7.12}$$

$$\int_{\Omega_f} \boldsymbol{N}_{pd}^T \left(\frac{\partial \boldsymbol{N}_{vi}}{\partial x_d} \boldsymbol{v}_i + \frac{\partial \boldsymbol{N}_{vb}}{\partial x_d} \boldsymbol{v}_b\right) + \boldsymbol{N}_{pd}^T \left(\frac{\partial \boldsymbol{N}_{wi}}{\partial y_d} \boldsymbol{w}_i + \frac{\partial \boldsymbol{N}_{wb}}{\partial y_d} \boldsymbol{w}_b\right) \mathrm{d}\Omega_f = -\int_{\Omega_f} \boldsymbol{N}_{pd}^T \frac{\partial \boldsymbol{N}_{in}}{\partial x_d} \boldsymbol{v}_{in} \, \mathrm{d}\Omega_f \tag{7.13}$$

with the fracture height $h = \boldsymbol{n}_d^T \boldsymbol{N}_s [\![\boldsymbol{u}]\!]^{t+\Delta t}$, and the spatial derivatives in physical space given for the mapping $x_d = \xi$, $y_d = \eta h/2$ as:

$$\frac{\partial \boldsymbol{N}_{pd}}{\partial x_d} = \frac{\partial \boldsymbol{N}_f}{\partial \xi} \otimes \boldsymbol{N}_3 - \frac{\eta}{\boldsymbol{n}^T \boldsymbol{N}_s [\![\boldsymbol{u}]\!]^{t+\Delta t}} \boldsymbol{n}^T \frac{\partial \boldsymbol{N}_s}{\partial \xi} [\![\boldsymbol{u}]\!]^{t+\Delta t} \boldsymbol{N}_f \otimes \frac{\partial \boldsymbol{N}_3}{\partial \eta} \tag{7.14}$$

$$\frac{\partial \boldsymbol{N}_{pd}}{\partial y_d} = \frac{2}{\boldsymbol{n}^T \boldsymbol{N}_s [\![\boldsymbol{u}]\!]^{t+\Delta t}} \boldsymbol{N}_f \otimes \frac{\partial \boldsymbol{N}_3}{\partial \eta} \tag{7.15}$$

The boundary conditions from Eq. 7.4-7.5 are enforced through their weak forms as:

$$\begin{aligned}\int_{\Gamma_d^\pm} & n_1 \boldsymbol{N}_{wb}^T \boldsymbol{N}_{vb} \boldsymbol{v}_b + n_2 \boldsymbol{N}_{wb}^T \boldsymbol{N}_{wb} \boldsymbol{w}_b + k_i \boldsymbol{N}_{wb}^T \boldsymbol{N}_{pd} \boldsymbol{p}_d - k_i \boldsymbol{N}_{wb}^T \boldsymbol{N}_f \boldsymbol{p} \\ & + \frac{1}{2\Delta t} \boldsymbol{N}_{wb}^T \boldsymbol{n}^T \boldsymbol{N}_s \left([\![\boldsymbol{u}]\!]^{t+\Delta t} - [\![\boldsymbol{u}]\!]^{t} \right) \mathrm{d}\Gamma^\pm = \boldsymbol{0}\end{aligned} \tag{7.16}$$

$$\int_{\Gamma_d^\pm} t_1 \boldsymbol{N}_{vb}^T \boldsymbol{N}_{vb} \boldsymbol{v}_b + t_2 \boldsymbol{N}_{vb}^T \boldsymbol{N}_{wb} \boldsymbol{w}_b \, \mathrm{d}\Gamma^\pm = \boldsymbol{0} \tag{7.17}$$

using the normal vector $\boldsymbol{n} = [n_1 \ n_2]$ and tangential vector $\boldsymbol{t} = [t_1 \ t_2]$, taking into account large deformations.

7.1.2. COUPLING

The coupling terms used in the momentum balance, Eq. 2.46, and the mass balance , Eq. 5.17, for the porous material are given by:

$$\boldsymbol{f}_d = \int_{\Gamma_d^\pm} \boldsymbol{N}_d^T \left(\boldsymbol{\tau}_d^{t+\Delta t} - \boldsymbol{n}_d \boldsymbol{N}_{pd} \boldsymbol{p}_d^{t+\Delta t} \right) \mathrm{d}\Gamma_d^\pm \tag{7.18}$$

$$\boldsymbol{q}_d = \Delta t k_i \int_{\Gamma_d^\pm} \boldsymbol{N}_f^T \boldsymbol{N}_{pd} \boldsymbol{p}_d^{t+\Delta t} - \boldsymbol{N}_f^T \boldsymbol{N}_f \boldsymbol{p}^{t+\Delta t} \, \mathrm{d}\Gamma_d^\pm \tag{7.19}$$

These Equations for the porous material and the set of equations for the fracture, Eqs. 7.11-7.13 and 7.16-7.17, are solved in an iterative manner until both have achieved a converged solution at $t + \Delta t$. An iteration of the Newton-Raphson solver for the poroelastic material is performed first, after which the fluid flow inside the fracture is updated using the newly obtained fracture opening heights and pressures. At this point, the error of the poroelastic Newton-Raphson solver is checked (the fracture is exactly resolved since its system of equations is linear) and if the convergence criteria are not reached, another iteration of first solving the poroelastic domain and then the fracture fluid velocity is performed.

To aid in the convergence of this iterative scheme, an additional term is added to the tangential stiffness matrix of the poroelastic material, estimating the influence of changes in interstitial fluid pressure and opening height on the discontinuity pressure. This term is based on Eq. 7.5, neglecting the changes n vertical fluid velocity to obtain:

$$\partial p_d^{t+\Delta t} = -\frac{1}{2k_i \Delta t} \partial h^{t+\Delta t} + \frac{1}{2} \partial p_p^+ + \frac{1}{2} \partial p_p^- \tag{7.20}$$

This allows the stiffness terms related to the discontinuity to be estimated as:

$$\frac{\partial \boldsymbol{f}_d}{\partial \boldsymbol{p}} = -\frac{\gamma}{2} \int_{\Gamma_s^\pm} \boldsymbol{N}_d^T \boldsymbol{n}_d \boldsymbol{N}_f^\pm \, \mathrm{d}\Gamma_d^\pm \tag{7.21}$$

$$\frac{\partial \boldsymbol{f}_d}{\partial \boldsymbol{u}} = \int_{\Gamma_d^\pm} \boldsymbol{N}_d^T \frac{\partial \boldsymbol{\tau}_s}{\partial \boldsymbol{u}} \boldsymbol{N}_d \, \mathrm{d}\Gamma_d^\pm + \frac{\gamma}{2k_i \Delta t} \int_{\Gamma_d^\pm} \boldsymbol{N}_s^T \boldsymbol{n}_d^T \boldsymbol{n}_d \boldsymbol{N}_d \, \mathrm{d}\Gamma_d^\pm \tag{7.22}$$

$$\frac{\partial \boldsymbol{q}_d}{\partial \boldsymbol{p}} = \int_{\Gamma_d^\pm} -\Delta t k_i \boldsymbol{N}_f^T \boldsymbol{N}_f \, \mathrm{d}\Gamma_d^\pm - \frac{\Delta t k_i \gamma}{2} \int_{\Gamma_d^\pm} \boldsymbol{N}_f^T \boldsymbol{N}_f^\pm \, \mathrm{d}\Gamma_d^\pm \tag{7.23}$$

$$\frac{\partial \boldsymbol{q}_d}{\partial \boldsymbol{u}} = -\frac{\gamma}{2} \int_{\Gamma_d^\pm} \boldsymbol{N}_f^T \boldsymbol{n}_d \boldsymbol{N}_d \, \mathrm{d}\Gamma_d^\pm \tag{7.24}$$

using a stabilising factor $0 < \gamma < 1$. This factor is applied to the tangential terms relating to the interior of the fracture, with $\gamma = 0$ corresponding to none of these terms being included and $\gamma = 1$ fully including these terms. It was found that $\gamma = 1/2$ provided a reasonable convergence speed, while maintaining a non-oscillatory and stable convergence.

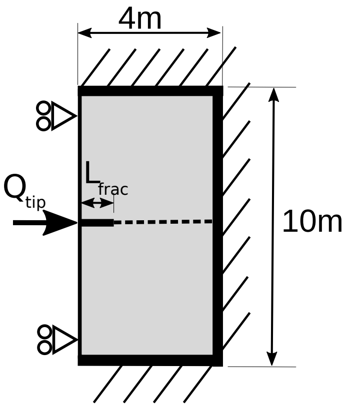

Figure 7.2: Overview of used geometry and boundary conditions

7.2. COMPARISON SUB-GRID AND STOKES FLOW MODELS

To compare the direct simulation of Stokes flow with a discontinuous pressure model, a typical case consisting of a 10 × 4 m domain is simulated (Figure 7.2). A horizontal fracture is present at the centre-left of this domain, with this fracture having a length $L_{frac} = 2$ m in Sections 7.2.1 and 7.2.3 (and not being allowed to propagate), and an initial length $L_{frac} = 0.5$ m in Section 7.2.2. A fluid inflow $Q_{in} = 10^{-6}$ m^2/s is imposed on the left fracture inlet, the porous material is characterised by a Young's modulus $E = 20$ GPa, Poisson ratio $\nu = 0.2$, porosity $n_f = 0.2$, intrinsic permeability $k = 10^{-16}$ m^2, Biot coefficient $\alpha = 1.0$, and bulk modulus $K_s = 10$ GPa. The fluid uses viscosity $\mu = 10^{-3}$ Pa s and bulk modulus $K_f = 1$ GPa, and the discontinuity uses $k_i = 10^{-10}$ m/Pa s. For the propagating fracture case from Section 7.2.2 an exponential traction-separation law is used, using $f_t = 1$ MPa and fracture energy $\mathcal{G}_c = 1$ kN/m. The temporal discretisation uses time steps of $\Delta t = 1$ s and the spatial discretisation uses 10 horizontal elements near the top and bottom boundary, with additional refinement layers inserted near the interface as shown in Figure 7.3

7.2.1. NON-PROPAGATING FRACTURES

The fluid pressures resulting from the non-propagating fracture case are shown in Figure 7.3. Both models show similar interstitial fluid pressures inside the porous material, and the Stokes flow model obtains a near to constant pressure over the fracture height. While the discontinuous pressure model obtained a quadratic convergence rate due to the used consistent stiffness matrix, the Stokes flow only obtained the linear rate shown in Figure 7.4. This reduced convergence is caused by the iterative coupling between the Stokes flow and the poroelastic material, with only an approximation of the effects of the fracture included in the poroelastic part, and no interaction with the poroelastic material included in the Stokes flow part. As a result, the discontinuous pressure model requires less iterations to obtain a converged solution, and solely requires a single system of equations to be solved, making this method much faster compared to direct simulation of the Stokes flow within the fracture.

The effect of inserting additional refinement layers on the fluid pressure in the centre of the fracture is shown in Figure 7.5. While both methods obtain the same pressure when 5 mesh refinement layers are used, the discontinuous pressure model obtains slightly more accurate results for coarser meshes. Similar results are observed for the fracture outflow in Figure 7.6. In addtion to the discontinuous pressure model providing slightly more accurate results for coarser meshes, the use of a lumped integration scheme also suppresses fracture outflow oscillations. In contrast, no lumped integration scheme was possible for the

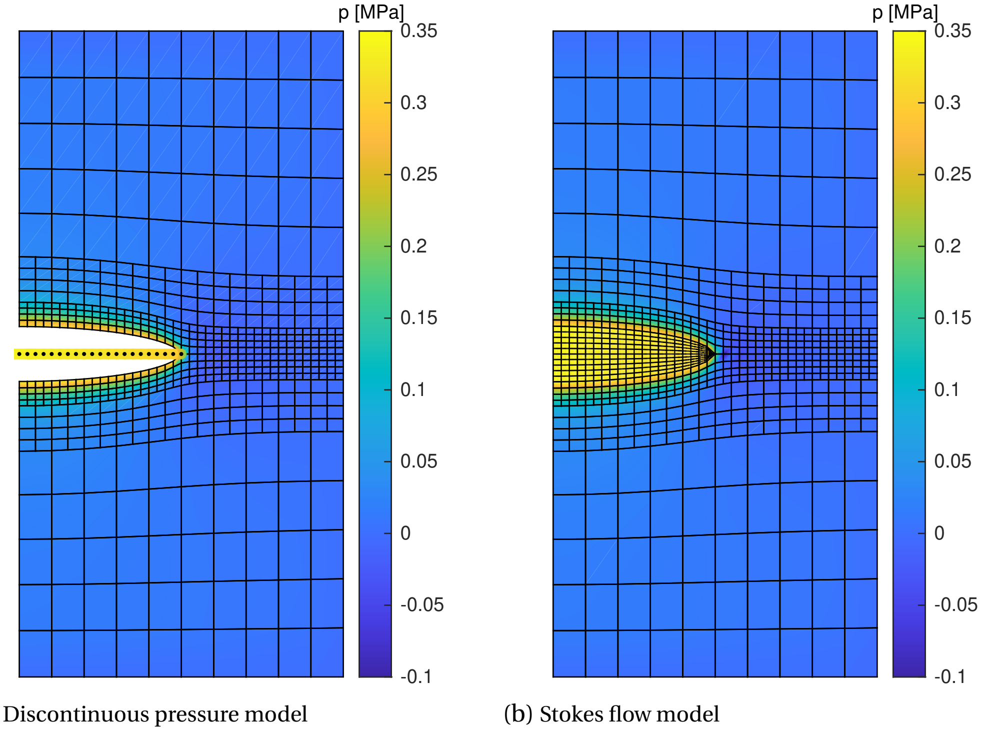

(a) Discontinuous pressure model

(b) Stokes flow model

Figure 7.3: Fluid pressure at $t = 200$ s for the non-propagating fracture case from Section 7.2.1. Vertical displacements magnified by 10^4

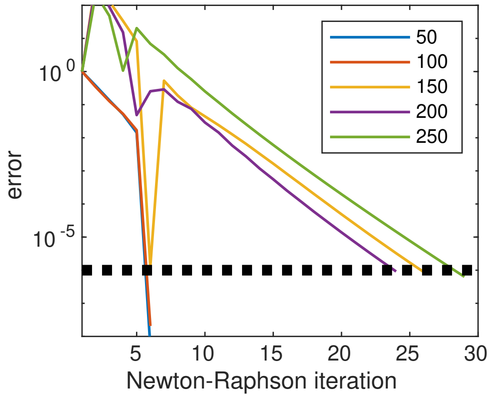

Figure 7.4: Energy based residual for the Stokes model at the selected time steps shown in the legend.

Stokes flow model due to the interface permeability matrix being non-square, resulting in the oscillations seen for the three refinement layer mesh.

Finally, a comparison between the velocity profile inside the fracture resulting from the Stokes flow and from post-processing the discontinuous pressure model are shown in Figure 7.7. These velocity profiles correspond to each other, and it can thus be included that both models give the same results for the overall influence of the fracture as well as for the fluid behaviour inside the fracture.

7.2.2. PROPAGATING FRACTURES

Results for the propagating fracture case are shown in Figure 7.8. Similar to the results from the previous section, both the Stokes flow and discontinuous pressure model obtain the same fracture propagation behaviour for finer meshes, while the discontinuous pressure

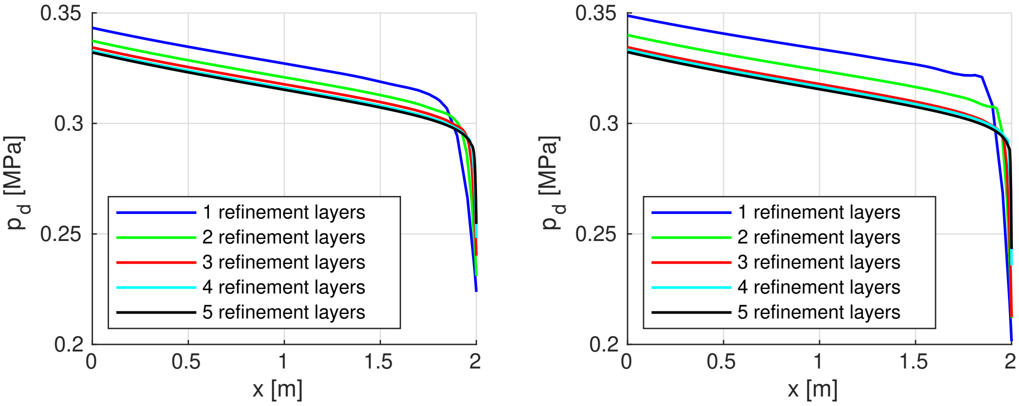

(a) Discontinuous pressure model (b) Stokes flow model

Figure 7.5: Pressure in the centre of the discontinuity at $t = 200$ s.

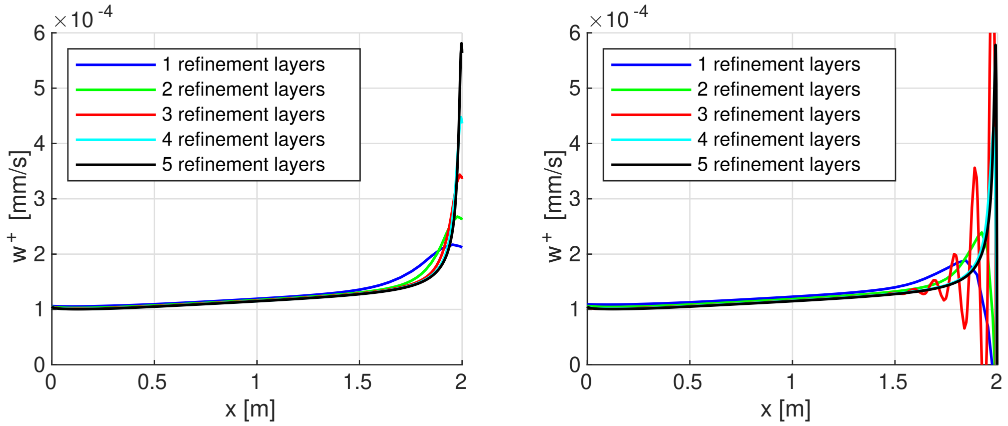

(a) Discontinuous pressure model (b) Stokes flow model

Figure 7.6: Fracture outflow at $t = 200$ s.

model provides slightly more accurate results for coarser meshes. However, the accuracy for both these methods at coarser meshes is dominated by the element-wise fracture propagation.

The velocity inside the propagating fracture is shown in Figure 7.9 for the Stokes flow simulations. Due to the traction separation law used for the recently fractured elements, a sudden change in fracture apperture occurs at $x = 0.5$ m. As a result, peaks in the vertical velocity are observed. These peaks, however, are orders of magnitude lower than the horizontal velocity, indicating that the assumptions made for the discontinuous pressure model are justified.

7.2.3. ENHANCED OPENING HEIGHTS

The final case presented redefines the fracture opening height as $h = h_0(2 - x_d) + \boldsymbol{n}_d^T \boldsymbol{N}_s [\![\boldsymbol{u}]\!]$, introducing an offset to the opening height h_0. This offset allows fractures with an increased opening height to be simulated, without this additional opening height needing to be represented by the solid displacement around the interface elements. This allows fractures which are outside the assumptions of the discontinuous pressure model to be simulated. It should be noted, however, that these opening heights used in this section are not realistic, and merely serve to investigate the limits of the presented models.

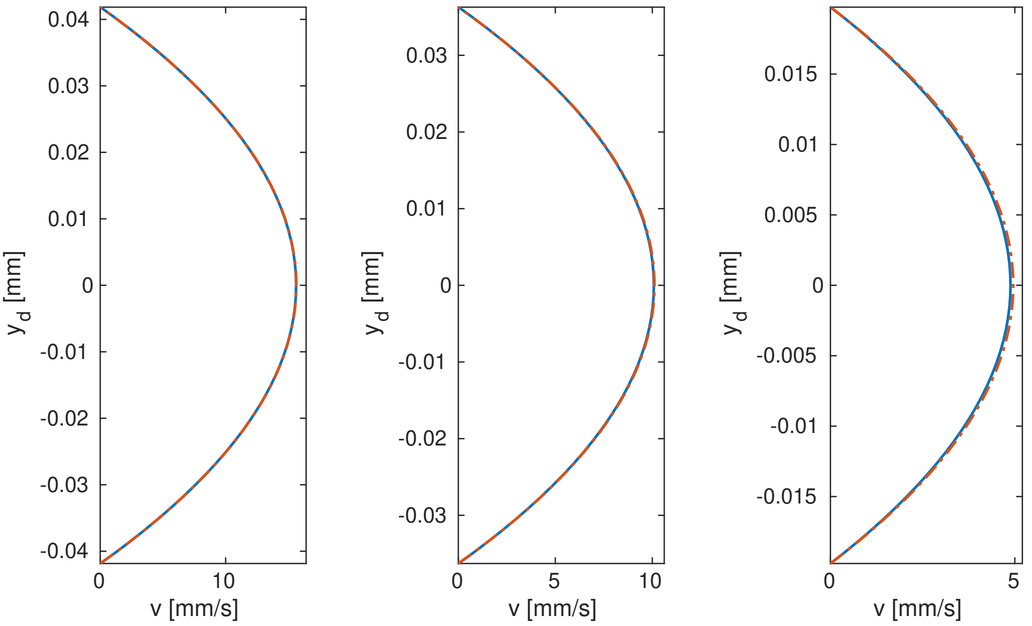

(a) $x = 0.25$ m (b) $x = 1.0$ m (c) $x = 1.75$ m

Figure 7.7: Fluid velocity profiles inside the fracture at $t = 200$ s. Red dashed line corresponds to the discontinuous pressure model, and the blue solid line to the Stokes flow model.

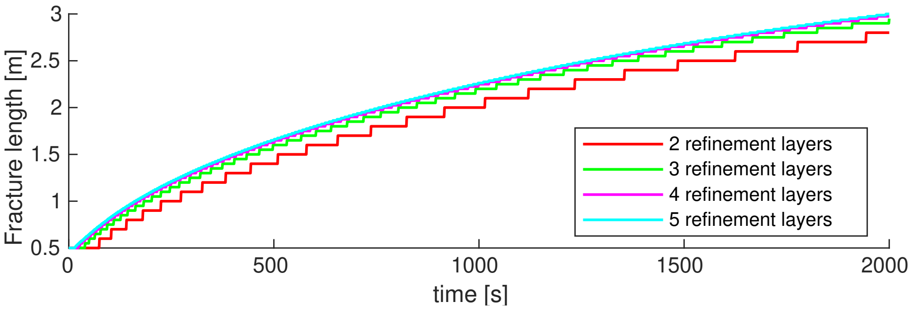

(a) Discontinuous pressure model

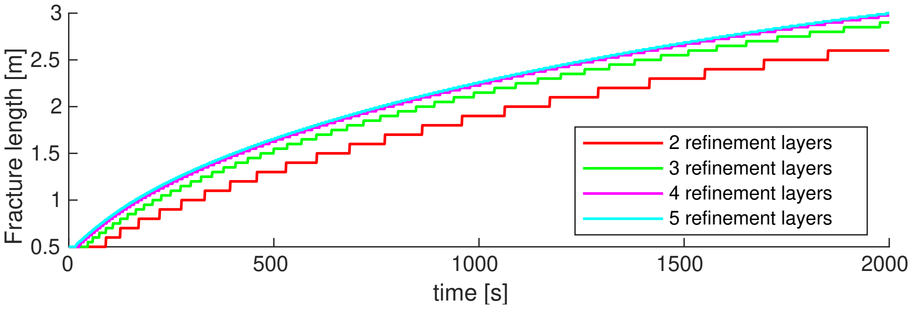

(b) Stokes flow model

Figure 7.8: Fracture propagation length

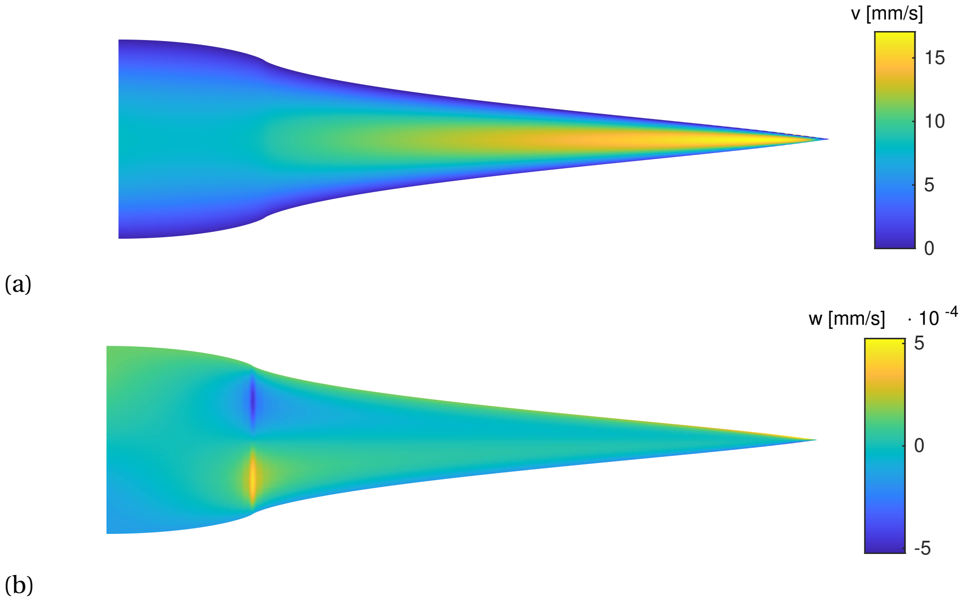

Figure 7.9: Fluid velocity inside the propagating fracture using the Stokes flow model with the five refinement layer mesh at $t = 20$ min.

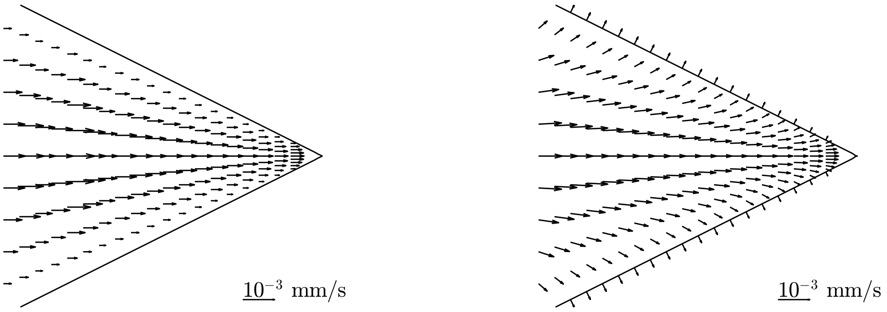

(a) Discontinuous pressure model

(b) Stokes flow model

Figure 7.10: Direction and magnitude of the fluid flow within the fracture at $t = 10$ s using $h_0 = 2$ m.

The velocity magnitude and directions are shown in Figure 7.10 using $h_0 = 2$ m. While the discontinuous pressure model is only able to represent a unidirectional flow, the Stokes flow model presents a two-dimensional flow in which both velocity components are comparable. Furthermore, the no-slip boundary condition for the Stokes flow allows for large deformations and thus allows for a non-zero horizontal velocity component at the fracture walls. This is also observed in Figure 7.11, where a clear difference in velocity profile is seen for the $h_0 = 2$ m case. In contrast, the simulations with smaller fracture apertures do not display any difference between the two models.

An effect of the increased opening height is the reduced resistance to fluid flow inside the fracture, resulting in a constant pressure within the complete fracture. Due to this constant pressure the fluid flow into the poroelastic material is solely governed by the interface permeability term, while the transport inside the fracture plays a negligible role. Therefore, even though a clear two-dimensional flow profile is obtained for the Stokes flow simulations, the resulting interstitial fluid pressure is the same between the two models. It can thus be concluded that even if the "small opening height compared to fracture length" assumption is not satisfied, the discontinuous pressure model is still able to accurately include the overall interactions between the pressurised fracture and the surrounding porous material.

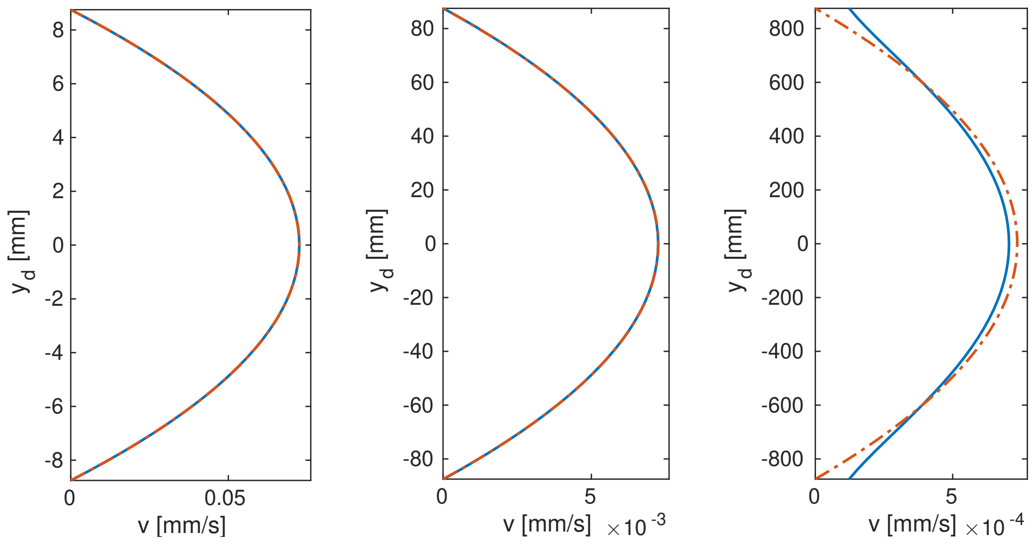

(a) $h_0 = 2$ cm (b) $h_0 = 20$ cm (c) $h_0 = 2$ m

Figure 7.11: Fluid velocity profiles inside the fracture at $t = 10$ s and $x = 0.25$ m. Red dashed line corresponds to the discontinuous pressure model, and the blue solid line to the Stokes flow model.

7.3. CONCLUSION

This chapter presented a method to directly simulate Stokes flow within a pressurised and propagating fracture. This model allows both velocity components to be simulated, thereby capturing a more detailed fluid behaviour inside the fracture compared to a discontinuous pressure model. To aid with the mesh generation for the interior of the fracture, the tensor product structure of NURBS was exploited, and the fracture mesh was generated in a parametric space to allow it to automatically adapt to changes in fracture opening height.

Comparing the direct simulation of Stokes flow to a discontinuous pressure model has demonstrated the accuracy and efficiency of the discontinuous pressure model. Both models obtained similar results for static and propagating fractures, with the discontinuous pressure model being slightly more accurate for coarser meshes. Furthermore, the discontinuous pressure model obtained a quadratic convergence rate compared to the linear rate for the Stokes flow, and only requires a single system of equations to be solved, making it significantly more efficient.

Finally, simulations outside of the assumptions of the discontinuous pressure model have shown the still limited validity of using this model. While the results for the fluid velocity inside the fracture become inaccurate once the fracture aperture is comparable to its length, the influence of the fracture on the surrounding porous material is still accurately represented.

8

SHEAR FRACTURES: INERTIA AND PLASTICITY

The presence of an interstitial fluid in porous media can have a strong effect on the stresses. This, in turn, influences the propagation of fractures and the occurrence of plastic deformations. Seismic activity has been related to changes in interstitial pressure [52, 81, 150, 243], and experiments have shown that increases in fluid pressure can trigger earthquakes [205] and cause instabilities in underground formations [167].

Simulation of shear-based fracture propagation is often combined with both small scale plasticity using a traction-separation law and large scale off-fault plasticity using plastic flow rules. When fluids are included, this is mainly achieved by assuming the porous material to behave as either a "drained" or "undrained" material [93, 94, 220, 231], simplifying the governing equations to solely depend on the solid displacement. These assumptions neglect the fluid diffusion, whereas including this has been shown to influence the plastic strains [47] and fracture propagation velocity [103].

Another often made simplification is to neglect the fluid acceleration term in Darcy's law [38], which is argued to not influence results in the low frequency response limit [247, 248]. Simulations which used the fluid velocity as a separate degree of freedom have shown that including the fluid acceleration can alter the obtained solutions [156], and including these fluid acceleration terms results in additional damping for pressure and shear stress waves [20, 176, 177]. This additional damping can alter the crack propagation [134], and for highly permeable materials result in large differences compared to when the fluid acceleration terms are neglected [245].

Simulations using a non-associated plasticity model, as is commonly used for geomaterials, often suffer a severe mesh dependence and when implicit time discretisation schemes are used, have issues converging. While the issues with the convergence have been argued to originate from the non-symmetric stiffness matrix [80, 218], they and the mesh-dependence have been linked to the loss of ellipticity of the system when ideal plasticity is simulated [194, 195]. Several methods have been proposed to resolve this loss of ellipticity. One of these methods is to regularise the plasticity model by adding viscosity to the formulation[72, 214, 235], introducing a timescale to the plastic deformations. Other than regularising the system, this timescale and the resulting lengthscale have also been shown to prevent spurious oscillations in implicit schemes [51] and increase the maximum allowed time step in explicit schemes [60].

A different method to regularise a problem containing non-associated plasticity is to use a Cosserat continuum [62]. By including the micro-rotation as a degree of freedom, a length scale is introduced, restoring the well-posedness [193, 194, 195] and removing mesh-dependence issues relating to the discretisation [35, 36, 37]. Since they prevent issues relating to mesh dependency, Cosserat continua are often used when simulating shear bands [74, 109, 112] and analysis failure and collapse of geomaterials [10, 138, 229]. The improvements in well-posedness have also been linked to an improved convergence [161].

This chapter will focus on combining fluid flows inside porous materials with shear-based fracture propagation and non-associated plasticity, resulting in a realistic representation of porous geo-materials. The governing equations will be derived neglecting as few terms as possible, while still adhering to the standard displacement-pressure formulation. The effect of including the often neglected fluid acceleration terms will be analysed through simulations with and without these terms. The effects of including fluid flows inside the porous material will be investigated, comparing the results to the drained and undrained limits. Finally, an in-depth look at the interaction between the interstitial fluid pressure and the fracture propagation will be performed, aimed at investigating stepwise fracture propagation.

The contents of this chapter is strongly based on results previously published in [5, 8]. Furthermore, the code used to represent the non-associated plasticity is based on the finite element code from [195], which has been adapted to allow for isogeometric elements and the possible inclusion of visco-plasticity.

8.1. GOVERNING EQUATIONS

8.1.1. COSSERAT CONTINUUM

Next to the linear displacements of the solid, u_x and u_y, a Cosserat continuum introduces a Cosserat microrotation ω_z [62], which are combined in the displacement vector for the solid $\boldsymbol{u} = \left[u_x\ u_y\ \omega_z\right]^T$ [36]. Introducing the Cosserat length scale ℓ_c, the relation between these displacements and the total strain, assuming plane-strain conditions, is given through:

$$\boldsymbol{\varepsilon} = \boldsymbol{L}\boldsymbol{u} = \begin{bmatrix} \frac{\partial}{\partial x} & 0 & 0 \\ 0 & \frac{\partial}{\partial y} & 0 \\ 0 & 0 & 0 \\ 0 & \frac{\partial}{\partial x} & -1 \\ \frac{\partial}{\partial y} & 0 & 1 \\ 0 & 0 & \ell_c \frac{\partial}{\partial x} \\ 0 & 0 & \ell_c \frac{\partial}{\partial y} \end{bmatrix} \begin{bmatrix} u_x \\ u_y \\ \omega_z \end{bmatrix} \tag{8.1}$$

with the strain vector given by $\boldsymbol{\varepsilon} = \left[\varepsilon_{xx}\quad \varepsilon_{yy}\quad \varepsilon_{zz}\quad \varepsilon_{xy}\quad \varepsilon_{yx}\quad \ell_c\kappa_{xz}\quad \ell_c\kappa_{yz}\right]^T$. In contrast to standard continua, the stresses and strains are non-symmetric in a Cosserat continuum, $\sigma_{xy} \neq \sigma_{yx}$, and are therefore separately included in the stress and strain vectors: $\boldsymbol{\sigma}_s = [\sigma_{xx}\quad \sigma_{yy}\quad \sigma_{zz}\quad \sigma_{xy}\quad \sigma_{yx}\quad m_{xz}/\ell_c\quad m_{yz}/\ell_c]^T$ with σ_{xx} etc. the Cauchy stress tensor components, and m_{xz} and m_{yz} the couple-stresses. The stresses are assumed to be linearly related to the elastic strain through:

$$\boldsymbol{\sigma}_s = \boldsymbol{D}_{el}\boldsymbol{\varepsilon}_{el} \tag{8.2}$$

with the linear-elastic stiffness matrix for a Cosserat continuum under plane-strain conditions given by [37]:

$$\boldsymbol{D}_{el} = \begin{bmatrix} a(1-\nu) & a\nu & a\nu & 0 & 0 & 0 & 0 \\ a\nu & a(1-\nu) & a\nu & 0 & 0 & 0 & 0 \\ a\nu & a\nu & a(1-\nu) & 0 & 0 & 0 & 0 \\ 0 & 0 & 0 & G+G_c & G-G_c & 0 & 0 \\ 0 & 0 & 0 & G-G_c & G+G_c & 0 & 0 \\ 0 & 0 & 0 & 0 & 0 & 2G & 0 \\ 0 & 0 & 0 & 0 & 0 & 0 & 2G \end{bmatrix} \tag{8.3}$$

using $a = E/((1+\nu)(1-2\nu))$ and $G = E/(2+2\nu)$.

The momentum balance for the fluid and solid using a Cosserat continuum is given by:

$$\boldsymbol{L}^T\left(\boldsymbol{\sigma}_s - \alpha p\boldsymbol{m}\right) - \boldsymbol{\rho}_s\left(1-n_f\right)\ddot{\boldsymbol{u}} - \boldsymbol{\rho}_f n_f \boldsymbol{I}_c^T \ddot{\boldsymbol{u}}_f - \boldsymbol{\rho}_f \boldsymbol{I}_c^T\left(\boldsymbol{q}\cdot\nabla\right)\boldsymbol{q} = \boldsymbol{0} \tag{8.4}$$

with the matrix $\boldsymbol{I}_c^T$ used to convert the linear displacements from the fluid, $\boldsymbol{u}_f$, to the combined linear displacement and Cosserat rotation form of the solid displacement. This matrix, and the density matrices for the fluid and solid, are given by:

$$\boldsymbol{\rho}_s = \begin{bmatrix} \rho_s & 0 & 0 \\ 0 & \rho_s & 0 \\ 0 & 0 & \Theta \end{bmatrix} \qquad \boldsymbol{I}_c = \begin{bmatrix} 1 & 0 & 0 \\ 0 & 1 & 0 \end{bmatrix}$$
$$\boldsymbol{\rho}_f = \begin{bmatrix} \rho_f & 0 & 0 \\ 0 & \rho_f & 0 \\ 0 & 0 & 0 \end{bmatrix} \qquad \boldsymbol{m}^T = \begin{bmatrix} 1 & 1 & 1 & 0 & 0 & 0 & 0 \end{bmatrix} \tag{8.5}$$

using the rotational inertia $\Theta = 2\rho_s \ell_c^2/(1+\nu)$ [35].

The mass balance, Eq. 2.8, is written in a form compatible with a Cosserat continuum as:

$$\frac{1}{M}\dot{p} - \alpha\nabla\cdot(\boldsymbol{I}_c\dot{\boldsymbol{u}}) - \nabla\cdot\boldsymbol{q} = 0 \tag{8.6}$$

and Darcy's law combined with the momentum balance of a Newtonian fluid as:

$$\boldsymbol{q} = n_f\left(\dot{\boldsymbol{u}}_f - \boldsymbol{I}_c\dot{\boldsymbol{u}}\right) = -\frac{k}{\mu}\left(\nabla p + \rho_f\ddot{\boldsymbol{u}}_f + \frac{\rho_f}{n_f}\left(\boldsymbol{q}\cdot\nabla\right)\boldsymbol{q}\right) \tag{8.7}$$

8.1.2. ACCELERATION AND INERTIA TERMS

The convective momentum transport terms in Eq. 8.4 and Eq. 8.7, $(\boldsymbol{q}\cdot\nabla)\boldsymbol{q}$, require gradients of the fluid flux. These gradients can only be obtained if the fluid flux uses its own interpolation functions, requiring the fluid flux to be used as an additional degree of freedom. However, this convective momentum transport term is almost always negligibly small compared to the pressure gradient driven fluid flow or the acceleration driven fluid flow [247], and is therefore neglected here.

The fluid acceleration term in the momentum balance, Eq. 8.4, is replaced by the Darcy fluid flux by its definition from Eq. 8.7, resulting in:

$$\boldsymbol{L}^T\left(\boldsymbol{\sigma}_s - \alpha p\boldsymbol{m}\right) - \overline{\boldsymbol{\rho}}\ddot{\boldsymbol{u}} - \boldsymbol{\rho}_f\boldsymbol{I}_c^T\dot{\boldsymbol{q}} = \boldsymbol{0} \tag{8.8}$$

with the volume-averaged density $\overline{\boldsymbol{\rho}} = (1-n_f)\boldsymbol{\rho}_s + n_f\boldsymbol{\rho}_f$, using the density matrices from Eq. 8.5. Similarly, substituting the definition of the fluid flux in Eq. 8.7 results in:

$$\boldsymbol{q} = -\frac{k}{\mu}\left(\nabla p + \rho_f\left(\boldsymbol{I}_c\ddot{\boldsymbol{u}} + \frac{1}{n_f}\dot{\boldsymbol{q}}\right)\right) \tag{8.9}$$

The time derivative of the fluid flux is discretised at time $t+\Delta t$ using a θ-scheme as:

$$\dot{\boldsymbol{q}}^{t+\Delta t} = \frac{1}{\theta\Delta t}\left(\boldsymbol{q}^{t+\Delta t} - \boldsymbol{q}^t\right) + \left(1-\frac{1}{\theta}\right)\dot{\boldsymbol{q}}^t \tag{8.10}$$

using the fluid flux $\boldsymbol{q}^t$ and change in fluid flux $\dot{\boldsymbol{q}}^t$ at the old time as history variables. Using this time discretisation, Equation 8.9 is partially discretised at time $t+\Delta t$ as:

$$\boldsymbol{q}^{t+\Delta t} = -\frac{k}{\mu}\left(\nabla p^{t+\Delta t} + \rho_f\left(\boldsymbol{I}_c\ddot{\boldsymbol{u}}^{t+\Delta t} + \frac{1}{n_f}\left(\frac{1}{\theta\Delta t}\left(\boldsymbol{q}^{t+\Delta t} - \boldsymbol{q}^t\right) + \left(1-\frac{1}{\theta}\right)\dot{\boldsymbol{q}}^t\right)\right)\right) \tag{8.11}$$

$$\boldsymbol{q}^{t+\Delta t} = \left(1 + \frac{\rho_f k}{n_f\mu\theta\Delta t}\right)^{-1}\left(-\frac{k}{\mu}\nabla p^{t+\Delta t} - \frac{k\rho_f}{\mu}\boldsymbol{I}_c\ddot{\boldsymbol{u}}^{t+\Delta t} - \frac{k\rho_f}{\mu n_f}\left((1-\frac{1}{\theta})\dot{\boldsymbol{q}}^t - \frac{1}{\theta\Delta t}\boldsymbol{q}^t\right)\right) \tag{8.12}$$

with the fluid flux $\boldsymbol{q}^{t+\Delta t}$ only depending on the displacement and interstitial fluid pressure at the new time step, and history variables related to the old time.

Partial time-discretising Eq. 8.6 at time $t+\Delta t$, and substituting this expression for the fluid flux results in:

$$\begin{aligned}&\frac{1}{M}\dot{p}^{t+\Delta t} + \alpha\nabla\cdot\left(\boldsymbol{I}_c\dot{\boldsymbol{u}}^{t+\Delta t}\right)\\ &\quad + \left(1+\frac{\rho_f k}{n_f\mu\theta\Delta t}\right)^{-1}\nabla\cdot\left(-\frac{k}{\mu}\nabla p^{t+\Delta t} - \frac{k\rho_f}{\mu}\boldsymbol{I}_c\ddot{\boldsymbol{u}}^{t+\Delta t} - \frac{k\rho_f}{\mu n_f}\left((1-\frac{1}{\theta})\dot{\boldsymbol{q}}^t - \frac{1}{\theta\Delta t}\boldsymbol{q}^t\right)\right) = 0\end{aligned} \tag{8.13}$$

Similar for the momentum balance, Eq. 8.8, discretising the fluid flux derivative $\dot{\boldsymbol{q}}$ using Eq. 8.10, and substituting the explicit expression for the fluid flux, Eq. 8.12, gives:

$$\begin{aligned}\boldsymbol{L}^T\left(\boldsymbol{\sigma}_s^{t+\Delta t} - \alpha p^{t+\Delta t}\boldsymbol{m}\right) - \left(\overline{\boldsymbol{\rho}} - An_f\boldsymbol{\rho}_f\right)\ddot{\boldsymbol{u}}_s^{t+\Delta t} + An_f\boldsymbol{I}_c^T\nabla p^{t+\Delta t}&\\ + \boldsymbol{\rho}_f\boldsymbol{I}_c^T(1-A)\left(\frac{1}{\theta\Delta t}\boldsymbol{q}^t - \left(1-\frac{1}{\theta}\right)\dot{\boldsymbol{q}}^t\right) = \boldsymbol{0}&\end{aligned} \tag{8.14}$$

with the constant A defined as:

$$A = \frac{\rho_f\frac{k}{\mu}}{n_f\theta\Delta t + \rho_f\frac{k}{\mu}} \tag{8.15}$$

Equations 8.13 and 8.14 are used to describe the saturated porous material in the standard displacement-pressure formulation, while still including the fluid and solid acceleration driven fluid flow and using separate inertia terms for the fluid and solid.

DRAINED AND UNDRAINED ASSUMPTIONS

The above equations are commonly simplified by assuming the porous material to either behave as a "drained" or "undrained" material. The two assumptions are assumed to represent the limiting cases for a highly permeable and impermeable material.

Under the undrained assumption, the deformations of the porous material are assumed to occur fast compared to any fluid flow, and the main interest in these solid deformations. This allows the permeability to be assumed zero, removing all fluid flow. In contrast, the drained assumption is used when the porous material has a high permeability, or a fluid with a low viscosity is simulated. Under this assumption, the interstitial pressure in the complete domain is set equal to a reference pressure, and kept constant. It is furthermore assumed that the inertia of the fluid is negligible, and under the drained assumption the momentum balance only includes a term for the solid inertia.

In the above equations, when the permeability approaches zero, the constant A and all fluid flux terms also approach zero. This removes the separate inertia terms for the solid and fluid, and results in Eq. 8.14 using a single inertia term with the volume averaged density. This low permeability limit corresponds to the assumptions made by the undrained assumption.

In contrast, when a high permeability is used, the constant A approaches one. This removes the contribution of the fluid density to the volume averaged mass matrix, instead using a separate inertia term for the fluid solely depending on the pressure gradient. Interestingly, it follows from the momentum balance that in this high permeability limit the fluid inertia term solely depends on the current pressure gradient and not on the history variables that were used to perform the time discretisation of the fluid flux time derivative. Looking at the mass balance from Eq. 8.13, using a high permeability and neglecting any acceleration related terms would result in a fluid flux capable of removing any pressure gradients. However, assuming a very high permeability ($\frac{\rho_f k}{n_f\mu\theta\Delta t} >> 1$) and retaining the acceleration driven fluid flow terms allows this equation to be rewritten to:

$$\frac{1}{M}\dot{p}^{t+\Delta t}+\alpha\boldsymbol{\nabla}\cdot\left(\boldsymbol{I}_c\ddot{\boldsymbol{u}}^{t+\Delta t}\right)+\boldsymbol{\nabla}\cdot\left(-\frac{n_f\theta\Delta t}{\rho_f}\boldsymbol{\nabla}p^{t+\Delta t}-n_f\theta\Delta t\boldsymbol{I}_c\ddot{\boldsymbol{u}}^{t+\Delta t}-\theta\Delta t\left(\left(1-\frac{1}{\theta}\right)\dot{\boldsymbol{q}}^t-\frac{1}{\theta\Delta t}\boldsymbol{q}^t\right)\right)=0$$

This equation shows that while the fluid flux scales with the permeability when neglecting inertia related terms, this is no longer the case when including acceleration driven fluid flows. For these cases, the fluid flux is still limited by the inertia of the fluid. Interestingly, this equation and the momentum balance using $A=1$ also show that for sufficiently high permeabilities the mass and momentum balances no longer depend on the permeability of the porous material. This indicates that there is an upper limit for the pressure changes and fluid fluxes, even when acceleration terms are included. This upper limit, however, does not correspond to the drained limit, indicating that large differences might occur between the drained and high permeability limits.

8.1.3. PLASTICITY

The plastic deformations are modeled using a non-associated Drucker-Prager model. This model is defined by the yield function:

$$f=\sqrt{3J_2}+\alpha p_s-k \tag{8.16}$$

and the plastic potential function:

$$g=\sqrt{3J_2}+\beta p_s \tag{8.17}$$

using the solid pressure p_s (positive for tension) and the second invariant of the deviatoric stresses J_2. The solid pressure for a Cosserat continuum is obtained through [37]:

$$p_s=\begin{bmatrix}\frac{1}{3} & \frac{1}{3} & \frac{1}{3} & 0 & 0 & 0 & 0\end{bmatrix}\boldsymbol{\sigma}_s \tag{8.18}$$

and the second invariant of the deviatoric stresses is given by [37]:

$$J_2=\frac{1}{2}\boldsymbol{\sigma}^T\boldsymbol{P}\boldsymbol{\sigma}=\frac{1}{2}\begin{bmatrix}\sigma_{xx}\\ \sigma_{yy}\\ \sigma_{zz}\\ \sigma_{xy}\\ \sigma_{yx}\\ m_{xz}/\ell_c\\ m_{yz}/\ell_c\end{bmatrix}^T\begin{bmatrix}2/3 & -1/3 & -1/3 & 0 & 0 & 0 & 0\\ -1/3 & 2/3 & -1/3 & 0 & 0 & 0 & 0\\ -1/3 & -1/3 & 2/3 & 0 & 0 & 0 & 0\\ 0 & 0 & 0 & 1/2 & 1/2 & 0 & 0\\ 0 & 0 & 0 & 1/2 & 1/2 & 0 & 0\\ 0 & 0 & 0 & 0 & 0 & 1 & 0\\ 0 & 0 & 0 & 0 & 0 & 0 & 1\end{bmatrix}\begin{bmatrix}\sigma_{xx}\\ \sigma_{yy}\\ \sigma_{zz}\\ \sigma_{xy}\\ \sigma_{yx}\\ m_{xz}/\ell_c\\ m_{yz}/\ell_c\end{bmatrix} \tag{8.19}$$

The constant used in Eq. 8.16 and 8.17 are related to the cohesion c, the dilatency angle ψ and the angle of internal friction ϕ by:

$$\alpha=\frac{6\sin\phi}{3-\sin\phi}\qquad\beta=\frac{6\sin\psi}{3-\sin\psi}\qquad k=c\frac{6\cos\phi}{3-\sin\phi}$$

The stresses are bounded by the yield function through $f\leq 0$, and the plastic strains are obtained through:

$$\hat{\boldsymbol{\epsilon}}_p=\hat{\lambda}\boldsymbol{m} \tag{8.20}$$

with the $\hat{\square}$ symbol indicating a path-dependent derivative. The direction of the plastic flow is given by:

$$\boldsymbol{m}=\frac{\boldsymbol{m}^*}{||\boldsymbol{m}^*||}\qquad \boldsymbol{m}^*=\begin{cases}\frac{\partial g}{\partial\sigma} & \text{if } p_s\leq k\\ \left(\boldsymbol{D}^e\right)^{-1}\left(\boldsymbol{\sigma}_{trial}-\boldsymbol{\sigma}_{apex}\right) & \text{if } p_s>k\end{cases} \tag{8.21}$$

using the stresses at the apex of the Drucker-Prager plasticity cone $\boldsymbol{\sigma}_{apex}$.

In a discretised form, and at integration point level, the stresses are first predicted assuming only elastic deformations to occur during the current time step:

$$\boldsymbol{\sigma}_{trial}^{t+\Delta t} = \boldsymbol{D}_{el}\left(\boldsymbol{B}\boldsymbol{u}^{t+\Delta t} - \boldsymbol{\epsilon}_{p}^{t+\Delta t}\right) \tag{8.22}$$

using the total plastic strain $\boldsymbol{\epsilon}_p^t$ that occurred up to and including the previous time step. These trial stresses are substituted into the yield function from Eq. 8.16, and if the yield function exceeds the criterion $f \leq 0$ plastic deformations occur at the integration point. In this case, the two criteria that must be fulfilled are:

$$\mathbf{0} = \boldsymbol{\sigma}_s^{t+\Delta t} - \left(\boldsymbol{\sigma}_{trial}^{t+\Delta t} - \widehat{\Delta\lambda}\boldsymbol{D}_{el}\boldsymbol{m}\right) \tag{8.23a}$$

$$0 = f(\boldsymbol{\sigma}_s^{t+\Delta t}) \tag{8.23b}$$

These equations are solved iteratively through a Newton-Raphson algorithm [40] :

$$\begin{bmatrix} \boldsymbol{\sigma}_s^{t+\Delta t} \\ \widehat{\Delta\lambda} \end{bmatrix}_{j+1} = \begin{bmatrix} \boldsymbol{\sigma}_s^{t+\Delta t} \\ \widehat{\Delta\lambda} \end{bmatrix}_{j} - \boldsymbol{C}_{eff}^{-1} \begin{bmatrix} \boldsymbol{\sigma}_s^{t+\Delta t} - \left(\boldsymbol{\sigma}_{trial} - \widehat{\Delta\lambda}\boldsymbol{D}_{el}\boldsymbol{m}\right) \\ f \end{bmatrix}_{j} \tag{8.24}$$

with the effective compliance given by:

$$\boldsymbol{C}_{eff} = \begin{bmatrix} \boldsymbol{I} + \widehat{\Delta\lambda}_j \boldsymbol{D}_{el}\frac{\partial \boldsymbol{m}}{\partial \boldsymbol{\sigma}} & \boldsymbol{D}_{el}\boldsymbol{m} \\ \left(\frac{\partial f}{\partial \boldsymbol{\sigma}}\right)^T & 0 \end{bmatrix} \tag{8.25}$$

Upon reaching converged stresses, the effective compliance is also used to determine the effective tangential stiffness matrix by first inverting the effective compliance, then selecting the upper-left 7×7 sub-matrix and multiplying with $\boldsymbol{D}_{el}\left(\boldsymbol{I} - \widehat{\Delta\lambda}\boldsymbol{D}_{el}\frac{\partial \boldsymbol{m}}{\partial \boldsymbol{\sigma}_{trial}}\right)$. If the solid pressure exceeds the pressure at the apex, this results in an effective stiffness $\boldsymbol{D}_{eff} = \mathbf{0}$, since $\widehat{\Delta\lambda}\boldsymbol{D}_{el}\frac{\partial \boldsymbol{m}}{\partial \boldsymbol{\sigma}_{trial}} = \boldsymbol{I}$ in the absence of any rate-dependent plasticity.

8.1.4. Discontinuity model

The fracture uses the discontinuous pressure model presented in Chapter 5, which, in the case of a closed fracture, reduces to:

$$0 = k_i\left(p^+ + p^- - 2p_d\right) \tag{8.26}$$

with the coupling terms for the flow imposed on the porous material given by Eq. 5.1 and 5.2 as:

$$\boldsymbol{n}_d \cdot \boldsymbol{q}_d^+ = k_i\left(p^+ - p_d\right) \tag{8.27}$$

$$\boldsymbol{n}_d \cdot \boldsymbol{q}_d^- = k_i\left(p^- - p_d\right) \tag{8.28}$$

The tractions at the discontinuity are given in a local coordinate system as:

$$\boldsymbol{\tau}_{\Gamma_d}^{\pm} = \begin{bmatrix} \tau_{ds} \\ \tau_{dn} - p_d \\ \tau_{\omega} \end{bmatrix} \tag{8.29}$$

with the normal and couple tractions used to enforce a continuous Cosserat microrotation and prevent negative fracture opening heights through:

$$\tau_{dn} = k_n [\![u_n]\!] \qquad \tau_{\omega} = \ell^2 k_{\omega} [\![\omega_z]\!] \tag{8.30}$$

using the dummy stiffness k_n and k_ω. The tractions in tangential direction are given through an exponential traction-separation law:

$$\tau_{ds} = f_r \tau_{dn} + (f_p - f_r)\tau_{dn} e^{-2[\![\mathrm{dx}]\!]/D_c} \tag{8.31}$$

using the peak and residual coefficients of friction f_p and f_r, the weakening distance $D_c = 2G_c/(f_p\tau_{dn} - f_r\tau_{dn})$, and the fracture energy G_c. While for shear fractures it is more common to use a linear degradation function [83, 85, 106, 220, 230], this exponential function is used to aid in the convergence of the non-linear solver by using a smooth function. The history parameter $[\![\mathrm{dx}]\!]$ is the maximum tangential displacement jump obtained during the simulation, and is either equal to this maximum if obtained in a previous time step, or the current displacement jump if this jump exceeds the previously obtained maximum.

8.1.5. BOUNDARY CONDITIONS

To prevent reflecting stress waves at the domain boundary, absorbing boundary conditions are used. For these boundary conditions, it is presumed that the Cosserat rotation mainly influences the stresses near the fracture and plastic deformation zones, and does not significantly alter the stresses at the domain boundary. This allows standard absorbing boundary conditions to be used, describing the traction at the boundary by [103, 136, 151, 213] :

$$\boldsymbol{\tau} = \boldsymbol{C}\dot{\boldsymbol{u}} = \overline{\boldsymbol{\rho}} \begin{bmatrix} c_p & 0 & 0 \\ 0 & c_s & 0 \\ 0 & 0 & 0 \end{bmatrix} \dot{\boldsymbol{u}} \tag{8.32}$$

with the damping matrix $\boldsymbol{C}$ using the pressure and shear wave speeds c_p and c_s respectively.

8.2. DISCRETISATION

The time discretisation of the governing equations, Eq. 8.13 and 8.14, is performed using a Newmark scheme for the solid displacement:

$$\dot{\boldsymbol{u}}^{t+\Delta t} = \frac{\gamma}{\beta\Delta t}\left(\boldsymbol{u}^{t+\Delta t} - \boldsymbol{u}^t\right) - \left(\frac{\gamma}{\beta} - 1\right)\dot{\boldsymbol{u}}^t - \left(\frac{\Delta t\gamma}{2\beta} - \Delta t\right)\ddot{\boldsymbol{u}}^t \tag{8.33a}$$

$$\ddot{\boldsymbol{u}}^{t+\Delta t} = \frac{1}{\beta\Delta t^2}\left(\boldsymbol{u}^{t+\Delta t} - \boldsymbol{u}^t\right) - \frac{1}{\beta\Delta t}\dot{\boldsymbol{u}}^t - \left(\frac{1}{2\beta} - 1\right)\ddot{\boldsymbol{u}}^t \tag{8.33b}$$

and, similar to the fluid flux, a θ-scheme for the interstitial fluid pressure:

$$\dot{p}^{t+\Delta t} = \frac{1}{\theta\Delta t}\left(p^{t+\Delta t} - p^t\right) + \left(1 - \frac{1}{\theta}\right)\dot{p}^t \tag{8.34}$$

This discretisation introduces history variables in the control points for the interstitial pressure, velocity, and acceleration at the old time. These history variables are updated once the current time step is completed. The plasticity model introduces a history variable for the plastic strain $\boldsymbol{\epsilon}_p^t$, which in contrast to the time dependent history variables, is dependent on the loading path. To properly include this path dependence, the plastic strain history variable is updated after each time step and during the current time step at the moment the fracture propagates. This allows the plastic strain to capture the high stresses at the fracture tip, and the decrease in stresses once the fracture is propagated.

The last history dependent parameter that requires updating is the mesh itself to allow the fracture to propagate. While several different moments are suggested in literature for this propagation, for instance introducing a zero duration propagation step [45, 46, 146] or considering the fracture propagation to occur at the end of time steps [155, 173, 184, 206], it is chosen here to consider the fracture propagation as part of the time step and implicit integration scheme. Therefore, once a converged solution is reached, the stresses ahead of the fracture are checked and if these stresses exceed the fracture strength, $\sigma_{yx} > f_p \sigma_{yy}$ for a horizontal shear fracture, this fracture is propagated a single element length. This results in a fully implicit scheme, in which the mass and momentum balance are fulfilled at the end of the time step even when the fracture propagates.

Corresponding to the previous chapter, the interstitial and discontinuity fluid pressures are discretised using cubic Bézier extracted T-splines, and the linear displacements using quartic T-splines, fulfilling the inf-sup condition. No requirement is placed on the Cosserat microrotation through the inf-sup condition, since no direct coupling occurs between the fluid pressure and the Cosserat rotation. Therefore, to limit the required amount of degrees of freedom, cubic T-splines are used to discretise the Cosserat rotation. This results in a standard finite element discretisation:

$$\boldsymbol{u} = \sum_{el=1}^{n_{el}} \boldsymbol{N}_s^{el} \boldsymbol{u}^{el} \tag{8.35}$$

$$p = \sum_{el=1}^{n_{el}} \boldsymbol{N}_f^{el} \boldsymbol{p}^{el} \tag{8.36}$$

$$p_d = \sum_{el_i=1}^{n_{el_i}} \boldsymbol{N}_{pd}^{el_i} \boldsymbol{p}_{\boldsymbol{d}}^{el_i} \tag{8.37}$$

where the interpolants for the solid displacements are now split into separate components for the linear displacements, $\boldsymbol{N}_x$ and $\boldsymbol{N}_y$ (using quartic T-splines), and the Cosserat rotation $\boldsymbol{N}_\omega$ (using cubic T-splines):

$$\boldsymbol{N}_s = \begin{bmatrix} \boldsymbol{N}_x & \boldsymbol{0} & \boldsymbol{0} \\ \boldsymbol{0} & \boldsymbol{N}_y & \boldsymbol{0} \\ \boldsymbol{0} & \boldsymbol{0} & \boldsymbol{N}_\omega \end{bmatrix} \tag{8.38}$$

This spatial and temporal discretisation allows the momentum balance, Eq. 8.14 to be discretised as:

$$\boldsymbol{f}_{ext} - \boldsymbol{f}_{int} - \boldsymbol{f}_d = \boldsymbol{0} \tag{8.39}$$

with the external force vector including contributions due to traction and absorbing boundary conditions:

$$\boldsymbol{f}_{ext} = \int_{\Gamma_t} \boldsymbol{N}_s^T \overline{\boldsymbol{\tau}} + \boldsymbol{N}_s^T \boldsymbol{R}^T \boldsymbol{S} \boldsymbol{R} \boldsymbol{N}_s \left(\frac{\gamma}{\beta \Delta t} \left(\boldsymbol{u}^{t+\Delta t} - \boldsymbol{u}_t \right) - \left(\frac{\gamma}{\beta} - 1 \right) \dot{\boldsymbol{u}}^t - \left(\frac{\Delta t \gamma}{2\beta} - \Delta t \right) \ddot{\boldsymbol{u}}^t \right) \mathrm{d}\Gamma \tag{8.40}$$

The internal force vector is discretised as:

$$\begin{aligned} \boldsymbol{f}_{int} = & \int_\Omega \boldsymbol{B}^T \boldsymbol{\sigma}_s^{t+\Delta t} - \alpha \boldsymbol{B}^T \boldsymbol{m} \boldsymbol{N}_f \boldsymbol{p}^{t+\Delta t} \, \mathrm{d}\Omega \\ & + \int_\Omega \boldsymbol{N}_s^T \left(\overline{\boldsymbol{\rho}} - A n_f \boldsymbol{\rho}_f \right) \boldsymbol{N}_s \left(\frac{1}{\beta \Delta t^2} \left(\boldsymbol{u}^{t+\Delta t} - \boldsymbol{u}^t \right) - \frac{1}{\beta \Delta t} \dot{\boldsymbol{u}}^t - \left(\frac{1}{2\beta} - 1 \right) \ddot{\boldsymbol{u}}^t \right) \mathrm{d}\Omega \\ & - \int_\Omega A n_f \boldsymbol{N}_s^T \boldsymbol{I}_c^T \nabla \boldsymbol{N}_f \boldsymbol{p}^{t+\Delta t} + (1 - A) \boldsymbol{N}_s^T \boldsymbol{\rho}_{\boldsymbol{f}} \boldsymbol{I}_c^T \left(\frac{1}{\theta \Delta t} \boldsymbol{q}^t - \left(1 - \frac{1}{\theta} \right) \dot{\boldsymbol{q}}^t \right) \mathrm{d}\Omega \end{aligned} \tag{8.41}$$

and the forces related to the discontinuity are obtained from:

$$\boldsymbol{f}_d = \int_{\Gamma_d} \boldsymbol{N}_s^T \boldsymbol{R}^T \left(\boldsymbol{\tau}_{\Gamma_d} \right)^{t+\Delta t} \mathrm{d}\Gamma_d \tag{8.42}$$

using the interface tractions defined in Eq. 8.29.

Similarly, the mass conservation from Eq. (8.13) is discretised as:

$$\boldsymbol{q}_{ext} - \boldsymbol{q}_{int} - \boldsymbol{q}_d = \mathbf{0} \tag{8.43}$$

with the external fluxes defined as:

$$\boldsymbol{q}_{ext} = \Delta t \int_{\Gamma_q} \boldsymbol{N}_f^T \overline{q} \, \mathrm{d}\Gamma_q \tag{8.44}$$

and the internal flux vector as:

$$\begin{aligned}
\boldsymbol{q}_{int} = &- \int_\Omega \frac{1}{M} \boldsymbol{N}_f^T \boldsymbol{N}_f \left(\frac{1}{\theta} \left(\boldsymbol{p}^{t+\Delta t} - \boldsymbol{p}^t \right) + \Delta t \left(1 - \frac{1}{\theta} \right) \dot{\boldsymbol{p}}^t \right) \mathrm{d}\Omega \\
&- \int_\Omega \alpha \boldsymbol{N}_f^T \boldsymbol{I}_c \boldsymbol{B} \left(\frac{\gamma}{\beta} \left(\boldsymbol{u}^{t+\Delta t} - \boldsymbol{u}^t \right) - \Delta t \left(\frac{\gamma}{\beta} - 1 \right) \dot{\boldsymbol{u}}^t - \Delta t^2 \left(\frac{\gamma}{2\beta} - 1 \right) \ddot{\boldsymbol{u}}^t \right) \mathrm{d}\Omega \\
&- \frac{k \Delta t}{\mu} \left(1 + \frac{\rho_f k}{n_f \mu \theta \Delta t} \right)^{-1} \int_\Omega \left(\nabla \boldsymbol{N}_f \right)^T \nabla \boldsymbol{N}_f \boldsymbol{p}^{t+\Delta t} + \frac{\rho_f}{n_f} \left(\nabla \boldsymbol{N}_f \right)^T \left(\left(1 - \frac{1}{\theta} \right) \dot{\boldsymbol{q}}^t - \frac{1}{\theta \Delta t} \boldsymbol{q}^t \right) \\
&+ \rho_f \left(\nabla \boldsymbol{N}_f \right)^T \boldsymbol{I}_c \boldsymbol{N}_s \left(\frac{1}{\beta \Delta t^2} \left(\boldsymbol{u}^{t+\Delta t} - \boldsymbol{u}^t \right) - \frac{1}{\beta \Delta t} \dot{\boldsymbol{u}}^t - \left(\frac{1}{2\beta} - 1 \right) \ddot{\boldsymbol{u}}^t \right) \mathrm{d}\Omega
\end{aligned} \tag{8.45}$$

The fluxes due to the fluid flow normal to the fracture are given by:

$$\boldsymbol{q}_d = k_i \Delta t \int_{\Gamma_d^\pm} \boldsymbol{N}_f^T \left(\boldsymbol{N}_{pd} \boldsymbol{p}_d^{t+\Delta t} - \boldsymbol{N}_f \boldsymbol{p}^{t+\Delta t} \right) \mathrm{d}\Gamma_d \tag{8.46}$$

and the mass balance for the interior of the fracture, Eq. (8.26), is discretised as:

$$k_i \Delta t \int_{\Gamma_d} \boldsymbol{N}_{pd}^T \boldsymbol{N}_f \left(\boldsymbol{p}^{+\ t+\Delta t} + \boldsymbol{p}^{-\ t+\Delta t} \right) - 2 \boldsymbol{N}_{pd}^T \boldsymbol{N}_{pd} \boldsymbol{p}_d^{t+\Delta t} \, \mathrm{d}\Gamma_d = \mathbf{0} \tag{8.47}$$

As was the case in the previous chapters, these equations are solved in a monolithic manner using a Newton-Raphson scheme. The system matrices used for this scheme are given in Appendix C.3. A quadratic convergence rate was obtained using these system matrices, aided by the regularising effect of the Cosserat continuum.

8.3. RESULTS

A typical shear fracture case is simulated [220, 231], consisting of a 500 m × 250 m domain with a 75 m long horizontal fracture in the centre, as shown in Figure 8.1. This fracture is propagated along a pre-inserted C^0 continuity line, and is therefore only allowed to propagate horizontally. Absorbing and traction boundary conditions are imposed at all boundaries, using $\tau_{xx} = 8.55$ MPa, $\tau_{yy} = 10$ MPa, and $\tau_{xy} = \tau_{yx} = 1.8$ MPa.

The porous material is characterised by a Young's modulus $E = 10$ GPa, Poisson ratio $\nu = 0.25$, Cosserat shear modulus $G_c = 4$ GPa, Cosserat length scale $\ell_c = 1$ cm, and density $\rho_s = 2500\ \mathrm{kg/m^3}$. A water-like fluid is used with $\mu = 1\ \mathrm{mPa \cdot s}$ and $\rho_f = 1000\ \mathrm{kg/m^3}$. The bulk modulus of the solid is $K_s = 10$ GPa, the fluid bulk modulus $K_f = 2$ GPa, the Biot coefficient $\alpha = 1.0$, a porosity $n_f = 0.3$, and the interface permeability $k_i = 10^{-10}$ m/Pas. A peak friction coefficient $f_p = 0.45$, residual friction coefficient $f_r = 0.045$, and fracture energy $\mathcal{G}_c = 17.4\ \mathrm{kJ/m^2}$ are used. A cohesionless, non-dilatant Drucker-Prager plasticity model ($c = 0, \psi = 0°$) is adopted, with an angle of internal friction $\phi = 31°$. The intrinsic permeability of the porous material was varied between $k = 10^{-10}\ \mathrm{m^2}$ and $k = 10^{-7}\ \mathrm{m^2}$, and additional simulations were performed using the undrained ($k = 0\ \mathrm{m^2}$) and the drained ($p = 0$ Pa and $\boldsymbol{q} = 0$ m/s) assumptions.

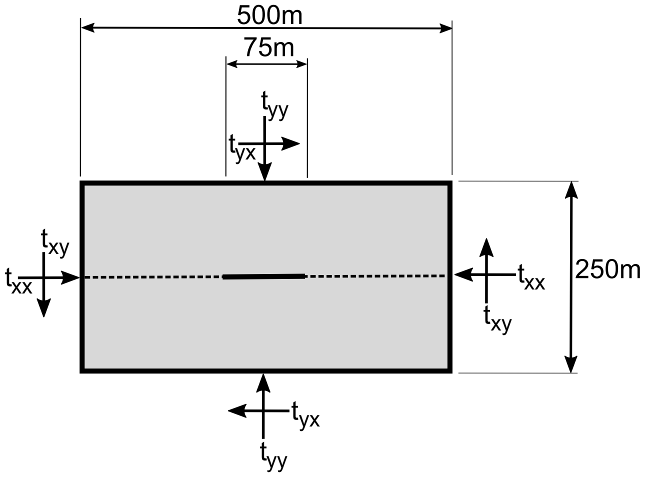

Figure 8.1: Overview of used geometry and traction boundary conditions

The spatial discretisation uses quartic T-splines for the horizontal and vertical displacements, and cubic T-splines for the Cosserat rotation, interstitial fluid pressure, and discontinuity pressure. Three different meshes were used to study the effects of mesh refinement: The first mesh uses a layer of 320 × 10 elements at the discontinuity, with the discontinuity and C^0 continuity line in the centre of this layer. This is encompassed by layers of 160 × 5 and 80 × 15 Bézier extracted elements, and this mesh will be hereafter referred to as 320 × 50. The second mesh adds an extra refinement layer of 640 × 10 elements at the discontinuity, resulting in the 640 × 60 mesh. The final mesh halves all elements horizontally and vertically, resulting in 1280 × 120 elements.

The initial conditions of zero interstitial and discontinuity pressure and equilibrium for the solid stresses are imposed by simulating the first $t_0 = 1$ s using large time steps $\Delta t = 0.01$ s while constraining the fluid pressure to $p = 0$ and not allowing any plastic deformations or fracture propagation. After these initial conditions are achieved, the constraints on the pressure, fracture propagation, and plasticity are removed, and the remainder of the simulation is performed using $\Delta t = 0.04$ ms. This time step is small enough to have the fracture only propagate twice (due to symmetry) every 5-10 time steps using the finest mesh. The parameters used for the Newmark and θ-schemes were $\beta = 0.4$, $\gamma = 0.75$, and $\theta = 1.0$.

8.3.1. EFFECT OF INCLUDING ACCELERATION TERMS

To analyse the effect of including acceleration driven flow and using separate inertia terms, these terms are added one-by-one. The first simulation uses only the pressure gradient driven flow, the $\frac{k}{\mu}\nabla p$ term in Equation 8.9, and uses only a single inertia term in the momentum balance of Eq. 8.8, neglecting the acceleration of the fluid relative to the solid. After this, the solid acceleration driven fluid flow, $\frac{k\rho_f}{\mu}\boldsymbol{I}_c\ddot{\boldsymbol{u}}$, and the fluid acceleration driven fluid flow, $\frac{k\rho_f}{n_f\mu}\dot{\boldsymbol{q}}$, one-by-one. For the last simulation, two separate inertia terms are used by including the $\boldsymbol{\rho}_f\boldsymbol{I}_c^T\dot{\boldsymbol{q}}$ term from Eq. 8.8. All these simulations have been carried out using an intrinsic permeability $k = 10^{-8}$ m^2 and use the 640 × 60 mesh.

The resulting interstital fluid pressures are shown in Figure 8.2. When no acceleration driven fluid flow is included, the only changes in pressure are caused by the slight compression of the solid and the therein contained fluid. This causes slight increases in pressure in the compression sides of the fracture, the top right and bottom left quarters of the domain. Due to the high permeability of the domain, these pressure regions are diffused over a large area.

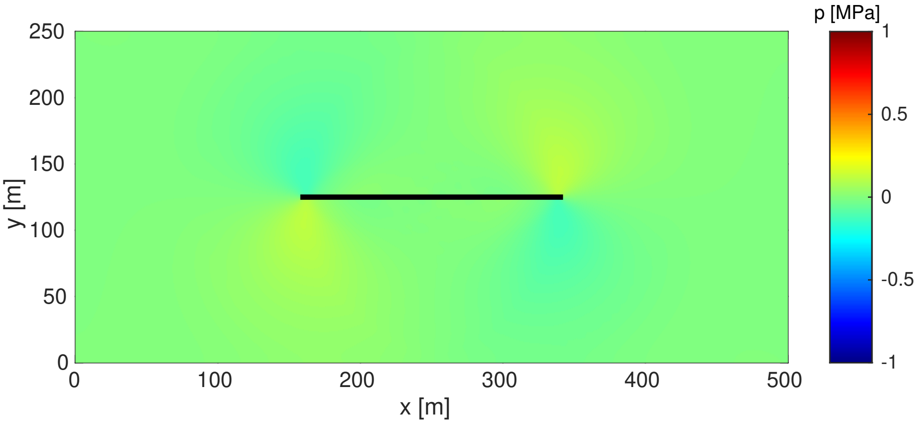

(a) Single inertia term in the momentum balance and no acceleration terms in Darcy's law

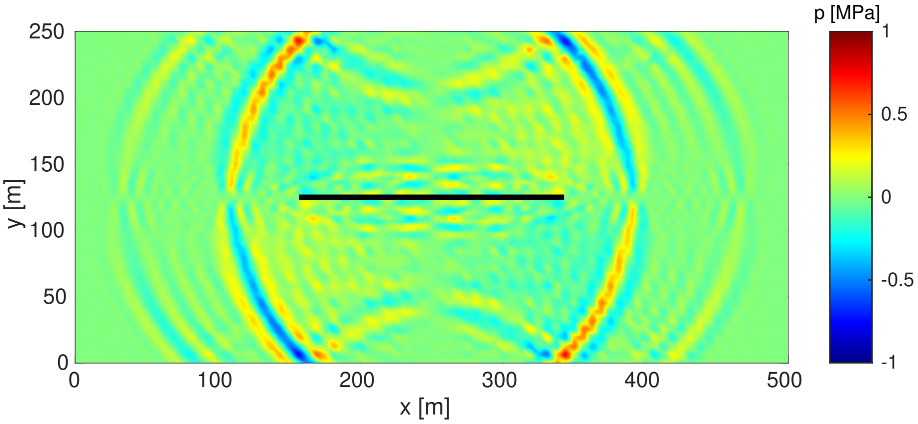

(b) Single inertia term in the momentum balance and only solid acceleration terms in Darcy's law

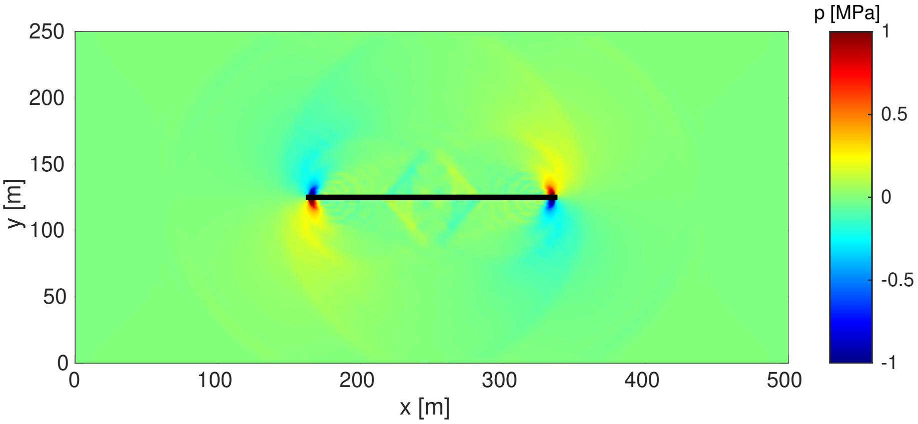

(c) Single inertia term in the momentum balance and all acceleration terms in Darcy's law

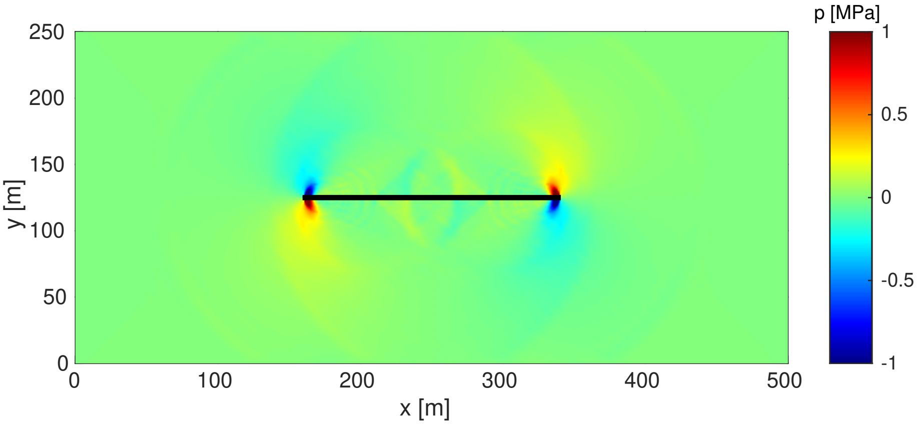

(d) All terms in the momentum balance and in Darcy's law

Figure 8.2: Interstitial fluid pressure at $t - t_0 = 52$ ms when using different acceleration and inertia terms.

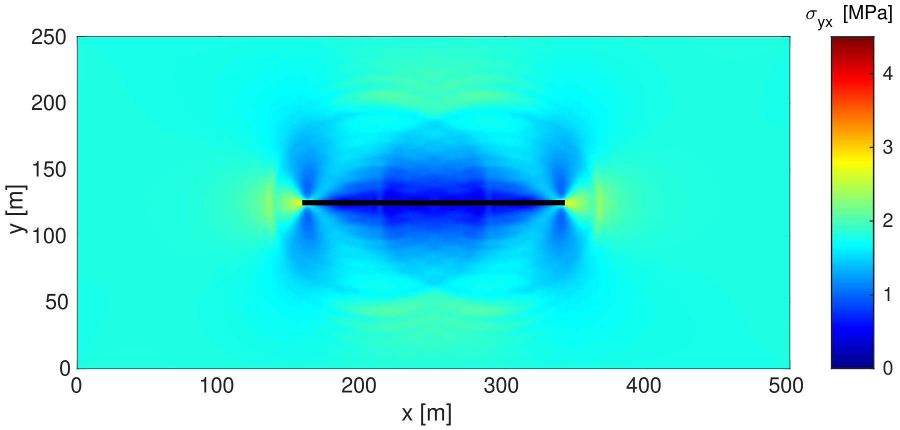

(a) Single inertia term in the momentum balance and no acceleration terms in Darcy's law

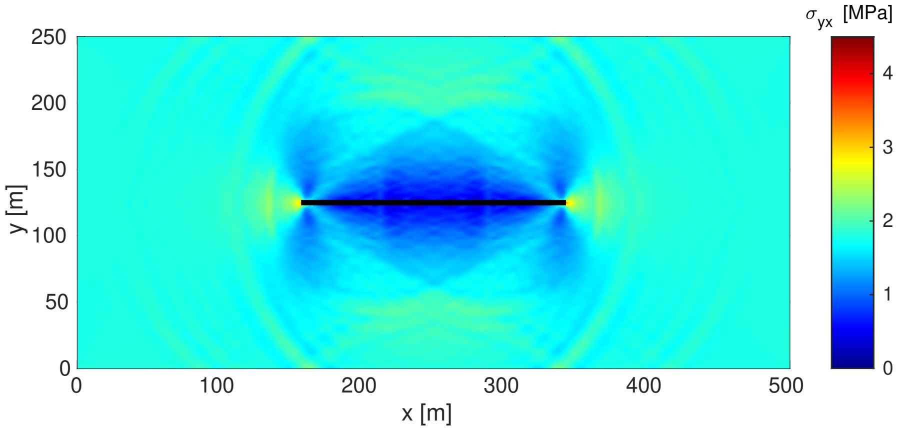

(b) Single inertia term in the momentum balance and only solid acceleration terms in Darcy's law

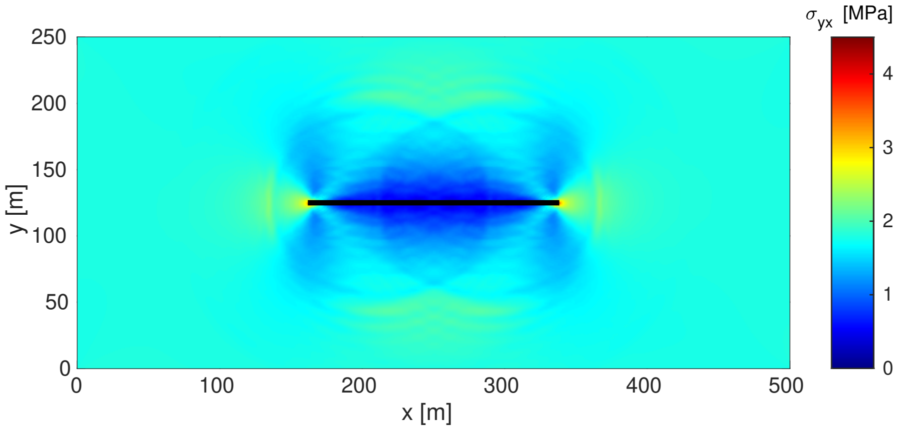

(c) Single inertia term in the momentum balance and all acceleration terms in Darcy's law

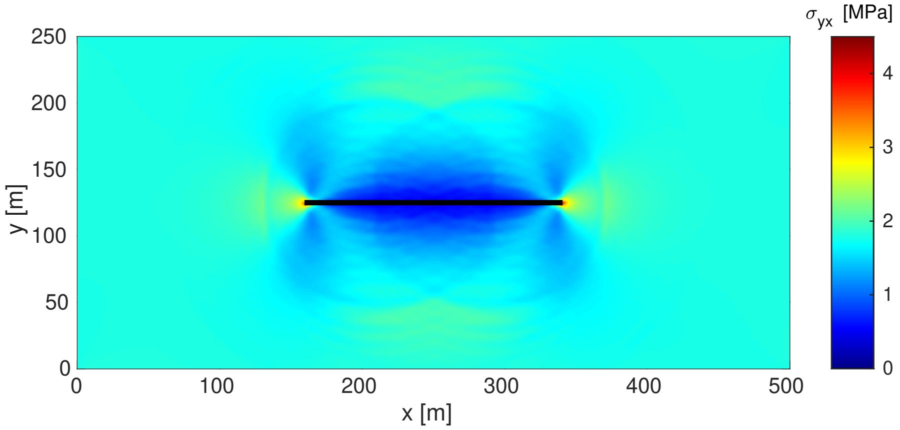

(d) All terms in the momentum balance and in Darcy's law

Figure 8.3: Shear stress σ_{yx} at $t - t_0 = 52$ ms when using different acceleration and inertia terms.

Including the solid acceleration driven fluid flow causes the interstitial fluid pressure to react to stress waves, as shown in Figure 8.2b. For the compression sides of the fracture, this causes fluid to flow away from the location of the pressure waves, resulting in low pressure areas encapsulated by two high pressure areas. The opposite is seen on the extensional sides of the fracture. However, the inclusion of the solid acceleration driven fluid flow also results in severe pressure oscillations throughout the domain, caused by the coupling between the fluid fluxes and the solid acceleration.

Figure 8.2c shows that adding the fluid acceleration removes these oscillations and adds additional damping, limiting the distance the stress waves travel from the fracture tips. Including the fluid acceleration driven fluid flow also increases the pressure near the fracture tips, resulting in higher pressures at the compression side and lower pressure at the extensional sides compared to the case with only the solid acceleration included. Finally, adding the inertia for the fluid acceleration relative to the solid to the momentum balance does not visibly alter the interstitial fluid pressure, as shown in Figure 8.2d.

The shear stress is shown in Figure 8.3. Similar to the interstitial fluid pressure, slight oscillations are seen when only the solid acceleration driven fluid flow is included, and these oscillations disappear once the fluid acceleration is added. The damping added through the fluid acceleration also reduces the distance travelled by shear stress waves before disappearing. Comparing the shear stress for the cases with and without separate inertia terms shows slightly larger differences compared to those obtained for the pressure. However, the differences are still fairly limited, and are not located near the fracture tips.

It can be concluded that the acceleration driven flow has a significant effect on both the fluid pressure and solid stresses, and needs to be included in the formulation. However, separate inertia terms in the mass balance have a much more limited effect, while resulting in lengthy terms in the internal force vector. Therefore, the remainder of this chapter will only include the acceleration driven fluid flow terms, and the separate inertia terms will not be included.

8.3.2. MESH SENSITIVITY

The three meshes were used to simulate the cases using $k = 10^{-8}$ m^2 and $k = 10^{-10}$ m^2, and assuming drained and undrained conditions. The result for the $k = 10^{-10}$ m^2 case, Figure 8.4b, shows only a small influence of the element size, as is the case for the undrained and drained cases (not shown). The coarse mesh shows small jumps in the fracture length, with these jumps corresponding to two element lengths due to the symmetry of the problem. Upon mesh refinement, these steps decrease in size. These steps originate from the element-wise fracture propagation imposing a minimum propagation length. If the shear stress is not sufficient to extend the discontinuity a complete element-length, no propagation takes place. Only when the stress at the furthest integration point away from the fracture tip surpasses the fracture strength does the complete element become fractured and the total discontinuity length is increased by one element-length.

It is important to note that this step-wise propagation is solely a numerical artefact, and does not have any physical origin. As long as the time step size is chosen such that at most a single element fractures per time step, this stepwise propagation will occur. In contrast, when the time step size is increased such that at least one element fractures every step, this stepwise propagation will not occur, and the fracture will show a more continuous propagation.

The results for the $k = 10^{-8}$ m^2 case are shown in Figure 8.4a. In contrast to the other cases, there is a clear difference between the three meshes. Using the coarse mesh, the fracture propagation pauses halfway through the simulation before continuing to prop-

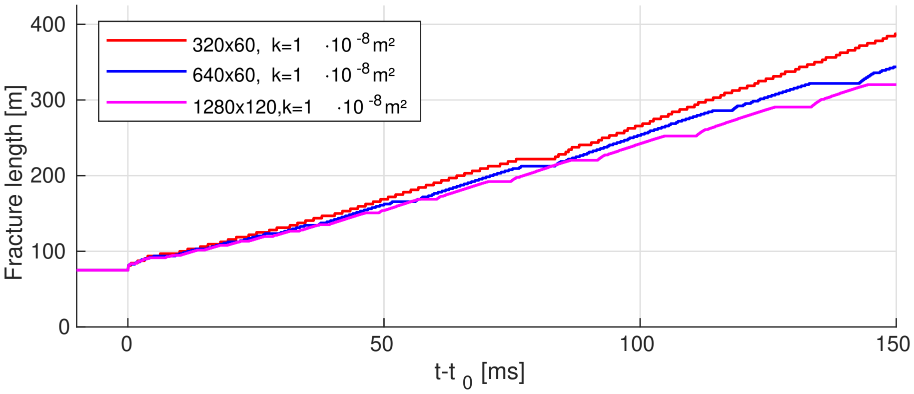

(a) $k = 1 \cdot 10^{-8}$ m^2

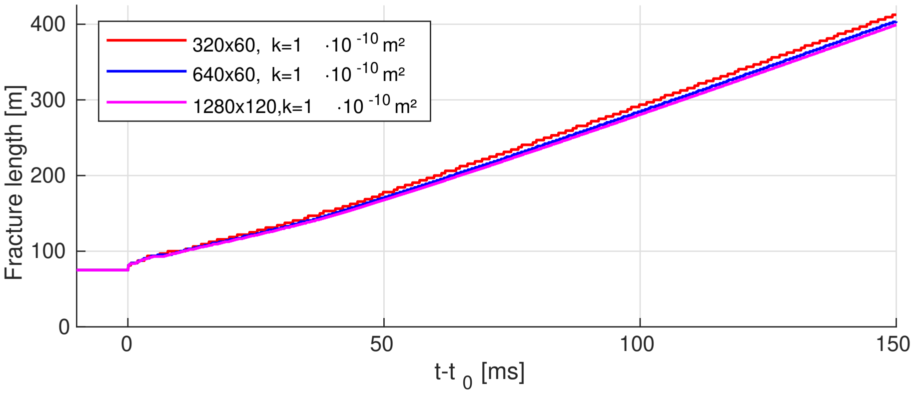

(b) $k = 1 \cdot 10^{-10}$ m^2

Figure 8.4: Effect of mesh refinement

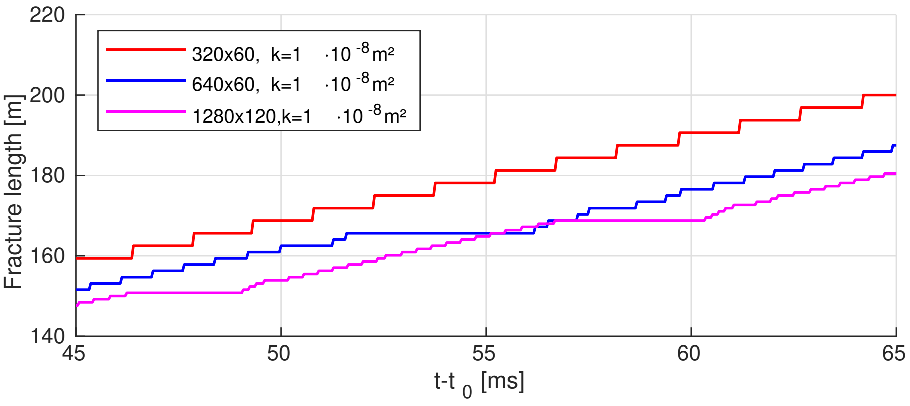

Figure 8.5: Effect of mesh refinement using $k = 10^{-8}$ m^2

agate shortly after. This "stick-slip" like behaviour becomes more common upon mesh refinement, resulting in a significant difference between the meshes in the discontinuity length. This behaviour is different from the element-size dependence previously observed, as shown in Figure 8.5. The small steps still exist for all meshes, while the "stick-slip" like behaviour introduces large plateaus for the finer meshes.

8.3.3. EFFECT OF PERMEABILITY

Results for the complete range of simulated permeabilities are shown in Figure 8.6 using the 1280×120 mesh. Stick-slip like behaviour is observed for the cases using a high permeability,

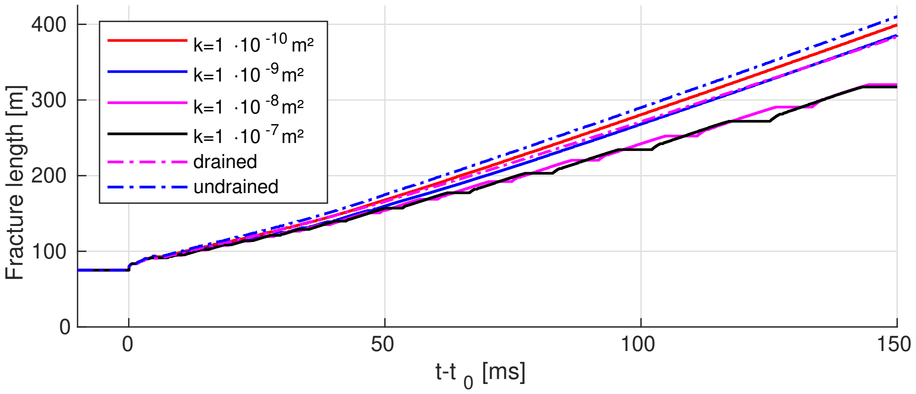

Figure 8.6: Fracture length using several values for the intrinsic permeability

whereas a smooth fracture propagation is observed for cases with a lower permeability, and the drained and undrained cases. Due to this lack of stepwise propagation, the $k = 10^{-10}$ m^2 simulation approaches the undrained case. In contrast, large differences are observed between the drained and high permeability cases, as was suggested based on the governing equations in Section 8.1.2. However, only limited differences occur between the $k = 10^{-7}$ m^2 and $k = 10^{-8}$ m^2 cases, suggesting that these results approach a high-permeability limit.

The plastic strain around the right fracture tip is shown in Figure 8.7. The drained and undrained cases show similar results as observed in [231], with the plasticity being limited to the extensional side of the fracture, and plastic deformations occurring over a larger area for the drained compared to the undrained case. While the $k = 10^{-10}$ m^2 results approach the undrained case, the high permeability cases show significant differences compared to the drained case. Large amounts of plastic deformation are seen at the locations where the fracture propagation pauses, with a small drop in plastic strain directly after these pauses. Overall, the area in which plastic strain occurs surpasses the drained case, again confirming that these high permeability cases do not approach the drained assumption limit.

8.3.4. "STICK-SLIP" LIKE BEHAVIOUR

The stick-slip like behaviour is explained by looking at the $k = 10^{-8}$ m^2 results at the four different times shown in Figure 8.8. The interstitial fluid pressure at these times is given in Figure 8.9 and the shear stresses responsible for propagating the fracture in Figure 8.10.

At the moment the fracture propagation restarts, there is a low pressure region on the compression side next to a small high pressure region just behind the fracture tip, and a high pressure region next to a small low pressure region on the extensional side (subfigures a). The large low pressure region (compression side) and high pressure region (extensional side) detach during fracture propagation and diffuse away. The small high pressure region (compression side) and low pressure region (extensional side) start increasing in size while the fracture propagates (subfigures b). The inclusion of acceleration-driven fluid flows causes fluid to move from the newly created low pressure region to the high pressure zone near to the crack tip (for the compression side), further increasing the size and magnitude of this high pressure zone. Once this high pressure zone grows to overtake the fracture tip, the fracture propagation arrests (subfigures c), while due to the inclusion of acceleration driven fluid flow the pressure region flows past the fracture tip. Only once the high pressure region above the fracture and the low pressure region below the fracture have fully surpassed the crack tip, fracture propagation is resumed again and a new high pressure region (on top) and low pressure region (below the crack) start to build up again. This alternating build up and

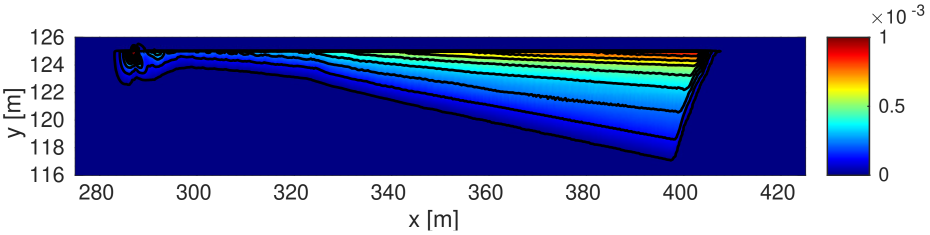

(a) Drained

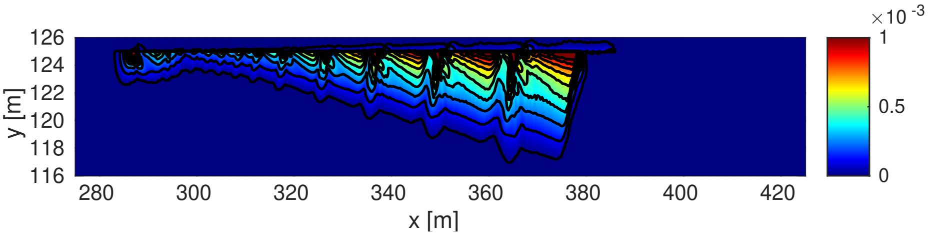

(b) $k = 10^{-7}$ m^2

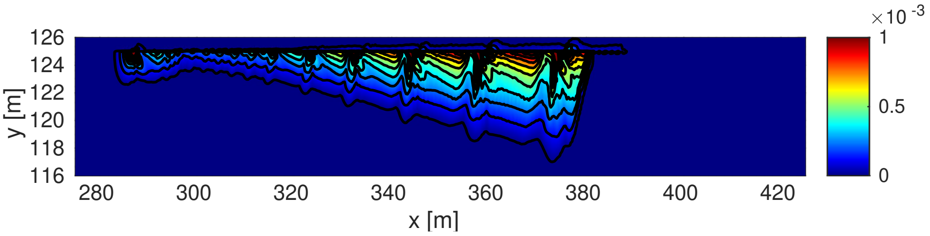

(c) $k = 10^{-8}$ m^2

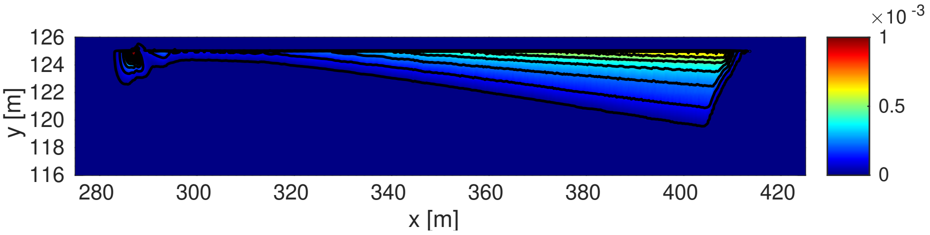

(d) $k = 10^{-10}$ m^2

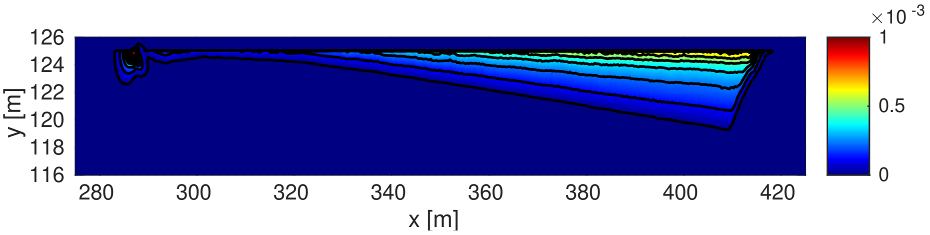

(e) Undrained

Figure 8.7: Plastic strain $(\epsilon_{xx}^2 + \epsilon_{yy}^2)^{0.5}$ at time $t - t_0 = 120$ ms

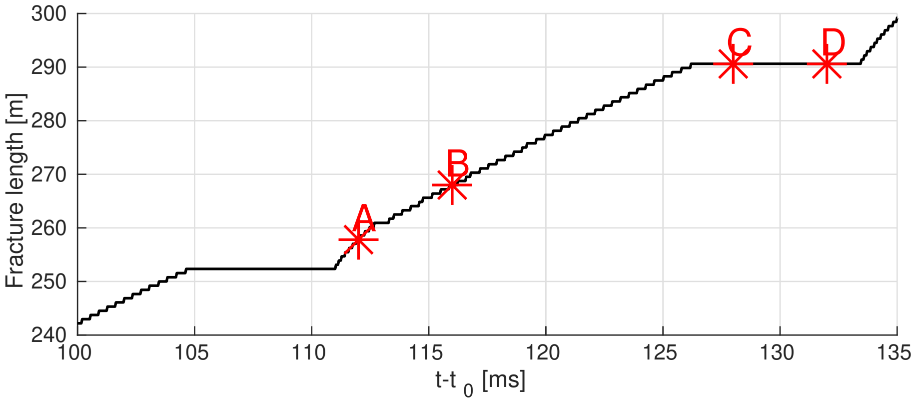

Figure 8.8: Locations of Figures 8.9 and 8.10 using $k = 10^{-8}$

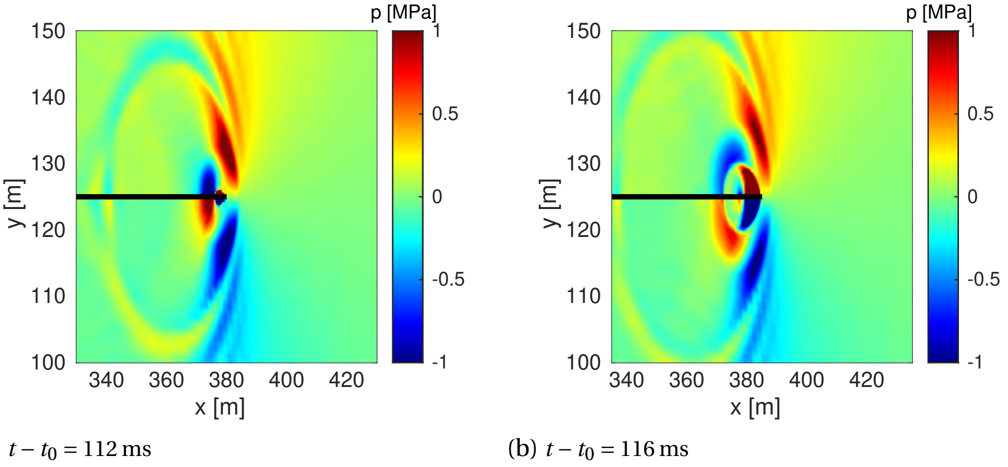

(a) $t - t_0 = 112$ ms

(b) $t - t_0 = 116$ ms

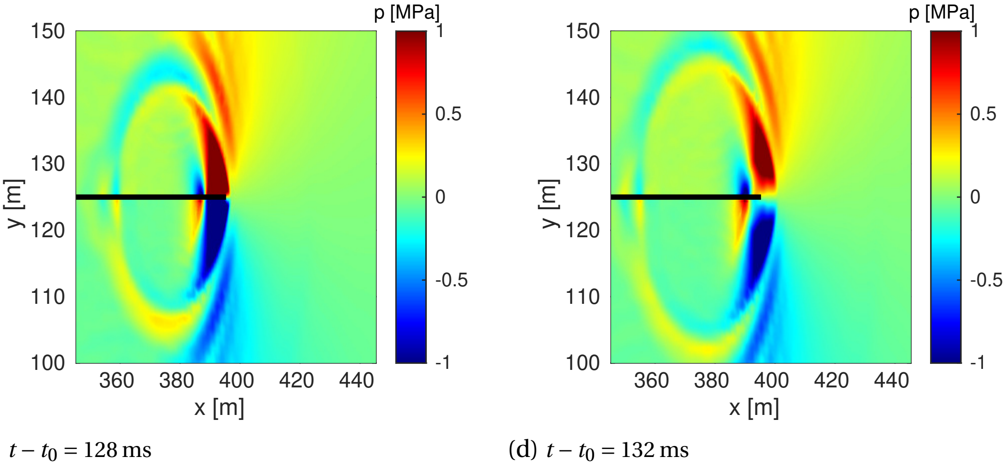

(c) $t - t_0 = 128$ ms

(d) $t - t_0 = 132$ ms

Figure 8.9: Interstitial fluid pressure around the right crack tip using $k = 10^{-8}$ m^2 at the times shown in Figure 8.8

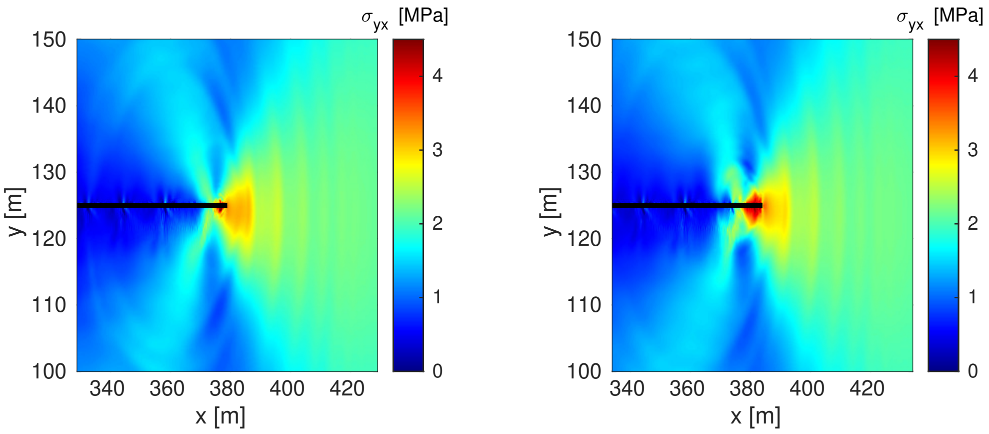

(a) $t - t_0 = 112\,\mathrm{ms}$

(b) $t - t_0 = 116\,\mathrm{ms}$

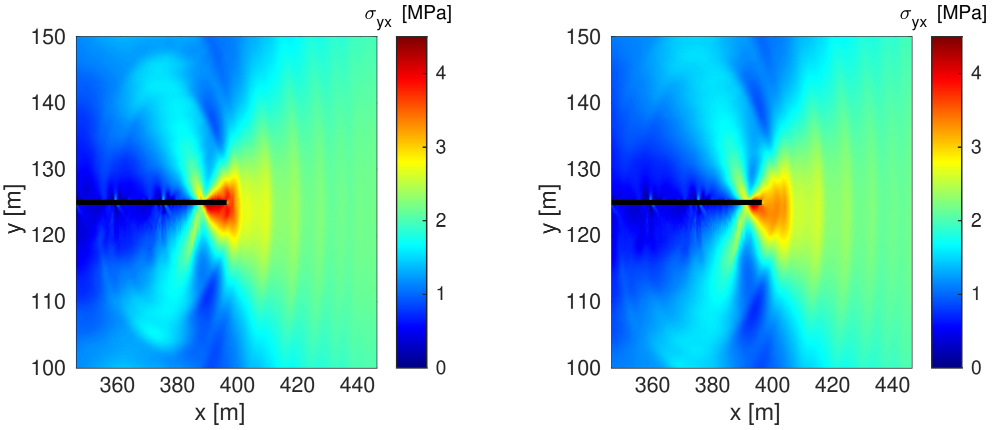

(c) $t - t_0 = 128\,\mathrm{ms}$

(d) $t - t_0 = 132\,\mathrm{ms}$

Figure 8.10: Shear stress σ_{yx} around the right crack tip using $k = 10^{-8}\ \mathrm{m}^2$ at the times shown in Figure 8.8

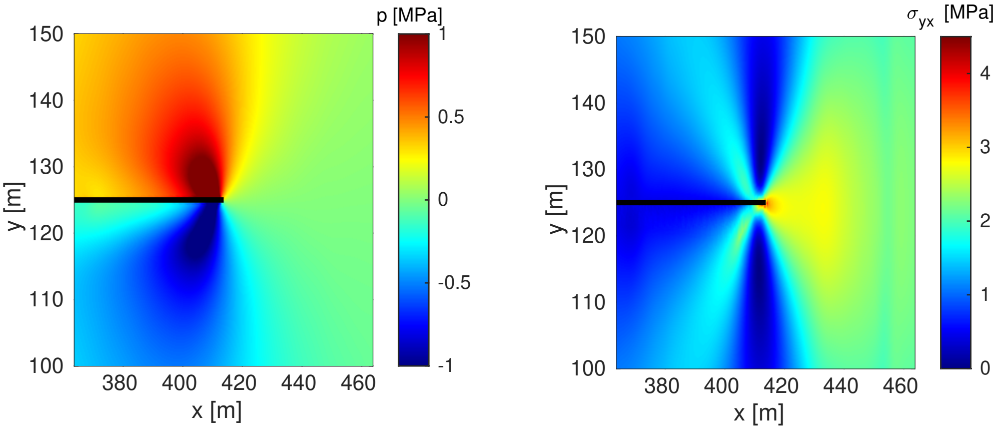

(a) Interstitial fluid pressure

(b) Shear stress σ_{yx}

Figure 8.11: Interstitial fluid pressure and shear stress for $k = 10^{-10}\ \mathrm{m}^2$ at $t - t_0 = 120\,\mathrm{ms}$

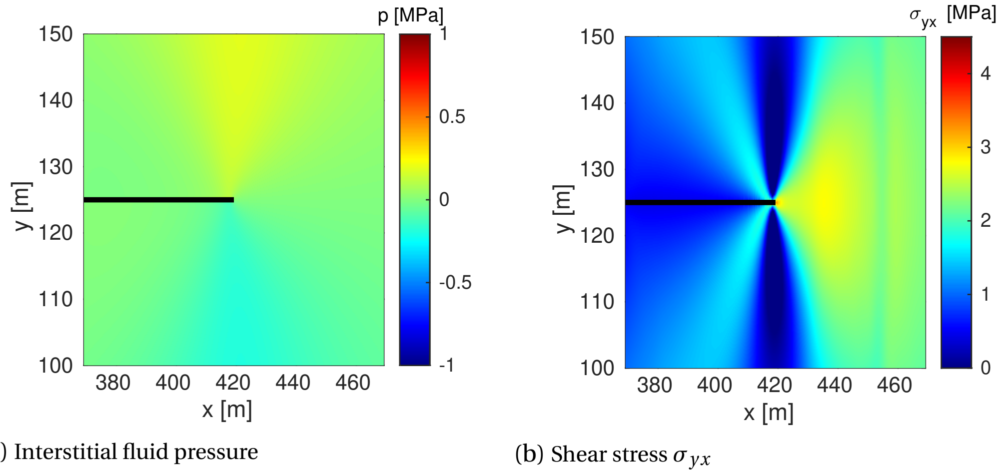

(a) Interstitial fluid pressure

(b) Shear stress σ_{yx}

Figure 8.12: Interstitial fluid pressure and shear stress for $k = 10^{-8}$ m^2 without acceleration terms in Darcy's law at $t - t_0 = 120$ ms

shedding of high and low pressure regions keeps repeating, resulting in repeating pauses in the fracture propagation.

The effect of this alternating build up of high and low pressure zones on the shear stress is shown in Figure 8.10. While the shear stress starts of concentrated around the fracture tip, the developing pressure zones diffuse this shear stress over a larger region as the fracture propagates. Once the propagation arrests, the shear stress is distributed over a significantly larger region compared to the beginning, as shown in subfigure c. During the propagation pause, the shear stress becomes more concentrated around the fracture tip again due to the fluid pressure diffusing away, and once the fracture propagation restarts, these shear stresses are limited to a small region at the crack tips again.

Results from a case using a lower permeability, Figure 8.11, or when no acceleration driven fluid flow is included, Figure 8.12, show that these opposite pressure regions do not occur. For the low permeability case the acceleration driven fluid flow terms are too small to significantly alter the pressure, and the only change in interstitial fluid pressure is due to the compression caused by solid deformations. Both these cases also show the high shear stress to be limited to a small region at the crack tips, and do not show the growing and shrinking of this region observed for the high permeability case with acceleration driven fluid flow. This indicates that the observed stick-slip like behaviour is solely caused by the acceleration driven fluid flow, and therefore requires these terms to be included to obtain a realistic representation of the fracture propagation.

8.3.5. SUPERCRITICAL FRACTURE PROPAGATION

A second case using a combination of external tractions to cause the propagation velocity to exceed the shear wave speed is now considered. This case uses $\tau_{xx} = 19$ MPa, $\tau_{yy} = 10$ MPa, $\tau_{xy} = \tau_{yx} = 2.4$ MPa, and all other properties corresponding to those previously described. All simulations used the 1280 × 120 mesh.

The manner of fracture propagation is hown in Figure 8.13. In contrast to the previous case, no stick-slip like behaviour occurs for simulations using a high permeability. Furthermore, even the simulations using a high permeability approximate the undrained fracture propagation velocity, with the fracture for the drained case propagating slower. This can be explained by looking at the interstitial fluid pressure near the fracture tip, Figure 8.14. Comparing the interstitial pressures for the $k = 10^{-8}$ m^2, $k = 10^{-10}$ m^2, and undrained cases

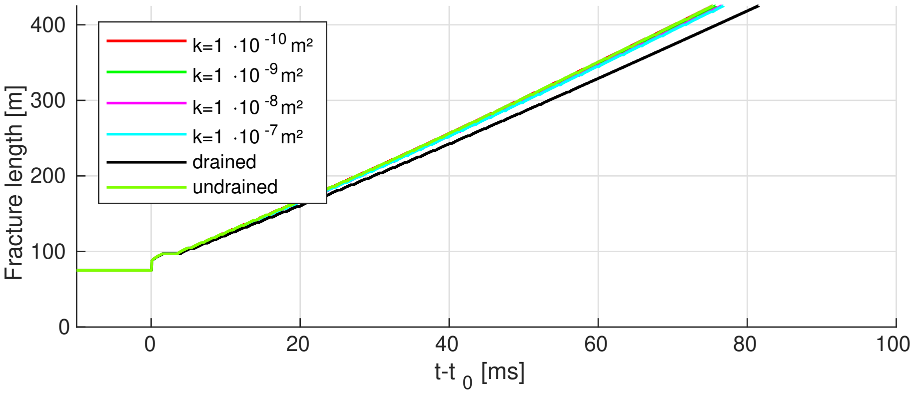

(a) Total fracture length

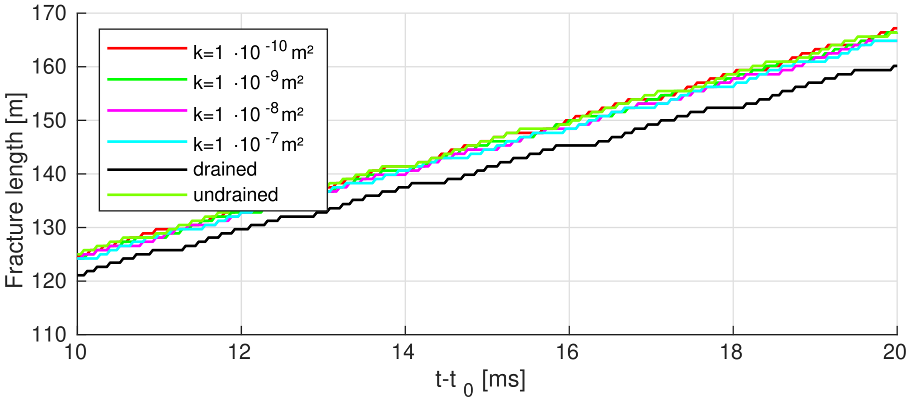

(b) Zoomed near the start of fracture propagation

Figure 8.13: Fracture length using the supershear load case

shows that the pressures near the crack tip are similar, which explains the similar fracture velocity obtained for these cases. The high pressure regions next to low pressure regions that were observed in the previous case using $k = 10^{-8}$ m^2 do still occur for this case, but due to the rapidly propagating fracture these pressure regions do not surpass the fracture and are thus unable to cause the stick-slip behaviour described before. However, the acceleration driven fluid flow still results in a pressure increase near the crack tip, compensating for the increased fluid diffusion due to the higher permeability.

While no stick-slip behaviour was observed to originate from the interstitial fluid pressure, small arrests in the propagation still occurred for all cases, as shown in Figure 8.13b. These small pauses are independent of the used permeability, only occur up to $t - t_0 \approx 40$ ms (corresponding to a fracture from x = 125 m-375 m), and do not occur after this initial period where only the small element-sized steps are seen. These small pauses originate from oscillations in the shear stress, as shown in Figure 8.15. Initially, the domain is in a static equilibrium. Once the initial conditions are achieved, and propagation and plastic deformations are allowed, the fracture propagates faster than the surrounding stresses can adapt. This results in the fracture propagating through the stresses originating from the initial conditions, causing small stress oscillations to occur. These stress oscillations disappear once the fracture propagates out of area influenced by the initial fracture, thereby limiting these small oscillations to only occur near the start of the simulations.

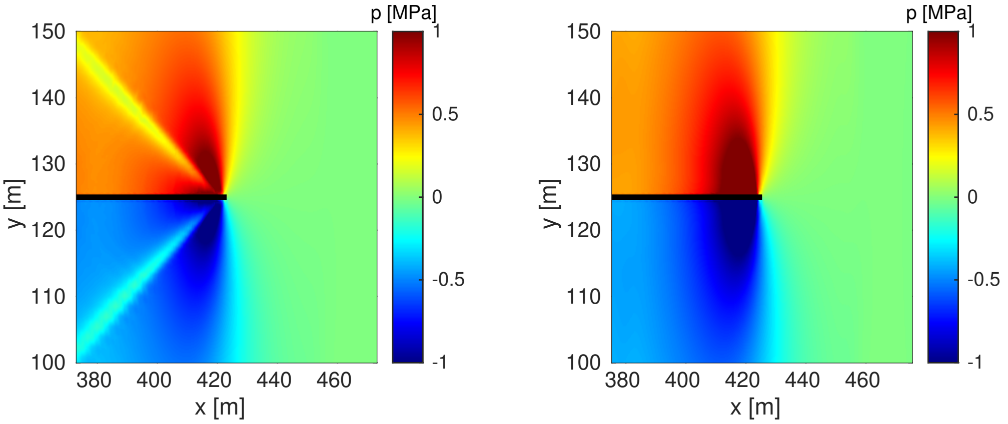

(a) $k = 10^{-8}$ m^2

(b) $k = 10^{-10}$ m^2

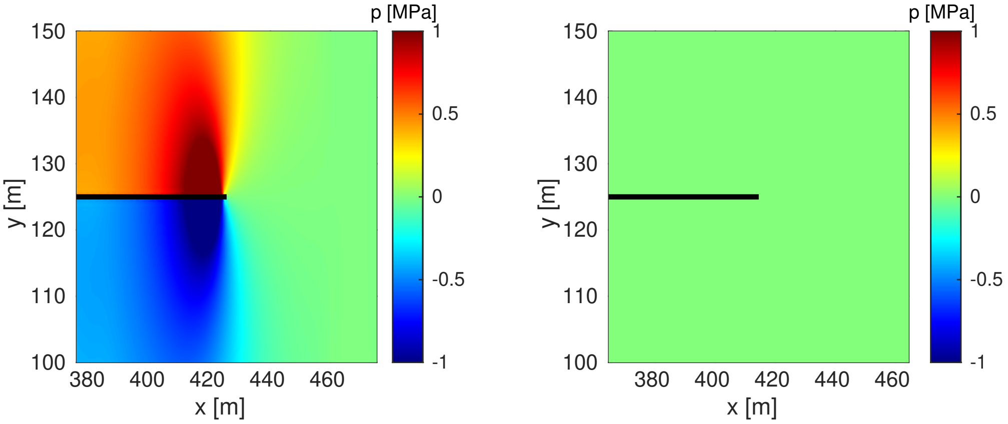

(c) Undrained

(d) Drained

Figure 8.14: Interstitial fluid pressure using the supershear load case at $t - t_0 = 60$ ms

8.4. CONCLUSION

In this chapter, the formulation for a poroelastic medium has been extended to include separate inertia terms for the fluid and solid, and to include acceleration driven fluid flows. The derived formulation includes the fluid acceleration while still using a displacement-pressure formulation, in contrast to other pre-existing formulations which either use a displacement-pressure-fluid velocity to include these terms or neglect the fluid acceleration terms to preserve the displacement pressure formulation. This formulation was combined with a shear based traction-separation law and a discontinuous pressure model to include fractures. Bézier extracted T-splines were used for the spatial discretisation, and special attention was paid in the temporal discretisation to preserve the path or time dependence of the "time" derivatives.

While the use of separate inertia terms for the solid and fluid had only a slight influence on the obtained results, the effects of including acceleration-driven fluid flows were larger. Including solid acceleration driven fluid flow allowed the interstitial fluid pressure to react to stress waves, but resulted in severe oscillations throughout the domain. Adding the fluid acceleration term resolved these oscillations, provided additional damping for stress waves, and increased the interstitial fluid pressure near the fracture tips.

Through a mesh refinement study and simulations using a range of intrinsic permeabilities three different manners of step-wise propagation were observed. The first type originates from the element-wise fracture propagation only allowing for complete elements to

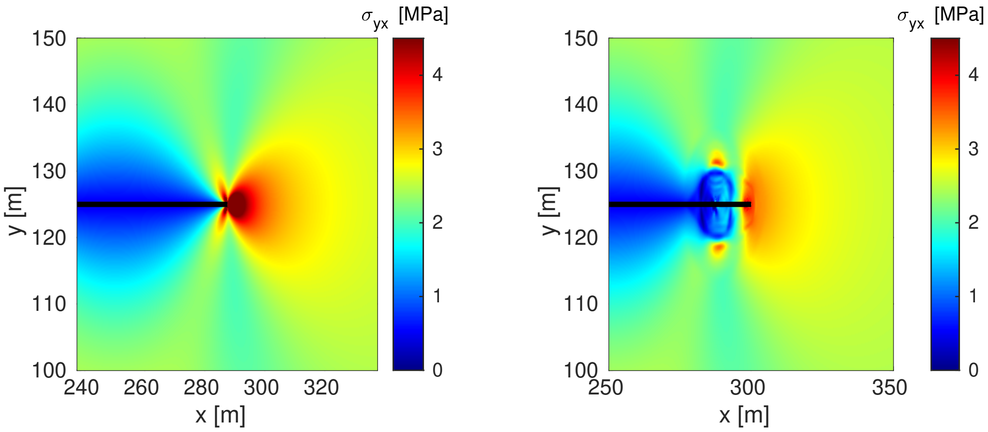

(a) $t - t_0 = 0$ ms (b) $t - t_0 = 4$ ms

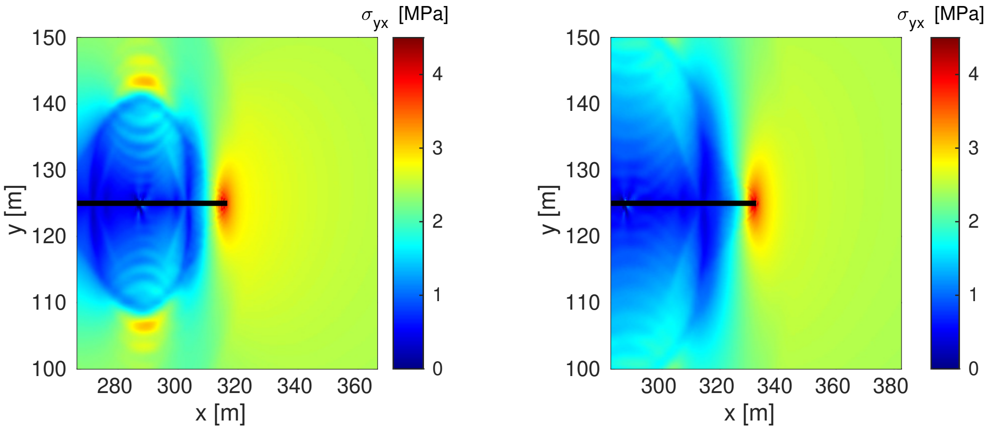

(c) $t - t_0 = 12$ ms (d) $t - t_0 = 20$ ms

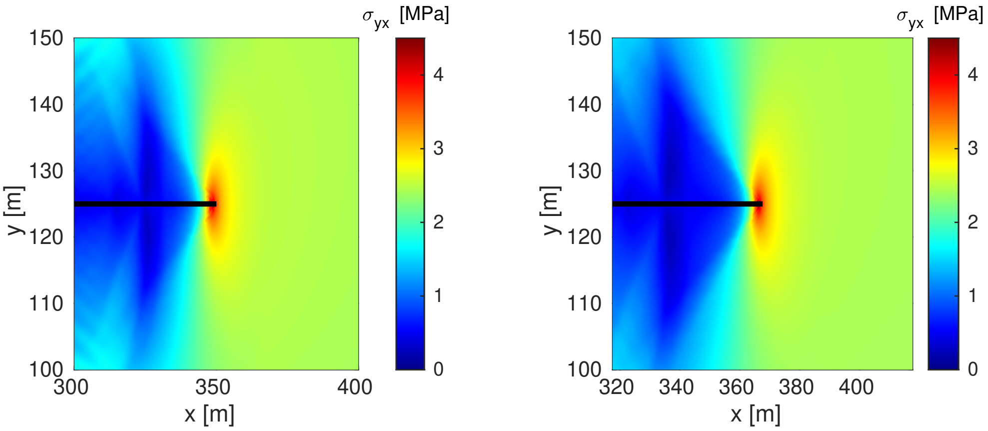

(e) $t - t_0 = 28$ ms (f) $t - t_0 = 32$ ms

Figure 8.15: Shear stress σ_{yx} using the supershear load case with $k = 10^{-8}$ m^2

fracture. When this is combined with a time step small enough to have either none or one element fracture, it results in small jumps in the fracture propagation length. Since these steps originate from the spatial discretisation used, they are solely of a numerical nature and do not have any physical origin.

The second manner of stepwise propagation observed was a stick-slip like behaviour caused by the acceleration driven fluid flow. This flow results in alternating high and low pressure regions near the fracture tip, and once one of these regions grows past the fracture tip, the propagation pauses until the fluid pressure is reduced again. Since this depends on the acceleration driven fluid flows, this stick-slip like behaviour only occurs when the porous material has a high permeability, and was shown to require a sufficiently fine mesh to be visible during the simulations.

Finally, simulations in which the discontinuity propagation velocity was above the shear wave speed showed that initial conditions are also able to cause small arrests. Since these arrests are caused by the pre-existing stresses surrounding the discontinuity not adapting fast enough to the new length of the fracture, this stepwise propagation disappears once the discontinuity grows past the zone influenced by these initial conditions.

9

NUMERICAL SUB-GRID MODEL

In the previous chapter it was seen that inertial effects can greatly influence the obtained results for shear-based fractures. Extending this to pressurised fractures, however, is not possible using existing sub-grid models. The basis of all subgrid models is an analytically derived velocity profile [39], which limits the types of fluid behaviour that can be included. For instance, while a sub-grid model for a non-Newtonian power law fluid was derived in Chapter 2, this can not be extended to more complicated fluid rheologies such as Carreau fluids [48] since an analytic velocity profile does no longer exist. A similar issue occurs when trying to include inertial effects: The time dependence can only be included for a limited number of cases for which analytical solutions are available and therefore inertial effects can not be included in standard sub-grid formulations.

In this chapter, a sub-grid model will be detailed which does not depend on an analytical solution, but instead numerically obtains a velocity profile within the fracture in each integration point. This results in two distinct scales, the macro scale on which the mass and momentum balance are solved, and the fracture scale on which the velocity profiles are obtained. This scheme will be described for Newtonian fluids in Section 9.1, explaining how the velocity profiles are resolved and how inertial effects within the fracture are included. This formulation is extended to non-Newtonian Carreau fluids in Section 9.2, showcasing the ability of the sub-grid model to include fluids for which no analytic velocity profile exists. Finally, simulations using the derived numerical sub-grid model are preformed to show the abilities of the derived models, and highlight the effect of including inertial forces inside the fracture. The contents of this chapter is strongly based on results previously published in [2].

9.1. NEWTONIAN FLUIDS

The behaviour of the porous material saturated with a Newtonian fluid is described using the equations from the previous chapter, including acceleration-driven fluid flow. While the effects of plastic deformations will not be investigated in this chapter, a Cosserat continuum is used to make the equations described here compatible with plasticity. The mass and momentum balance are given by a reordered version of Eqs. 8.13 and 8.14 as:

$$\boldsymbol{L}^T\left(\boldsymbol{\sigma}_s^{t+\Delta t} - \alpha p^{t+\Delta t}\boldsymbol{m}\right) - \overline{\boldsymbol{\rho}}\ddot{\boldsymbol{u}}^{t+\Delta t} - \boldsymbol{\rho}_f \boldsymbol{I}_c^T\left(\frac{1}{\theta\Delta t}\left(\boldsymbol{q}^{t+\Delta t} - \boldsymbol{q}^t\right) + \left(1 - \frac{1}{\theta}\right)\dot{\boldsymbol{q}}^t\right) = \boldsymbol{0} \tag{9.1}$$

$$\frac{1}{M}\dot{p}^{t+\Delta t} + \alpha\boldsymbol{\nabla}\cdot\left(\boldsymbol{I}_c\dot{\boldsymbol{u}}^{t+\Delta t}\right) + \boldsymbol{\nabla}\cdot\boldsymbol{q}^{t+\Delta t} = 0 \tag{9.2}$$

with the fluid flux at $t+\Delta t$ used in both these equations given by Eq. 8.12 as:

$$\boldsymbol{q}^{t+\Delta t} = \left(1 + \frac{\rho_f k}{n_f \mu \theta \Delta t}\right)^{-1}\left(-\frac{k}{\mu}\boldsymbol{\nabla}p^{t+\Delta t} - \frac{k\rho_f}{\mu}\boldsymbol{I}_c\ddot{\boldsymbol{u}}^{t+\Delta t} - \frac{k\rho_f}{\mu n_f}\left((1-\frac{1}{\theta})\dot{\boldsymbol{q}}^t - \frac{1}{\theta\Delta t}\boldsymbol{q}^t\right)\right) \tag{9.3}$$

The matrices used in these Equations are given in Eq. 8.5.

The mass conservation inside the fracture is given in the (x_d, y_d) coordinate system of Fig. 2.1 for a slightly compressible fluid as:

$$\frac{\partial v}{\partial x_d} + \frac{\partial w}{\partial y_d} + \frac{1}{K_f}\dot{p}_d = 0 \tag{9.4}$$

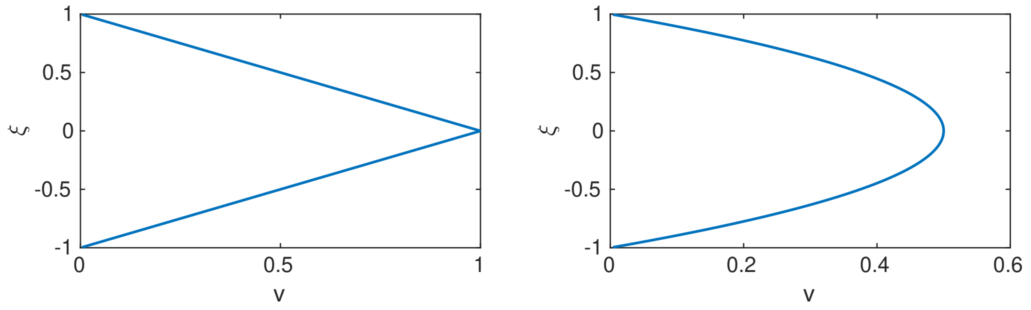

(a) Two linear elements (b) One quadratic element

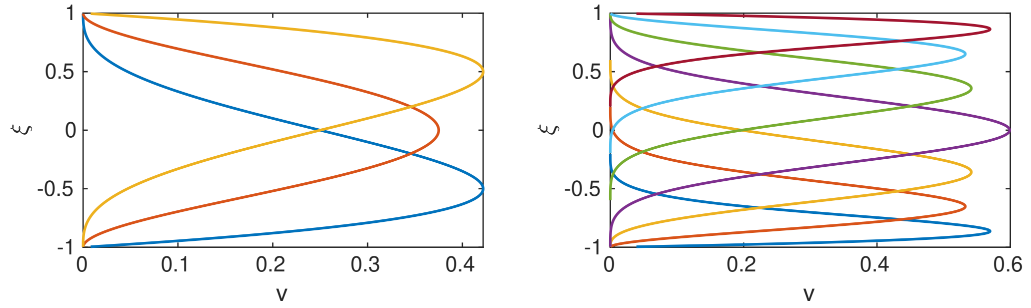

(c) One quartic elements (d) Five quartic elements

Figure 9.1: Example of fracture-scale discretisation

Integrating over the fracture height and substituting the definitions for the fluid flux at the walls, Eqs. 5.1 and 5.2, results in:

$$k_i\left(p^{+\,t+\Delta t}+p^{-\,t+\Delta t}-2p_d^{t+\Delta t}\right)+\frac{\partial}{\partial x_d}q_x+\dot{h}^{t+\Delta t}+\frac{h}{K_f}\dot{p}_d^{t+\Delta t}=0 \tag{9.5}$$

with q_x the fluid transport within the fracture and the fracture height h given by:

$$h=h_0+\boldsymbol{n}\cdot[\![\boldsymbol{u}]\!] \tag{9.6}$$

The offset h_0 is used to allow for an initial opening height, without his height needing to be reflected in the discretisation and initial deformations. This allows for notched specimens to be represented as part of the discontinuity, instead of the notch being represented through the mesh. These notched domains are often used in experiments to localize the fracture propagation to a set location [123, 127, 163, 175, 202].

9.1.1. FRACTURE SCALE MODEL

The fluid flux q_x in Eq. 9.5 is determined at each integration point inside the fracture using a separate model. This model gives the fluid flux as a function of the opening height and discontinuity pressure gradient, and is fully integrated in the monolithic scheme used for the macro scale through the derivatives of the fluid flux with regards to the pressure gradient and opening height.

The starting point to obtain this fracture fluid flux is the momentum balance in x_d direction:

$$\rho_f\frac{\partial v}{\partial t}+\rho_f v\frac{\partial v}{\partial x_d}+\rho_f w\frac{\partial v}{\partial y_d}=-\frac{\partial p_d}{\partial x_d}+\mu\frac{\partial^2 v}{\partial y_d^2} \tag{9.7}$$

where we assume the velocity gradient in tangential direction is negligible compared to the gradient in normal direction. This equation is combined with no-slip boundary conditions:

$$v(h/2)=v(-h/2)=0 \tag{9.8}$$

The convective momentum terms in Eq. 9.7 are neglected because these terms are assumed to be small compared to the inertial and diffusive terms. Furthermore, the $\frac{\partial v}{\partial x_d}$ term requires the tangential velocity gradient, which can not be obtained solely through information within the integration point. Finally, the time derivative is discretised through a θ-scheme, resulting in:

$$\rho_f\left(\frac{1}{\theta\Delta t}(v^{t+\Delta t}-v^t)+(1-\frac{1}{\theta})\dot{v}^t\right)+\frac{\partial p_d}{\partial x_d}-\mu\frac{\partial^2 v}{\partial y_d^2}=0 \tag{9.9}$$

This time-discretised equation not only depends on the current velocity $v^{t+\Delta t}$, but also on the history of the velocity at the old time step, $\dot{v}^t$ and v^t. This makes it impossible to describe the velocity profile through an analytic solution, as is usually done for sub-grid models. Instead, the velocity profile within the integration points is discretised through a finite element scheme:

$$v=\sum_{el}^{n_{el}}\boldsymbol{N}_v^{el}(\xi)\boldsymbol{v}^{el} \tag{9.10}$$

using the Bézier extracted NURBS $\boldsymbol{N}_v(\xi)$ to discretise the fracture height using the parametric coordinate $\xi=\frac{2}{h}y_d$. This allows the same NURBS discretisation to be used for all velocity profiles inside all integration points, without needing to re-mesh the fracture height. To enforce the no-slip boundary condition from Eq. 9.8 the spline basis functions that are non-zero at the walls are removed, as shown in Figure 9.1. The discretisation from Eq. 9.10 is used for the new velocity $v^{t+\Delta t}$, and the old and change in velocity which are updated at the end of each converged time step.

Using this discretisation, the weak form of Eq. 9.9 is discretised as:

$$\frac{h}{2}\int_{-1}^{1}\rho_f\boldsymbol{N}_v^T\left(\frac{1}{\theta\Delta t}(\boldsymbol{N}_v\boldsymbol{v}^{t+\Delta t}-\boldsymbol{N}_v\boldsymbol{v}^t)+(1-\frac{1}{\theta})\boldsymbol{N}_v\dot{\boldsymbol{v}}^t\right)+\boldsymbol{N}_v^T\frac{\partial p_d}{\partial x_d}-\frac{4\mu}{h^2}\left(\frac{\partial \boldsymbol{N}_v}{\partial \xi}\right)^T\frac{\partial \boldsymbol{N}_v}{\partial \xi}\boldsymbol{v}^{t+\Delta t}\mathrm{d}\xi=0 \tag{9.11}$$

which is rewritten to:

$$\frac{\rho_f h^2}{4\mu}\boldsymbol{C}\left(\frac{1}{\theta\Delta t}\boldsymbol{v}^{t+\Delta t}-\frac{1}{\theta\Delta t}\boldsymbol{v}^t+(1-\frac{1}{\theta})\dot{\boldsymbol{v}}^t\right)+\frac{h^2}{4\mu}\frac{\partial p_d}{\partial x_d}\boldsymbol{w}+\boldsymbol{D}\boldsymbol{v}^{t+\Delta t}=\boldsymbol{0} \tag{9.12}$$

using the definitions:

$$\boldsymbol{C}=\int_{-1}^{1}\boldsymbol{N}_v^T\boldsymbol{N}_v\mathrm{d}\xi \tag{9.13}$$

$$\boldsymbol{D}=\int_{-1}^{1}\left(\frac{\partial \boldsymbol{N}_v}{\partial \xi}\right)^T\frac{\partial \boldsymbol{N}_v}{\partial \xi}\mathrm{d}\xi \tag{9.14}$$

$$\boldsymbol{w}=\int_{-1}^{1}\boldsymbol{N}_v^T\mathrm{d}\xi \tag{9.15}$$

These two matrices and vector are solely dependent on the NURBS used for the discretisation, and do not depend on the fracture opening height. This allows these matrices to only be calculated once, and thereafter be used to obtain the velocity profiles for all integration points and time steps.

Using Eq. 9.12, the velocity profile is explicitly given as a function of the pressure gradient and fracture height in the integration point, and history variables as:

$$\boldsymbol{v}^{t+\Delta t}=\boldsymbol{Q}^{-1}\left(\frac{\rho_f h^2}{4\mu}\boldsymbol{C}\left(\frac{1}{\theta\Delta t}\boldsymbol{v}^t-(1-\frac{1}{\theta})\dot{\boldsymbol{v}}^t\right)-\frac{h^2}{4\mu}\frac{\partial p_d}{\partial x_d}\boldsymbol{w}\right) \tag{9.16}$$

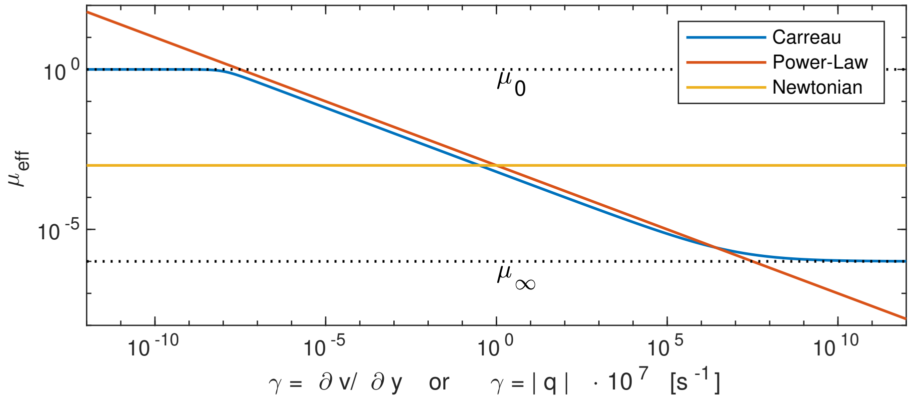

Figure 9.2: Comparison between Newtonian and Carreau fluid models using the properties from section 9.3 and a power-law model ($\mu_0 = 1\ \mathrm{mPa \cdot s}^n$, $n = 0.6$)

with:

$$\boldsymbol{Q} = \frac{\rho_f h^2}{4\mu\theta\Delta t}\boldsymbol{C} + \boldsymbol{D} \tag{9.17}$$

Finally, integrating the obtained velocity profile results in the fluid flux at the integration point:

$$q_x = \frac{h}{2}\boldsymbol{w}^T\boldsymbol{v}^{t+\Delta t} = \boldsymbol{w}^T\boldsymbol{Q}^{-1}\left(\frac{\rho_f h^3}{8\mu}\boldsymbol{C}\left(\frac{1}{\theta\Delta t}\boldsymbol{v}^t - (1-\frac{1}{\theta})\dot{\boldsymbol{v}}^t\right) - \frac{h^3}{8\mu}\frac{\partial p_d}{\partial x_d}\boldsymbol{w}\right) \tag{9.18}$$

which is used in Eq. 9.5 to include the fluid flow within the fracture. The derivatives required to fully integrate Eq. 9.18 into a single monolithic scheme and obtain a quadratic convergence rate are given as:

$$\frac{\partial q_x}{\partial \frac{\partial p_d}{\partial x_d}} = -\frac{h^3}{8\mu}\boldsymbol{w}^T\boldsymbol{Q}^{-1}\boldsymbol{w} \tag{9.19}$$

and

$$\begin{aligned}\frac{\partial q_x}{\partial h} =& \boldsymbol{w}^T\boldsymbol{Q}^{-1}\left(\frac{3\rho_f h^2}{8\mu}\boldsymbol{C}\left(\frac{1}{\theta\Delta t}\boldsymbol{v}^t - (1-\frac{1}{\theta})\dot{\boldsymbol{v}}^t\right) - \frac{3h^2}{8\mu}\frac{\partial p_d}{\partial x_d}\boldsymbol{w}\right)\\ &-\boldsymbol{w}^T\boldsymbol{Q}^{-1}\left(\frac{\rho_f h}{2\mu\theta\Delta t}\boldsymbol{C}\right)\boldsymbol{Q}^{-1}\left(\frac{\rho_f h^3}{8\mu}\boldsymbol{C}\left(\frac{1}{\theta\Delta t}\boldsymbol{v}^t - (1-\frac{1}{\theta})\dot{\boldsymbol{v}}^t\right) - \frac{h^3}{8\mu}\frac{\partial p_d}{\partial x_d}\boldsymbol{w}\right)\end{aligned} \tag{9.20}$$

If a single quadratic element, Figure 9.1b, is used to discretise the velocity profile, this profile will be the shape of a fully developed Newtonian fluid their velocity profile (a parabola). For this case, the matrices used in the discretisation become scalars: $\boldsymbol{C} = 4/15$, $\boldsymbol{D} = 2/3$, and $\boldsymbol{w}^T = 2/3$. As a result, the fluid flux from Eq. 9.18 is given for a quadratic velocity profile as:

$$q_x = \left(\frac{\rho_f h^2}{10\mu\Delta t} + 1\right)^{-1}\left(\frac{\rho_f h^3}{30\mu}\left(\frac{1}{\theta\Delta t}\boldsymbol{v}^t - (1-\frac{1}{\theta})\dot{\boldsymbol{v}}^t\right) - \frac{h^3}{12\mu}\frac{\partial p_d}{\partial x_d}\right)$$

which, in the case of negligible inertia ($\rho_f h^2 << 10\mu\Delta t$) reduces to the cubic law, $q_x = -\frac{h^3}{12\mu}\frac{\partial p_d}{\partial x_d}$.

9.2. Extension to Carreau fluids

The ability of the numerical sub-grid model to represent fluids for which no analytic velocity profile is available is demonstrated by extending the previously derived equations to a Carreau fluid [48]. In contrast to power-law fluids, a Carreau fluid uses an upper limit μ_0 and a lower limit μ_∞ for the effective viscosity, and smoothly transitions between these two extremes. The effective viscosity is given as a function of shear rate $\dot{\gamma}$ as:

$$\mu_{eff} = \mu_\infty + \left(\mu_0 - \mu_\infty\right)\left(1 + a_c^2\dot{\gamma}^2\right)^{(n-1)/2} \tag{9.21}$$

using the same non-Newtonian fluid index as used for power-law fluids. The constant a_c indicates the required shear rate to transition from the viscosity limits. A comparison between these fluid models is shown in Figure 9.2. The shear rate inside the fracture is defined as $\dot{\gamma} = \partial v/\partial y_d$, and approximated in the porous material as $\dot{\gamma} = |\boldsymbol{q}|/(c\sqrt{k})$ [77, 160, 170]. The coefficient c corrects for the influence of the small-scale geometry of the porous material on the shear rate, fulfilling a similar function as k_f^* from Eq. 2.13. However, where a clear definition of this factor is available for power-law fluids, no such definition exists for Carreau fluids and this factor is usually determined experimentally.

9.2.1. Porous material

The mass and momentum balance from Eqs. 9.1 and 9.2 are both valid for a non-Newtonian fluid, with the only change being the definition of the fluid flux from Eq. 9.3. This fluid flux is now given by:

$$\begin{aligned}
&-\nabla p^{t+\Delta t} - \rho_f \boldsymbol{I}_c \ddot{\boldsymbol{u}}^{t+\Delta t} + \frac{\rho_f}{n_f \theta \Delta t}\boldsymbol{q}^t - \frac{\rho_f}{n_f}(1-\frac{1}{\theta})\dot{\boldsymbol{q}}^t = \\
&\left(\frac{\mu_0-\mu_\infty}{k}\left(1+\frac{a_c^2}{c^2k}\left(\boldsymbol{q}^{t+\Delta t}\right)^T\boldsymbol{q}^{t+\Delta t}\right)^{\frac{n-1}{2}} + \frac{\mu_\infty}{k} + \frac{\rho_f}{n_f\theta\Delta t}\right)\boldsymbol{q}^{t+\Delta t}
\end{aligned} \tag{9.22}$$

In contrast to power-law fluids, this equation is not invertible. Therefore, the equation needs to be solved through an iterative process for each integration point inside the porous material to obtain the new fluid flux $\boldsymbol{q}^{t+\Delta t}$, which can then be used in Eqs. 9.1 and 9.2. This iterative process is given, in discretised form, as:

$$\frac{\partial RHS}{\partial \boldsymbol{q}^{t+\Delta t}}\Delta\boldsymbol{q}_j^{t+\Delta t} = LHS - RHS_j \tag{9.23}$$

using the definitions:

$$\begin{aligned}
LHS = &-\nabla \boldsymbol{N}_f \boldsymbol{p}^{t+\Delta t} - \rho_f \boldsymbol{I}_c \boldsymbol{N}_s\left(\frac{1}{\beta\Delta t^2}\left(\boldsymbol{u}^{t+\Delta t} - \boldsymbol{u}^t\right) - \frac{1}{\beta\Delta t}\dot{\boldsymbol{u}}^t - \left(\frac{1}{2\beta}-1\right)\ddot{\boldsymbol{u}}^t\right) \\
&+ \frac{\rho_f}{n_f\theta\Delta t}\boldsymbol{q}^t - \frac{\rho_f}{n_f}(1-\frac{1}{\theta})\dot{\boldsymbol{q}}^t
\end{aligned} \tag{9.24}$$

$$RHS_j = \left(\frac{\mu_0-\mu_\infty}{k}\left(1+\frac{a_c^2}{c^2k}\left(\boldsymbol{q}_j^{t+\Delta t}\right)^T\boldsymbol{q}_j^{t+\Delta t}\right)^{\frac{n-1}{2}} + \frac{\mu_\infty}{k} + \frac{\rho_f}{n_f\theta\Delta t}\right)\boldsymbol{q}_j^{t+\Delta t} \tag{9.25}$$

$$\begin{aligned}
\frac{\partial RHS}{\partial \boldsymbol{q}^{t+\Delta t}} = &\left(\frac{\mu_0-\mu_\infty}{k}\left(1+\frac{a_c^2}{c^2k}\left(\boldsymbol{q}_j^{t+\Delta t}\right)^T\boldsymbol{q}_j^{t+\Delta t}\right)^{\frac{n-1}{2}} + \frac{\mu_\infty}{k} + \frac{\rho_f}{n_f\theta\Delta t}\right)\boldsymbol{I}_2 \\
&+ (n-1)\frac{a_c^2}{c^2k}\frac{\mu_0-\mu_\infty}{k}\left(1+\frac{a_c^2}{c^2k}\left(\boldsymbol{q}_j^{t+\Delta t}\right)^T\boldsymbol{q}_j^{t+\Delta t}\right)^{\frac{n-3}{2}}\boldsymbol{q}_j^{t+\Delta t}\boldsymbol{q}_j^{t+\Delta t\,T}
\end{aligned} \tag{9.26}$$

with $\boldsymbol{I}_2$ the 2×2 identity matrix. Once a converged fluid flux is obtained, this flux is used in Eqs.9.1 and 9.2, with the tangential matrix required to obtain a quadratic convergence rate for the complete monolithic scheme defined as:

$$\frac{\partial \boldsymbol{q}^{t+\Delta t}}{\partial p^{t+\Delta t}} = \left(\frac{\partial RHS}{\partial \boldsymbol{q}^{t+\Delta t}}\right)^{-1} \left(-\boldsymbol{\nabla N}_f\right) \tag{9.27}$$

$$\frac{\partial \boldsymbol{q}^{t+\Delta t}}{\partial \boldsymbol{u}^{t+\Delta t}} = \left(\frac{\partial RHS}{\partial \boldsymbol{q}^{t+\Delta t}}\right)^{-1} \left(-\frac{\rho_f}{\beta \Delta t^2} \boldsymbol{I}_c \boldsymbol{N}_s\right) \tag{9.28}$$

using the new fluid flux in the integration points to obtain $\partial RHS / \partial \boldsymbol{q}^{t+\Delta t}$ from Eq. 9.26.

9.2.2. FRACTURE FLOW MODEL

The equivalent of Eq. 9.7, the momentum balance in x_d direction inside the fracture becomes for a Carreau fluid:

$$\frac{\rho_f}{\theta \Delta t}\left(v^{t+\Delta t} - v^t\right) + \rho_f \left(1 - \frac{1}{\theta}\right) \dot{v}^t + \frac{\partial p_d^{t+\Delta t}}{\partial x_d} - \frac{\partial}{\partial y_d}\left(\left(\mu_\infty + (\mu_0 - \mu_\infty)\left(1 + a_c^2 \left(\frac{\partial v^{t+\Delta t}}{\partial y_d}\right)^2\right)^{\frac{n-1}{2}}\right) \frac{\partial v^{t+\Delta t}}{\partial y_d}\right) = 0 \tag{9.29}$$

which is discretised in a form similar to Eq. (9.12):

$$\frac{\rho_f h^2}{4\mu_\infty} \boldsymbol{C} \left(\frac{1}{\theta \Delta t} \boldsymbol{v}^{t+\Delta t} - \frac{1}{\theta \Delta t} \boldsymbol{v}^t + (1 - \frac{1}{\theta}) \dot{\boldsymbol{v}}^t\right) + \frac{h^2}{4\mu_\infty} \frac{\partial p_d}{\partial x_d} \boldsymbol{w} + \left(\boldsymbol{D} + \frac{\mu_0 - \mu_\infty}{\mu_\infty} \boldsymbol{D}_{nn}\right) \boldsymbol{v}^{t+\Delta t} = \boldsymbol{0} \tag{9.30}$$

with $\boldsymbol{C}$, $\boldsymbol{D}$, and $\boldsymbol{w}$ as in Eqs. (9.13)-(9.15). The non-linear term representing the behaviour of the Carreau fluid is given by:

$$\boldsymbol{D}_{nn} = \int_{-1}^{1} \left(\frac{\partial \boldsymbol{N}_v}{\partial \xi}\right)^T \left(1 + \frac{4a_c^2}{h^2} \left(\frac{\partial \boldsymbol{N}_v}{\partial \xi} \boldsymbol{v}^{t+\Delta t}\right)^2\right)^{\frac{n-1}{2}} \frac{\partial \boldsymbol{N}_v}{\partial \xi} \,\mathrm{d}\xi \tag{9.31}$$

Equation 9.30 is iteratively solved through:

$$\boldsymbol{Q}_{nn} \Delta \boldsymbol{v}_{j+1}^{t+\Delta t} = -\frac{\rho_f h^2}{4\mu_\infty} \boldsymbol{C} \left(\frac{1}{\theta \Delta t} \boldsymbol{v}_j^{t+\Delta t} - \frac{1}{\theta \Delta t} \boldsymbol{v}^t + (1 - \frac{1}{\theta}) \dot{\boldsymbol{v}}^t\right) - \frac{h^2}{4\mu_\infty} \frac{\partial p_d}{\partial x_d} \boldsymbol{w} - \left(\boldsymbol{D} + \frac{\mu_0 - \mu_\infty}{\mu_\infty} \boldsymbol{D}_{nnj}\right) \boldsymbol{v}_j^{t+\Delta t} \tag{9.32}$$

with the tangential matrix given by:

$$\boldsymbol{Q}_{nn} = \left(\frac{\rho_f h^2}{4\mu_\infty \theta \Delta t} \boldsymbol{C} + \boldsymbol{D} + \frac{\mu_0 - \mu_\infty}{\mu_\infty} \frac{\partial \boldsymbol{D}_{nn} \boldsymbol{v}^{t+\Delta t}}{\partial \boldsymbol{v}^{t+\Delta t}}\right) \tag{9.33}$$

with:

$$\frac{\partial \boldsymbol{D}_{nn} \boldsymbol{v}^{t+\Delta t}}{\partial \boldsymbol{v}^{t+\Delta t}} = \boldsymbol{D}_{nn} + \int_{-1}^{1} \frac{4a_c^2 (n-1)}{h^2} \left(1 + \frac{4a_c^2}{h^2} \left(\frac{\partial \boldsymbol{N}_v}{\partial \xi} \boldsymbol{v}^{t+\Delta t}\right)^2\right)^{\frac{n-3}{2}} \left(\frac{\partial \boldsymbol{N}_v}{\partial \xi} \boldsymbol{v}^{t+\Delta t}\right)^2 \left(\frac{\partial \boldsymbol{N}_v}{\partial \xi}\right)^T \frac{\partial \boldsymbol{N}_v}{\partial \xi} \,\mathrm{d}\xi \tag{9.34}$$

The converged velocity profile is used in Eq. 9.18 to obtain the fluid flux inside the fracture, and used in 9.5 to incorparate the fluid flow inside the fracture in the description of the porous material. Finally, the matrices required to fully integrate the fracture scale model with the monolithic solver are given by:

$$\frac{\partial q_x}{\partial \frac{\partial p_d^{t+\Delta t}}{\partial x_d}} = -\frac{h^3}{8\mu_\infty} \boldsymbol{w}^T \boldsymbol{Q}_{nn}^{-1} \boldsymbol{w} \tag{9.35}$$

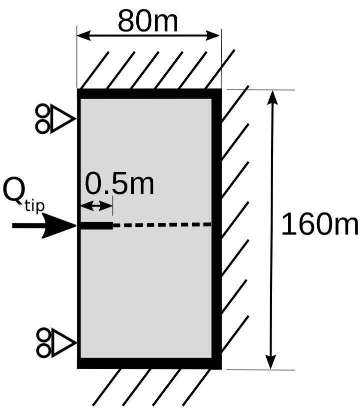

Figure 9.3: Overview of the simulated domain

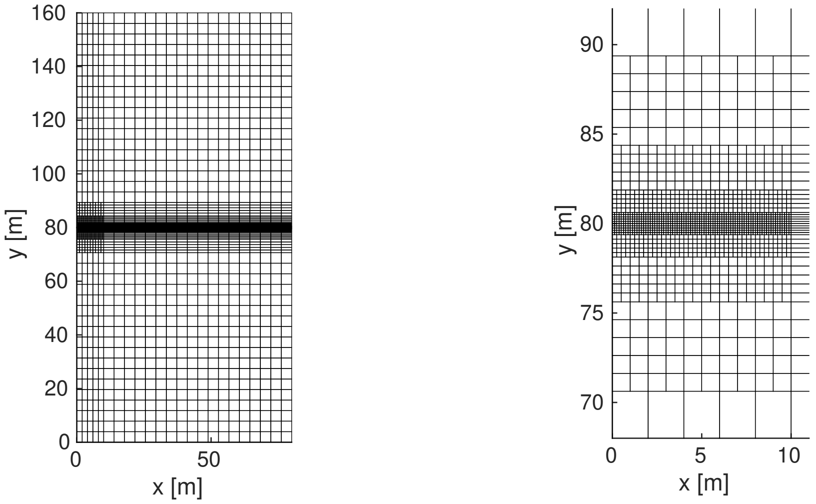

(a) Total mesh

(b) Zoomed around discontinuity

Figure 9.4: Discretisation used for the numerical subgrid cases

$$
\begin{aligned}
\frac{\partial q_x}{\partial h} = \frac{1}{2}\boldsymbol{w}^T\boldsymbol{v}^{t+\Delta t} - \frac{h}{2}\boldsymbol{w}^T\boldsymbol{Q}_{nn}^{-1}\Bigg(\frac{2\rho_f h}{4\mu_\infty}\boldsymbol{C}\left(\frac{1}{\theta\Delta t}\boldsymbol{v}^{t+\Delta t} - \frac{1}{\theta\Delta t}\boldsymbol{v}^t + (1-\frac{1}{\theta})\dot{\boldsymbol{v}}^t\right) \\
+\frac{2h}{4\mu_\infty}\frac{\partial p_d^{t+\Delta t}}{\partial x_d}\boldsymbol{w} + \frac{\mu_0-\mu_\infty}{\mu_\infty}\frac{\partial \boldsymbol{D}_{nn}}{\partial h}\boldsymbol{v}^{t+\Delta t}\Bigg)
\end{aligned}
\tag{9.36}
$$

with the derivative of the non-linear diffusion matrix with respect to the height:

$$
\frac{\partial \boldsymbol{D}_{nn}}{\partial h} = -\frac{4a_c^2(n-1)}{h^3}\int_{-1}^{1}\left(\frac{\partial \boldsymbol{N}_v}{\partial \xi}\right)^T\left(1+\frac{4a_c^2}{h^2}\left(\frac{\partial \boldsymbol{N}_v}{\partial \xi}\boldsymbol{v}^{t+\Delta t}\right)^2\right)^{\frac{n-3}{2}}\left(\frac{\partial \boldsymbol{N}_v}{\partial \xi}\boldsymbol{v}^{t+\Delta t}\right)^2\frac{\partial \boldsymbol{N}_v}{\partial \xi}\,\mathrm{d}\xi \tag{9.37}
$$

9.3. RESULTS

To show the capabilities of the numeric subgrid scale model, a typical fracture propagation case is used [163, 206]. This case consists of a 80 × 160 m domain with a 0.5 m fracture in the centre, as shown in Figure 9.3. This fracture is allowed to propagate along a horizontal C^0 continuity line, and has an initial opening height $h_0 = 0.05$ mm. An inflow of $Q_{in} = 0.5\cdot10^{-4}$ m^2/s is imposed on the left fracture tip. The porous material is described using Young's modulus $E = 15$ GPa, Poisson ratio $\nu = 0.2$, solid material density $\rho_s = 2500$ kg/m^3, bulk modulus $K_s = 30$ GPa, porosity $n_f = 0.2$, intrinsic permeability $k = 10^{-14}$ m^2, Biot coefficient $\alpha = 1.0$, Cosserat length scale $\ell = 10$ mm, and Cosserat shear modulus $G_c = 4$ GPa.

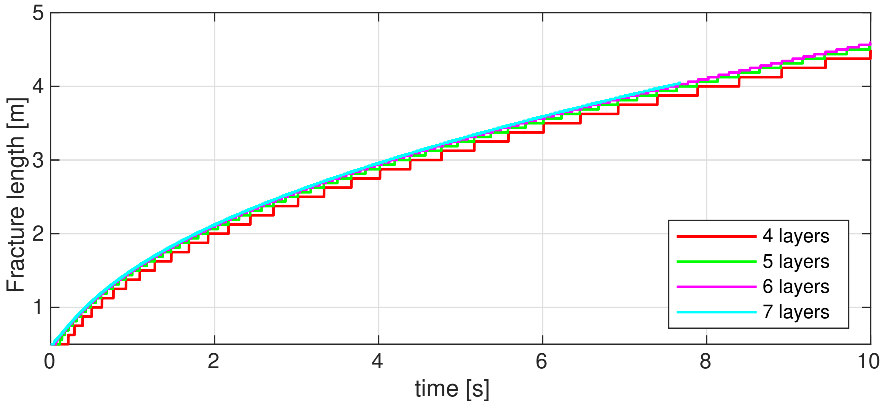

(a) Carreau fluid

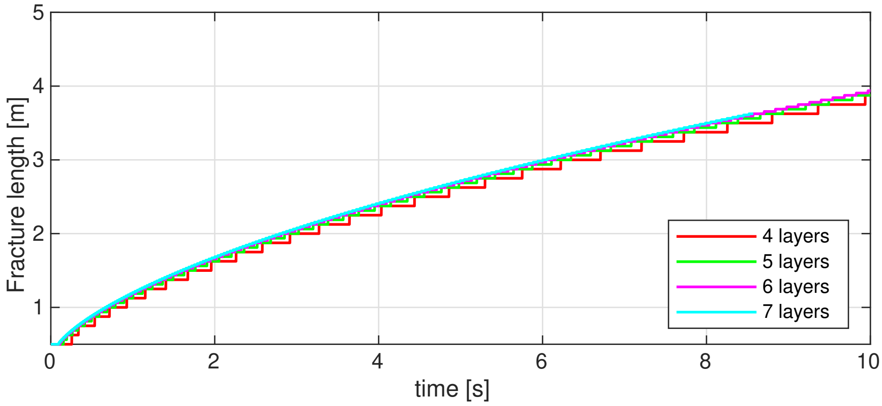

(b) Newtonian fluid

Figure 9.5: Fracture propagation length resulting from the mesh refinement study using $\Delta t = 1$ ms and 5 quartic fracture-scale elements

The discontinuity is described using interface permeability $k_i = 10^{-10}$ m/Pas and an exponential traction-separation law with tensile strength $f_t = 0.1$ MPa and fracture energy $\mathcal{G}_c = 100$ N/m. Two different fluids have been used for the simulations, a Newtonian water-like fluid and a shear thinning fluid. Both these fluids use density $\rho_f = 10^3$ kg/m^3 and bulk modulus $K_f = 1$ GPa, and the Newtonian fluid uses viscosity $\mu = 10^{-3}$ Pa s, whereas the viscosity of the shear-thinning Carreau fluid is described through the fluid index $n = 0.6$, viscosity limits $\mu_0 = 1$ Pa s and $\mu_\infty = 10^{-6}$ Pa s, and the constants $c = 1$, $a_c = 10^8$ s. This results in the shear-rate dependence shown in Figure 9.2.

The domain is discretised using quartic T-splines for the solid deformations, and cubic T-splines for the Cosserat microrotation, and interstitial and discontinuity fluid pressures. Since most of the relevant phenomena occur near the discontinuity, small elements are used near the discontinuity while coarser elements are used near the top, right, and bottom boundaries, resulting in distinct refinement layers as shown in Figure 9.4. The four refinement layer mesh uses small elements with $dx = dy = 0.125$ m, with every additional refinement layer halving the element size, resulting in the five layer mesh with element size $dx = dy = 62.5$ mm, 6 layer mesh with element size $dx = dy = 31.25$ mm, and 7 layer mesh with element size $dx = dy = 15.625$ mm near the discontinuity. The fracture scale discretisation was performed using 20 quartic spline-based elements. The temporal discretisation is performed using $\beta = 0.4$, $\gamma = 0.75$, $\theta = 1.0$, and using time step size $\Delta t = 1$ ms for the mesh refinement study, whereas the timestep refinement study used $\Delta t = 100$ ms, $\Delta t = 10$ ms, $\Delta t = 1$ ms, $\Delta t = 0.1$ ms, $\Delta t = 0.01$ ms. All simulations were performed for a total dura-

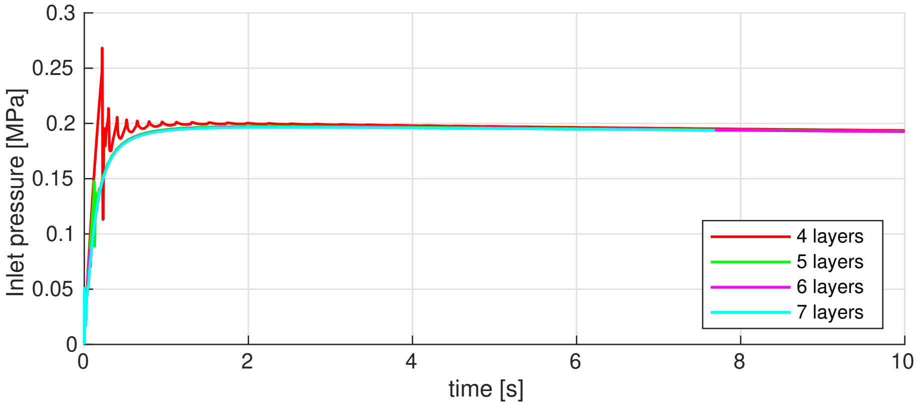

(a) Carreau fluid

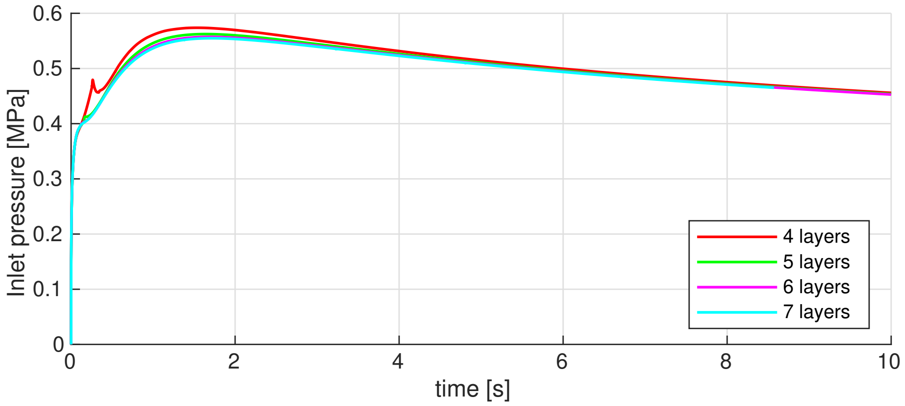

(b) Newtonian fluid

Figure 9.6: Discontinuity pressure at the inlet resulting from the mesh refinement study using $\Delta t =$ 1 ms and 5 quartic fracture-scale elements

tion of 10 s, with the exception of the simulations using the 7 layer mesh or using the finest timesteps 0.1 ms and 0.01 ms, which were terminated once they coincided with the results from coarser meshes and timesteps.

9.3.1. MESH AND TIMESTEP REFINEMENT

The resulting fracture propagation lengths using the different mesh refinement levels are shown in Figure 9.5. While the effect of the element-wise propagation associated with interface elements is clearly visible for the coarser meshes, even these meshes obtain a correct fracture propagation length. The discontinuity pressure at the inlet of the fracture is shown in Figure 9.6. For a Newtonian fluid, the coarsest mesh shows a pressure oscillation at the moment the first new element fractures, with this pressure peak disappearing upon mesh refinement. Stronger oscillations occur for the Carreau fluid, with these oscillations again coinciding with the fracture propagation steps. Upon mesh refinement, these oscillations decrease in magnitude while increasing in frequency, confirming that they are an effect of the element-wise propagation and the sudden increase in fracture volume caused by it.

The inlet discontinuity pressure resulting from the time step refinement study using the six layer mesh are shown in Figure 9.7. The results for the Newtonian fluid are not dependent on the time step size, with even the coarsest time step providing corrects results. For the Carreau fluid, however, refining the time step results in larger and more frequent oscillations near the start of the simulation and the onset of the fracture propagation. These pressure oscillations are also shown in Figure 9.8. The coarsest time step does not display these

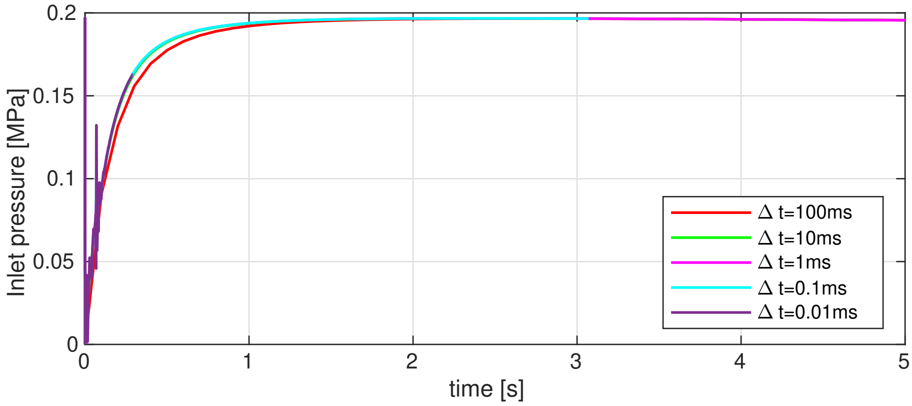

(a) Carreau fluid

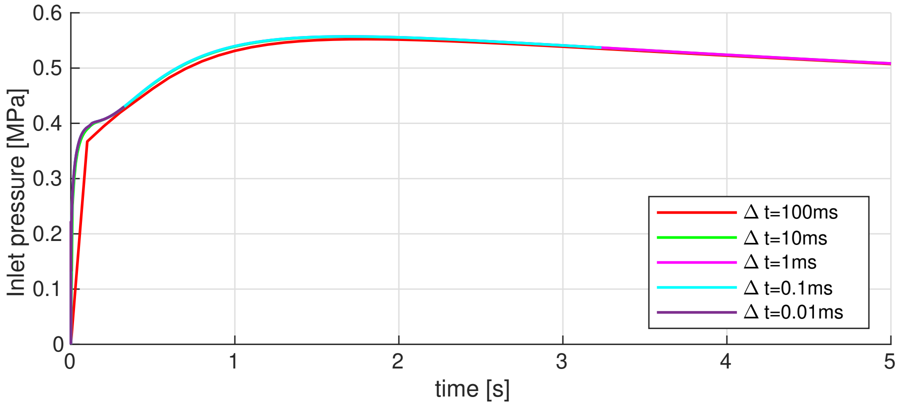

(b) Newtonian fluid

Figure 9.7: Discontinuity pressure at the inlet resulting from the timestep refinement study using the six layer mesh and 5 quartic fracture-scale elements

oscillations, since their frequency is much higher than the timestep size. Using $\Delta t = 10$ s shows the initial oscillation, and using $\Delta t = 1$ s shows some oscillations for both the start of the simulation, and the moment of first fracture propagation. However, very small time steps are needed to properly capture the magnitude of these oscillations, with only the two smallest time steps capturing the pressure peaks resulting from the fracture propagation.

The pressure inside the complete discontinuity using the smallest time step is shown in Figure 9.9a for the start of the simulation. At this start, a large increase in pressure occurs to enforce the imposed fracture inflow while overcoming the effects of the fluid inertia. However, it is likely that most of the pressure oscillations seen at $t = 0.1$ ms are due to the inability of the discretisation to correctly represent the strong pressure gradient near this inlet, and not caused by any physical phenomena. Once created, these pressure oscillations start to travel through the fracture while diffusing over time. Similar travelling pressure waves are created at the onset of fracture propagation, as shown in Figure 9.9b, with the sudden increase in fracture volume causing a sharp decrease in fluid pressure. Even though most of these pressure oscillations are unlikely to have a physical origin, their behaviour once created shows the abilities of the numerical fracture flow model to include inertial effect inside the fracture. Although the velocity profile is solely determined from history variables within the integration points, and solely uses the pressure gradient and opening height from the macro scale discretisation, this seems sufficient to consistently include the interactions between the sub-grid schemes in the integration points.

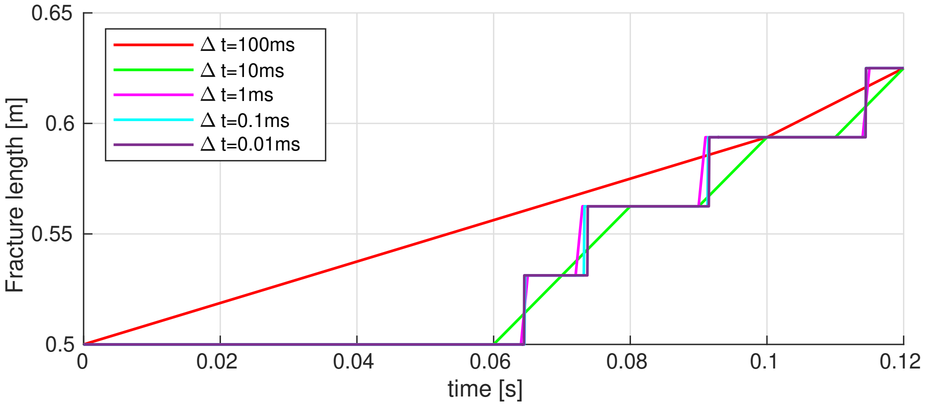

(a) Fracture length

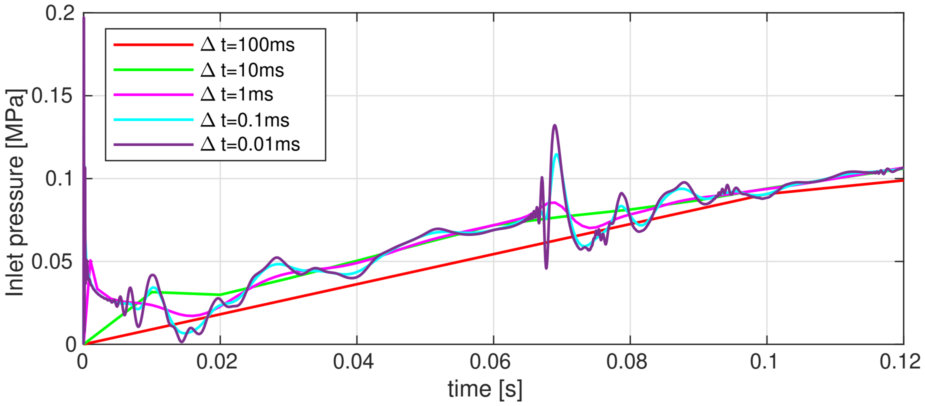

(b) Discontinuity pressure at the inlet

Figure 9.8: Results near the start of the simulations for the timestep refinement study for a Carreau fluid using the six layer mesh and 5 quartic fracture-scale elements

9.3.2. FRACTURE SCALE MESH REFINEMENT

The height discretisation used for the fracture scale model is varied while using a constant time step size $\Delta t = 1$ ms and using the six layer mesh. The pressures inside the discontinuity at $t = 1$ s are shown in Figure 9.11. Small differences are seen for the Newtonian fluid using the linear and quadratic discretisation, while no differences occur upon further increasing the discretisation order and using finer elements. This is explained by the velocity profile inside the fracture corresponding to a quadratic parabola, Figure 9.10a. Due to the small fracture opening and relatively long simulation time inertial effects are negligible, resulting in a single quadratic spline exactly resolving the velocity profile, and therefore sufficing for the discretisation.

Slightly larger differences occur for the Carreau fluid, Figures 9.11b and 9.10b. Since the velocity profile is no longer a quadratic parabola, using quartic elements and using five elements changes the obtained profile. However, these changes are small, and therefore the effect of the discretisation on the discontinuity pressure is limited. This indicates that an approximation of the velocity profile suffices to obtain accurate pressures inside the discontinuity, whereas a finer discretisation is required to accurately capture the velocity profile itself.

9.3.3. INITIAL OPENING HEIGHT

Velocity profiles for the simulations using a Newtonian fluid with varying initial opening heights are shown in Figure 9.12. In contrast to the previous subsection, these profiles show

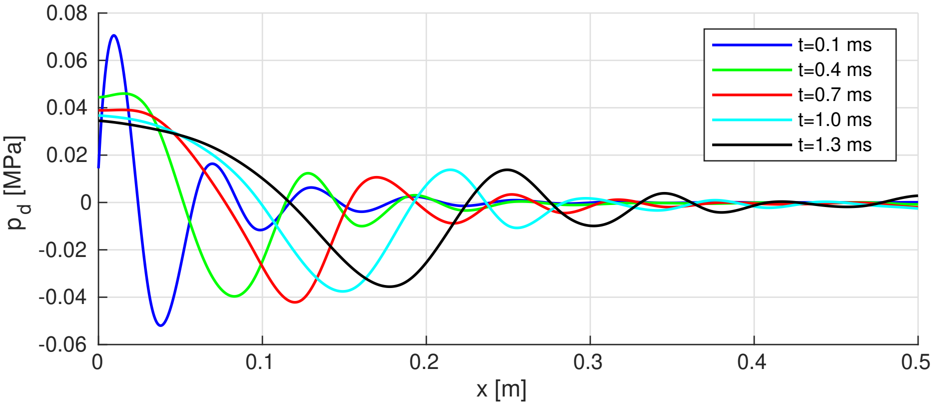

(a) Start of the simulations

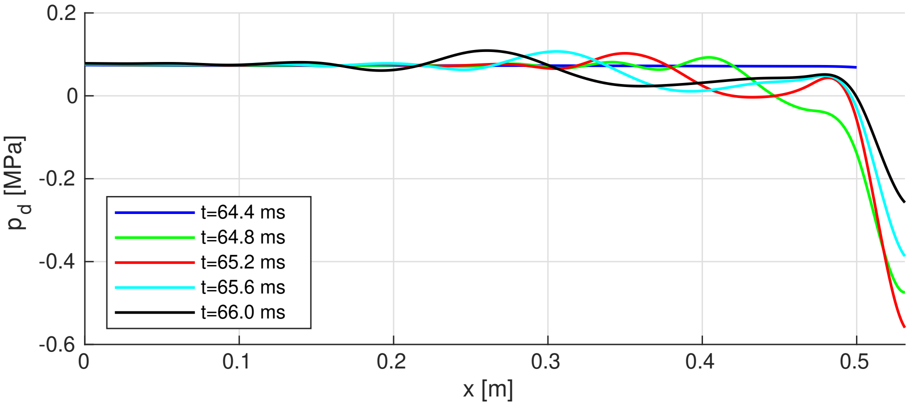

(b) Moment of first fracture propagation

Figure 9.9: Pressure waves inside the discontinuity using $\Delta t = 0.01$ ms

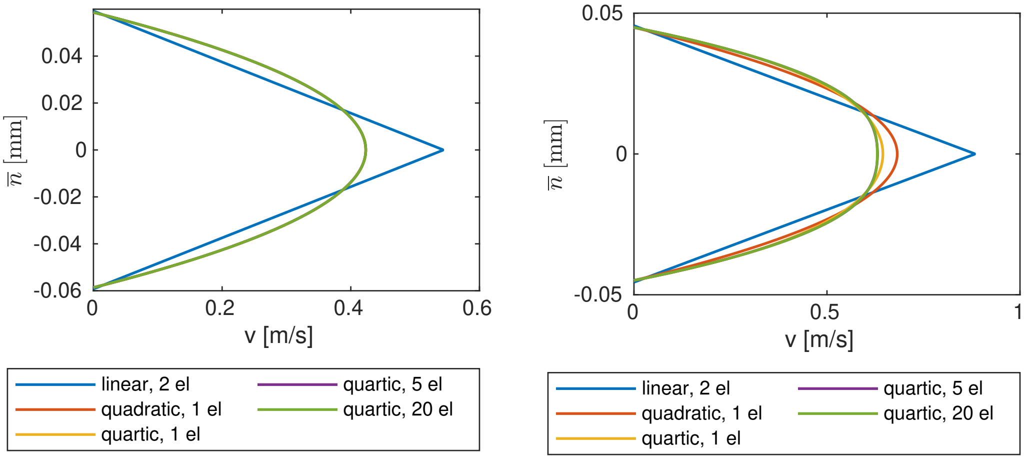

(a) Newtonian fluid

(b) Carreau fluid

Figure 9.10: Effect of the discretisation on the fluid velocity profile at $x = 0.25$ m, $t = 1$ s

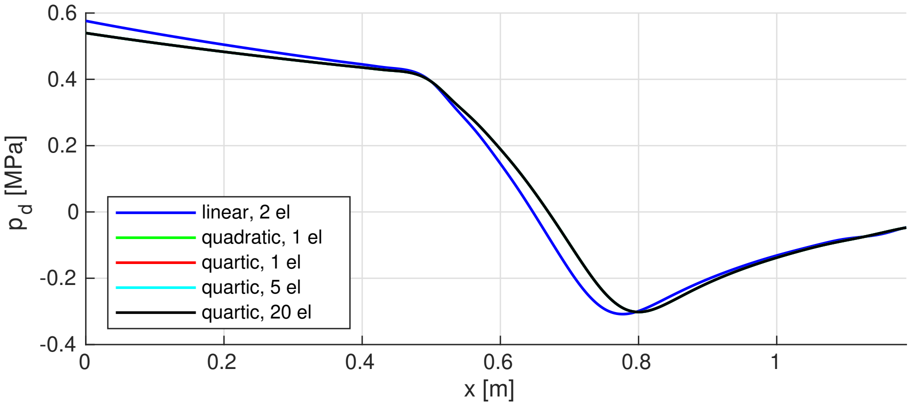

(a) Newtonian fluid

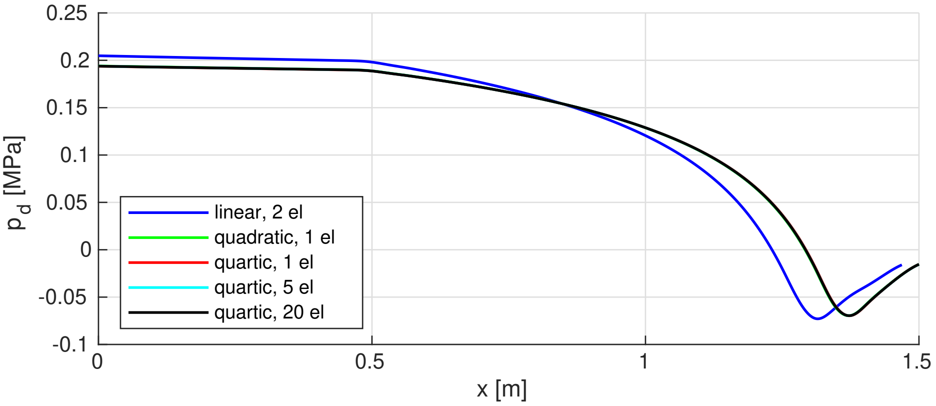

(b) Carreau fluid

Figure 9.11: Effect of the discretisation on the discontinuity pressure at $t = 1$ s

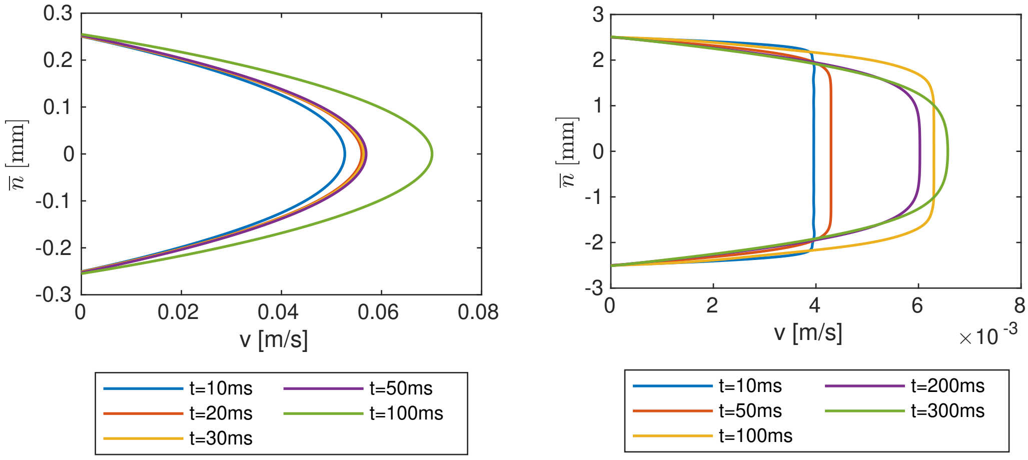

(a) $h_0 = 0.5$ mm (b) $h_0 = 5$ mm

Figure 9.12: Fluid velocity profile at $x = 0.25$ m for varying initial opening heights

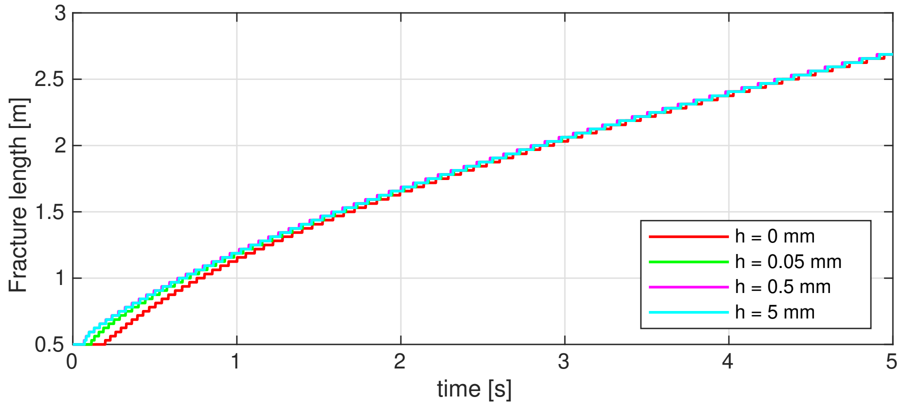

(a) Newtonian fluid

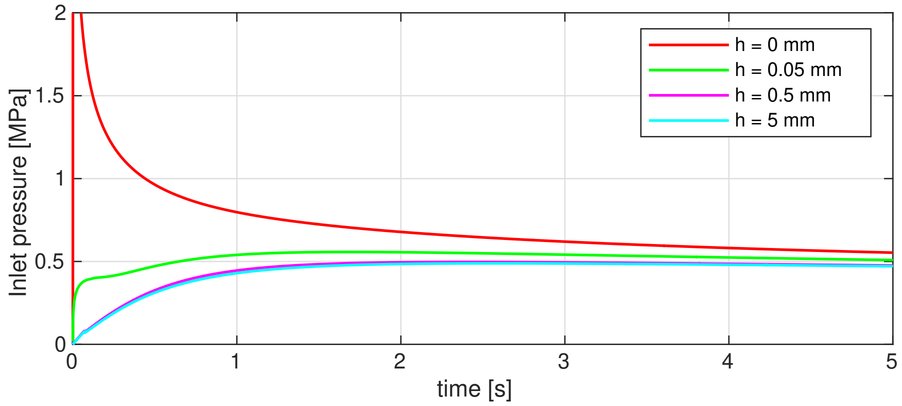

(b) Carreau fluid

Figure 9.13: Effect of initial opening height on the discontinuity pressure at the left boundary.

a large influence of the fluid inertia, thereby deviating from a fully developed parabolic profile. Since the response time of the fluid inside the fracture scales approximately with $\rho_f h^2/\mu$, providing a large offset to the fracture opening greatly increases the importance of the inertia terms. The profiles for the $h_0 = 5$ mm case highlight the ability of the derived model to represent inertial effects, and the strong velocity gradients near the wall when a sufficiently fine discretisation is employed.

The effect of the initial opening height on the propagation velocity is shown in Figure 9.13. When no initial height is present, these solutions approximate the analytic solution for a simplified case [217]. Increasing the initial opening height allows the fluid to flow through the fracture easier, thereby reducing the pressure required to move the nearly incompressible fluid, and thus reducing the inlet pressure. However, these effects are limited to the start of the simulation. The fracture length is nearly independent of the opening height, and the inlet pressure approaches a similar value for all cases near the end of the simulations. This indicates that even though a small opening height inhibits the fluid flow, and a large initial opening height causes significant changes in the velocity profile, including these effects has a limited influence on the fracture propagation.

9.4. CONCLUSION

This chapter presented a numeric fracture scale model which allows non-Newtonian fluids and inertial effects to be included in a subgrid scale fracture flow scheme. By numerically resolving the velocity profile in every integration point and coupling this profile to the macro-scale mass conservation fluid behaviour for which no analytic solution exists can be represented.

The capabilities of this model have been demonstrated for Newtonian and non-Newtonian Carreau fluids through the simulation of a typical fracture propagation case. These simulations showed that coarse time steps and meshes suffice to correctly simulate the fracture propagation and macro-scale behaviour, while finer meshes and time steps are required to capture the fluid behaviour inside the discontinuity. When extremely small time steps are used, the presented model is capable of resolving travelling pressure waves inside the discontinuity. This indicates that fluid inertial effects are properly included, and that the coupling between the macro scale pressure gradients and the inertial effects separately resolved within each integration point is strong enough to capture these pressure waves.

When inertial effects are negligible, a single quadratic spline suffices for the discretisation of the fluid velocity profile for a Newtonian fluid. This same discretisation suffices for Carreau fluids to obtain a correct fracture propagation behaviour, while slightly finer meshes are needed to obtain an accurate velocity profile. When the fracture opening is sufficiently high, inertial effects are no longer negligible, and a fine discretisation of the velocity profile is needed to capture the strong velocity gradients near the wall.

10

CONCLUSION

In this thesis, sub-grid models for fluid flows inside fractures in poroelastic material have been presented. These models have been derived, implemented, verified, and used to show the relevance of including the additional physical behaviour included by these models:

- The first model presented was a continuous pressure model extended to describe a non-Newtonian power-law fluid, both inside the fracture and inside the poroelastic material. It was shown that including this non-Newtonian rheology had a significant effect on the fluid transported through the fracture.
- Models were presented for bubbly and separated multiphase flows. These models are able to represent the interactions within the fracture without this interior having to be simulated. These interactions were shown to have a significant influence on the obtained results by comparison with a cubic law formulation. Furthermore, these models allow for a detailed description of the fluid within the fracture to be reconstructed through post-processing.
- The model for power-law fluids was extended to allow for pressurised and propagating fractures. It was shown that shear-thinning fluids have an increased leak-off from the fracture to the surrounding porous material, whereas shear-thickening fluids flow slower through the fracture and thereby obtain lower pressures near the fracture tip. These two effects lead to a significantly different fracture propagation velocity: Depending on the permeability of the porous material, using either shear-thinning or shear-thickening fluids will result in a higher propagation velocity.
- The discontinuous pressure model was compared to simulations which directly simulated the Stokes flow within the fracture. This showed the accuracy of the discontinuous pressure model, which is able to correctly represent the fluid flow within the fracture for reasonable opening heights, and still describes the overall effect of the fracture on the surrounding porous material when the fracture aperture is outside of the assumed limits.
- A numerical two-scale approach was detailed, numerically resolving the velocity profile inside the fracture at each integration point, coupled to the mass conservation equations for the fracture. This two-scale approach allowed for inertial effects within the fracture to be included, and allowed for fluid rheologies for which an analytic velocity profile is not available. It was shown that this model was able to capture travelling pressure waves within the discontinuity when sufficiently small time steps are used, with these pressure waves causing oscillations in the inlet pressure.

In addition to these models, other findings were:

- A continuous pressure model was used to show the advantages of using a spline-based spatial discretisation, with this discretisation allowing for a continuous fracture inflow and interior velocity, whereas this is not attained when using Lagrangian elements.
- A study on the convergence rate of the non-linear solver was performed, studying the effects of including tangential stiffness terms related to the fracture. It was shown that

quadratic convergence was only possible when including all terms related to the fracture, at the cost of having to recalculate the system matrices for each iteration. When using a linear line-search, some of these terms could be omitted while retaining a linear and non-oscillatory convergence rate, which allows for a constant and symmetric stiffness matrix to be used.

- It was shown that the increased continuity of NURBS, combined with their inability to represent only fractured elements, resulted in a non-physical fracture inflow surrounding the fracture tips. To avoid this additional fracture inflow a special tip integration scheme was detailed. It was furthermore shown that a lumped integration scheme in required to prevent fracture inflow velocities.

- The mesh generation for unequal order meshes using T-splines was detailed, inserting interface elements solely to represent the fracture. This was shown to remove the need of using a dummy stiffness and permeability, and removed the need for a special integration scheme around the fracture tip. Simulations showed the effect of using T-splines compared to NURBS, with T-splines obtaining a fully closed fracture at the fracture tip whereas NURBS obtained a small aperture at the tip. In contrast, NURBS were able to represent a sharper decrease in opening height compared to T-splines, but this effect was shown to be localized to only a couple of elements near the fracture tip.

- A scheme was derived which allowed inertial effects of the fluid and solid to be included inside the standard pressure-displacement formulation. It was shown that including the solid inertia term in the fluid flux definition resulted in strong pressure changes around stress waves, but also caused severe oscillations. Adding the fluid inertia as a separate term provided additional damping, removing these oscillations and reducing the magnitude of the pressure and stress waves as they propagate.

- Simulations using a shear fracture showed the interactions between the interstitial fluid pressure and the fracture propagation for fractures propagating near to the wave speed. The propagating fracture results in zones of increased pressure near the fracture tips. Once these zones overtake the tips the fracture propagation pauses until these zones diffuse away. Once the pressure at the fracture tips is reduced, the fracture starts again. This repeats, resulting in pauses in the fracture propagation.

A

Verifications

A.1. Verification Newtonian fluids

A.1.1. One-dimensional case

The Terzaghi consolidation problem has been used for the first verification case [100, 228]. The geometry consists of an 1 mm × 8 mm rectangular domain, as shown in Figure A.1. An external force $\overline{\boldsymbol{\tau}} = 1$ MPa is applied on the top, while the sides are constrained in horizontal direction, and the bottom of the domain in both directions. An initial pressure of $p_0 = 1$ MPa is present at the start of the simulations in the complete domain, and a zero pressure boundary condition is imposed on the bottom. The used parameters are given in Table A.1.

The domain has been discretised using 8 elements in the vertical direction. For the FEM simulations, quadratic interpolants have been used for the solid deformations and fluid pressure, whereas quartic and cubic interpolants have been used for the IGA simulations. A constant time step of $\Delta t = 1$ s has been used.

The analytic solution for this problem is given by [228]:

$$\frac{p}{p_0} = \frac{4}{\pi}\sum_{i=1}^{\infty}\frac{(-1)^{i-1}}{2i-1}cos\left(\frac{\pi}{2}(2i-1)\frac{y}{H}\right)e^{-(2i-1)^2\frac{\pi^2}{4}\frac{c_v t}{H^2}} \tag{A.1}$$

with H the height of the domain, and the consolidation coefficient c_v determined by:

$$c_v = \frac{k}{\mu_0(\frac{1}{M}+\alpha^2 m_v)} \tag{A.2}$$

The confined compressibility m_v is defined as:

$$m_v = \frac{1}{K_s + \frac{4}{3}\frac{E}{2(1+\nu)}} \tag{A.3}$$

The interstitial fluid pressure resulting from the simulations is shown in Figure A.2. The IGA simulation matches almost exactly to the analytic solution, whereas the FEM simulation shows very slight differences. The fluid flux, Figure A.3, has small differences between the IGA and FEM, and the analytic solution. The FEM solution also shows jumps in the fluid flux due to the C^0 inter-element continuity of the pressure, resulting in discontinuous fluid fluxes.

A.1.2. Two-dimensional case

The second Verification case is the finite domain problem described in [129], and consists of a rectangular 11m × 10m domain on which on external load is applied to the middle 1m on the top, as shown in Figure A.4. The deformations at the bottom of the domain are constrained in horizontal and vertical direction, while the sides are constrained in horizontal direction. Zero pressure boundary conditions are present at all boundaries. This domain is discretised using 22 × 20 elements, using quadratic elements for the FEM simulations, while using quartic and cubic NURBS for the IGA simulations. A constant time-step of $\Delta t = 1\cdot 10^5$s has been used, and all other parameters are given in Table A.2.

To compare the simulation results to the results from the analytic solution given in [129], the obtained interstitial pressure p, displacements u_x and u_y, and time t are non-dimensionalised using:

$$t_D = \frac{C_f}{W^2}t \tag{A.4}$$

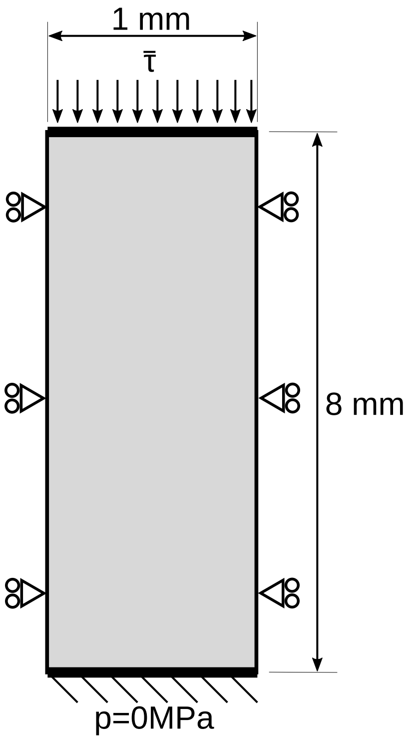

Figure A.1: Geometry of the one-dimensional verification case

Parameter	Value	
a	1	mm
H	8	mm
$\overline{\boldsymbol{\tau}}$	1	MPa
p_0	1	MPa
E	6	GPa
ν	0.4	
n_f	0.5	
α	1	
K_s	3.6	GPa
K_f	3	GPa
k	$4 \cdot 10^{-17}$	m^2
μ_0	20	Pa s
n	1	

Table A.1: Parameters used for the 1D verification case

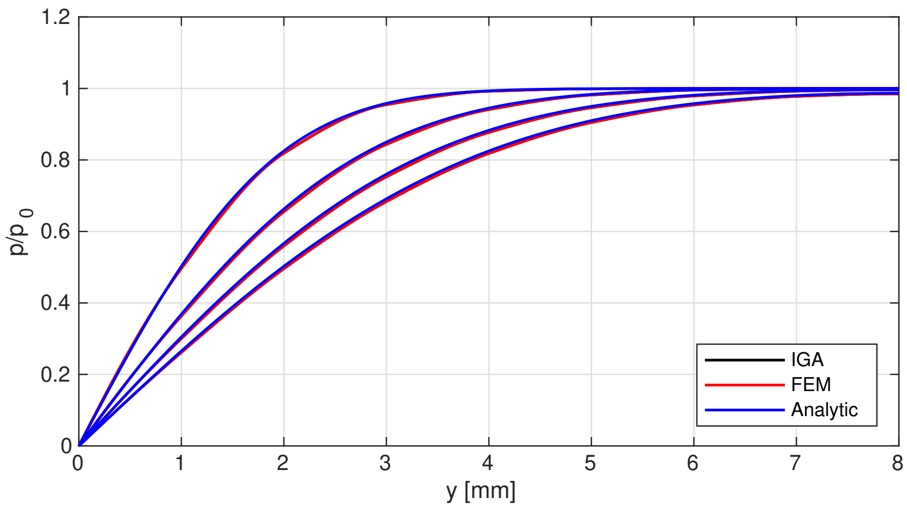

Figure A.2: Fluid pressure at t = 250s, t = 500s, t = 750s, and t = 1000s for the one-dimensional verification case.

$$W_D = \frac{1}{H} u_y \tag{A.5}$$

$$p_D = \frac{1}{\left(\frac{1}{1-2\nu}+1\right)\frac{E}{2(1+\nu)}} p \tag{A.6}$$

The interstitial fluid pressure in the centre of the domain is shown in Figure A.5. The IGA and the FEM results both match to the analytic results, with the IGA results having a slightly higher interstital pressure throughout the simulation. The IGA results for the vertical

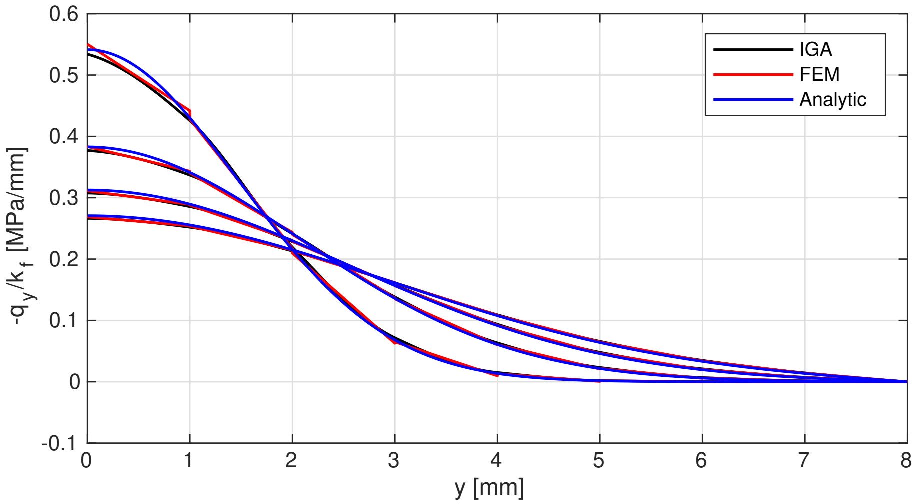

Figure A.3: Fluid flux at $t = 250$s, $t = 500$s, $t = 750$s, and $t = 1000$s for the one-dimensional verification case.

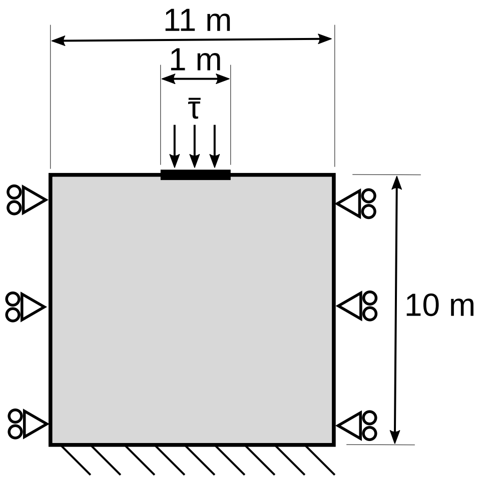

Figure A.4: Geometry of the two-dimensional verification case

Parameter	Value	
$\bar{\boldsymbol{\tau}}$	0.065	MPa
E	3.9494	MPa
ν	0.25	
n_f	0.5	
α	0.94577	
K_s	2.4216	MPa
K_f	2.4216	MPa
k	$7.870 \cdot 10^{-11}$	mm^2
μ_0	1	mPa s
n	1	
W	11	m
H	10	m
C_f/W^2	$1.228 \cdot 10^{-9}$	

Table A.2: Parameters used for the 2D verification case

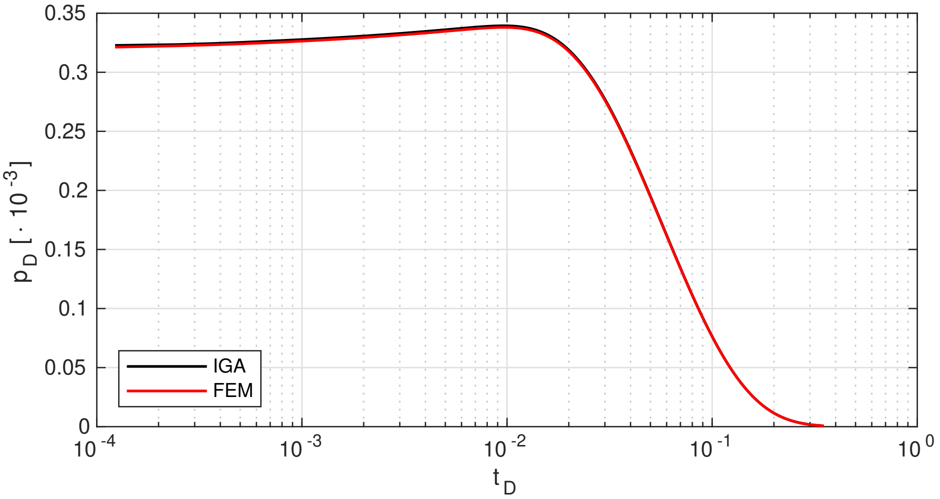

Figure A.5: Interstitial fluid pressure in the centre of the domain.

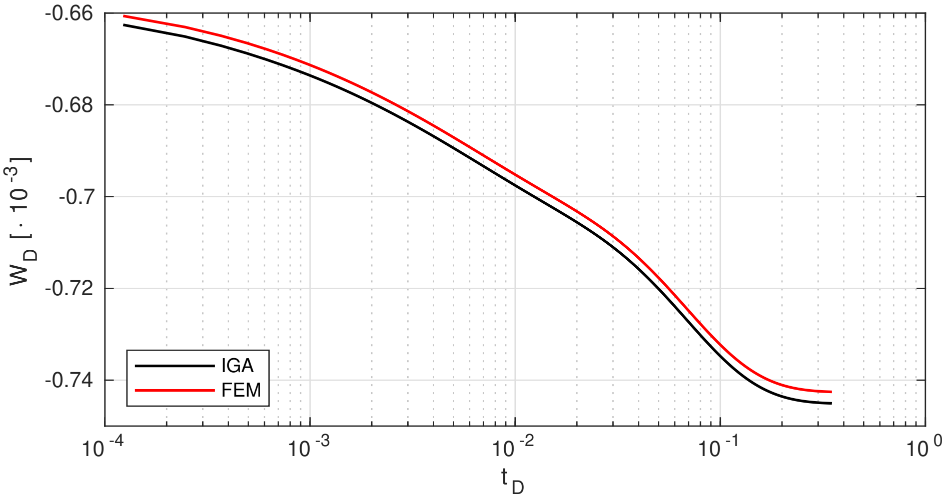

Figure A.6: Vertical displacement in the centre of the domain.

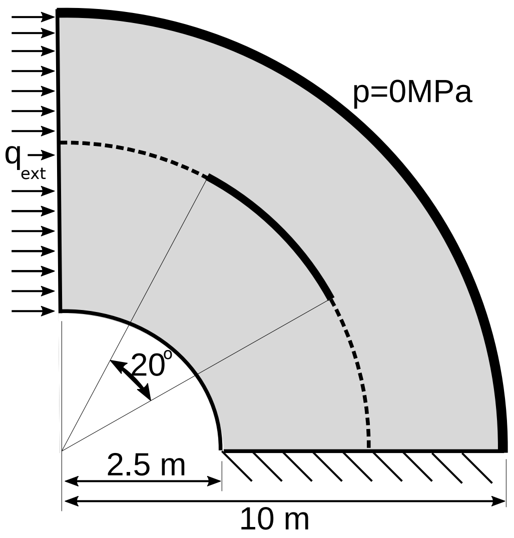

Figure A.7: Geometry of the curved beam verification case

Parameter	Value	
q_{ext}	0.1	m/s
E	9	GPa
ν	0.4	
n_f	0.3	
α	1	
M	$1 \cdot 10^{1}5$	GPa
k	$4 \cdot 10^{-6}$	mm^2
μ_0	1	mPa s
n	1	

Table A.3: Parameters used for the curved beam case

displacement, Figure A.6, also match to the analytic solution. The FEM results have slightly lower vertical displacements, while showing a similar trend as the IGA and analytic results.

A.1.3. CURVED BEAM WITH A FRACTURE

The next verification case is the curved beam problem from [232]. The case consists of a curved beam with an inner radius of 2.5m and an outer radius of 10m. A crack is located in the centre of the beam, at a radius of 6.25m, as shown in Figure A.7. No displacements are allowed at the bottom, while a zero pressure boundary condition is imposed on the outer radius. An external flow $q_{ext} = 0.1$m/s is applied to the left edge, while the bottom and inner radius have no-outflow boundary conditions. Both the FEM and IGA simulations used a mesh of 18×20 elements, and a time-step of $\Delta t = 1.0$s has been used. Interface elements were inserted along the discontinuity, for the fractured and non-fractured elements. An advantage of the NURBS mesh compared to the FEM mesh is that the NURBS are able to exactly represent the curved geometry of the beam, whereas the FEM mesh only approximates the curved geometry by using linear segments.

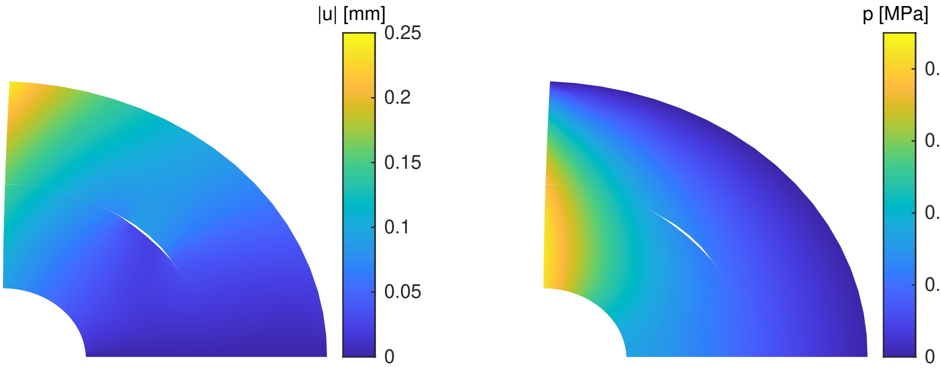

(a) Displacement (b) Pressure

Figure A.8: Deformations and interstitial fluid pressure using IGA after 10s for the curved beam verification case. Deformations are magnified with a factor of 1000.

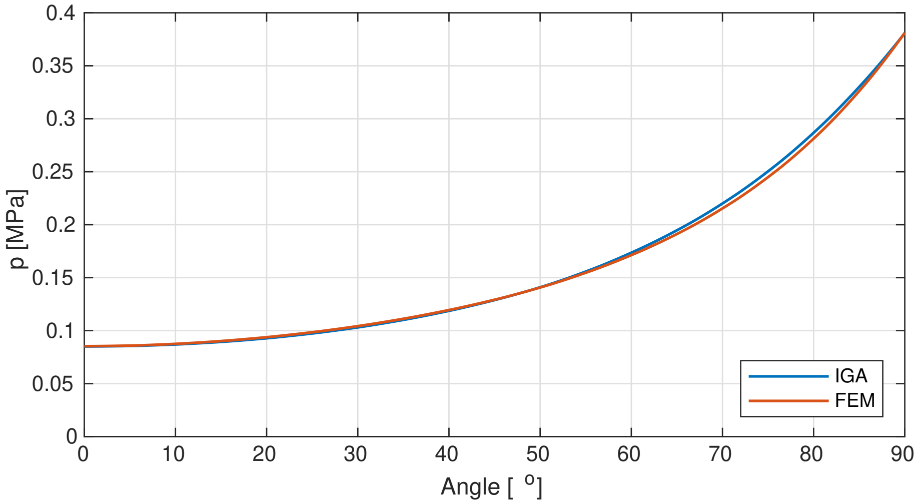

Figure A.9: Pressure along the discontinuity line after $t = 10$s.

The displacement and interstitial pressure resulting from the IGA simulation are shown in Figure A.8. These displacements are visually the same as the displacements obtained through the FEM simulations, and corresponds to the solution provided in [232]. The interstitial fluid pressure along the discontinuity line is shown in Figure A.9. The IGA simulation has a slightly higher pressure, but both simulations correspond to the reference results.

A.1.4. FRACTURED PLATE

The final verification case for Newtonian fluids is the square plate problem from [232]. The case consists of a square plate, with a fluid flux imposed at the bottom and a zero pressure boundary condition at the top. The middle of the plate contains a fracture under an angle γ, with a horizontal length of 4m, as shown in Figure A.10. The fracture is not allowed to propagate. The domain has been discretised using 40×20 elements, and interface elements have been inserted for the fractured and non-fractured parts of the discontinuity line. The material properties correspond to the previous case, and are given in Table A.3.

The displacement and pressure at steady state resulting from the IGA simulation using $\gamma = 20°$ are shown in Figure A.11, and the velocity inside the fracture for the IGA and FEM simulations is shown in Figure A.12. Comparing the displacement to [232] shows large differences, with the obtained results obtained here showing double the displacement. Com-

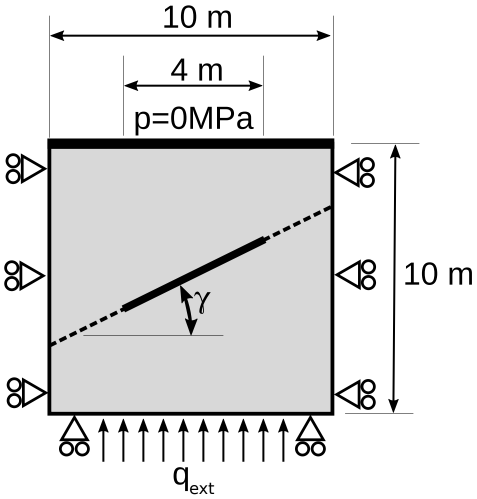

Figure A.10: Geometry for the fractured plate verification case

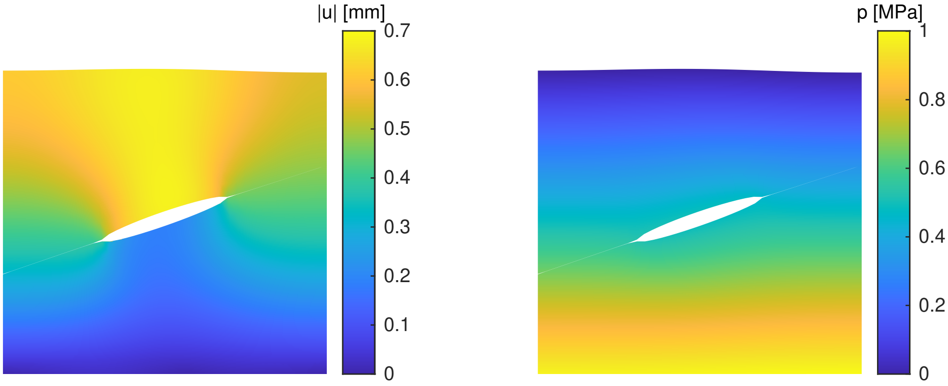

(a) Displacement

(b) Pressure

Figure A.11: Results from the IGA simulation for the fractured plate verification problem at steady state ($t = 40$s). Deformations are magnified with a factor of 1000.

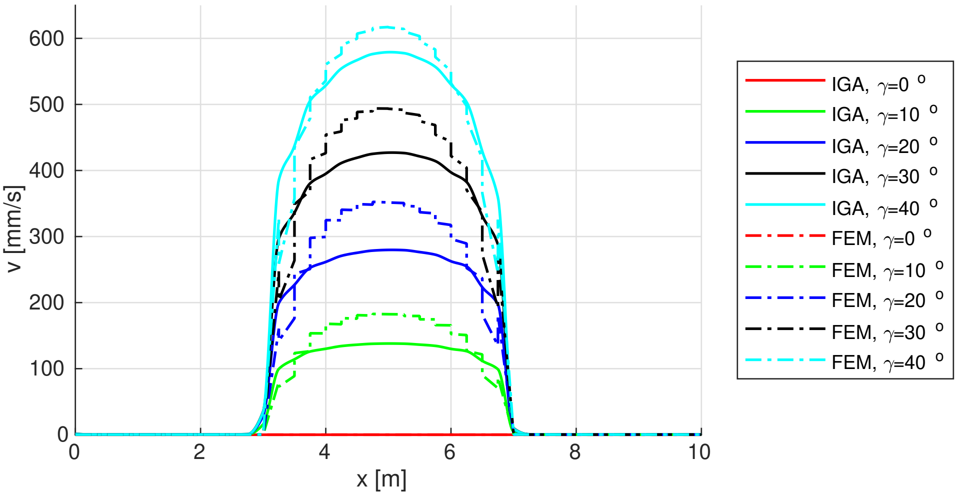

Figure A.12: Tangential fluid velocity in the centre of the fracture at steady state ($t = 40$s)

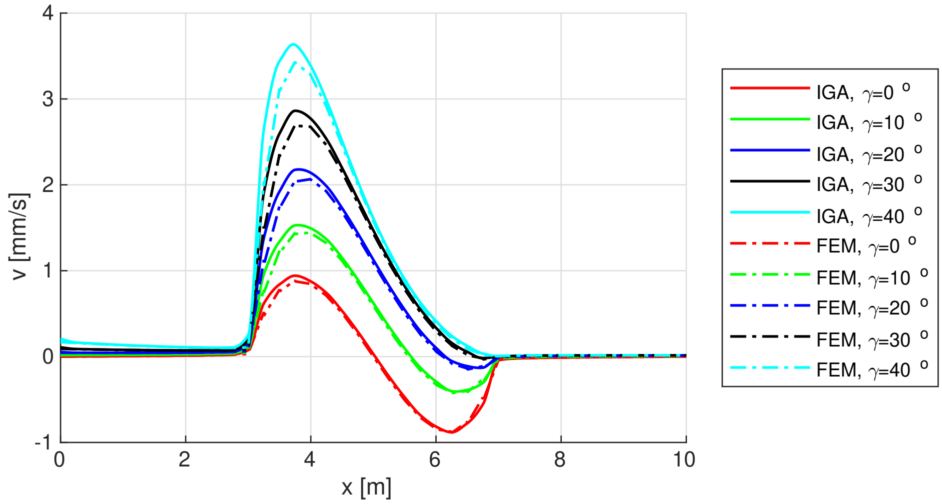

Figure A.13: Tangential fluid velocity in the centre of the fracture at $t = 1$s

paring the velocity in the centre of the fracture shows an even larger difference, with the velocity obtained here being up to a factor 100 higher. Whereas for the $\gamma = 0°$ case no fluid flow is obtained at steady state, the reference results obtain a fluid flow towards the centre of the fracture. Furthermore, only the $\gamma = 40°$ case has a fully positive velocity in the reference case, while all the velocities are positive in the results obtained here.

Comparing the results at $t = 1$s obtained here (Figure A.13) to the reference results, given at steady state, provides a better match. These velocities are fully dominated by the pressure gradients caused by the opening of the fracture. Since the fracture opens the most in the middle, most fluid is absorbed near the middle and the lowest pressure is achieved here. This lower pressure in the middle causes fluid to flow from both sides. This effect is dampened by the imposed fluid flow at the bottom boundary increasing the pressure nearer to the bottom, which creates an asymmetry for the angled fracture cases. While these results show a similar trend as presented in [232], different values are obtained and the results are mirrored. One possible explanation for the values being different can be attributed to the time-step size, which results in the presented results being obtained in a single step. However, since a similar trend is observed it can be concluded that the results presented in the reference case [232] are not at steady state, but at an unmentioned time before a steady-state solution is achieved.

A.2. VERIFICATION NON-NEWTONIAN FLUIDS

A.2.1. ONE-DIMENSIONAL UNCOUPLED CASE

The first case simulated for 1D uncoupled non-Newtonian flow is the same as for 1D coupled Newtonian flow with 2 differences: The biot coefficient $\alpha = 0$ in order to uncouple the fluid motion from the solid deformations, and instead of a Newtonian fluid, a shear thinning fluid with $n = 0.5$ ($k_f^* = 7.0 \cdot 10^{-7} (\mathrm{m/Pa})^n/\mathrm{s}$) and a shear-thickening fluid with $n = 2.0$ ($k_f^* = 3.5 \cdot 10^{-6} (\mathrm{m/Pa})^n/\mathrm{s}$) have been used. This uncoupling is necessary since no analytic solutions are available for non-Newtonian flow through poroelastic materials. By uncoupling the solid deformations from the fluid pressure, the fluid equation can be solved by MATLAB in order to verify the correct implementation. Since the coupling between deformations and pressure has already been verified for one-dimensional and two-dimensional cases, and this implementation is the same for non-Newtonian fluids, this solid-fluid coupling should also be correct for non-Newtonian flow and need no further verification.

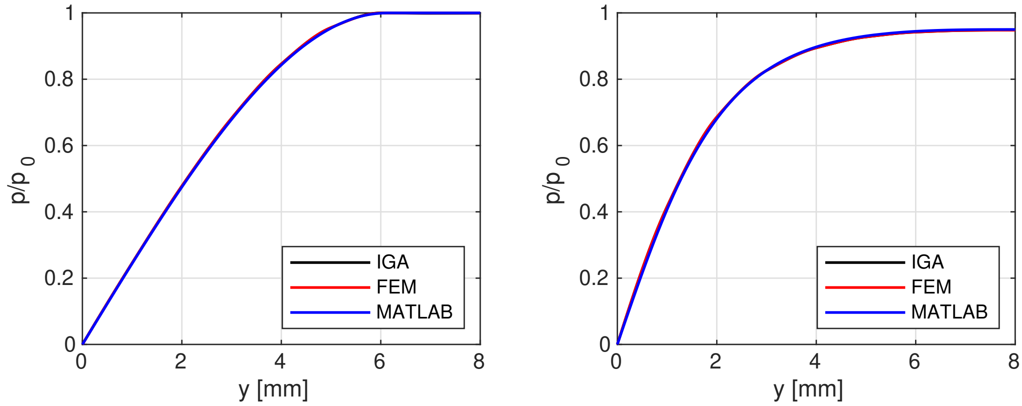

(a) $n = 0.5$ at $t = 500$s (b) $n = 2.0$ at $t = 15$s

Figure A.14: Results for the one-dimensional verification case using a non-Newtonian fluid.

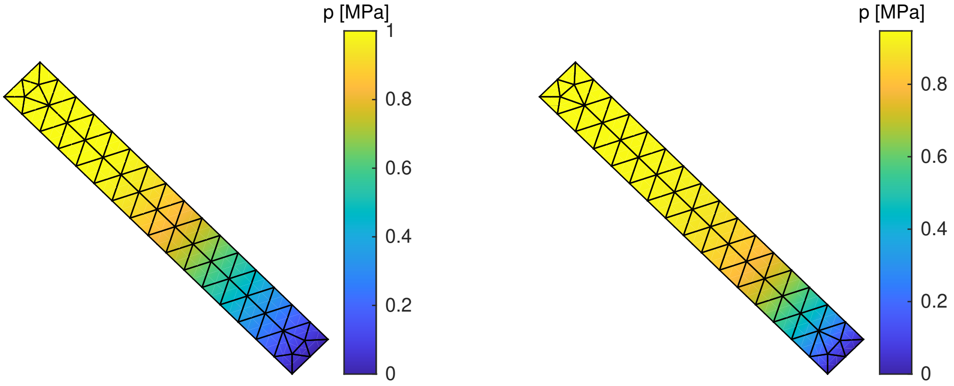

(a) $n = 0.5$ at $t = 500$s (b) $n = 2.0$ at $t = 15$s

Figure A.15: Mesh and interstitial fluid pressure for the two-dimensional non-Newtonian verification case.

The reference solution is obtained by using the MATLAB function *pdepe* to solve:

$$\frac{1}{M}\frac{\partial p}{\partial t} = k_f^* \left|\frac{\partial p}{\partial x}\right|^{1/n-1} \frac{\partial p}{\partial x} \tag{A.7}$$

subject to the boundary conditions:

$$\left.\frac{\partial p}{\partial x}\right|_{x=h} = 0$$

$$p_{x=0} = 0$$

and an initial pressure of $p_0 = 1$MPa.

The simulations were performed using a time-step of $\Delta t = 10$s for the shear-thinning case, and $\Delta t = 1$s for the shear-thickening case. The results of these simulations are shown in Figure A.14, showing good agreement between the solutions obtained through MATLAB and the FEM and IGA results.

A.2.2. TWO-DIMENSIONAL UNCOUPLED CASE

In order to verify the correct coupling between fluid flow directions in the non-Newtonian porous flow implementation, the one-dimensional case is rotated 45 degrees, and triangular elements are used to mesh the domain. This ensures that, at least for most elements,

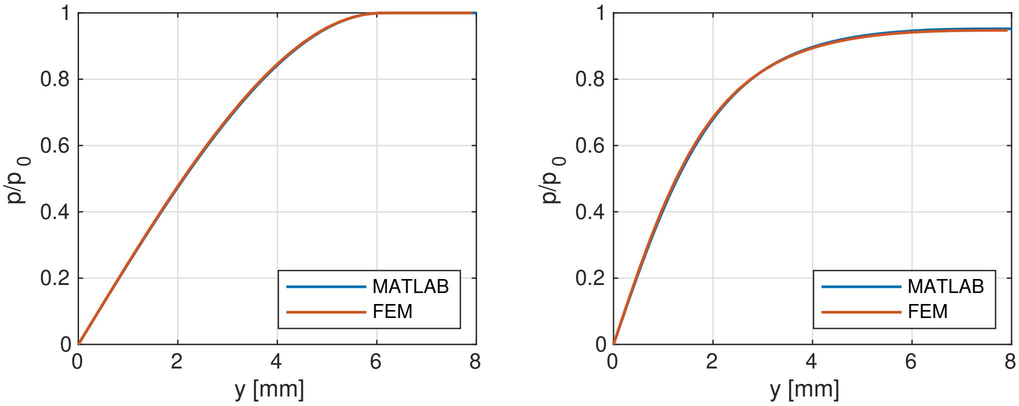

(a) $n = 0.5$ at $t = 500$s (b) $n = 2.0$ at $t = 15$s

Figure A.16: Comparison between the reference results and the simulation results for the two-dimensional verification case.

the element edges are not perpendicular to the flow direction. Since this can only be done for finite elements, and not for IGA, this verification was only done for the finite element implementation. The used mesh can be seen in Figure A.15.

The results from the two-dimensional simulations are given in Figure A.15 and A.16. What can be seen is that the results correspond well to the MATLAB one-dimensional results. This, combined with the correct results for the 2D Newtonian coupled simulation, thus confirm that the finite element implementation for the equations for non-Newtonian power-law fluids through deformable porous media is working correctly.

A.3. VERIFICATION PRESSURISED FRACTURES

A.3.1. FRACTURED PLATE

To verify the correct implementation of the discontinuity pressure fracture model, a case similar to the one described in [173] was simulated. The geometry of the problem corresponds to the fractured plate case shown in Figure A.10, with the fracture using $\gamma = 30°$. The boundary conditions for the displacements are the same as for the fractured plate problem, while an interstitial fluid pressure of 0.5MPa has been applied to the bottom of the domain and 0.0MPa to the top of the domain. This will ensure a more constant pressure gradient throughout the domain, ensuring that the differences in pressure originate from the influence of the fracture and not from changes in pressure at the boundary.

The properties of the interior of the domain are given in table A.3, corresponding to the properties used for the curved beam and fractured plate cases. The interface permeability for the fracture has been varied between $k_i = 1 \cdot 10^{-6}$m/Pa s and $k_i = 1 \cdot 10^{-12}$m/Pa s, ranging from a close to continuous pressure to a mostly impermeable fracture. A dummy permeability of $k_{i,d} = 0.5 \cdot 10^{-3}$m/Pa s has been used for the non-fractured interface elements to enforce a continuous pressure over the discontinuity. The domain is discretised using 80×40 Bézier extracted elements, quartic NURBS have been used for the solid displacement, and cubic NURBS for the interstitial and discontinuity pressures.

The interstitial fluid pressure resulting from the simulations is shown in Figure A.20. With a high interface permeability, the pressure is almost continuous across the fracture, and the fracture is opened. In contrast, the low interface permeability results in a pressure jump across the fracture, and prevents the fracture from opening due to the low discontinuity pressure inside the fracture. These results correspond to the results from [173].

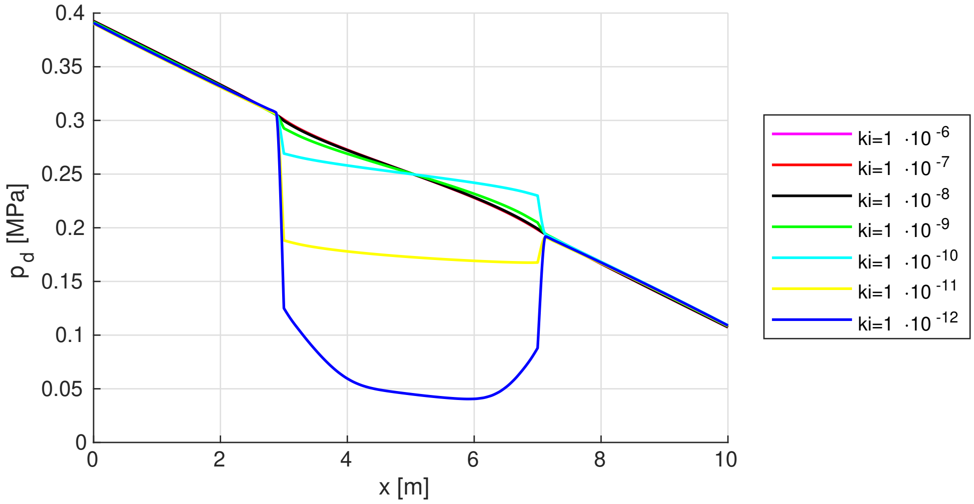

Figure A.17: Pressure inside the discontinuity at t = 50s for the pressurised discontinuous pressure verification case.

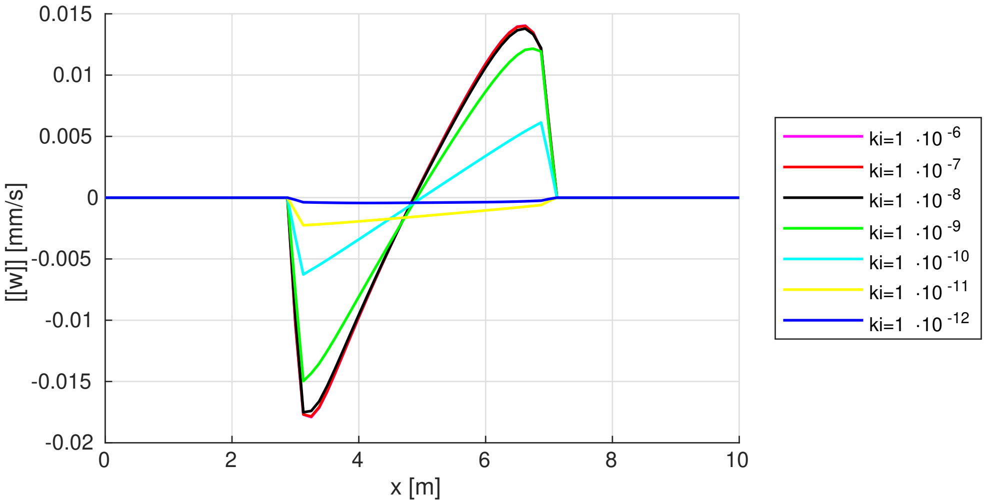

Figure A.18: Fracture outflow along the discontinuity at t = 50s for the pressurised discontinuous pressure verification case.

The pressure inside the discontinuity is shown in Figure A.17. This pressure also shows a similar behaviour as the reference results, with a continuous pressure for a high permeability, while obtaining a jump in discontinuity pressure between the fractured and non-fractured interface elements for lower permeabilities. The Fracture outflow, Figure A.18 confirms this, with high outflows for higher permeabilities, and a similar outflow profile as obtained for the continuous pressure model in section A.1.4. Finally the fluid flow normal to the discontinuity is shown in Figure A.19. This shows the blocking effect of low-permeability fractures, reducing the fluid flow passing through the fracture, while enhancing the flow around the tips of the fracture. Since all these conclusions correspond to the results from [173], it can be concluded that the discontinuous pressure model is working correctly for Newtonian fluids.

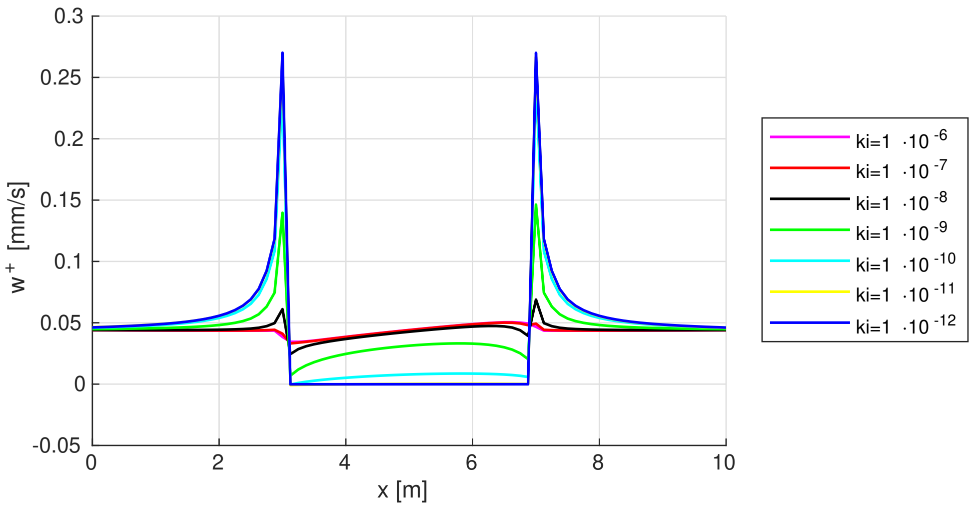

Figure A.19: Fluid velocity normal to the top discontinuity at $t = 50$s for the pressurised discontinuous pressure verification case.

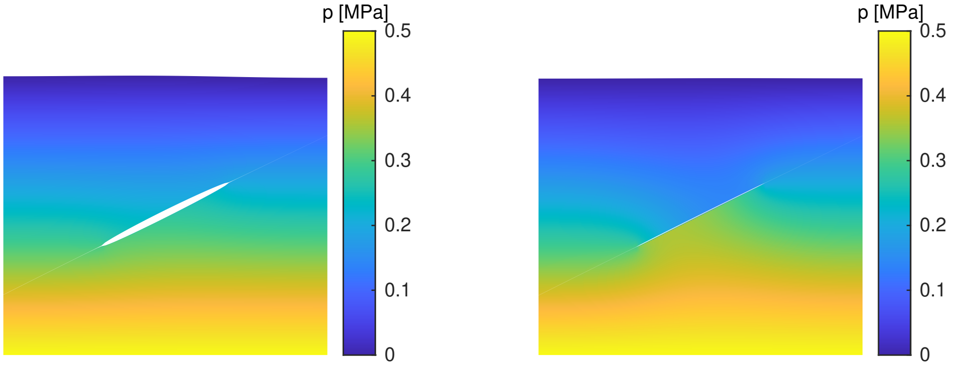

(a) $k_i = 1 \cdot 10^{-9}$m/Pa s

(b) $k_i = 1 \cdot 10^{-12}$m/Pa s

Figure A.20: Interstitial fluid pressure at $t = 50$s for the pressurised discontinuous pressure verification case.

A.4. VERIFICATION MULTIPHASE FLOWS

The results from the multiphase flow model for the interior domain, and the cubic law fracture flow model are compared to results from [108]. The simulated case consists of a square 1m × m domain, with a 0.9m diagonal fracture in the centre. A wetting phase fluid inflow is imposed on the bottom left, while constant wetting and non-wetting pressures are imposed to the top right. A time-step of Δt = 15 min is used, and the domain is discretised using 30 × 30 elements for the non-fractured case, and 80 × 40 elements for the fractured case.

The used model to relate the capillarity pressure to the saturation and permeability is:

$$\begin{aligned} S_w &= e^{-p_c/B} \\ k_{rw} &= S_w^{\kappa_i} \\ k_{rn} &= (1-S_w)^{\kappa_i} \end{aligned} \tag{A.8}$$

with $\kappa_i = \kappa_m$ for the interior of the domain, and $\kappa_i = \kappa_f$ for the cubic law flow model used for the interior of the fracture.

The wetting phase saturation for the non-fractured case is given in Figure A.22a, and for the fractured case (using the cubic law model) in Figure A.22b. Both of these results

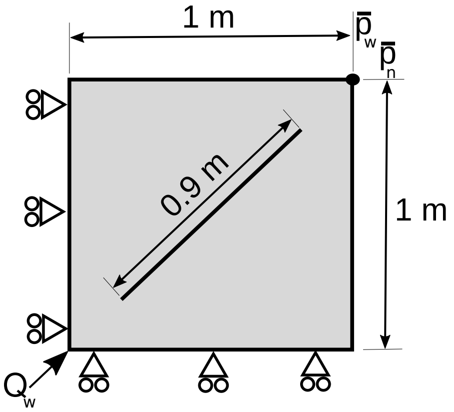

Figure A.21: Geometry of the multiphase verification case

Parameter	Value	
E	20	GPa
ν	0.2	
n_f	0.2	
α	1	
K_s	36	GPa
K_w	2.15	GPa
K_n	1.5	GPa
k	$9.86 \cdot 10^{-10}$	mm^2
μ_w	1	mPa s
μ_n	0.45	mPa s
$\overline{p}_w$	0	MPa
$\overline{p}_n$	0.3	MPa
Q_w	$2.32 \cdot 10^{-8}$	m^2/s
B	0.1	MPa
κ_m	5	
κ_f	3	

Table A.4: Parameters used for the multiphase verification case

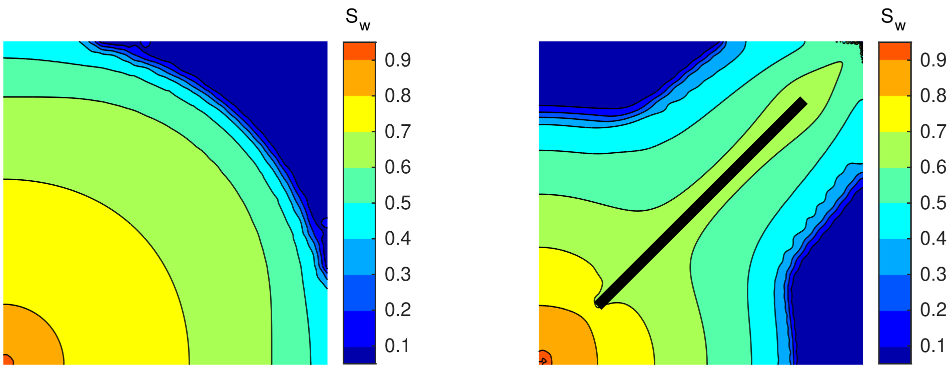

(a) Non-fractured (b) Fractured

Figure A.22: Wetting phase saturation after $t = 50$ days for the multiphase verification cases.

correspond to results presented in [108], thus confirming that the multiphase fluid flows are correctly simulated inside the porous medium and inside the fracture.

B

Convergence rate of Cosserat and rate-dependent continua

In this appendix, the regularising effect on the convergence of using a Cosserat continuum and a standard continuum with viscoplasticity when simulating problems containing shear fractures and non-associated plasticity will be compared. To focus on the effects of the used continuum model, no fluid will be included. Both the linear displacement and the Cosserat rotation (for the Cosserat continuum cases) are using cubic T-splines for their discretisation.

B.1. Viscoplasticity

The viscoplasticity is modelled using a linear Perzyna viscoplasticity model, limiting the rate of plastic deformation by:

$$\dot{\boldsymbol{\epsilon}} = \frac{f}{\eta \sigma_0} \boldsymbol{m} \tag{B.1}$$

using the viscosity parameter η and reference stress σ_0. This can be incorporated in the return-mapping scheme of Eq. 8.23 as:

$$\mathbf{0} = \boldsymbol{\sigma}_s^{t+\Delta t} - \left(\boldsymbol{\sigma}_{trial}^{t+\Delta t} - \widehat{\Delta\lambda} \boldsymbol{D}_{el} \boldsymbol{m} \right) \tag{B.2a}$$

$$0 = f(\boldsymbol{\sigma}_s^{t+\Delta t}) - \frac{\eta \sigma_0}{\Delta t} \widehat{\Delta\lambda} \tag{B.2b}$$

with the iterative scheme, Eq. 8.24, becoming

$$\begin{bmatrix} \boldsymbol{\sigma}_s^{t+\Delta t} \\ \widehat{\Delta\lambda} \end{bmatrix}_{j+1} = \begin{bmatrix} \boldsymbol{\sigma}_s^{t+\Delta t} \\ \widehat{\Delta\lambda} \end{bmatrix}_j - \boldsymbol{C}_{eff}^{-1} \begin{bmatrix} \boldsymbol{\sigma}_s^{t+\Delta t} - \left(\boldsymbol{\sigma}_{trial} - \widehat{\Delta\lambda} \boldsymbol{D}_{el} \boldsymbol{m} \right) \\ f - \frac{\eta \sigma_0}{\Delta t} \widehat{\Delta\lambda} \end{bmatrix}_j \tag{B.3}$$

with the effective compliance now given by:

$$\boldsymbol{C}_{eff} = \begin{bmatrix} \boldsymbol{I} + \widehat{\Delta\lambda}_j \boldsymbol{D}_{el} \frac{\partial \boldsymbol{m}}{\partial \boldsymbol{\sigma}} & \boldsymbol{D}_{el} \boldsymbol{m} \\ \left(\frac{\partial f}{\partial \boldsymbol{\sigma}} \right)^T & -\frac{\eta \sigma_0}{\Delta t} \end{bmatrix} \tag{B.4}$$

with the effective stiffness determined in the same manner as used without viscoplasticity, inverting the effective compliance matrix, selecting the upper-left 7 × 7 sub-matrix and multiplying with $\boldsymbol{D}_{el} \left(\boldsymbol{I} - \widehat{\Delta\lambda} \boldsymbol{D}_{el} \frac{\partial \boldsymbol{m}}{\partial \boldsymbol{\sigma}_{trial}} \right)$. In contrast to rate-independent plasticity models, in the case that the stresses exceeds the apex of the Drucker-Prager cone, this effective stiffness is non-zero.

B.2. Simplified case

To compare the convergence rate of a Cosserat continuum with a standard continuum with and without viscoplasticity, a simple case without propagating fractures is first considered. This case consists of a rectangular 1m × 2m domain with a pre-existing discontinuity at the centre, as shown in Figure B.1a. Absorbing boundary conditions and a normal traction of $\tau_n = 1$ MPa are applied to the edges of the domain. Two different values for the tangential traction are studied, using $\tau_t = 0.2$ MPa with $\Delta t = 0.1$ ms, and $\tau_t = 0.4$ MPa with $\Delta t = 1.0$ ms. The simulation starts from a static equilibrium without any plastic deformations, obtained by simulating the first $t_0 = 1$ s without enabling plasticity. After this initial period, plasticity

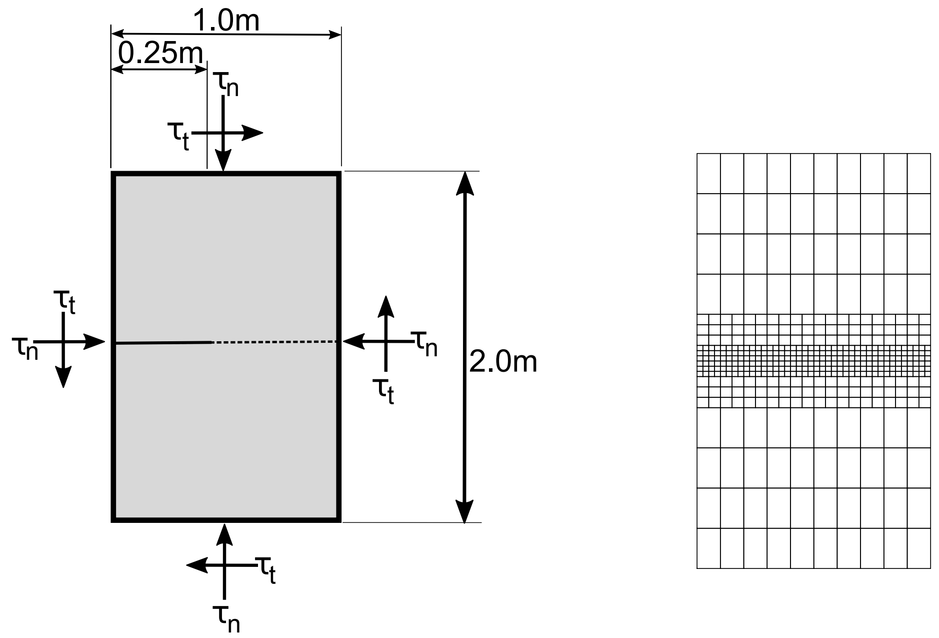

(a) Geometry

(b) Mesh

Figure B.1: Mesh and geometry used for the simplified case.

is allowed and the smaller time steps are used. At this moment, a short burst of plastic deformation occurs around the fracture tip, spread out over several time steps due to the inertia of the solid. This case is an approximation of the sudden load changes as a result of a propagating fracture.

The material is represented by Young's modulus $E = 10$ GPa, Poisson ratio $\nu = 0.25$, and density $\rho = 2500\,\mathrm{kg/m^3}$. A cohesionless Drucker-Prager plasticity model is used with an angle of internal friction $\phi = 30°$ and dilatency angle $\psi = 0°$. For the cases in which a Cosserat continuum is used, the Cosserat shear modulus is taken as $G_c = 4$ GPa and the Cosserat length scale values used are $\ell_c = 0.1$ mm, $\ell_c = 1$ mm, $\ell_c = 10$ mm, and $\ell_c = 100$ mm. The cases using a standard continuum with viscoplasticity used: $\eta\sigma_0 = 0\,\mathrm{Pa\cdot s}$ (no viscoplasticity), $\eta\sigma_0 = 10^3\,\mathrm{Pa\cdot s}$ ($\ell_v = 0.4$ mm), $\eta\sigma_0 = 10^4\,\mathrm{Pa\cdot s}$ ($\ell_v = 4$ mm), $\eta\sigma_0 = 10^5\,\mathrm{Pa\cdot s}$ ($\ell_v = 40$ mm), and $\eta\sigma_0 = 10^6\,\mathrm{Pa\cdot s}$ ($\ell_v = 400$ mm), approximating the length scale over which the plastic deformations are spread by $\ell_v = 2\eta\sigma_0/(\rho E)^{0.5}$. It should be noted that the length scale related to the area over which the plastic strain is distributed in a Cosserat continuum is approximately 4-5 times the Cosserat length scale [35], and therefore the simulations using $\ell_c = 0.1$ mm and $\eta\sigma_0 = 10^3\,\mathrm{Pa\cdot s}$ ($\ell_v = 0.4$ mm) use a comparable length scale.

Since no interstitial fluid is included in these simulations, the linear displacements and Cosserat microrotation are all discretised using cubic T-splines. 40 Bézier extracted elements are used near the discontinuity, with coarser elements used away from this discontinuity, as shown in Figure B.1b. The Newmark time discretisation uses $\beta = 0.4$ and $\Gamma = 0.75$, and the Newton-Raphson iterative scheme is considered to be converged when the normalised error reaches $error_j < 10^{-9}$.

The stabilising effect of adding viscoplasticity is demonstrated in Figure B.2, showing the convergence during the first time step in which plasticity is allowed to occur. When no viscoplasticity or Cosserat continuum is used, the simulation diverges during this time step. Including even a small amount of viscosity, thereby introducing a time/length scale to the problem, regularises the formulation and results in well-converging simulations. This

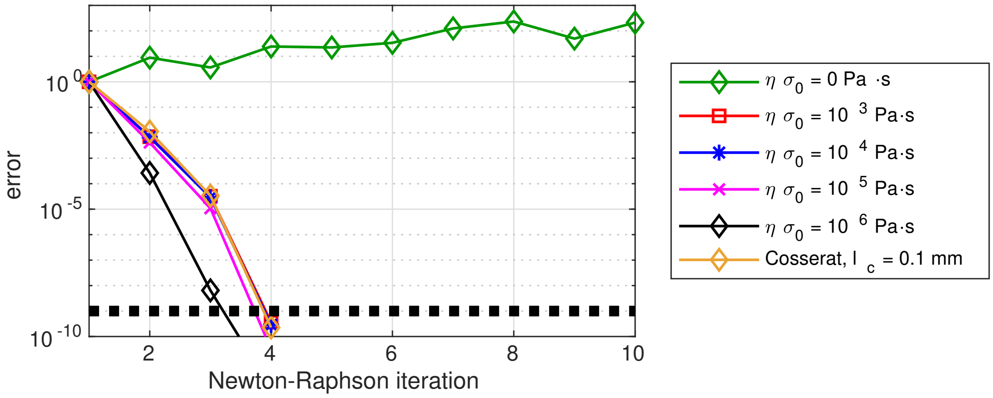

Figure B.2: Convergence behaviour using a standard continuum with varying amounts of viscoplasticity, and a Cosserat continuum using $\ell_c = 0.1$ mm for $\tau_t = 0.2$ MPa. The dotted line is the used convergence criterium.

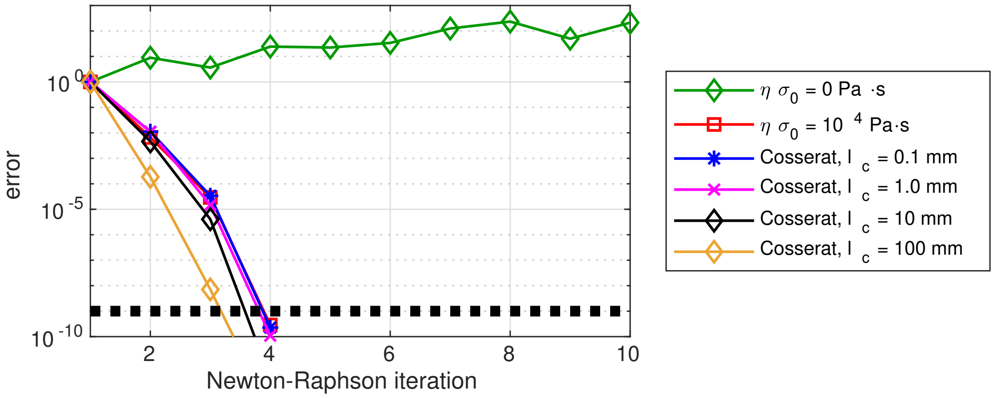

Figure B.3: Convergence behaviour using a Cosserat continuum with varying Cosserat length scales for $\tau_t = 0.2$ MPa.

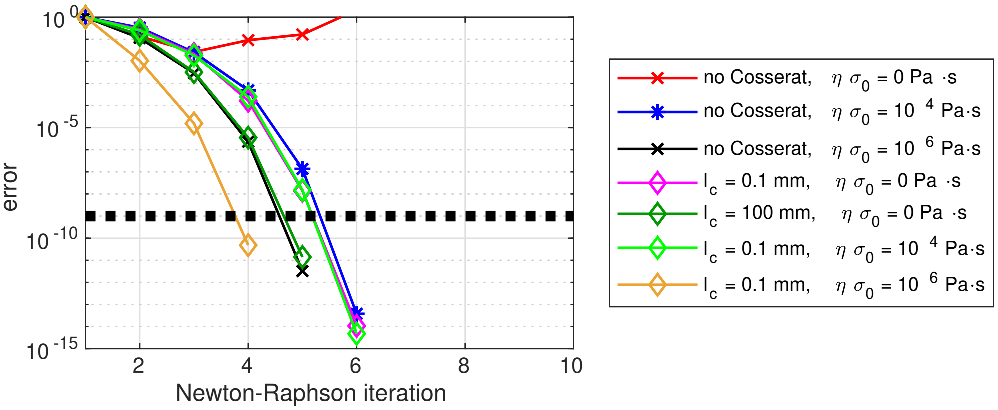

Figure B.4: Convergence behaviour using varying combinations of Cosserat length scale and viscosity parameters for $\tau_t = 0.4$ MPa.

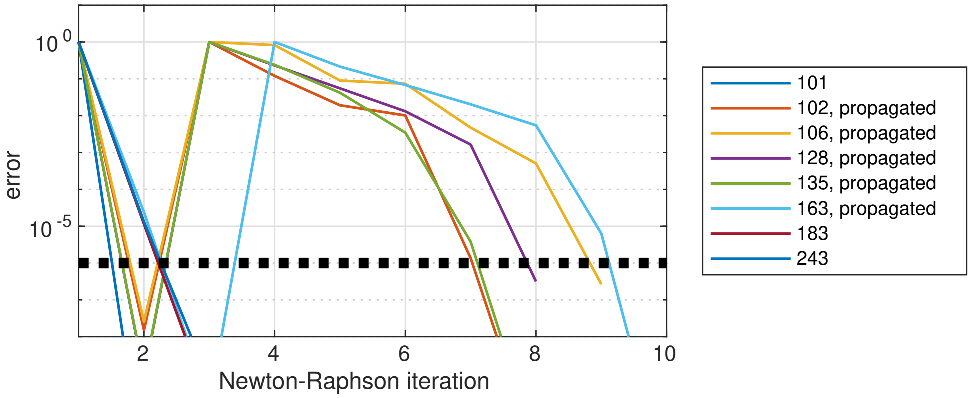

Figure B.5: Convergence during selected time steps using a standard continuum with $\eta\sigma_0 = 10^5$ Pa·s.

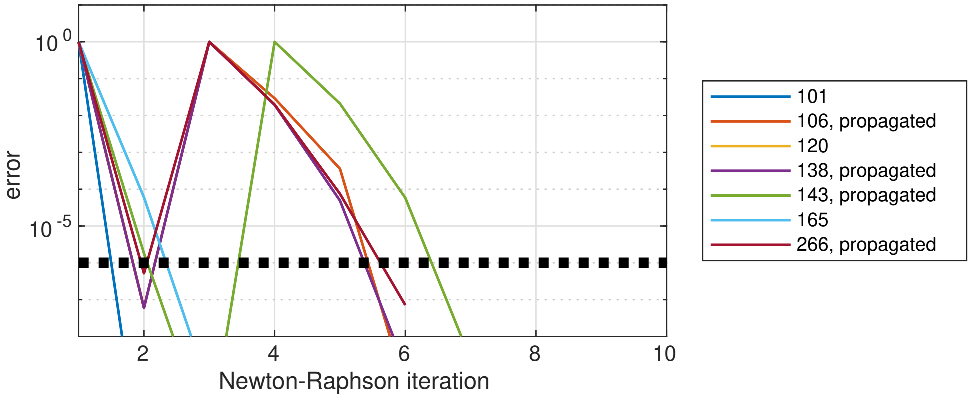

Figure B.6: Convergence during selected time steps using a Cosserat continuum continuum with $\ell_c = 10$ mm.

improved convergence is independent on the used value of the viscoplasticity as long as this value does not start to dominate the problem itself by severely limiting the amount of plastic strain.

Using a Cosserat continuum, a similar improvement in the convergence is observed (Figure B.3). As was the case using viscoplasticity, the introduction of a length scale significantly improves the convergence rate, even if the length scale is small. Comparing the convergence between the standard and Cosserat continua shows that these introduced length scales influence the convergence extremely similarly: A small length scale results in a converged time step in four iterations, and increasing the length scale to $\ell_c = 100$ mm, $\ell_v = 400$ mm further results in nearly identical improvement in the convergence rate.

The behaviour using a larger external traction and time step size ($\tau_t = 0.4$ MPa, $\Delta t = 1$ ms) is shown in Figure B.4. A quadratic convergence rate can be clearly seen for all simulations using a Cosserat continuum or a standard continuum with viscoplasticity. Comparing the cases with a low internal length scale shows that the introduced length scale itself is improving the convergence, and not necessarily the addition of time dependent plasticity or a Cosserat microrotation. Increasing this length scale also results in a similar improved convergence. Interestingly, combining a large amount of viscoplasticity with a small Cosserat length scale further aids in the convergence, improving beyond the convergence behaviour obtained by solely using a Cosserat continuum or viscoplasticity.

B.3. FRACTURE PROPAGATION CASE

To show the improved convergence persists in the presence of propagating fractures, the case from Figure 8.1 is simulated using a standard continuum with $\eta\sigma_0 = 10^5\text{Pa}\cdot\text{s}$ and a Cosserat continuum with $\ell_c = 10$ mm. The domain is discretised using a mesh of $(160/80/40)\times 40$ Bézier extracted elements with $\Delta t = 1$ ms in this section, whereas Section B.3.1 uses a $(320/160/50)\times 40$ mesh with $\Delta t = 0.1$ ms. The Drucker-Prager plasticity model uses $c = 0$, $\phi = 31^\circ$, $\psi = 0^\circ$, and all other properties are taken identical to those of Section B.2.

The convergence during selected time steps is shown in Figure B.5 using a standard continuum with viscoplasticity, and in Figure B.6 using a Cosserat continuum. The steps in which no fracture propagation occurs converge within three iterations for both cases. The steps with fracture propagation show a large peak in the error, corresponding to the first step after propagation, on which the new convergence criteria is based. After this initial peak, both cases show an approximately quadratic convergence rate, with the standard continuum exhibiting slight oscillations, resulting in a slightly slower convergence compared to the Cosserat continuum. However, even in the presence of propagating fractures, and using a fairly large time step, both simulations converge without any issues. This indicates that the use of a Cosserat continuum enables the simulation of fracture propagation combined with plasticity, without the need to alter the plasticity model used. Similar results are possible using a standard continuum, but require alterations to the plasticity model to use a rate-dependent formulation.

B.3.1. INFLUENCE OF STABILISATION

While in previous section it was shown that increasing the length scale resulted in an improved convergence, this also alters the problem being simulated. To illustrate this, simulations using a 320×50 mesh have been performed, using a smaller time step to eliminate errors relating to the temporal discretisation. The results for varying Cosserat length scales are presented in Figure B.7, and for varying viscosity parameters in Figure B.8. When a small length scale is used, both the Cosserat continuum and the standard continuum obtain comparable plastic strains. Increasing the Cosserat length scale results in the stresses, and therefore the plastic strains, to be spread over a larger area. This results in the area influenced by the plastic strains becoming more rounded, as is visible in the plastic strains near the fracture tip. Further increasing the Cosserat length scale spreads the stresses over an even larger area, decreasing the plastic deformations near the fracture, and for unrealistically large values severely limiting plastic deformations and the region influenced by them.

In contrast, using viscoplasticity spreads the plastic deformations over time instead, allowing the stresses to exceed the yield function. This allows the region influenced by the plastic strains to retain its triangular shape, without rounding this zone near the fracture tip for larger length scales. Since the viscoplasticity only works in regions already having plastic deformations, it does not alter the region of plastic deformations as much as a Cosserat continuum, even for high viscosity parameter values. However, in contrast to a Cosserat continuum, using viscoplasticity allows the stresses to exceed the yield function. Furthermore, comparing the plastic strain near the discontinuity shows that for low values of the length scale, a standard continuum limits the plasticity slightly more compared to a Cosserat continuum.

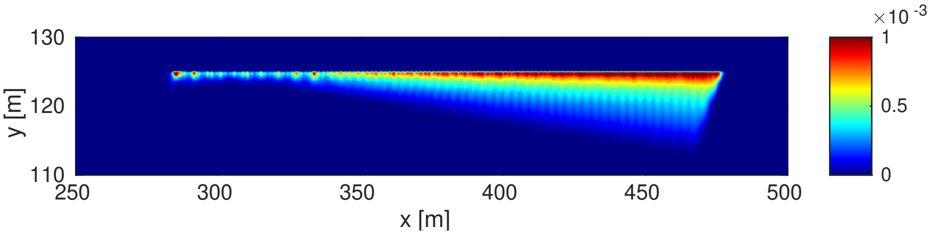

(a) $\ell_c = 10\,\mathrm{mm}$

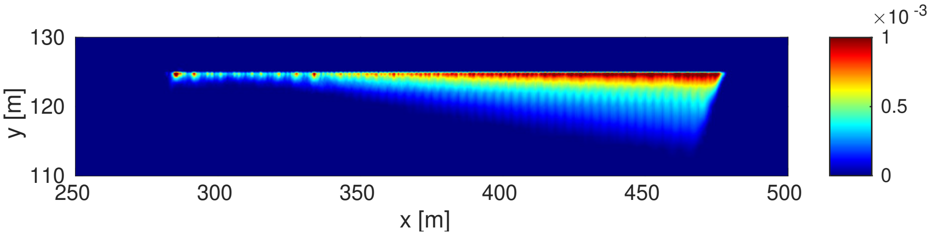

(b) $\ell_c = 100\,\mathrm{mm}$

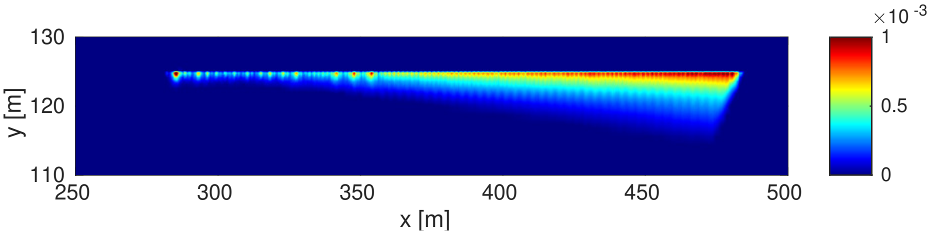

(c) $\ell_c = 1\,\mathrm{m}$

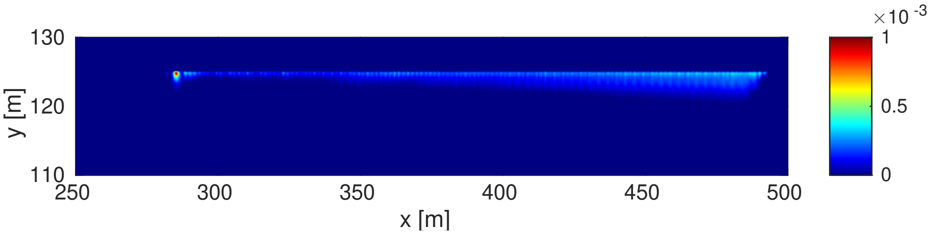

(d) $\ell_c = 5\,\mathrm{m}$

Figure B.7: Plastic strain $(\epsilon_{xx}^2 + \epsilon_{yy}^2)^{1/2}$ at $t = 1.2$ s using a Cosserat continuum.

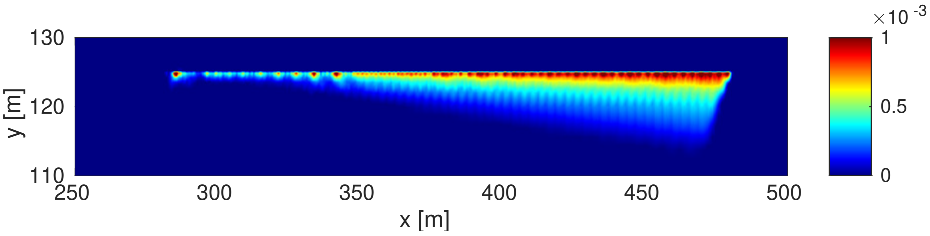

(a) $\eta\sigma_0 = 10^5$ Pa·s

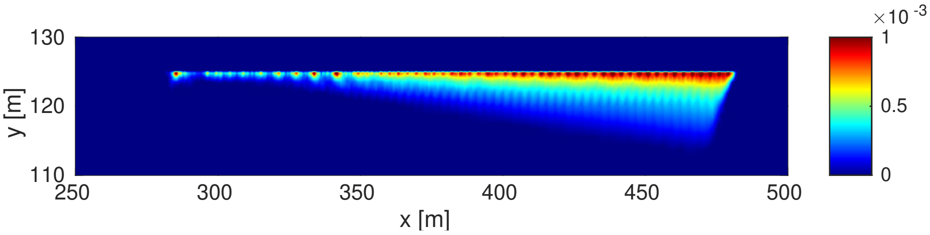

(b) $\eta\sigma_0 = 10^6$ Pa·s

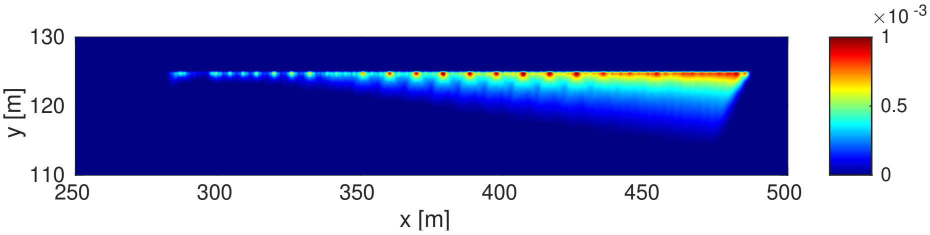

(c) $\eta\sigma_0 = 10^7$ Pa·s

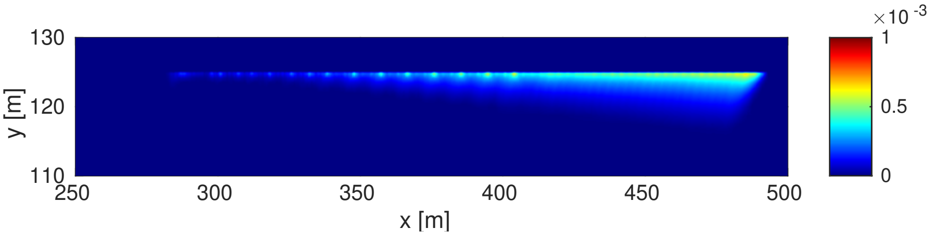

(d) $\eta\sigma_0 = 5 \cdot 10^7$ Pa·s

Figure B.8: Plastic strain $(\epsilon_{xx}^2 + \epsilon_{yy}^2)^{1/2}$ at $t = 1.2$ s using a standard continuum.

C

TANGENTIAL STIFFNESS MATRICES

C.1. MULTIPHASE FLOWS

The system of non-linear equations is solved using a Newton-Raphson iterative method. For this, the discretised equations are linearised as:

$$\begin{bmatrix} \boldsymbol{K}+\boldsymbol{K}_d & \boldsymbol{Q}_{sw}+\boldsymbol{Q}_{d,sw} & \boldsymbol{Q}_{sn}+\boldsymbol{Q}_{d,sn} \\ \boldsymbol{Q}_{ws}+\boldsymbol{Q}_{d,ws}+\boldsymbol{H}_{d,ws} & \boldsymbol{H}_{ww}+\boldsymbol{C}_{ww}+\boldsymbol{Q}_{ww}+\boldsymbol{Q}_{d,ww}+\boldsymbol{H}_{d,ww} & \boldsymbol{H}_{wn}+\boldsymbol{C}_{wn}+\boldsymbol{Q}_{wn}+\boldsymbol{Q}_{d,wn}+\boldsymbol{H}_{d,wn} \\ \boldsymbol{Q}_{ns}+\boldsymbol{Q}_{d,ns}+\boldsymbol{H}_{d,ns} & \boldsymbol{H}_{nw}+\boldsymbol{C}_{nw}+\boldsymbol{Q}_{nw}+\boldsymbol{Q}_{d,nw}+\boldsymbol{H}_{d,nw} & \boldsymbol{H}_{nn}+\boldsymbol{C}_{nn}+\boldsymbol{Q}_{nn}+\boldsymbol{Q}_{d,nn}+\boldsymbol{H}_{d,nn} \end{bmatrix}$$

$$\begin{bmatrix} \mathrm{d}\boldsymbol{u} \\ \mathrm{d}\boldsymbol{p}_w \\ \mathrm{d}\boldsymbol{p}_n \end{bmatrix} = \begin{bmatrix} \boldsymbol{f}_{ext} \\ \boldsymbol{q}_{w,ext} \\ \boldsymbol{q}_{n,ext} \end{bmatrix} - \begin{bmatrix} \boldsymbol{f}_{int}+\boldsymbol{f}_d \\ \boldsymbol{q}_{w,int}+\boldsymbol{q}_{w,d} \\ \boldsymbol{q}_{n,int}+\boldsymbol{q}_{n,d} \end{bmatrix} \tag{C.1}$$

with the external and internal forces defined in Eq. 2.47, 4.48, and 4.49, and the fluxes defined in Eq. 4.52-4.55.

The tangential stiffness sub-matrices related to the interior forces and fluxes are given by:

$$\boldsymbol{K} = \int_\Omega \boldsymbol{B}^T \boldsymbol{D}_{el} \boldsymbol{B} \,\mathrm{d}\Omega \tag{C.2}$$

$$\boldsymbol{Q}_{sw} = -\int_\Omega \alpha \left(S_w - p_w \frac{\partial S_w}{\partial p_c}\right) \boldsymbol{B}^T \boldsymbol{m} \boldsymbol{N}_w + \alpha \left(p_n \frac{\partial S_w}{\partial p_c}\right) \boldsymbol{B}^T \boldsymbol{m} \boldsymbol{N}_n \,\mathrm{d}\Omega \tag{C.3}$$

$$\boldsymbol{Q}_{sn} = -\int_\Omega \alpha \left(S_n - p_n \frac{\partial S_w}{\partial p_c}\right) \boldsymbol{B}^T \boldsymbol{m} \boldsymbol{N}_n + \alpha \left(p_w \frac{\partial S_w}{\partial p_c}\right) \boldsymbol{B}^T \boldsymbol{m} \boldsymbol{N}_w \,\mathrm{d}\Omega \tag{C.4}$$

$$\boldsymbol{Q}_{ws} = -\int_\Omega \alpha S_w \boldsymbol{N}_w^T \boldsymbol{m}^T \boldsymbol{B} \,\mathrm{d}\Omega \tag{C.5}$$

$$\boldsymbol{Q}_{ww} = \int_\Omega \alpha \left(\boldsymbol{m}^T \boldsymbol{B} \left(\boldsymbol{u}^{t+\Delta t} - \boldsymbol{u}^t\right)\right) \frac{\partial S_w}{\partial p_c} \boldsymbol{N}_w^T \boldsymbol{N}_w \,\mathrm{d}\Omega \tag{C.6}$$

$$\boldsymbol{Q}_{wn} = -\int_\Omega \alpha \left(\boldsymbol{m}^T \boldsymbol{B} \left(\boldsymbol{u}^{t+\Delta t} - \boldsymbol{u}^t\right)\right) \frac{\partial S_w}{\partial p_c} \boldsymbol{N}_w^T \boldsymbol{N}_n \,\mathrm{d}\Omega \tag{C.7}$$

$$\boldsymbol{Q}_{ns} = -\int_\Omega \alpha S_n \boldsymbol{N}_n^T \boldsymbol{m}^T \boldsymbol{B} \,\mathrm{d}\Omega \tag{C.8}$$

$$\boldsymbol{Q}_{nw} = -\int_\Omega \alpha \left(\boldsymbol{m}^T \boldsymbol{B} \left(\boldsymbol{u}^{t+\Delta t} - \boldsymbol{u}^t\right)\right) \frac{\partial S_w}{\partial p_c} \boldsymbol{N}_n^T \boldsymbol{N}_w \,\mathrm{d}\Omega \tag{C.9}$$

$$\boldsymbol{Q}_{nn} = \int_\Omega \alpha \left(\boldsymbol{m}^T \boldsymbol{B} \left(\boldsymbol{u}^{t+\Delta t} - \boldsymbol{u}^t\right)\right) \frac{\partial S_w}{\partial p_c} \boldsymbol{N}_n^T \boldsymbol{N}_n \,\mathrm{d}\Omega \tag{C.10}$$

$$\boldsymbol{C}_{ww} = -\int_\Omega \left(\frac{1}{M_{ww}} - \left(p_w^{t+\Delta t} - p_w^t\right) \frac{\partial 1/M_{ww}}{\partial p_c} - \left(p_n^{t+\Delta t} - p_n^t\right) \frac{\partial 1/M_{wn}}{\partial p_c}\right) \boldsymbol{N}_w^T \boldsymbol{N}_w \,\mathrm{d}\Omega \tag{C.11}$$

$$\boldsymbol{C}_{wn} = -\int_\Omega \left(\frac{1}{M_{wn}} + \left(p_w^{t+\Delta t} - p_w^t\right) \frac{\partial 1/M_{ww}}{\partial p_c} + \left(p_n^{t+\Delta t} - p_n^t\right) \frac{\partial 1/M_{wn}}{\partial p_c}\right) \boldsymbol{N}_w^T \boldsymbol{N}_n \,\mathrm{d}\Omega \tag{C.12}$$

$$\boldsymbol{C}_{nw} = -\int_\Omega \left(\frac{1}{M_{nw}} - \left(p_w^{t+\Delta t} - p_w^t\right) \frac{\partial 1/M_{nw}}{\partial p_c} - \left(p_n^{t+\Delta t} - p_n^t\right) \frac{\partial 1/M_{nn}}{\partial p_c}\right) \boldsymbol{N}_n^T \boldsymbol{N}_w \,\mathrm{d}\Omega \tag{C.13}$$

$$\boldsymbol{C}_{nn} = -\int_\Omega \left(\frac{1}{M_{nn}} + \left(p_w^{t+\Delta t} - p_w^t\right) \frac{\partial 1/M_{nw}}{\partial p_c} + \left(p_n^{t+\Delta t} - p_n^t\right) \frac{\partial 1/M_{nn}}{\partial p_c}\right) \boldsymbol{N}_n^T \boldsymbol{N}_w \,\mathrm{d}\Omega \tag{C.14}$$

$$\boldsymbol{H}_{ww} = -\Delta t \int_\Omega k_w k_{rw} (\nabla \boldsymbol{N}_w)^T \nabla \boldsymbol{N}_w - k_w \frac{\partial k_{rw}}{\partial S_w}\frac{\partial S_w}{\partial p_c}\left((\nabla \boldsymbol{N}_w \boldsymbol{p}_w)^T \nabla \boldsymbol{N}_w\right)^T \boldsymbol{N}_w \,\mathrm{d}\Omega \tag{C.15}$$

$$\boldsymbol{H}_{wn} = -\Delta t \int_\Omega k_w \frac{\partial k_{rw}}{\partial S_w}\frac{\partial S_w}{\partial p_c}\left((\nabla \boldsymbol{N}_w \boldsymbol{p}_w)^T \nabla \boldsymbol{N}_w\right)^T \boldsymbol{N}_n \,\mathrm{d}\Omega \tag{C.16}$$

$$\boldsymbol{H}_{nw} = -\Delta t \int_\Omega k_n \frac{\partial k_{rn}}{\partial S_w}\frac{\partial S_w}{\partial p_c}\left((\nabla \boldsymbol{N}_n \boldsymbol{p}_n)^T \nabla \boldsymbol{N}_n\right)^T \boldsymbol{N}_w \,\mathrm{d}\Omega \tag{C.17}$$

$$\boldsymbol{H}_{nn} = -\Delta t \int_\Omega k_n k_{rn} (\nabla \boldsymbol{N}_n)^T \nabla \boldsymbol{N}_n + k_n \frac{\partial k_{rn}}{\partial S_w}\frac{\partial S_w}{\partial p_c}\left((\nabla \boldsymbol{N}_n \boldsymbol{p}_n)^T \nabla \boldsymbol{N}_n\right)^T \boldsymbol{N}_n \,\mathrm{d}\Omega \tag{C.18}$$

with all variables determined by using the updated displacements and pressures, and all values determined in the integration points.

The tangential stiffness sub-matrices related to the forces at the discontinuity are given by:

$$\boldsymbol{K}_d = \int_{\Gamma_d} \boldsymbol{N}_d^T \boldsymbol{R}\boldsymbol{D}_d \boldsymbol{R}\boldsymbol{N}_d \,\mathrm{d}\Gamma_d \tag{C.19}$$

$$\boldsymbol{Q}_{d,sw} = -\int_{\Gamma_d} \left(S_w + (p_n - p_w)\frac{\partial S_w}{\partial p_c}\right) \boldsymbol{N}_d^T \boldsymbol{n}_{\Gamma_d} \boldsymbol{N}_w \,\mathrm{d}\Gamma_d \tag{C.20}$$

$$\boldsymbol{Q}_{d,sn} = -\int_{\Gamma_d} \left(S_n - (p_n - p_w)\frac{\partial S_w}{\partial p_c}\right) \boldsymbol{N}_d^T \boldsymbol{n}_{\Gamma_d} \boldsymbol{N}_n \,\mathrm{d}\Gamma_d \tag{C.21}$$

The terms related to the fluid absorbed by the fracture opening are independent of the fracture flow model, and given by:

$$\boldsymbol{Q}_{d,ws} = -\int_{\Gamma_d} (S_w + (S_w^{t+\Delta t} - S_w^t) \boldsymbol{N}_w^T \boldsymbol{n}_{\Gamma_d}^T \boldsymbol{N}_d \,\mathrm{d}\Gamma_d \tag{C.22}$$

$$\boldsymbol{Q}_{d,ww} = \int_{\Gamma_d} \left(\frac{\partial S_w}{\partial p_c}\left(\boldsymbol{n}_{\Gamma_d}^T \boldsymbol{N}_d \left(\boldsymbol{u}^{t+\Delta t} - \boldsymbol{u}^t\right)\right) + \left(\boldsymbol{n}_{\Gamma_d}^T \boldsymbol{N}_d \boldsymbol{u}\right)\frac{\partial S_w}{\partial p_c}\right) \boldsymbol{N}_w^T \boldsymbol{N}_w \,\mathrm{d}\Gamma_d \tag{C.23}$$

$$\boldsymbol{Q}_{d,wn} = -\int_{\Gamma_d} \left(\frac{\partial S_w}{\partial p_c}\left(\boldsymbol{n}_{\Gamma_d}^T \boldsymbol{N}_d \left(\boldsymbol{u}^{t+\Delta t} - \boldsymbol{u}^t\right)\right) + \left(\boldsymbol{n}_{\Gamma_d}^T \boldsymbol{N}_d \boldsymbol{u}\right)\frac{\partial S_w}{\partial p_c}\right) \boldsymbol{N}_w^T \boldsymbol{N}_n \,\mathrm{d}\Gamma_d \tag{C.24}$$

$$\boldsymbol{Q}_{d,ns} = -\int_{\Gamma_d} (S_n + (S_n^{t+\Delta t} - S_n^t) \boldsymbol{N}_n^T \boldsymbol{n}_{\Gamma_d}^T \boldsymbol{N}_d \,\mathrm{d}\Gamma_d \tag{C.25}$$

$$\boldsymbol{Q}_{d,nw} = -\int_{\Gamma_d} \left(\frac{\partial S_w}{\partial p_c}\left(\boldsymbol{n}_{\Gamma_d}^T \boldsymbol{N}_d \left(\boldsymbol{u}^{t+\Delta t} - \boldsymbol{u}^t\right)\right) + \left(\boldsymbol{n}_{\Gamma_d}^T \boldsymbol{N}_d \boldsymbol{u}\right)\frac{\partial S_w}{\partial p_c}\right) \boldsymbol{N}_n^T \boldsymbol{N}_w \,\mathrm{d}\Gamma_d \tag{C.26}$$

$$\boldsymbol{Q}_{d,nn} = \int_{\Gamma_d} \left(\frac{\partial S_w}{\partial p_c}\left(\boldsymbol{n}_{\Gamma_d}^T \boldsymbol{N}_d \left(\boldsymbol{u}^{t+\Delta t} - \boldsymbol{u}^t\right)\right) + \left(\boldsymbol{n}_{\Gamma_d}^T \boldsymbol{N}_d \boldsymbol{u}\right)\frac{\partial S_w}{\partial p_c}\right) \boldsymbol{N}_n^T \boldsymbol{N}_n \,\mathrm{d}\Gamma_d \tag{C.27}$$

The final terms, related to the sub-grid model used to model the fracture in and outflow, depend on the flow type assumed for the flow inside the fracture. For the cubic-law model, the tangential stiffness matrices are given by:

$$\boldsymbol{H}_{d,ws}^{cubic} = -\Delta t \int_{\Gamma_d} \frac{S_w^3}{4\mu_w}\left(\boldsymbol{n}_{\Gamma_d}^T \boldsymbol{N}_d \boldsymbol{u}\right)^2 (\nabla \boldsymbol{N}_w \boldsymbol{p}_w)(\nabla \boldsymbol{N}_w)^T \boldsymbol{n}_{\Gamma_d}^T \boldsymbol{N}_d \,\mathrm{d}\Gamma_d \tag{C.28}$$

$$\begin{aligned}\boldsymbol{H}_{d,ww}^{cubic} = -\Delta t \int_{\Gamma_d} & \frac{S_w^3}{12\mu_w}\left(\boldsymbol{n}_{\Gamma_d}^T \boldsymbol{N}_d \boldsymbol{u}\right)^3 (\nabla \boldsymbol{N}_w)^T \nabla \boldsymbol{N}_w \\ & - \frac{S_w^2}{4\mu_w}\left(\boldsymbol{n}_{\Gamma_d}^T \boldsymbol{N}_d \boldsymbol{u}\right)^3 (\nabla \boldsymbol{N}_w \boldsymbol{p}_w)\frac{\partial S_w}{\partial p_c}(\nabla \boldsymbol{N}_w)^T \boldsymbol{N}_w \,\mathrm{d}\Gamma_d\end{aligned} \tag{C.29}$$

$$\boldsymbol{H}_{d,wn}^{cubic} = -\Delta t \int_{\Gamma_d} \frac{S_w^2}{4\mu_w}\left(\boldsymbol{n}_{\Gamma_d}^T \boldsymbol{N}_d \boldsymbol{u}\right)^3 (\nabla \boldsymbol{N}_w \boldsymbol{p}_w)\frac{\partial S_w}{\partial p_c}(\nabla \boldsymbol{N}_w)^T \boldsymbol{N}_n \,\mathrm{d}\Gamma_d \tag{C.30}$$

$$\boldsymbol{H}_{d,ns}^{cubic} = -\Delta t \int_{\Gamma_d} \frac{S_n^3}{4\mu_n}\left(\boldsymbol{n}_{\Gamma_d}^T \boldsymbol{N}_d \boldsymbol{u}\right)^2 (\nabla \boldsymbol{N}_n \boldsymbol{p}_n)(\nabla \boldsymbol{N}_n)^T \boldsymbol{n}_{\Gamma_d}^T \boldsymbol{N}_d \,\mathrm{d}\Gamma_d \tag{C.31}$$

$$\boldsymbol{H}_{d,nw}^{cubic} = -\Delta t \int_{\Gamma_d} \frac{S_n^2}{4\mu_n} \left(\boldsymbol{n}_{\Gamma_d}^T \boldsymbol{N}_d \boldsymbol{u}\right)^3 \left(\boldsymbol{\nabla N}_n \boldsymbol{p}_n\right) \frac{\partial S_w}{\partial p_c} \left(\boldsymbol{\nabla N}_n\right)^T \boldsymbol{N}_w \,\mathrm{d}\Gamma_d \tag{C.32}$$

$$\begin{aligned}\boldsymbol{H}_{d,nn}^{cubic} = -\Delta t \int_{\Gamma_d} & \frac{S_n^3}{12\mu_n} \left(\boldsymbol{n}_{\Gamma_d}^T \boldsymbol{N}_d \boldsymbol{u}\right)^3 \left(\boldsymbol{\nabla N}_n\right)^T \boldsymbol{\nabla N}_n \\ & - \frac{S_w^2}{4\mu_w} \left(\boldsymbol{n}_{\Gamma_d}^T \boldsymbol{N}_d \boldsymbol{u}\right)^3 \left(\boldsymbol{\nabla N}_w \boldsymbol{p}_w\right) \frac{\partial S_w}{\partial p_c} \left(\boldsymbol{\nabla N}_n\right)^T \boldsymbol{N}_n \,\mathrm{d}\Gamma_d\end{aligned} \tag{C.33}$$

for the volume-averaged bubbly flow by:

$$\begin{aligned}\boldsymbol{H}_{d,ws}^{bubbly} = -\Delta t \int_{\Gamma_d} & \frac{\Delta t S_w}{4\left(S_w\mu_w + S_n\mu_n\right)} \left(\boldsymbol{n}_{\Gamma_d}^T \boldsymbol{N}_d \boldsymbol{u}^{t+\Delta t}\right)^2 \\ & \left(S_w \boldsymbol{\nabla N}_w \boldsymbol{p}_w^{t+\Delta t} + S_n \boldsymbol{\nabla N}_n \boldsymbol{p}_n^{t+\Delta t}\right) \left(\boldsymbol{\nabla N}_w\right)^T \boldsymbol{n}_{\Gamma_d}^T \boldsymbol{N}_d \,\mathrm{d}\Gamma_d\end{aligned} \tag{C.34}$$

$$\begin{aligned}\boldsymbol{H}_{d,ww}^{bubbly} = -\Delta t \int_{\Gamma_d} & \frac{1}{12\left(S_w\mu_w + S_n\mu_n\right)} \left(\boldsymbol{n}_{\Gamma_d}^T \boldsymbol{N}_d \boldsymbol{u}^{t+\Delta t}\right)^3 \Bigg(\Bigg(\left(S_w \boldsymbol{\nabla N}_w \boldsymbol{p}_w + S_n \boldsymbol{\nabla N}_n \boldsymbol{p}_n\right) \\ & \left(-\frac{\partial S_w}{\partial p_c} + \frac{-S_w}{S_w\mu_w + S_n\mu_n}\left(-\frac{\partial S_w}{\partial p_c}\mu_w + \frac{\partial S_w}{\partial p_c}\mu_n\right)\right) \\ & + S_w\left(-\frac{\partial S_w}{\partial p_c}\boldsymbol{\nabla N}_w \boldsymbol{p}_w + \frac{\partial S_w}{\partial p_c}\boldsymbol{\nabla N}_n \boldsymbol{p}_n\right)\Bigg) \left(\boldsymbol{\nabla N}_w\right)^T \boldsymbol{N}_w + S_w^2 \left(\boldsymbol{\nabla N}_w\right)^T \boldsymbol{\nabla N}_w\Bigg) \,\mathrm{d}\Gamma_d\end{aligned} \tag{C.35}$$

$$\begin{aligned}\boldsymbol{H}_{d,wn}^{bubbly} = -\Delta t \int_{\Gamma_d} & \frac{1}{12\left(S_w\mu_w + S_n\mu_n\right)} \left(\boldsymbol{n}_{\Gamma_d}^T \boldsymbol{N}_d \boldsymbol{u}^{t+\Delta t}\right)^3 \Bigg(\Bigg(\left(S_w \boldsymbol{\nabla N}_w \boldsymbol{p}_w + S_n \boldsymbol{\nabla N}_n \boldsymbol{p}_n\right) \\ & \left(\frac{\partial S_w}{\partial p_c} + \frac{-S_w}{S_w\mu_w + S_n\mu_n}\left(\frac{\partial S_w}{\partial p_c}\mu_w - \frac{\partial S_w}{\partial p_c}\mu_n\right)\right) \\ & + S_w\left(\frac{\partial S_w}{\partial p_c}\boldsymbol{\nabla N}_w \boldsymbol{p}_w - \frac{\partial S_w}{\partial p_c}\boldsymbol{\nabla N}_n \boldsymbol{p}_n\right)\Bigg) \left(\boldsymbol{\nabla N}_w\right)^T \boldsymbol{N}_n + S_w S_n \left(\boldsymbol{\nabla N}_w\right)^T \boldsymbol{\nabla N}_n\Bigg) \,\mathrm{d}\Gamma_d\end{aligned} \tag{C.36}$$

$$\begin{aligned}\boldsymbol{H}_{d,ns}^{bubbly} = -\Delta t \int_{\Gamma_d} & \frac{\Delta t S_n}{4\left(S_w\mu_w + S_n\mu_n\right)} \left(\boldsymbol{n}_{\Gamma_d}^T \boldsymbol{N}_d \boldsymbol{u}^{t+\Delta t}\right)^2 \\ & \left(S_w \boldsymbol{\nabla N}_w \boldsymbol{p}_w^{t+\Delta t} + S_n \boldsymbol{\nabla N}_n \boldsymbol{p}_n^{t+\Delta t}\right) \left(\boldsymbol{\nabla N}_w\right)^T \boldsymbol{n}_{\Gamma_d}^T \boldsymbol{N}_d \mathrm{d}\,\Gamma_d\end{aligned} \tag{C.37}$$

$$\begin{aligned}\boldsymbol{H}_{d,nw}^{bubbly} = -\Delta t \int_{\Gamma_d} & \frac{1}{12\left(S_w\mu_w + S_n\mu_n\right)} \left(\boldsymbol{n}_{\Gamma_d}^T \boldsymbol{N}_d \boldsymbol{u}^{t+\Delta t}\right)^3 \Bigg(\Bigg(\left(S_w \boldsymbol{\nabla N}_w \boldsymbol{p}_w + S_n \boldsymbol{\nabla N}_n \boldsymbol{p}_n\right) \\ & \left(\frac{\partial S_w}{\partial p_c} + \frac{-S_n}{S_w\mu_w + S_n\mu_n}\left(-\frac{\partial S_w}{\partial p_c}\mu_w + \frac{\partial S_w}{\partial p_c}\mu_n\right)\right) \\ & + S_n\left(-\frac{\partial S_w}{\partial p_c}\boldsymbol{\nabla N}_w \boldsymbol{p}_w + \frac{\partial S_w}{\partial p_c}\boldsymbol{\nabla N}_n \boldsymbol{p}_n\right)\Bigg) \left(\boldsymbol{\nabla N}_n\right)^T \boldsymbol{N}_w + S_n S_w \left(\boldsymbol{\nabla N}_n\right)^T \boldsymbol{\nabla N}_w\Bigg) \,\mathrm{d}\Gamma_d\end{aligned} \tag{C.38}$$

$$\begin{aligned}\boldsymbol{H}_{d,nn}^{bubbly} = -\Delta t \int_{\Gamma_d} & \frac{1}{12\left(S_w\mu_w + S_n\mu_n\right)} \left(\boldsymbol{n}_{\Gamma_d}^T \boldsymbol{N}_d \boldsymbol{u}^{t+\Delta t}\right)^3 \Bigg(\Bigg(\left(S_w \boldsymbol{\nabla N}_w \boldsymbol{p}_w + S_n \boldsymbol{\nabla N}_n \boldsymbol{p}_n\right) \\ & \left(-\frac{\partial S_w}{\partial p_c} + \frac{-S_n}{S_w\mu_w + S_n\mu_n}\left(\frac{\partial S_w}{\partial p_c}\mu_w - \frac{\partial S_w}{\partial p_c}\mu_n\right)\right) \\ & + S_n\left(\frac{\partial S_w}{\partial p_c}\boldsymbol{\nabla N}_w \boldsymbol{p}_w - \frac{\partial S_w}{\partial p_c}\boldsymbol{\nabla N}_n \boldsymbol{p}_n\right)\Bigg) \left(\boldsymbol{\nabla N}_n\right)^T \boldsymbol{N}_n + S_n^2 \left(\boldsymbol{\nabla N}_n\right)^T \boldsymbol{\nabla N}_n\Bigg) \,\mathrm{d}\Gamma_d\end{aligned} \tag{C.39}$$

and for the separated flow model by:

$$\begin{aligned}\boldsymbol{H}_{d,ws}^{separated} = -\Delta t \int_{\Gamma_d} & \frac{1}{\mu_w} \left(\boldsymbol{n}_{\Gamma_d}^T \boldsymbol{N}_d \boldsymbol{u}\right)^2 \left(\boldsymbol{\nabla N}_w \boldsymbol{p}_w \left(\frac{1}{4} - \frac{3}{8}S_n + \frac{1}{8}S_n^3\right)\right. \\ & \left. + \left(\boldsymbol{\nabla N}_n \boldsymbol{p}_n - \boldsymbol{\nabla N}_w \boldsymbol{p}_w\right)\left(\frac{3}{8}S_n - \frac{3}{4}S_n^2 + \frac{3}{8}S_n^3\right)\right) \left(\boldsymbol{\nabla N}_w\right)^T \boldsymbol{n}_{\Gamma_d}^T \boldsymbol{N}_d \,\mathrm{d}\Gamma_d\end{aligned} \tag{C.40}$$

$$\begin{aligned}\boldsymbol{H}_{d,ww}^{separated} = & -\Delta t \int_{\Gamma_d} \frac{1}{\mu_w} \left(\boldsymbol{n}_{\Gamma_d}^T \boldsymbol{N}_d \boldsymbol{u}\right)^3 \left(\left(\nabla \boldsymbol{N}_w \boldsymbol{p}_w \left(\frac{1}{8} S_n^2 - \frac{1}{8}\right) + \left(\nabla \boldsymbol{N}_n \boldsymbol{p}_n - \nabla \boldsymbol{N}_w \boldsymbol{p}_w\right)\right.\right. \\ & \left.\left.\left(\frac{1}{8} - \frac{1}{2} S_n + \frac{3}{8} S_n^2\right)\right) \frac{\partial S_w}{\partial p_c} \left(\nabla \boldsymbol{N}_w\right)^T \boldsymbol{N}_w + \left(\frac{1}{12} - \frac{2}{8} S_n - \frac{1}{12} S_n^3 + \frac{1}{4} S_n^2\right) \left(\nabla \boldsymbol{N}_w\right)^T \nabla \boldsymbol{N}_w\right) \mathrm{d}\Gamma_d\end{aligned} \tag{C.41}$$

$$\begin{aligned}\boldsymbol{H}_{d,wn}^{separated} = & \Delta t \int_{\Gamma_d} \frac{1}{\mu_w} \left(\boldsymbol{n}_{\Gamma_d}^T \boldsymbol{N}_d \boldsymbol{u}\right)^3 \left(\left(\nabla \boldsymbol{N}_w \boldsymbol{p}_w \left(\frac{1}{8} S_n^2 - \frac{1}{8}\right) + \left(\nabla \boldsymbol{N}_n \boldsymbol{p}_n - \nabla \boldsymbol{N}_w \boldsymbol{p}_w\right)\right.\right. \\ & \left.\left.\left(\frac{1}{8} - \frac{1}{2} S_n + \frac{3}{8} S_n^2\right)\right) \frac{\partial S_w}{\partial p_c} \left(\nabla \boldsymbol{N}_w\right)^T \boldsymbol{N}_n + \left(\frac{1}{4} S_n^2 - \frac{1}{8} S_n - \frac{1}{8} S_n^3\right) \left(\nabla \boldsymbol{N}_w\right)^T \nabla \boldsymbol{N}_n\right) \mathrm{d}\Gamma_d\end{aligned} \tag{C.42}$$

$$\begin{aligned}\boldsymbol{H}_{d,ns}^{separated} = & -\Delta t \int_{\Gamma_d} \frac{1}{\mu_w} \left(\boldsymbol{n}_{\Gamma_d}^T \boldsymbol{N}_d \boldsymbol{u}\right)^2 \left(\frac{1}{12\mu_n} S_n^3 \nabla \boldsymbol{N}_n \boldsymbol{p}_n + \frac{1}{8\mu_w} \nabla \boldsymbol{N}_w \boldsymbol{p}_w \left(S_n - S_n^3\right)\right. \\ & \left. + \frac{1}{4\mu_w} \left(\nabla \boldsymbol{N}_n \boldsymbol{p}_n - \nabla \boldsymbol{N}_w \boldsymbol{p}_w\right) \left(S_n^2 - S_n^3\right)\right) \left(\nabla \boldsymbol{N}_n\right)^T \boldsymbol{n}_{\Gamma_d}^T \boldsymbol{N}_d \, \mathrm{d}\Gamma_d\end{aligned} \tag{C.43}$$

$$\begin{aligned}\boldsymbol{H}_{d,nw}^{separated} = & \Delta t \int_{\Gamma_d} \left(\boldsymbol{n}_{\Gamma_d}^T \boldsymbol{N}_d \boldsymbol{u}\right)^3 \left(\left(-\frac{1}{4\mu_n} S_n^2 \nabla \boldsymbol{N}_n \boldsymbol{p}_n + \frac{1}{\mu_w} \nabla \boldsymbol{N}_w \boldsymbol{p}_w \left(\frac{3}{8} S_n^2 - \frac{1}{8}\right)\right.\right. \\ & \left. + \frac{1}{\mu_w} \left(\nabla \boldsymbol{N}_n \boldsymbol{p}_n - \nabla \boldsymbol{N}_w \boldsymbol{p}_w\right) \left(\frac{3}{4} S_n^2 - \frac{1}{2} S_n\right)\right) \frac{\partial S_w}{\partial p_c} \left(\nabla \boldsymbol{N}_n\right)^T \boldsymbol{N}_n \\ & \left. + \left(\frac{1}{8\mu_w} \left(S_n^3 - S_n\right) + \frac{1}{4\mu_w} \left(S_n^2 - S_n^3\right)\right) \left(\nabla \boldsymbol{N}_n\right)^T \nabla \boldsymbol{N}_w\right) \mathrm{d}\Gamma_d\end{aligned} \tag{C.44}$$

$$\begin{aligned}\boldsymbol{H}_{d,nn}^{separated} = & -\Delta t \int_{\Gamma_d} \left(\boldsymbol{n}_{\Gamma_d}^T \boldsymbol{N}_d \boldsymbol{u}\right)^3 \left(\left(-\frac{1}{4\mu_n} S_n^2 \nabla \boldsymbol{N}_n \boldsymbol{p}_n + \frac{1}{\mu_w} \nabla \boldsymbol{N}_w \boldsymbol{p}_w \left(\frac{3}{8} S_n^2 - \frac{1}{8}\right)\right.\right. \\ & \left. + \frac{1}{\mu_w} \left(\nabla \boldsymbol{N}_n \boldsymbol{p}_n - \nabla \boldsymbol{N}_w \boldsymbol{p}_w\right) \left(\frac{3}{4} S_n^2 - \frac{1}{2} S_n\right)\right) \frac{\partial S_w}{\partial p_c} \left(\nabla \boldsymbol{N}_n\right)^T \boldsymbol{N}_n \\ & \left. + \left(\frac{1}{12\mu_n} S_n^3 + \frac{1}{4\mu_w} \left(S_n^2 - S_n^3\right)\right) \left(\nabla \boldsymbol{N}_n\right)^T \nabla \boldsymbol{N}_n\right) \mathrm{d}\Gamma_d\end{aligned} \tag{C.45}$$

C.2. DISCONTINUOUS PRESSURE MODEL

The discretised equations are linearised using a Newton-Raphson scheme, resulting in:

$$\begin{bmatrix} \boldsymbol{K} + \boldsymbol{K}_d & \boldsymbol{Q} & \boldsymbol{Q}_d \\ \boldsymbol{Q}^T & \boldsymbol{C} + \boldsymbol{H} + \boldsymbol{H}_{d,p} & \boldsymbol{H}_{d,d} \\ \boldsymbol{Q}_d^T + \boldsymbol{H}_{dp,u} & \boldsymbol{H}_{d,d}^T & \boldsymbol{H}_{d,dp} + \boldsymbol{H}_{dp,dp} \end{bmatrix} \begin{bmatrix} \mathrm{d}\boldsymbol{u} \\ \mathrm{d}\boldsymbol{p} \\ \mathrm{d}\boldsymbol{p}_d \end{bmatrix} = \begin{bmatrix} \boldsymbol{f}_{ext} \\ \boldsymbol{q}_{ext} \\ \boldsymbol{q}_{d,ext} \end{bmatrix} - \begin{bmatrix} \boldsymbol{f}_{int} + \boldsymbol{f}_d \\ \boldsymbol{q}_{int} + \boldsymbol{q}_d \\ \boldsymbol{q}_{d,int} + \boldsymbol{q}_{d,d} \end{bmatrix} \tag{C.46}$$

with the forces defined in Eq 2.48,2.47,5.16, the fluid fluxes for the porous media in Eq. 2.52, 2.53, 5.18, and for the fracture in 5.20, 5.21, 5.22. The tangential stiffness sub-matrices are given by:

$$\boldsymbol{K} = \frac{\partial \boldsymbol{f}_{int}}{\partial \boldsymbol{u}} = \int_{\Omega} \boldsymbol{B}^T \boldsymbol{D} \boldsymbol{B} \, \mathrm{d}\Omega \tag{C.47}$$

$$\boldsymbol{K}_d = \frac{\partial \boldsymbol{f}_d}{\partial \boldsymbol{u}} = \int_{\Gamma_d} \boldsymbol{N}_d^T \boldsymbol{R}^T \boldsymbol{D}_d \boldsymbol{R} \boldsymbol{N}_d \, \mathrm{d}\Gamma_d \tag{C.48}$$

$$\boldsymbol{Q} = \frac{\partial \boldsymbol{f}_{int}}{\partial \boldsymbol{p}} = -\int_{\Omega} \alpha \boldsymbol{B}^T \boldsymbol{m} \boldsymbol{N}_f \, \mathrm{d}\Omega \tag{C.49}$$

$$\boldsymbol{Q}_d = \frac{\partial \boldsymbol{f}_d}{\partial \boldsymbol{p}_d} = -\int_{\Gamma_d} \boldsymbol{N}_d^T \boldsymbol{n}_{\Gamma_d} \boldsymbol{N}_{pd} \mathrm{d}\Gamma_d \tag{C.50}$$

$$\boldsymbol{C} = \frac{\partial \boldsymbol{q}_{int1}}{\partial \boldsymbol{p}} = -\int_{\Omega} \frac{1}{M} \boldsymbol{N}_f^T \boldsymbol{N}_f \, \mathrm{d}\Omega \tag{C.51}$$

$$\boldsymbol{H} = \frac{\partial \boldsymbol{q}_{int2}}{\partial \boldsymbol{p}} = -\int_{\Omega} \frac{k_f^* \Delta t}{n} \left|\nabla \boldsymbol{p}^{t+\Delta t}\right|^{\frac{1}{n}-1} \left(\nabla \boldsymbol{N}_f\right)^T \nabla \boldsymbol{N}_f \,\mathrm{d}\Omega \tag{C.52}$$

$$\boldsymbol{H}_{d,p} = \frac{\partial \boldsymbol{q}_d}{\partial \boldsymbol{p}} = -\int_{\Gamma_d^{\pm}} k_i^{el} \Delta t \boldsymbol{N}_f^T \boldsymbol{N}_f \,\mathrm{d}\Gamma_d \tag{C.53}$$

$$\boldsymbol{H}_{d,d} = \frac{\partial \boldsymbol{q}_d}{\partial \boldsymbol{p}_d} = \int_{\Gamma_d^{\pm}} k_i^{el} \Delta t \boldsymbol{N}_f^T \boldsymbol{N}_{pd} \,\mathrm{d}\Gamma_d \tag{C.54}$$

$$\boldsymbol{H}_{d,dp} = \frac{\partial \boldsymbol{q}_{d,d}}{\partial \boldsymbol{p}_d} = -2\int_{\Gamma_d} k_i^{el} \Delta t \boldsymbol{N}_{pd}^T \boldsymbol{N}_{pd} \,\mathrm{d}\Gamma_d \tag{C.55}$$

$$\boldsymbol{H}_{dp,u} = \frac{\partial \boldsymbol{q}_{d,int}}{\partial \boldsymbol{u}} = -\int_{\Gamma_d} \Delta t \mu_0^{-\frac{1}{n}} \left|\nabla \boldsymbol{N}_{pd} \boldsymbol{p}_d^{t+\Delta t}\right|^{\frac{1}{n}-1} \left(\frac{\boldsymbol{n}_{\Gamma_d} \boldsymbol{N}_d \boldsymbol{u}^{t+\Delta t}}{2}\right)^{\frac{1}{n}+1} \nabla \boldsymbol{N}_{pd} \boldsymbol{p}_d^{t+\Delta t} \nabla \boldsymbol{N}_{pd}^T \boldsymbol{n}_{\Gamma_d} \boldsymbol{N}_d \,\mathrm{d}\Gamma_d \tag{C.56}$$

$$\boldsymbol{H}_{dp,dp} = \frac{\partial \boldsymbol{q}_{d,int}}{\partial \boldsymbol{p}_d} = -\int_{\Gamma_d} \Delta t \frac{2}{2n+1} \mu_0^{-\frac{1}{n}} \left|\nabla \boldsymbol{N}_{pd} \boldsymbol{p}_d^{t+\Delta t}\right|^{\frac{1}{n}-1} \left(\frac{\boldsymbol{n}_{\Gamma_d} \boldsymbol{N}_d \boldsymbol{u}^{t+\Delta t}}{2}\right)^{\frac{1}{n}+2} \nabla\, \boldsymbol{N}_{pd}^T \nabla \boldsymbol{N}_{pd} \,\mathrm{d}\Gamma_d \tag{C.57}$$

C.3. COSSERAT CONTINUUM

The discretised equations are solved using a monolithic Newton-Raphson scheme, calculating the iterative increments through:

$$\begin{bmatrix} \boldsymbol{K} + \boldsymbol{M} + \boldsymbol{K}_d + \boldsymbol{K}_{ext} & \boldsymbol{Q}_s + \boldsymbol{M}_f & \boldsymbol{Q}_d \\ \boldsymbol{Q}_f + \boldsymbol{A}_s & \boldsymbol{C}_f + \boldsymbol{H} + \boldsymbol{H}_d & \boldsymbol{H}_{dd} \\ \boldsymbol{0} & \boldsymbol{H}_{dd}^T & \boldsymbol{H}_{df} \end{bmatrix} \begin{bmatrix} \mathrm{d}\boldsymbol{u} \\ \mathrm{d}\boldsymbol{p} \\ \mathrm{d}\boldsymbol{p}_d \end{bmatrix} = \begin{bmatrix} \boldsymbol{f}_{ext} \\ \boldsymbol{q}_{ext} \\ \boldsymbol{0} \end{bmatrix} - \begin{bmatrix} \boldsymbol{f}_{int} + \boldsymbol{f}_d \\ \boldsymbol{q}_{int} + \boldsymbol{q}_d \\ \boldsymbol{q}_{d,int} \end{bmatrix} \tag{C.58}$$

with the sub-matrices for the momentum balance given by:

$$\boldsymbol{K} = \int_{\Omega} \boldsymbol{B}^T \boldsymbol{D}_{eff} \boldsymbol{B} \,\mathrm{d}\Omega \tag{C.59}$$

$$\boldsymbol{M} = \int_{\Omega} \frac{1}{\beta \Delta t^2} \boldsymbol{N}_s^T \left(\overline{\boldsymbol{\rho}} - An_f \boldsymbol{\rho}_f\right) \boldsymbol{N}_s \,\mathrm{d}\Omega \tag{C.60}$$

$$\boldsymbol{K}_d = \int_{\Gamma_d} \boldsymbol{N}_s^T \boldsymbol{R}^T \boldsymbol{D}_i \boldsymbol{R} \boldsymbol{N}_s + \boldsymbol{N}_s^T \boldsymbol{R}^T \boldsymbol{D}_{czm} \boldsymbol{R} \boldsymbol{N}_s \,\mathrm{d}\Gamma_d \tag{C.61}$$

$$\boldsymbol{K}_{ext} = \int_{\Gamma} \frac{\gamma}{\beta \Delta t} \boldsymbol{N}_s^T \boldsymbol{R}^T \boldsymbol{S} \boldsymbol{R} \boldsymbol{N}_s \,\mathrm{d}\Gamma \tag{C.62}$$

$$\boldsymbol{Q}_s = -\int_{\Omega} \alpha \boldsymbol{B}^T \boldsymbol{m} \boldsymbol{N}_f \,\mathrm{d}\Omega \tag{C.63}$$

$$\boldsymbol{M}_f = -\int_{\Omega} An_f \boldsymbol{N}_s^T \boldsymbol{I}_c \nabla \boldsymbol{N}_f^T \,\mathrm{d}\Omega \tag{C.64}$$

$$\boldsymbol{Q}_d = -\int_{\Gamma_d} \boldsymbol{N}_s^T \boldsymbol{n}_{\Gamma_d} \boldsymbol{N}_{pd} \,\mathrm{d}\Gamma_d \tag{C.65}$$

The matrix which contains the dummy stiffness values used to prevent a negative fracture opening reads:

$$\boldsymbol{D}_i = \begin{bmatrix} d_n & 0 & 0 \\ 0 & 0 & 0 \\ 0 & 0 & d_\omega \end{bmatrix}$$

If the history variable is larger than the current tangential displacement, then the tangential stiffness component is given by:

$$D_{czm}(t,n) = -f_r d_n + (f_p - f_r)\exp\left(-2\llbracket \mathrm{d}x \rrbracket / D_c\right)\big(-d_n + d_n \llbracket u_n \rrbracket \cdot 2\llbracket \mathrm{d}x \rrbracket / D_c^2 \cdot 2\mathscr{G}_c / \big((f_p - f_r) d_n \llbracket u_n \rrbracket^2\big)\big)$$

Otherwise, the non-zero components read:

$$D_{czm}(t,t) = 2(f_p - f_r) d_n \llbracket u_n \rrbracket / D_c \exp\left(-2\llbracket u_t \rrbracket / D_c\right)$$
$$D_{czm}(t,n) = -f_r d_n + (f_p - f_r)\exp\left(-2\llbracket u_t \rrbracket / D_c\right)\big(-d_n + d_n \llbracket u_n \rrbracket \cdot 2\llbracket u_t \rrbracket / D_c^2 \cdot 2\mathscr{G}_c / \big((f_p - f_r) d_n \llbracket u_n \rrbracket^2\big)\big)$$

The sub-matrices related to the mass balances of the porous material and the fracture are given by:

$$\boldsymbol{Q}_f = -\int_\Omega \frac{\alpha\gamma}{\beta} \boldsymbol{N}_f^T \boldsymbol{I}_c \boldsymbol{B}\, \mathrm{d}\Omega \tag{C.66}$$

$$\boldsymbol{C}_f = -\int_\Omega \frac{1}{M\theta} \boldsymbol{N}_f^T \boldsymbol{N}_f\, \mathrm{d}\Omega \tag{C.67}$$

$$\boldsymbol{A}_s = -\int_\Omega \frac{k\rho_f}{\mu\Delta t\beta}\left(1 + \frac{\rho_f k}{n_f \mu\theta\Delta t}\right)^{-1} \left(\nabla \boldsymbol{N}_f\right)^T \boldsymbol{I}_c \boldsymbol{N}_s\, \mathrm{d}\Omega \tag{C.68}$$

$$\boldsymbol{H} = -\int_\Omega \frac{k\Delta t}{\mu}\left(1 + \frac{\rho_f k}{n_f \mu\theta\Delta t}\right)^{-1} \left(\nabla \boldsymbol{N}_f\right)^T \nabla \boldsymbol{N}_f\, \mathrm{d}\Omega \tag{C.69}$$

$$\boldsymbol{H}_d = -\int_{\Gamma_d} k_i \Delta t \boldsymbol{N}_f^T \boldsymbol{N}_f\, \mathrm{d}\Gamma_d \tag{C.70}$$

$$\boldsymbol{H}_{dd} = \int_{\Gamma_d} k_i \Delta t \boldsymbol{N}_f^T \boldsymbol{N}_{pd}\, \mathrm{d}\Gamma_d \tag{C.71}$$

$$\boldsymbol{H}_{df} = -\int_{\Gamma_d} 2k_i \Delta t \boldsymbol{N}_{pd}^T \boldsymbol{N}_{pd}\, \mathrm{d}\Gamma_d \tag{C.72}$$

D

DERIVATION OF MULTIPHASE POROELASTICITY

Formulations for the mass balances for multiphase fluid flow are given in [39, 108, 110, 155, 188]. However, these formulations differ and little to none of the derivation and used assumptions are given. Because of this, the equations for the mass balance will be derived in this section, and a dimensional analysis will be done to determine under which circumstances certain terms can be neglected.

MASS CONSERVATION

First, the mass conservation for the solid is used [110], and a constant porosity is assumed:

$$\frac{\partial(1-n_f)\rho_s}{\partial t} + \boldsymbol{\nabla}\cdot((1-n_f)\rho_s \boldsymbol{v}_s) = 0$$

$$(1-n_f)\frac{\partial \rho_s}{\partial t} + (1-n_f)\left(\rho_s \boldsymbol{\nabla}\cdot\boldsymbol{v}_s + \boldsymbol{v}_s\cdot\boldsymbol{\nabla}\rho_s\right) = 0 \tag{D.1}$$

with n_f the porosity, ρ_s the density of the solid, and $\boldsymbol{v}_s$ the velocity of the solid material. The time derivative of the density is rewritten as [39]:

$$\frac{\partial \rho_s}{\partial t} = \frac{\rho_s}{1-n_f}\left(\frac{\alpha - n_f}{K_s}\dot{\overline{p}} - (1-\alpha)\boldsymbol{\nabla}\cdot\boldsymbol{v}_s\right) \tag{D.2}$$

with K_s the bulk modulus of the solid material and $\dot{\overline{p}}$ the time derivative of the total pressure, defined as:

$$\begin{aligned}\dot{\overline{p}} &= \frac{\partial}{\partial t}\left(S_n p_n + S_w p_w\right)\\ &= \dot{S}_n p_n + S_n \dot{p}_n + \dot{S}_w p_w + S_w \dot{p}_w\\ &= \left(S_n - p_c\frac{\partial S_w}{\partial p_c}\right)\dot{p}_n + \left(S_w + p_c\frac{\partial S_w}{\partial p_c}\right)\dot{p}_w\end{aligned} \tag{D.3}$$

using p_π and S_π for the pressure and saturation of phase π. Substituting Equation D.2 in Equation D.1 results in:

$$\frac{\alpha - n_f}{K_s}\dot{\overline{p}} + \alpha\boldsymbol{\nabla}\cdot\boldsymbol{v}_s - n_f\boldsymbol{\nabla}\cdot\boldsymbol{v}_s + \frac{1-n_f}{\rho_s}\boldsymbol{v}_s\cdot\boldsymbol{\nabla}\rho_s = 0 \tag{D.4}$$

The mass conservation equation for the wetting fluid phase is [110]:

$$\frac{\partial n_f S_w \rho_w}{\partial t} + \boldsymbol{\nabla}\cdot\left(n_f S_w \rho_w \boldsymbol{v}_w\right) = 0$$

$$n_f\left(\rho_w \dot{S}_w + S_w\frac{\partial \rho_w}{\partial t}\right) + n_f\left(\rho_w\boldsymbol{\nabla}\cdot(S_w\boldsymbol{v}_w) + S_w\boldsymbol{v}_w\cdot\boldsymbol{\nabla}\rho_w\right) = 0 \tag{D.5}$$

Using the definition for the density change of the wetting phase [39]:

$$\frac{\partial \rho_w}{\partial t} = \frac{\rho_w}{K_w}\dot{p}_w \tag{D.6}$$

Equation D.5 can be rewritten to:

$$n_f\dot{S}_w + \frac{n_f S_w}{K_w}\dot{p}_w + n_f\boldsymbol{\nabla}\cdot(S_w\boldsymbol{v}_w) + \frac{n_f S_w}{\rho_w}\boldsymbol{v}_w\cdot\boldsymbol{\nabla}\rho_w = 0 \tag{D.7}$$

In the same manner, an expression is derived for the mass conservation of the non-wetting phase:

$$n_f \dot{S}_n + \frac{n_f S_n}{K_n}\dot{p}_n + n_f \boldsymbol{\nabla}\cdot(S_n \boldsymbol{v}_n) + \frac{n_f S_n}{\rho_n}\boldsymbol{v}_n \cdot \boldsymbol{\nabla}\rho_n = 0 \tag{D.8}$$

The time derivatives of the saturation are defined as:

$$\dot{S}_w = -\dot{S}_n = \frac{\partial S_w}{\partial p_c}\frac{\partial p_c}{\partial t} = (\dot{p}_n - \dot{p}_w)\frac{\partial S_w}{\partial p_c} \tag{D.9}$$

PRESSURE CHANGES

Multiplying Equation D.4 with S_w and adding this to the mass conservation of the wetting phase (Equation D.7) results in:

$$\begin{aligned}
&S_w\frac{\alpha - n_f}{K_s}\dot{\bar{p}} + \alpha S_w \boldsymbol{\nabla}\cdot\boldsymbol{v}_s + n_f\dot{S}_w + \frac{n_f S_w}{K_w}\dot{p}_w + n_f\boldsymbol{\nabla}\cdot(S_w\boldsymbol{v}_w) - n_f S_w\boldsymbol{\nabla}\cdot\boldsymbol{v}_s \qquad + R'_w = 0\\
&S_w\frac{\alpha - n_f}{K_s}\dot{\bar{p}} + \alpha S_w \boldsymbol{\nabla}\cdot\boldsymbol{v}_s + n_f\dot{S}_w + \frac{n_f S_w}{K_w}\dot{p}_w + \boldsymbol{\nabla}\cdot(n_f S_w(\boldsymbol{v}_w - \boldsymbol{v}_s)) - n_f\boldsymbol{v}_s\cdot\boldsymbol{\nabla}S_w + R'_w = 0
\end{aligned} \tag{D.10}$$

with R'_w defined as:

$$R'_w = S_w\frac{1-n_f}{\rho_s}\boldsymbol{v}_s\cdot\boldsymbol{\nabla}\rho_s + \frac{n_f S_w}{\rho_w}\boldsymbol{v}_w\cdot\boldsymbol{\nabla}\rho_w \tag{D.11}$$

Using the definition for the Darcy velocity, $\boldsymbol{q}_w = n_f S_w(\boldsymbol{v}_w - \boldsymbol{v}_s)$, Equation D.10 can be simplified to:

$$S_w\frac{\alpha - n_f}{K_s}\dot{\bar{p}} + \alpha S_w\boldsymbol{\nabla}\cdot\boldsymbol{v}_s + n_f\dot{S}_w + \frac{n_f S_w}{K_w}\dot{p}_w + \boldsymbol{\nabla}\cdot\boldsymbol{q}_w + R_w = 0 \tag{D.12}$$

and multiplying Equation D.4 with S_n and adding to the mass conservation equation of non-wetting phase (Equation D.8) results in:

$$S_n\frac{\alpha - n_f}{K_s}\dot{\bar{p}} + \alpha S_n\boldsymbol{\nabla}\cdot\boldsymbol{v}_s + n_f\dot{S}_n + \frac{n_f S_n}{K_n}\dot{p}_n + \boldsymbol{\nabla}\cdot\boldsymbol{q}_n + R_n = 0 \tag{D.13}$$

The groups R_w and R_n are defined as:

$$R_w = S_w\frac{1-n_f}{\rho_s}\boldsymbol{v}_s\cdot\boldsymbol{\nabla}\rho_s + \frac{n_f S_w}{\rho_w}\boldsymbol{v}_w\cdot\boldsymbol{\nabla}\rho_w - n_f\boldsymbol{v}_s\cdot\boldsymbol{\nabla}S_w \tag{D.14}$$

$$R_n = S_n\frac{1-n_f}{\rho_s}\boldsymbol{v}_s\cdot\boldsymbol{\nabla}\rho_s + \frac{n_f S_n}{\rho_n}\boldsymbol{v}_n\cdot\boldsymbol{\nabla}\rho_n - n_f\boldsymbol{v}_s\cdot\boldsymbol{\nabla}S_n \tag{D.15}$$

Substituting the definition for the total pressure derivative (Equation D.3) and for the saturation derivatives (Equation D.9) into Equation D.12 and D.13 results in the following system of equations:

$$\frac{1}{M_{ww}}\dot{p}_w + \frac{1}{M_{wn}}\dot{p}_n = -\alpha S_w\boldsymbol{\nabla}\cdot\boldsymbol{v}_s - \boldsymbol{\nabla}\cdot\boldsymbol{q}_w - R_w \tag{D.16}$$

$$\frac{1}{M_{nw}}\dot{p}_w + \frac{1}{M_{nn}}\dot{p}_n = -\alpha S_n\boldsymbol{\nabla}\cdot\boldsymbol{v}_s - \boldsymbol{\nabla}\cdot\boldsymbol{q}_n - R_n \tag{D.17}$$

with the coefficients defined as:

$$\begin{aligned}
\frac{1}{M_{ww}} &= S_w \frac{\alpha - n_f}{K_s}\left(S_w + p_c \frac{\partial S_w}{\partial p_c}\right) - n_f \frac{\partial S_w}{\partial p_c} + \frac{n_f S_w}{K_w} \\
\frac{1}{M_{wn}} &= S_w \frac{\alpha - n_f}{K_s}\left(S_n - p_c \frac{\partial S_w}{\partial p_c}\right) + n_f \frac{\partial S_w}{\partial p_c} \\
\frac{1}{M_{nw}} &= S_n \frac{\alpha - n_f}{K_s}\left(S_w + p_c \frac{\partial S_w}{\partial p_c}\right) + n_f \frac{\partial S_w}{\partial p_c} \\
\frac{1}{M_{nn}} &= S_n \frac{\alpha - n_f}{K_s}\left(S_n - p_c \frac{\partial S_w}{\partial p_c}\right) - n_f \frac{\partial S_w}{\partial p_c} + \frac{n_f S_n}{K_n}
\end{aligned} \tag{D.18}$$

DIMENSIONAL ANALYSIS

To determine which terms can be neglected, a dimensional analysis was performed. For this, the R terms are rewritten in term of the solid velocity and Darcy fluid flux:

$$\begin{aligned}
R_w &= S_w \frac{1 - n_f}{\rho_s} \boldsymbol{v}_s \cdot \boldsymbol{\nabla} \rho_s - n_f \boldsymbol{v}_s \cdot \boldsymbol{\nabla} S_w + \frac{1}{\rho_w} \boldsymbol{q}_w \cdot \boldsymbol{\nabla} \rho_w + \frac{n_f S_w}{\rho_w} \boldsymbol{v}_s \cdot \boldsymbol{\nabla} \rho_w \\
R_n &= S_n \frac{1 - n_f}{\rho_s} \boldsymbol{v}_s \cdot \boldsymbol{\nabla} \rho_s - n_f \boldsymbol{v}_s \cdot \boldsymbol{\nabla} S_n + \frac{1}{\rho_n} \boldsymbol{q}_n \cdot \boldsymbol{\nabla} \rho_n + \frac{n_f S_n}{\rho_n} \boldsymbol{v}_s \cdot \boldsymbol{\nabla} \rho_n
\end{aligned} \tag{D.19}$$

In order to make Equation D.16-D.19 dimensionless, the following normalisation is used:

$$\begin{aligned}
p &= P p^* \\
t &= \tau t^* \\
\boldsymbol{v}_\pi &= U_\pi \boldsymbol{v}_\pi^* \\
\boldsymbol{q}_\pi &= \frac{kP}{L \mu_\pi} \boldsymbol{q}_\pi^* \\
\boldsymbol{\nabla} &= \frac{1}{L} \boldsymbol{\nabla}^* \\
\frac{1}{\rho_\pi} \boldsymbol{\nabla} \rho_\pi &= \frac{P}{L K_\pi} \boldsymbol{\nabla}^* p^*
\end{aligned}$$

with π being s, w, n to indicate the different phases. This normalisation allows the M coefficients to be normalised as:

$$\frac{1}{M_{\pi\pi}} = \frac{1}{K_s} \frac{1}{M_{\pi\pi}^*}$$

and allows Equation D.12 to be normalised as:

$$\frac{P}{\tau K_s}\left(\frac{1}{M_{ww}^*} \dot{p}_w^* + \frac{1}{M_{wg}^*} \dot{p}_n^*\right) = -\frac{\alpha S_w U_s}{L} \boldsymbol{\nabla}^* \cdot \boldsymbol{v}_s^* - \frac{kP}{L^2 \mu_w} \boldsymbol{\nabla}^* \cdot \boldsymbol{q}_w^* - R_w$$

$$\frac{1}{M_{ww}^*} \dot{p}_w^* + \frac{1}{M_{wg}^*} \dot{p}_n^* = -\frac{U_s K_s \tau}{LP} \alpha S_w \boldsymbol{\nabla}^* \cdot \boldsymbol{v}_s^* - \frac{k \tau K_s}{L^2 \mu_w} \boldsymbol{\nabla}^* \cdot \boldsymbol{q}_w^* - R_w^* \tag{D.20}$$

with R_w^* defined as:

$$\begin{aligned}
R_w^* &= \frac{\tau K_s}{P}\left(\frac{P U_s}{L K_s} S_w (1 - n_f) \boldsymbol{v}_s^* \boldsymbol{\nabla}^* p^* - \frac{U_s}{L} n_f \boldsymbol{v}_s^* \cdot \boldsymbol{\nabla}^* S_w + \frac{k P^2}{L^2 K_w \mu_w} \boldsymbol{q}_w^* \cdot \boldsymbol{\nabla}^* p_w^* + \frac{U_s P}{L K_w} n_f S_w \boldsymbol{v}_s^* \cdot \boldsymbol{\nabla}^* p_w^*\right) \\
&= \frac{\tau U_s}{L} S_w (1 - n_f) \boldsymbol{v}_s^* \boldsymbol{\nabla}^* p^* - \frac{\tau K_s U_s}{PL} n_f \boldsymbol{v}_s^* \cdot \boldsymbol{\nabla}^* S_w + \frac{k P \tau K_s}{L^2 K_w \mu_w} \boldsymbol{q}_w^* \cdot \boldsymbol{\nabla}^* p_w^* + \frac{U_s \tau K_s}{L K_w} n_f S_w \boldsymbol{v}_s^* \cdot \boldsymbol{\nabla}^* p_w^*
\end{aligned} \tag{D.21}$$

For pressure driven flows the Darcy fluid velocity term of Equation D.20 is much larger than the solid velocity term. In contrast, for cases where flow is induced through compression of the porous material, both terms are of the same order of magnitude. When comparing the terms from R with the terms from Equation D.20, it can thus be concluded that terms can be neglected for pressure driven cases if they are much smaller than the Darcy fluid velocity term. For solid deformation driven cases, the R terms need to be smaller than both the Darcy velocity and the deformation terms. In the remainder of this section, the R terms will be compared to both, with on the left the comparison with the solid velocity, and on the right with the Darcy velocity.

The requirements for the first term in Equation D.21 to be neglected are:

$$\frac{K_s}{P} >> 1 \qquad \text{and} \qquad \frac{kK_s}{U_s L \mu_w} >> 1 \tag{D.22}$$

The first condition is almost always satisfied since pressures usually are in the order of MPa, while the solid bulk modulus is in the order of GPa. The second condition is also almost always satisfied: replacing K_s with P (which will always result in a smaller value) reduces this assumption to $(U_w - U_s)/U_s$. Since the solid only has small deformations, and the wetting phase velocity will be much larger than the solid velocity, this will be much larger than one. Both these conditions are always fulfilled, thus this term can be neglected for all cases.

The conditions for the second term are:

$$1 >> 1 \qquad \text{and} \qquad \frac{kP}{L\mu_w U_s} >> 1 \tag{D.23}$$

Since the first assumption is impossible to satisfy, this term can't be neglected when the simulated case is dominated by deformation induced flow. The second assumption corresponds to the second assumption for the first term, thus is valid. The second term of R_w can thus be neglected for pressure driven flows.

The conditions for the third term are:

$$\frac{U_s L K_w \mu_w}{P^2 k} >> 1 \qquad \text{and} \qquad \frac{K_w}{P} >> 1 \tag{D.24}$$

which are valid as long as the wetting phase is mostly incompressible. Finally the fourth term can be neglected if:

$$\frac{K_w}{P} >> 1 \qquad \text{and} \qquad \frac{kK_w}{U_s L \mu_w} >> 1 \tag{D.25}$$

Assuming the wetting fluid and the solid have comparable bulk moduli, these assumptions correspond to the assumption of D.22, and thus are satisfied, indicating the fourth term can be neglected.

The same can be done for the equation for the non-wetting phase, resulting in the following assumptions:

$$\frac{K_s}{P} >> 1 \qquad \text{and} \qquad \frac{kK_s}{U_s L \mu_w} >> 1 \tag{D.26}$$

$$1 >> 1 \qquad \text{and} \qquad \frac{kP}{L\mu_n U_s} >> 1 \tag{D.27}$$

$$\frac{U_s L K_n \mu_w}{P^2 k} >> 1 \qquad \text{and} \qquad \frac{K_n}{P} >> 1 \tag{D.28}$$

$$\frac{K_n}{P} >> 1 \qquad \text{and} \qquad \frac{kK_n}{U_s L \mu_n} >> 1 \tag{D.29}$$

Similarly to the wetting phase, the second term can't be neglected for deformation dominated cases. However, if the non-wetting phase represents a gas phase, the non-wetting phase can't be assumed to be incompressible. For this case, K_n is of the same order of the applied pressure, therefore the third term can't be neglected under any circumstance. The fourth term can also not be neglected for compression dominated flows.

RESULTING EQUATIONS

For fluid pressure driven flows, the resulting equations are:

$$\frac{1}{M_{ww}}\dot{p}_w + \frac{1}{M_{wn}}\dot{p}_n = -\alpha S_w \boldsymbol{\nabla} \cdot \boldsymbol{v}_s - \boldsymbol{\nabla} \cdot \boldsymbol{q}_w - \frac{1}{K_w}\boldsymbol{q}_w \cdot \boldsymbol{\nabla} p_w \tag{D.30}$$

$$\frac{1}{M_{nw}}\dot{p}_w + \frac{1}{M_{nn}}\dot{p}_n = -\alpha S_n \boldsymbol{\nabla} \cdot \boldsymbol{v}_s - \boldsymbol{\nabla} \cdot \boldsymbol{q}_n - \frac{1}{K_n}\boldsymbol{q}_n \cdot \boldsymbol{\nabla} p_n \tag{D.31}$$

with the Biot moduli given by Equation D.18. In these equations, the $\frac{1}{K_w}\boldsymbol{q}_w \cdot \boldsymbol{\nabla} p_w$ and $\frac{1}{K_n}\boldsymbol{q}_n \cdot \boldsymbol{\nabla} p_n$ terms can be neglected when an incompressible non-wetting phase is assumed. This corresponds to the equations from [110] for a compressible gas, and the equations from [188] for an incompressible non-wetting phase.

PUBLISHED PAPERS

[1] T. Hageman and R. de Borst. "A convergence study of monolithic simulations of flow and deformation in fractured poroelastic media". In: *International Journal for Numerical Methods in Engineering* 121.3 (2020), pp. 393–410. DOI: `10.1002/nme.6213`.

[2] T. Hageman and R. de Borst. "A refined two-scale model for Newtonian and non-Newtonian fluids in fractured poroelastic media". In: *Journal of Computational Physics* 441 (2021), p. 110424. DOI: `10.1016/j.jcp.2021.110424`.

[3] T. Hageman and R. de Borst. "Direct simulation vs subgrid scale modelling of fluid flow in fractured or fracturing porous media [Submitted]". In: *Computational Geosciences* (2021).

[4] T. Hageman and R. de Borst. "Flow of non-Newtonian fluids in fractured porous media: Isogeometric vs standard finite element discretisation". In: *International Journal for Numerical and Analytical Methods in Geomechanics* 43.11 (2019), pp. 2020–2037. DOI: `10.1002/nag.2948`.

[5] T. Hageman and R. de Borst. "Stick-slip like behavior in shear fracture propagation including the effect of fluid flow". In: *International Journal for Numerical and Analytical Methods in Geomechanics* 45.7 (2021), pp. 965–989. DOI: `10.1002/nag.3186`.

[6] T. Hageman and R. de Borst. "Sub-grid models for multiphase fluid flow inside fractures in poroelastic media". In: *Journal of Computational Physics* 414 (2020), p. 109481. DOI: `10.1016/j.jcp.2020.109481`.

[7] T. Hageman, K. M. Pervaiz Fathima, and R. de Borst. "Isogeometric analysis of fracture propagation in saturated porous media due to a pressurised non-Newtonian fluid". In: *Computers and Geotechnics* 112 (2019), pp. 272–283. DOI: `10.1016/j.compgeo.2019.04.030`.

[8] T. Hageman, S. A. Sabet, and R. de Borst. "Convergence in non-associated plasticity and fracture propagation for standard, rate-dependent, and Cosserat continua". In: *International Journal for Numerical Methods in Engineering* 122.3 (2021), pp. 777–795. DOI: `10.1002/nme.6561`.

[9] I. R. Abdelraziq and T. H. Nierat. “Rheology Properties of Castor Oil: Temperature and Shear Rate-dependence of Castor Oil Shear Stress”. In: *Journal of Material Science & Engineering* 05.01 (2015), pp. 1–6. DOI: `10.4172/2169-0022.1000220`.

[10] D. P. Adhikary and A. V. Dyskin. “A continuum model of layered rock masses with non-associative joint plasticity”. In: *International Journal for Numerical and Analytical Methods in Geomechanics* 22.4 (1998), pp. 245–261. DOI: `10.1002/(SICI)1096-9853(199804)22:4<245::AID-NAG916>3.0.CO;2-R`.

[11] M. Ahmad, A. Amin, Abdullah, M. S. Akram, and M. R. Usman. “Characterization and rheological behaviour of various Pakistani crude oils”. In: *Brazilian Journal of Petroleum and Gas* 9.3 (2015), pp. 85–94. DOI: `10.5419/bjpg2015-0009`.

[12] I. Y. Akkutlu, Y. Efendiev, M. Vasilyeva, and Y. Wang. “Multiscale model reduction for shale gas transport in poroelastic fractured media”. In: *Journal of Computational Physics* 353 (2018), pp. 356–376. DOI: `10.1016/j.jcp.2017.10.023`.

[13] I. Ambartsumyan, E. Khattatov, T. Nguyen, and I. Yotov. “Flow and transport in fractured poroelastic media”. In: *GEM - International Journal on Geomathematics* 10.1 (2019), pp. 1–34. DOI: `10.1007/s13137-019-0119-5`.

[14] I. Ambartsumyan, E. Khattatov, I. Yotov, and P. Zunino. “A Lagrange multiplier method for a Stokes–Biot fluid–poroelastic structure interaction model”. In: *Numerische Mathematik* 140.2 (2018), pp. 513–553. DOI: `10.1007/s00211-018-0967-1`.

[15] M. F. El-Amin, R. Meftah, A. Salama, and S. Sun. “Numerical Treatment of Two-phase Flow in Porous Media Including Specific Interfacial Area”. In: *Procedia Computer Science* 51 (2015), pp. 1249–1258. DOI: `10.1016/j.procs.2015.05.306`.

[16] P. Angot, F. Boyer, and F. Hubert. “Asymptotic and numerical modelling of flows in fractured porous media”. In: *ESAIM: Mathematical Modelling and Numerical Analysis* 43.2 (2009), pp. 239–275. DOI: `10.1051/m2an/2008052`.

[17] J. Q. Bao, E. Fathi, and S. Ameri. “A unified finite element method for the simulation of hydraulic fracturing with and without fluid lag”. In: *Engineering Fracture Mechanics* 162 (2016), pp. 164–178. DOI: `10.1016/J.ENGFRACMECH.2016.05.017`.

[18] K. Bao, A. Lavrov, and H. M. Nilsen. “Numerical modeling of non-Newtonian fluid flow in fractures and porous media”. In: *Computational Geosciences* 21.5-6 (2017), pp. 1313–1324. DOI: `10.1007/s10596-017-9639-y`.

[19] O. R. Barani, A. R. Khoei, and M. Mofid. “Modeling of cohesive crack growth in partially saturated porous media; a study on the permeability of cohesive fracture”. In: *International Journal of Fracture* 167.1 (2011), pp. 15–31. DOI: `10.1007/s10704-010-9513-6`.

[20] J. P. Bardet. “The damping of saturated poroelastic soils during steady-state vibrations”. In: *Applied Mathematics and Computation* 67.1-3 (1995), pp. 3–31. DOI: `10.1016/0096-3003(94)00052-6`.

[21] Y. Bazilevs, V. M. Calo, J. A. Cottrell, J. A. Evans, T. J. R. Hughes, S. Lipton, M. A. Scott, and T. W. Sederberg. “Isogeometric analysis using T-splines”. In: *Computer Methods in Applied Mechanics and Engineering* 199.5-8 (2010), pp. 229–263. DOI: `10.1016/j.cma.2009.02.036`.

[22] Y. Bazilevs, M. C. Hsu, and M. A. Scott. “Isogeometric fluid-structure interaction analysis with emphasis on non-matching discretizations, and with application to wind turbines”. In: *Computer Methods in Applied Mechanics and Engineering* 249-252 (2012), pp. 28–41. DOI: `10.1016/j.cma.2012.03.028`.

[23] G. S. Beavers and D. D. Joseph. “Boundary conditions at a naturally permeable wall”. In: *Journal of Fluid Mechanics* 30.1 (1967), pp. 197–207. DOI: `10.1017/S0022112067001375`.

[24] Y. W. Bekele, E. Fonn, T. Kvamsdal, A. M. Kvarving, and S. Nordal. “On Mixed Isogeometric Analysis of Poroelasticity”. In: (2017).

[25] E. A. Bergkamp, C. V. Verhoosel, J. J. C. Remmers, and D. M. J. Smeulders. “A staggered finite element procedure for the coupled Stokes-Biot system with fluid entry resistance”. In: *Computational Geosciences* (2020), pp. 1–26. DOI: `10.1007/s10596-019-09931-7`.

[26] B. Berkowitz. “Characterizing flow and transport in fractured geological media: A review”. In: *Advances in Water Resources* 25.8-12 (2002), pp. 861–884. DOI: `10.1016/S0309-1708(02)00042-8`.

[27] I. Berre, F. Doster, and E. Keilegavlen. “Flow in Fractured Porous Media: A Review of Conceptual Models and Discretization Approaches”. In: *Transport in Porous Media* 130.1 (2019), pp. 215–236. DOI: `10.1007/s11242-018-1171-6`.

[28] M. A. Biot. “General theory of three-dimensional consolidation”. In: *Journal of Applied Physics* 12.2 (1941), pp. 155–164. DOI: `10.1063/1.1712886`.

[29] R. B. Bird. *Transport Phenomena*. Revised se. New York, New York: John Wiley & Sons, Inc., 2007.

[30] M. J. Blunt. “Flow in porous media — pore-network models and multiphase flow”. In: *Current Opinion in Colloid & Interface Science* 6.3 (2001), pp. 197–207. DOI: `10.1016/S1359-0294(01)00084-X`.

[31] M. J. Blunt, M. D. Jackson, M. Piri, and P. H. Valvatne. “Detailed physics, predictive capabilities and macroscopic consequences for pore-network models of multiphase flow”. In: *Advances in Water Resources* 25.8-12 (2002), pp. 1069–1089. DOI: `10.1016/S0309-1708(02)00049-0`.

[32] T. J. Boone and A. R. Ingraffea. “A numerical procedure for simulation of hydraulically-driven fracture propagation in poroelastic media”. In: *International Journal for Numerical and Analytical Methods in Geomechanics* 14.1 (1990), pp. 27–47. DOI: `10.1002/nag.1610140103`.

[33] M. J. Borden, M. A. Scott, J. A. Evans, and T. J. R. Hughes. “Isogeometric finite element data structures based on Bézier extraction of NURBS”. In: *International Journal for Numerical Methods in Engineering* 87.1-5 (2011), pp. 15–47. DOI: `10.1002/nme.2968`.

[34] R. de Borst and L. Chen. “The role of Bézier extraction in adaptive isogeometric analysis: Local refinement and hierarchical refinement”. In: *International Journal for Numerical Methods in Engineering* 113.6 (2018), pp. 999–1019. DOI: `10.1002/nme.5696`.

[35] R. de Borst and L. J. Sluys. “Localisation in a Cosserat continuum under static and dynamic loading conditions”. In: *Computer Methods in Applied Mechanics and Engineering* 90.1-3 (1991), pp. 805–827. DOI: `10.1016/0045-7825(91)90185-9`.

[36] R. de Borst, L. J. Sluys, H.-B. Mühlhaus, and J. Pamin. “Fundamental issues in finite element analyses of localization of deformation”. In: *Engineering Computations* 10.2 (1993), pp. 99–121. DOI: 10.1108/eb023897.

[37] R. de Borst. “Simulation of strain localization: A reappraisal of the Cosserat continuum”. In: *Engineering Computations* 8.4 (1991), pp. 317–332. DOI: 10.1108/eb023842.

[38] R. de Borst. *Computational Methods for Fracture in porous Media*. Elsevier, 2017.

[39] R. de Borst. “Fluid flow in fractured and fracturing porous media: A unified view”. In: *Mechanics Research Communications* 80 (2017), pp. 47–57. DOI: 10.1016/j.mechrescom.2016.05.004.

[40] R. de Borst, M. A. Crisfield, J. J. C. Remmers, and C. V. Verhoosel. *Non-Linear Finite Element Analysis of Solids and Structures*. Chichester, UK: John Wiley & Sons, Ltd, 2012. DOI: 10.1002/9781118375938.

[41] R. de Borst, J. Réthoré, and M.-A. Abellan. “A Numerical Approach for Arbitrary Cracks in a Fluid-Saturated Medium”. In: *Archive of Applied Mechanics* 75.10-12 (2006), pp. 595–606. DOI: 10.1007/s00419-006-0023-y.

[42] M. Bukac, I. Yotov, and P. Zunino. “Dimensional model reduction for flow through fractures in poroelastic media”. In: *ESAIM: Mathematical Modelling and Numerical Analysis* 51.4 (2016), pp. 1429–1471. DOI: 10.1051/m2an/2016069.

[43] A. P. Bunger, E. Detournay, and D. I. Garagash. “Toughness-dominated hydraulic fracture with leak-off”. In: *International Journal of Fracture* 134.2 (2005), pp. 175–190. DOI: 10.1007/s10704-005-0154-0.

[44] T. Cajuhi, L. Sanavia, and L. De Lorenzis. “Phase-field modeling of fracture in variably saturated porous media”. In: *Computational Mechanics* 61.3 (2018), pp. 299–318. DOI: 10.1007/s00466-017-1459-3.

[45] T. D. Cao, F. Hussain, and B. A. Schrefler. “Porous media fracturing dynamics: stepwise crack advancement and fluid pressure oscillations”. In: *Journal of the Mechanics and Physics of Solids* 111 (2018), pp. 113–133. DOI: 10.1016/j.jmps.2017.10.014.

[46] T. D. Cao, E. Milanese, E. W. Remij, P. Rizzato, J. J. C. Remmers, L. Simoni, J. M. Huyghe, F. Hussain, and B. A. Schrefler. “Interaction between crack tip advancement and fluid flow in fracturing saturated porous media”. In: *Mechanics Research Communications* 80 (2017), pp. 24–37. DOI: 10.1016/j.mechrescom.2016.09.011.

[47] F. Cappa. “Influence of hydromechanical heterogeneities of fault zones on earthquake ruptures”. In: *Geophysical Journal International* 185.2 (2011), pp. 1049–1058. DOI: 10.1111/j.1365-246X.2011.04994.x.

[48] P. J. Carreau. “Rheological Equations from Molecular Network Theories”. In: *Transactions of the Society of Rheology* 16.1 (1972), pp. 99–127. DOI: 10.1122/1.549276.

[49] B. Carrier and S. Granet. “Numerical modeling of hydraulic fracture problem in permeable medium using cohesive zone model”. In: *Engineering Fracture Mechanics* 79 (2012), pp. 312–328. DOI: 10.1016/j.engfracmech.2011.11.012.

[50] S. Caucao, G. N. Gatica, R. Oyarzúa, and N. Sánchez. “A Fully-Mixed Formulation for the Steady Double-Diffusive Convection System Based upon Brinkman–Forchheimer Equations”. In: *Journal of Scientific Computing* 85.2 (2020), p. 44. DOI: 10.1007/s10915-020-01305-x.

[51] M. Cervera, M. Chiumenti, and C. Agelet de Saracibar. “Softening, localization and stabilization: capture of discontinuous solutions in J2 plasticity”. In: *International Journal for Numerical and Analytical Methods in Geomechanics* 28.5 (2004), pp. 373–393. DOI: `10.1002/nag.341`.

[52] K. W. Chang and P. Segall. “Injection-induced seismicity on basement faults including poroelastic stressing”. In: *Journal of Geophysical Research: Solid Earth* 121.4 (2016), pp. 2708–2726. DOI: `10.1002/2015JB012561`.

[53] D. Chapelle and K. J. Bathe. “The inf-sup test”. In: *Computers & Structures* 47.4-5 (1993), pp. 537–545. DOI: `10.1016/0045-7949(93)90340-J`.

[54] E. Chekhonin and K. Levonyan. “Hydraulic fracture propagation in highly permeable formations, with applications to tip screenout”. In: *International Journal of Rock Mechanics and Mining Sciences* 50 (2012), pp. 19–28. DOI: `10.1016/J.IJRMMS.2011.12.006`.

[55] L. Chen and R. de Borst. “Locally Refined T-splines”. In: *International Journal for Numerical Methods in Engineering* 114.6 (2018), pp. 637–659. DOI: `10.1002/nme.5759`.

[56] L. Chen, C. V. Verhoosel, and R. de Borst. “Discrete fracture analysis using locally refined T-splines”. In: *International Journal for Numerical Methods in Engineering* 116.2 (2018), pp. 117–140. DOI: `10.1002/nme.5917`.

[57] L. Chen, E. J. Lingen, and R. de Borst. “Adaptive hierarchical refinement of NURBS in cohesive fracture analysis”. In: *International Journal for Numerical Methods in Engineering* 112.13 (2017), pp. 2151–2173. DOI: `10.1002/nme.5600`.

[58] L. Chiapponi, V. Ciriello, S. Longo, and V. Di Federico. “Non-Newtonian Backflow in an Elastic Fracture”. In: *Water Resources Research* 55.12 (2019), pp. 10144–10158. DOI: `10.1029/2019WR026071`.

[59] R. H. Christopher and S. Middleman. “Power-Law Flow through a Packed Tube”. In: *Industrial & Engineering Chemistry Fundamentals* 4.4 (1965), pp. 422–426. DOI: `10.1021/i160016a011`.

[60] I. Cormeau. “Numerical stability in quasi-static elasto/visco-plasticity”. In: *International Journal for Numerical Methods in Engineering* 9.1 (1975), pp. 109–127. DOI: `10.1002/nme.1620090110`.

[61] M. R. Correa and M. A. Murad. “A new sequential method for three-phase immiscible flow in poroelastic media”. In: *Journal of Computational Physics* 373 (2018), pp. 493–532. DOI: `10.1016/J.JCP.2018.06.069`.

[62] E. Cosserat and F. Cosserat. *Théorie des corps deformables.* Paris, 1909.

[63] J. A. Cottrell, T. J. R. Hughes, and Y. Bazilevs. *Isogeometric analysis: toward integration of CAD and FEA.* Wiley Blackwell, 2009.

[64] M. A. Crisfield. *Non-linear finite element analysis of solids and structures.* Chichester: Wiley, 1997.

[65] M. A. Crisfield. “An arc-length method including line searches and accelerations”. In: *International Journal for Numerical Methods in Engineering* 19.9 (1983), pp. 1269–1289. DOI: `10.1002/nme.1620190902`.

[66] L. Cueto-Felgueroso, C. Vila, D. Santillán, and J. C. Mosquera. “Numerical Modeling of Injection-Induced Earthquakes Using Laboratory-Derived Friction Laws”. In: *Water Resources Research* 54.12 (2018), pp. 9833–9859. DOI: `10.1029/2017WR022363`.

[67] E. Detournay. “Mechanics of Hydraulic Fractures”. In: *Annual Review of Fluid Mechanics* 48.1 (2016), pp. 311–339. DOI: `10.1146/annurev-fluid-010814-014736`.

[68] V. Di Federico, M. Pinelli, and R. Ugarelli. “Estimates of effective permeability for non-Newtonian fluid flow in randomly heterogeneous porous media”. In: *Stochastic Environmental Research and Risk Assessment* 24.7 (2010), pp. 1067–1076. DOI: `10.1007/s00477-010-0397-9`.

[69] R. Dimitri, L. De Lorenzis, M. A. Scott, P. Wriggers, R. L. Taylor, and G. Zavarise. “Isogeometric large deformation frictionless contact using T-splines”. In: *Computer Methods in Applied Mechanics and Engineering* 269 (2014), pp. 394–414. DOI: `10.1016/j.cma.2013.11.002`.

[70] C. J. van Duijn, A. Mikelić, and T. Wick. “A monolithic phase-field model of a fluid-driven fracture in a nonlinear poroelastic medium”. In: *Mathematics and Mechanics of Solids* 24.5 (2019), pp. 1530–1555. DOI: `10.1177/1081286518801050`.

[71] E. M. Dunham, D. Belanger, L. Cong, and J. E. Kozdon. “Earthquake Ruptures with Strongly Rate-Weakening Friction and Off-Fault Plasticity, Part 2: Nonplanar Faults”. In: *Bulletin of the Seismological Society of America* 101.5 (2011), pp. 2296–2307. DOI: `10.1785/0120100076`.

[72] T. Duretz, R. de Borst, and L. Le Pourhiet. “Finite Thickness of Shear Bands in Frictional Viscoplasticity and Implications for Lithosphere Dynamics”. In: *Geochemistry, Geophysics, Geosystems* 20.11 (2019), pp. 5598–5616. DOI: `10.1029/2019GC008531`.

[73] Dynaflow Research Group. *JEM/JIVE C++ software development kit for advanced numerical simulations*. 2020.

[74] B. Ebrahimian, A. Noorzad, and M. I. Alsaleh. “Modeling shear localization along granular soil–structure interfaces using elasto-plastic Cosserat continuum”. In: *International Journal of Solids and Structures* 49.2 (2012), pp. 257–278. DOI: `10.1016/J.IJSOLSTR.2011.09.005`.

[75] W. Ehlers and C. Luo. “A phase-field approach embedded in the Theory of Porous Media for the description of dynamic hydraulic fracturing, Part II: The crack-opening indicator”. In: *Computer Methods in Applied Mechanics and Engineering* 341 (2018), pp. 429–442. DOI: `10.1016/J.CMA.2018.07.006`.

[76] S. H. Emerman, D. L. Turcotte, and D. A. Spence. “Transport of magma and hydrothermal solutions by laminar and turbulent fluid fracture”. In: *Physics of the Earth and Planetary Interiors* 41.4 (1986), pp. 249–259. DOI: `10.1016/0031-9201(86)90004-X`.

[77] V. J. Ervin, E. W. Jenkins, and S. Sun. “Coupled generalized nonlinear stokes flow with flow through a porous medium”. In: *SIAM Journal on Numerical Analysis* 47.2 (2009), pp. 929–952. DOI: `10.1137/070708354`.

[78] T. Al-Fariss and K. L. Pinder. “Flow through porous media of a shear-thinning liquid with yield stress”. In: *The Canadian Journal of Chemical Engineering* 65.3 (1987), pp. 391–405. DOI: `10.1002/cjce.5450650306`.

[79] B. Flemisch, I. Berre, W. Boon, A. Fumagalli, N. Schwenck, A. Scotti, I. Stefansson, and A. Tatomir. “Benchmarks for single-phase flow in fractured porous media”. In: *Advances in Water Resources* 111 (2018), pp. 239–258. DOI: `10.1016/J.ADVWATRES.2017.10.036`.

[80] M. R. T. Fraters, W. Bangerth, C. Thieulot, A. C. Glerum, and W. Spakman. “Efficient and practical Newton solvers for non-linear Stokes systems in geodynamic problems”. In: *Geophysical Journal International* 218.2 (2019), pp. 873–894. DOI: 10.1093/gji/ggz183.

[81] M. E. French, W. Zhu, and J. Banker. “Fault slip controlled by stress path and fluid pressurization rate”. In: *Geophysical Research Letters* 43.9 (2016), pp. 4330–4339. DOI: 10.1002/2016GL068893.

[82] G.-F. Fuh, N. Morita, P. A. Boyd, and S. J. McGoffin. “A New Approach to Preventing Lost Circulation While Drilling”. In: *SPE Annual Technical Conference and Exhibition*. Society of Petroleum Engineers, 1992. DOI: 10.2118/24599-MS.

[83] M. Galis, C. Pelties, J. Kristek, P. Moczo, J.-P. Ampuero, and P. M. Mai. “On the initiation of sustained slip-weakening ruptures by localized stresses”. In: *Geophysical Journal International* 200.2 (2015), pp. 890–909. DOI: 10.1093/gji/ggu436.

[84] B. Ganis, M. E. Mear, A. Sakhaee-Pour, M. F. Wheeler, and T. Wick. “Modeling fluid injection in fractures with a reservoir simulator coupled to a boundary element method”. In: *Computational Geosciences* 18.5 (2014), pp. 613–624. DOI: 10.1007/s10596-013-9396-5.

[85] D. I. Garagash and L. N. Germanovich. “Nucleation and arrest of dynamic slip on a pressurized fault”. In: *Journal of Geophysical Research B: Solid Earth* 117.10 (2012), pp. 1–27. DOI: 10.1029/2012JB009209.

[86] J. Geertsma and F. de Klerk. “A Rapid Method of Predicting Width and Extent of Hydraulically Induced Fractures”. In: *Journal of Petroleum Technology* 21.12 (1969), pp. 1571–1581. DOI: 10.2118/2458-PA.

[87] M. T. van Genuchten. “A Closed-form Equation for Predicting the Hydraulic Conductivity of Unsaturated Soils1”. In: *Soil Science Society of America Journal* 44.5 (1980), p. 892. DOI: 10.2136/sssaj1980.03615995004400050002x.

[88] S. M. Ghiaasiaan and S. I. Abdel-Khalik. “Two-phase flow in microchannels”. In: *Advances in heat transfer* 34 (2001), pp. 145–254. DOI: 10.1016/S0065-2717(01)80012-5.

[89] D. Gläser, R. Helmig, B. Flemisch, and H. Class. “A discrete fracture model for two-phase flow in fractured porous media”. In: *Advances in Water Resources* 110 (2017), pp. 335–348. DOI: 10.1016/J.ADVWATRES.2017.10.031.

[90] E. Gordeliy and A. Peirce. “Coupling schemes for modeling hydraulic fracture propagation using the XFEM”. In: *Computer Methods in Applied Mechanics and Engineering* 253 (2013), pp. 305–322. DOI: 10.1016/J.CMA.2012.08.017.

[91] H. Hajibeygi, D. Karvounis, and P. Jenny. “A hierarchical fracture model for the iterative multiscale finite volume method”. In: *Journal of Computational Physics* 230.24 (2011), pp. 8729–8743. DOI: 10.1016/j.jcp.2011.08.021.

[92] P. Hennig, S. Müller, and M. Kästner. “Bézier extraction and adaptive refinement of truncated hierarchical NURBS”. In: *Computer Methods in Applied Mechanics and Engineering* 305 (2016), pp. 316–339. DOI: 10.1016/j.cma.2016.03.009.

[93] E. Hirakawa and S. Ma. “Dynamic fault weakening and strengthening by gouge compaction and dilatancy in a fluid-saturated fault zone”. In: *Journal of Geophysical Research: Solid Earth* 121.8 (2016), pp. 5988–6008. DOI: 10.1002/2015JB012509.

[94] E. Hirakawa and S. Ma. “Undrained gouge plasticity stabilizes rupture dynamics of rough faults”. In: *Bulletin of the Seismological Society of America* 108.6 (2018), pp. 3160–3168. DOI: 10.1785/0120180002.

[95] M. R. Hirmand, M. Vahab, K. D. Papoulia, and N. Khalili. “Robust simulation of dynamic fluid-driven fracture in naturally fractured impermeable media”. In: *Computer Methods in Applied Mechanics and Engineering* 357 (2019), p. 112574. DOI: 10.1016/j.cma.2019.112574.

[96] H. Hoteit and A. Firoozabadi. “An efficient numerical model for incompressible two-phase flow in fractured media”. In: *Advances in Water Resources* 31.6 (2008), pp. 891–905. DOI: 10.1016/J.ADVWATRES.2008.02.004.

[97] T. J. R. Hughes, J. A. Cottrell, and Y. Bazilevs. “Isogeometric analysis: CAD, finite elements, NURBS, exact geometry and mesh refinement”. In: *Computer Methods in Applied Mechanics and Engineering* 194.39-41 (2005), pp. 4135–4195. DOI: 10.1016/J.CMA.2004.10.008.

[98] T. J. R. Hughes. “Multiscale phenomena: Green’s functions, the Dirichlet-to-Neumann formulation, subgrid scale models, bubbles and the origins of stabilized methods”. In: *Computer Methods in Applied Mechanics and Engineering* 127.1-4 (1995), pp. 387–401. DOI: 10.1016/0045-7825(95)00844-9.

[99] F. Irzal, J. J. C. Remmers, C. V. Verhoosel, and R. de Borst. “An isogeometric analysis Bézier interface element for mechanical and poromechanical fracture problems”. In: *International Journal for Numerical Methods in Engineering* 97.8 (2014), pp. 608–628. DOI: 10.1002/nme.4615.

[100] F. Irzal, J. J. C. Remmers, C. V. Verhoosel, and R. de Borst. “Isogeometric finite element analysis of poroelasticity”. In: *International Journal for Numerical and Analytical Methods in Geomechanics* 37.May 2013 (2013), pp. 1891–1907. DOI: 10.1002/nag.2195.

[101] B. Jha and R. Juanes. “Coupled multiphase flow and poromechanics: A computational model of pore pressure effects on fault slip and earthquake triggering”. In: *Water Resources Research* 50.5 (2014), pp. 3776–3808. DOI: 10.1002/2013WR015175.

[102] J. Jiang and R. M. Younis. “An efficient fully-implicit multislope MUSCL method for multiphase flow with gravity in discrete fractured media”. In: *Advances in Water Resources* 104 (2017), pp. 210–222. DOI: 10.1016/J.ADVWATRES.2017.04.009.

[103] L. Jin and M. D. Zoback. “Fully Dynamic Spontaneous Rupture Due to Quasi-Static Pore Pressure and Poroelastic Effects: An Implicit Nonlinear Computational Model of Fluid-Induced Seismic Events”. In: *Journal of Geophysical Research: Solid Earth* 123.11 (2018), pp. 9430–9468. DOI: 10.1029/2018JB015669.

[104] R. Juanes. “A variational multiscale finite element method for multiphase flow in porous media”. In: *Finite Elements in Analysis and Design* 41.7-8 (2005), pp. 763–777. DOI: 10.1016/J.FINEL.2004.10.008.

[105] R. Juanes and T. W. Patzek. “Multiscale-stabilized finite element methods for miscible and immiscible flow in porous media”. In: *Journal of Hydraulic Research* 42.sup1 (2004), pp. 131–140. DOI: 10.1080/00221680409500056.

[106] N. Kame, J. R. Rice, and R. Dmowska. “Effects of prestress state and rupture velocity on dynamic fault branching”. In: *Journal of Geophysical Research: Solid Earth* 108.B5 (2003). DOI: 10.1029/2002JB002189.

[107] K. Khayrat and P. Jenny. “A multi-scale network method for two-phase flow in porous media”. In: *Journal of Computational Physics* 342 (2017), pp. 194–210. DOI: `10.1016/j.jcp.2017.04.023`.

[108] A. R. Khoei, N. Hosseini, and T. Mohammadnejad. “Numerical modeling of two-phase fluid flow in deformable fractured porous media using the extended finite element method and an equivalent continuum model”. In: *Advances in Water Resources* 94 (2016), pp. 510–528. DOI: `10.1016/j.advwatres.2016.02.017`.

[109] A. R. Khoei and K. Karimi. “An enriched-FEM model for simulation of localization phenomenon in Cosserat continuum theory”. In: *Computational Materials Science* 44.2 (2008), pp. 733–749. DOI: `10.1016/J.COMMATSCI.2008.05.019`.

[110] A. R. Khoei and T. Mohammadnejad. “Numerical modeling of multiphase fluid flow in deforming porous media: A comparison between two- and three-phase models for seismic analysis of earth and rockfill dams”. In: *Computers and Geotechnics* 38.2 (2011), pp. 142–166. DOI: `10.1016/j.compgeo.2010.10.010`.

[111] A. R. Khoei and S. M. S. Mortazavi. “Thermo-hydro-mechanical modeling of fracturing porous media with two-phase fluid flow using X-FEM technique”. In: *International Journal for Numerical and Analytical Methods in Geomechanics* 44.18 (2020), pp. 2430–2472. DOI: `10.1002/nag.3153`.

[112] A. R. Khoei, A. R. Tabarraie, and S. A. Gharehbaghi. “H-adaptive mesh refinement for shear band localization in elasto-plasticity Cosserat continuum”. In: *Communications in Nonlinear Science and Numerical Simulation* 10.3 (2005), pp. 253–286. DOI: `10.1016/S1007-5704(03)00126-6`.

[113] A. R. Khoei, M. Vahab, E. Haghighat, and S. Moallemi. “A mesh-independent finite element formulation for modeling crack growth in saturated porous media based on an enriched-FEM technique”. In: *International Journal of Fracture* 188.1 (2014), pp. 79–108. DOI: `10.1007/s10704-014-9948-2`.

[114] J. Kim, H. A. Tchelepi, and R. Juanes. “Stability and convergence of sequential methods for coupled flow and geomechanics: Drained and undrained splits”. In: *Computer Methods in Applied Mechanics and Engineering* 200.23-24 (2011), pp. 2094–2116. DOI: `10.1016/j.cma.2011.02.011`.

[115] J. Kim, H. A. Tchelepi, and R. Juanes. “Stability and convergence of sequential methods for coupled flow and geomechanics: Fixed-stress and fixed-strain splits”. In: *Computer Methods in Applied Mechanics and Engineering* 200.13-16 (2011), pp. 1591–1606. DOI: `10.1016/J.CMA.2010.12.022`.

[116] I. Kolo, L. Chen, and R. de Borst. “Strain-gradient elasticity and gradient-dependent plasticity with hierarchical refinement of NURBS”. In: *Finite Elements in Analysis and Design* 163 (2019), pp. 31–43. DOI: `10.1016/j.finel.2019.06.001`.

[117] A. Krischok and C. Linder. “A generalized inf–sup test for multi-field mixed-variational methods”. In: *Computer Methods in Applied Mechanics and Engineering* 357 (2019), p. 112497. DOI: `10.1016/j.cma.2019.06.008`.

[118] A. Lavrov. “Numerical modeling of steady-state flow of a non-Newtonian power-law fluid in a rough-walled fracture”. In: *Computers and Geotechnics* 50.0266 (2013), pp. 101–109. DOI: `10.1016/j.compgeo.2013.01.004`.

[119] A. Lavrov. “Redirection and channelization of power-law fluid flow in a rough-walled fracture”. In: *Chemical Engineering Science* 99 (2013), pp. 81–88. DOI: `10.1016/j.ces.2013.05.045`.

[120] S. Lee, A. Mikelić, M. F. Wheeler, and T. Wick. “Phase-field modeling of proppant-filled fractures in a poroelastic medium”. In: *Computer Methods in Applied Mechanics and Engineering* 312 (2016), pp. 509–541. DOI: 10.1016/j.cma.2016.02.008.

[121] S. Lee, A. Mikelić, M. F. Wheeler, and T. Wick. “Phase-Field Modeling of Two Phase Fluid Filled Fractures in a Poroelastic Medium”. In: *Multiscale Modeling & Simulation* 16.4 (2018), pp. 1542–1580. DOI: 10.1137/17M1145239.

[122] S. Lee, M. F. Wheeler, and T. Wick. “Iterative coupling of flow, geomechanics and adaptive phase-field fracture including level-set crack width approaches”. In: *Journal of Computational and Applied Mathematics* 314 (2017), pp. 40–60. DOI: 10.1016/J.CAM.2016.10.022.

[123] S. Lee, M. F. Wheeler, and T. Wick. “Pressure and fluid-driven fracture propagation in porous media using an adaptive finite element phase field model”. In: *Computer Methods in Applied Mechanics and Engineering* 305 (2016), pp. 111–132. DOI: 10.1016/j.cma.2016.02.037.

[124] Y. S. Lee, E. D. Wetzel, and N. J. Wagner. “The ballistic impact characteristics of Kevlar® woven fabrics impregnated with a colloidal shear thickening fluid”. In: *Journal of Materials Science* 38.13 (2003), pp. 2825–2833. DOI: 10.1023/A:1024424200221.

[125] Q. Lei, J.-P. Latham, and C.-F. Tsang. “The use of discrete fracture networks for modelling coupled geomechanical and hydrological behaviour of fractured rocks”. In: *Computers and Geotechnics* 85 (2017), pp. 151–176. DOI: 10.1016/j.compgeo.2016.12.024.

[126] S. Levasseur, R. Charlier, B. Frieg, and F. Collin. “Hydro-mechanical modelling of the excavation damaged zone around an underground excavation at Mont Terri Rock Laboratory”. In: *International Journal of Rock Mechanics and Mining Sciences* 47.3 (2010), pp. 414–425. DOI: 10.1016/J.IJRMMS.2010.01.006.

[127] T. P. Y. Lhomme. “Initiation of hydraulic fractures in natural sandstone”. PhD thesis. TU Delft, 2005.

[128] B. Li and H. A. Tchelepi. “Nonlinear analysis of multiphase transport in porous media in the presence of viscous, buoyancy, and capillary forces”. In: *Journal of Computational Physics* 297 (2015), pp. 104–131. DOI: 10.1016/j.jcp.2015.04.057.

[129] P. Li, K. Wang, and D. Lu. “Analytical Solution of Plane-Strain Poroelasticity due to Surface Loading within a Finite Rectangular Domain”. In: *International Journal of Geomechanics* 17.4 (2017), p. 04016089. DOI: 10.1061/(ASCE)GM.1943-5622.0000776.

[130] W. Li and C. Wei. “Stabilized low-order finite elements for strongly coupled poromechanical problems”. In: *International Journal for Numerical Methods in Engineering* 115.5 (2018), pp. 531–548. DOI: 10.1002/nme.5815.

[131] K.-A. Lie. *An Introduction to Reservoir Simulation Using MATLAB*. 2016.

[132] A. M. Linkov. “On comparison of thinning fluids used for hydraulic fracturing”. In: *International Journal of Engineering Science* 77 (2014), pp. 14–23. DOI: 10.1016/j.ijengsci.2013.12.005.

[133] M. Liu and P. Mostaghimi. “Reactive transport modelling in dual porosity media”. In: *Chemical Engineering Science* 190 (2018), pp. 436–442. DOI: 10.1016/j.ces.2018.06.005.

[134] B. Loret, F. M. F. Simões, and J. A. C. Martins. "Growth and decay of acceleration waves in non-associative elastic-plastic fluid-saturated porous media". In: *International Journal of Solids and Structures* 34.13 (1997), pp. 1583–1608. DOI: `10.1016/S0020-7683(96)00106-0`.

[135] I. Lunati and P. Jenny. "Multiscale finite-volume method for compressible multiphase flow in porous media". In: *Journal of Computational Physics* 216.2 (2006), pp. 616–636. DOI: `10.1016/j.jcp.2006.01.001`.

[136] J. Lysmer and R. L. Kuhlemeyer. "Finite dynamic model for infinite media". In: *Journal of the Engineering Mechanics Division* 95.4 (1969), pp. 859–878.

[137] G. W. Ma, H. D. Wang, L. F. Fan, and B. Wang. "Simulation of two-phase flow in horizontal fracture networks with numerical manifold method". In: *Advances in Water Resources* 108 (2017), pp. 293–309. DOI: `10.1016/J.ADVWATRES.2017.08.013`.

[138] M. T. Manzari. "Application of micropolar plasticity to post failure analysis in geomechanics". In: *International Journal for Numerical and Analytical Methods in Geomechanics* 28.10 (2004), pp. 1011–1032. DOI: `10.1002/nag.356`.

[139] V. Martin, J. Jaffré, and J. E. Roberts. "Modeling Fractures and Barriers as Interfaces for Flow in Porous Media". In: *SIAM Journal on Scientific Computing* 26.5 (2005), pp. 1667–1691. DOI: `10.1137/S1064827503429363`.

[140] S. May, J. Vignollet, and R. de Borst. "The role of the Bézier extraction operator for T-splines of arbitrary degree: linear dependencies, partition of unity property, nesting behaviour and local refinement". In: *International Journal for Numerical Methods in Engineering* 103.8 (2015), pp. 547–581. DOI: `10.1002/nme.4902`.

[141] G. Meschke and S. Grasberger. "Numerical Modeling of Coupled Hygromechanical Degradation of Cementitious Materials". In: *Journal of Engineering Mechanics* 129.4 (2003), pp. 383–392. DOI: `10.1061/(ASCE)0733-9399(2003)129:4(383)`.

[142] C. Miehe and S. Mauthe. "Phase field modeling of fracture in multi-physics problems. Part III. Crack driving forces in hydro-poro-elasticity and hydraulic fracturing of fluid-saturated porous media". In: *Computer Methods in Applied Mechanics and Engineering* 304 (2016), pp. 619–655. DOI: `10.1016/J.CMA.2015.09.021`.

[143] A. Mikelić, M. F. Wheeler, and T. Wick. "A Phase-Field Method for Propagating Fluid-Filled Fractures Coupled to a Surrounding Porous Medium". In: *Multiscale Modeling & Simulation* 13.1 (2015), pp. 367–398. DOI: `10.1137/140967118`.

[144] D. N. Mikhailov, M. J. Economides, and V. N. Nikolaevskiy. "Fluid leakoff determines hydraulic fracture dimensions: Approximate solution for non-Newtonian fracturing fluid". In: *International Journal of Engineering Science* 49.9 (2011), pp. 809–822. DOI: `10.1016/j.ijengsci.2011.03.021`.

[145] E. Milanese, P. Rizzato, F. Pesavento, S. Secchi, and B. A. Schreffler. "An Explanation for the Intermittent Crack Tip Advancement and Pressure Fluctuations in Hydraulic Fracturing". In: *Hydraul. Fracturing Journal* 2.November (2016), pp. 30–42.

[146] E. Milanese, T. D. Cao, L. Simoni, and B. A. Schrefler. "Fracturing in dry and saturated porous media". In: *Computational Methods in Applied Sciences* 46 (2018), pp. 265–288. DOI: `10.1007/978-3-319-60885-3_13`.

[147] E. Milanese, O. Yılmaz, J. F. Molinari, and B. A. Schrefler. "Avalanches in dry and saturated disordered media at fracture in shear and mixed mode scenarios". In: *Mechanics Research Communications* 80 (2017), pp. 58–68. DOI: `10.1016/j.mechrescom.2016.08.002`.

[148] E. Milanese, O. Yllmaz, J. F. Molinari, and B. Schrefler. “Avalanches in dry and saturated disordered media at fracture”. In: *Physical Review E* 93.4 (2016), p. 043002. DOI: `10.1103/PhysRevE.93.043002`.

[149] S. E. Minkoff, C. M. Stone, S. Bryant, M. Peszynska, and M. F. Wheeler. “Coupled fluid flow and geomechanical deformation modeling”. In: *Journal of Petroleum Science and Engineering* (2003). DOI: `10.1016/S0920-4105(03)00021-4`.

[150] Y. Miyake and H. Noda. “Fully dynamic earthquake sequence simulation of a fault in a viscoelastic medium using a spectral boundary integral equation method: does interseismic stress relaxation promote aseismic transients?” In: *Earth, Planets and Space* 71.1 (2019), p. 137. DOI: `10.1186/s40623-019-1113-8`.

[151] H. Modaressi and I. Benzenati. “Paraxial approximation for poroelastic media”. In: *Soil Dynamics and Earthquake Engineering* 13.2 (1994), pp. 117–129. DOI: `10.1016/0267-7261(94)90004-3`.

[152] T. Mohammadnejad and J. E. Andrade. “Numerical modeling of hydraulic fracture propagation, closure and reopening using XFEM with application to in-situ stress estimation”. In: *International Journal for Numerical and Analytical Methods in Geomechanics* 40.15 (2016), pp. 2033–2060. DOI: `10.1002/nag.2512`.

[153] T. Mohammadnejad and A. R. Khoei. “An extended finite element method for fluid flow in partially saturated porous media with weak discontinuities; the convergence analysis of local enrichment strategies”. In: *Computational Mechanics* 51.3 (2013), pp. 327–345. DOI: `10.1007/s00466-012-0732-8`.

[154] T. Mohammadnejad and A. R. Khoei. “An extended finite element method for hydraulic fracture propagation in deformable porous media with the cohesive crack model”. In: *Finite Elements in Analysis and Design* 73 (2013), pp. 77–95. DOI: `10.1016/j.finel.2013.05.005`.

[155] T. Mohammadnejad and A. R. Khoei. “Hydro-mechanical modeling of cohesive crack propagation in multiphase porous media using the extended finite element method”. In: *International Journal for Numerical and Analytical Methods in Geomechanics* 37.10 (2013), pp. 1247–1279. DOI: `10.1002/nag.2079`.

[156] L. Monforte, P. Navas, J. M. Carbonell, M. Arroyo, and A. Gens. “Low-order stabilized finite element for the full Biot formulation in soil mechanics at finite strain”. In: *International Journal for Numerical and Analytical Methods in Geomechanics* 43.7 (2019), pp. 1488–1515. DOI: `10.1002/nag.2923`.

[157] A. F. Morais, H. Seybold, H. J. Herrmann, and J. S. Andrade. “Non-Newtonian Fluid Flow through Three-Dimensional Disordered Porous Media”. In: *Physical Review Letters* 103.19 (2009), p. 194502. DOI: `10.1103/PhysRevLett.103.194502`.

[158] J. L. Mroginski, H. A. Di Rado, P. A. Beneyto, and A. M. Awruch. “A finite element approach for multiphase fluid flow in porous media”. In: *Mathematics and Computers in Simulation* 81.1 (2010), pp. 76–91. DOI: `10.1016/j.matcom.2010.07.001`.

[159] L. Mu, J. Wang, and X. Ye. “A stable numerical algorithm for the Brinkman equations by weak Galerkin finite element methods”. In: *Journal of Computational Physics* 273 (2014), pp. 327–342. DOI: `10.1016/j.jcp.2014.04.017`.

[160] S. Münzenmaier. “First-Order system least squares for generalized-Newtonian coupled Stokes-Darcy flow”. In: *Numerical Methods for Partial Differential Equations* 31.4 (2015), pp. 1150–1173. DOI: `10.1002/num.21939`.

[161] P. Neff and K. Chelminski. “Well-Posedness of Dynamic Cosserat Plasticity”. In: *Applied Mathematics and Optimization* 56.1 (2007), pp. 19–35. DOI: `10.1007/s00245-007-0878-5`.

[162] V. P. Nguyen, H. Lian, T. Rabczuk, and S. Bordas. “Modelling hydraulic fractures in porous media using flow cohesive interface elements”. In: *Engineering Geology* 225 (2017), pp. 68–82. DOI: `10.1016/J.ENGGEO.2017.04.010`.

[163] T. Ni, F. Pesavento, M. Zaccariotto, U. Galvanetto, Q. Z. Zhu, and B. A. Schrefler. “Hybrid FEM and peridynamic simulation of hydraulic fracture propagation in saturated porous media”. In: *Computer Methods in Applied Mechanics and Engineering* 366 (2020), p. 113101. DOI: `10.1016/j.cma.2020.113101`.

[164] M. J. Nicholl, H. Rajaram, and R. J. Glass. “Factors controlling satiated relative permeability in a partially-saturated horizontal fracture”. In: *Geophysical Research Letters* 27.3 (2000), pp. 393–396. DOI: `10.1029/1999GL006083`.

[165] A. A. Osiptsov. “Fluid Mechanics of Hydraulic Fracturing: a Review”. In: *Journal of Petroleum Science and Engineering* 156 (2017), pp. 513–535. DOI: `10.1016/j.petrol.2017.05.019`.

[166] H. Ouchi, A. Katiyar, J. York, J. T. Foster, and M. M. Sharma. “A fully coupled porous flow and geomechanics model for fluid driven cracks: a peridynamics approach”. In: *Computational Mechanics* 55.3 (2015), pp. 561–576. DOI: `10.1007/s00466-015-1123-8`.

[167] A. Ougier-Simonin and W. Zhu. “Effects of pore fluid pressure on slip behaviors: An experimental study”. In: *Geophysical Research Letters* 40.11 (2013), pp. 2619–2624. DOI: `10.1002/grl.50543`.

[168] M. Parchei Esfahani and R. Gracie. “On the undrained and drained hydraulic fracture splits”. In: *International Journal for Numerical Methods in Engineering* 118.12 (2019), pp. 741–763. DOI: `10.1002/nme.6036`.

[169] H. Pascal. “Nonsteady flow of non-Newtonian fluids through a porous medium”. In: *International Journal of Engineering Science* 21.3 (1983), pp. 199–210. DOI: `10.1016/0020-7225(83)90021-6`.

[170] J. R. A. Pearson and P. M. J. Tardy. “Models for flow of non-Newtonian and complex fluids through porous media”. In: *Journal of Non-Newtonian Fluid Mechanics* 102.2 (2002), pp. 447–473. DOI: `10.1016/S0377-0257(01)00191-4`.

[171] C. Peruzzo, D. T. Cao, E. Milanese, P. Favia, F. Pesavento, F. Hussain, and B. A. Schrefler. “Dynamics of fracturing saturated porous media and self-organization of rupture”. In: *European Journal of Mechanics - A/Solids* 74 (2019), pp. 471–484. DOI: `10.1016/J.EUROMECHSOL.2018.12.004`.

[172] C. Peruzzo, L. Simoni, and B. A. Schrefler. “On stepwise advancement of fractures and pressure oscillations in saturated porous media”. In: *Engineering Fracture Mechanics* 215 (2019), pp. 246–250. DOI: `10.1016/J.ENGFRACMECH.2019.05.006`.

[173] K. M. Pervaiz Fathima and R. de Borst. “Implications of single or multiple pressure degrees of freedom at fractures in fluid-saturated porous media”. In: *Engineering Fracture Mechanics* 213 (2019), pp. 1–20. DOI: `10.1016/J.ENGFRACMECH.2019.03.037`.

[174] L. Piegl and W. Tiller. *The NURBS Book*. 2nd. Berlin: Springer Berlin Heidelberg, 1997.

[175] F. Pizzocolo, J. M. Huyghe, and K. Ito. "Mode I crack propagation in hydrogels is step wise". In: *Engineering Fracture Mechanics* 97.1 (2013), pp. 72–79. DOI: `10.1016/j.engfracmech.2012.10.018`.

[176] T. Qiu and P. J. Fox. "Numerical analysis of 1-D compression wave propagation in saturated poroelastic media". In: *International Journal for Numerical and Analytical Methods in Geomechanics* 32.2 (2008), pp. 161–187. DOI: `10.1002/nag.621`.

[177] T. Qiu and Y. Huang. "Energy Dissipation in Nearly Saturated Poroviscoelastic Soil Columns during Quasi-Static Compressional Excitations". In: *Journal of Engineering Mechanics* 138.10 (2012), pp. 1263–1274. DOI: `10.1061/(ASCE)EM.1943-7889.0000428`.

[178] H. S. Rabbani, V. Joekar-Niasar, T. Pak, and N. Shokri. "New insights on the complex dynamics of two-phase flow in porous media under intermediate-wet conditions". In: *Scientific Reports* 7.1 (2017), p. 4584. DOI: `10.1038/s41598-017-04545-4`.

[179] T. Ramstad, N. Idowu, C. Nardi, and P.-E. Øren. "Relative Permeability Calculations from Two-Phase Flow Simulations Directly on Digital Images of Porous Rocks". In: *Transport in Porous Media* 94.2 (2012), pp. 487–504. DOI: `10.1007/s11242-011-9877-8`.

[180] P. G. Ranjith. "An experimental study of single and two-phase fluid flow through fractured granite specimens". In: *Environmental Earth Sciences* 59.7 (2010), pp. 1389–1395. DOI: `10.1007/s12665-009-0124-3`.

[181] P. G. Ranjith, S. K. Choi, and M. Fourar. "Characterization of two-phase flow in a single rock joint". In: *International Journal of Rock Mechanics and Mining Sciences* 43.2 (2006), pp. 216–223. DOI: `10.1016/j.ijrmms.2005.06.001`.

[182] S. Raza, S. H. Hejazi, and I. D. Gates. "Two phase flow of liquids in a narrow gap: Phase interference and hysteresis". In: *Physics of Fluids* 28.7 (2016), p. 074102. DOI: `10.1063/1.4953238`.

[183] E. W. Remij, F. Pesavento, Y. Bazilevs, D. M. J. Smeulders, B. A. Schrefler, and J. M. Huyghe. "Isogeometric Analysis of a Multiphase Porous Media Model for Concrete". In: *Journal of Engineering Mechanics* 144.2 (2018), p. 04017169. DOI: `10.1061/(ASCE)EM.1943-7889.0001380`.

[184] E. W. Remij, J. J. C. Remmers, J. M. Huyghe, and D. M. J. Smeulders. "An investigation of the step-wise propagation of a mode-II fracture in a poroelastic medium". In: *Mechanics Research Communications* 80 (2017), pp. 10–15. DOI: `10.1016/J.MECHRESCOM.2016.03.001`.

[185] E. W. Remij, J. J. C. Remmers, J. M. Huyghe, and D. M. J. Smeulders. "The enhanced local pressure model for the accurate analysis of fluid pressure driven fracture in porous materials". In: *Computer Methods in Applied Mechanics and Engineering* 286 (2015), pp. 293–312. DOI: `10.1016/J.CMA.2014.12.025`.

[186] G. Ren, J. Jiang, and R. M. Younis. "A Fully Coupled XFEM-EDFM Model for Multiphase Flow and Geomechanics in Fractured Tight Gas Reservoirs". In: *Procedia Computer Science* 80 (2016), pp. 1404–1415. DOI: `10.1016/J.PROCS.2016.05.449`.

[187] J. Réthoré, R. de Borst, and M.-A. Abellan. "A two-scale approach for fluid flow in fractured porous media". In: *International Journal for Numerical Methods in Engineering* 71.7 (2006), pp. 780–800. DOI: `10.1002/nme.1962`.

[188] J. Réthoré, R. de Borst, and M.-A. Abellan. "A two-scale model for fluid flow in an unsaturated porous medium with cohesive cracks". In: *Computational Mechanics* 42.2 (2008), pp. 227–238. DOI: 10.1007/s00466-007-0178-6.

[189] A. M. Robertson, A. Sequeira, and R. G. Owens. "Rheological models for blood". In: *Cardiovascular Mathematics*. Milano: Springer Milan, 2009, pp. 211–241. DOI: 10.1007/978-88-470-1152-6_6.

[190] C. Rodrigo, F. J. Gaspar, X. Hu, and L. T. Zikatanov. "Stability and monotonicity for some discretizations of the Biot's consolidation model". In: *Computer Methods in Applied Mechanics and Engineering* 298 (2016), pp. 183–204. DOI: 10.1016/J.CMA.2015.09.019.

[191] A. Rodríguez de Castro and M. Agnaou. "Numerical Investigation of the Apparent Viscosity Dependence on Darcy Velocity During the Flow of Shear-Thinning Fluids in Porous Media". In: *Transport in Porous Media* 129.1 (2019), pp. 93–120. DOI: 10.1007/s11242-019-01279-x.

[192] A. Rodríguez de Castro and G. Radilla. "Flow of yield stress and Carreau fluids through rough-walled rock fractures: Prediction and experiments". In: *Water Resources Research* 53.7 (2017), pp. 6197–6217. DOI: 10.1002/2017WR020520.

[193] J. W. Rudnicki and J. R. Rice. "Conditions for the localization of deformation in pressure-sensitive dilatant materials". In: *Journal of the Mechanics and Physics of Solids* 23.6 (1975), pp. 371–394. DOI: 10.1016/0022-5096(75)90001-0.

[194] S. A. Sabet and R. de Borst. "Mesh bias and shear band inclination in standard and non-standard continua". In: *Archive of Applied Mechanics* (2019), pp. 1–14. DOI: 10.1007/s00419-019-01593-2.

[195] S. A. Sabet and R. de Borst. "Structural softening, mesh dependence, and regularisation in non-associated plastic flow". In: *International Journal for Numerical and Analytical Methods in Geomechanics* (2019), nag.2973. DOI: 10.1002/nag.2973.

[196] H. Saboorian-Jooybari. "Analytical Estimation of Water-Oil Relative Permeabilities through Fractures". In: *Oil & Gas Science and Technology – Revue d'IFP Energies nouvelles* 71.3 (2016), p. 31. DOI: 10.2516/ogst/2014054.

[197] P. G. Saffman. "On the Boundary Condition at the Surface of a Porous Medium". In: *Studies in Applied Mathematics* 50.2 (1971), pp. 93–101. DOI: 10.1002/sapm197150293.

[198] S. Salimzadeh and N. Khalili. "A three-phase XFEM model for hydraulic fracturing with cohesive crack propagation". In: *Computers and Geotechnics* 69 (2015), pp. 82–92. DOI: 10.1016/j.compgeo.2015.05.001.

[199] D. Santillán, R. Juanes, and L. Cueto-Felgueroso. "Phase Field Model of Hydraulic Fracturing in Poroelastic Media: Fracture Propagation, Arrest, and Branching Under Fluid Injection and Extraction". In: *Journal of Geophysical Research: Solid Earth* 123.3 (2018), pp. 2127–2155. DOI: 10.1002/2017JB014740.

[200] J. C. J. Schellekens and R. de Borst. "On the numerical integration of interface elements". In: *International Journal for Numerical Methods in Engineering* 36.1 (1993), pp. 43–66. DOI: 10.1002/nme.1620360104.

[201] B. A. Schrefler and R. Scotta. "A fully coupled dynamic model for two-phase fluid flow in deformable porous media". In: *Computer Methods in Applied Mechanics and Engineering* 190.24-25 (2001), pp. 3223–3246. DOI: 10.1016/S0045-7825(00)00390-X.

[202] B. A. Schrefler, S. Secchi, and L. Simoni. “On adaptive refinement techniques in multi-field problems including cohesive fracture”. In: *Computer Methods in Applied Mechanics and Engineering* 195.4-6 (2006), pp. 444–461. DOI: `10.1016/j.cma.2004.10.014`.

[203] M. A. Scott, X. Li, T. W. Sederberg, and T. J. R. Hughes. “Local refinement of analysis-suitable T-splines”. In: *Computer Methods in Applied Mechanics and Engineering* 213-216 (2012), pp. 206–222. DOI: `10.1016/J.CMA.2011.11.022`.

[204] M. A. Scott, M. J. Borden, C. V. Verhoosel, T. W. Sederberg, and T. J. R. Hughes. “Isogeometric finite element data structures based on Bézier extraction of T-splines”. In: *International Journal for Numerical Methods in Engineering* 88.2 (2011), pp. 126–156. DOI: `10.1002/NME.3167`.

[205] M. M. Scuderi, C. Collettini, and C. Marone. “Frictional stability and earthquake triggering during fluid pressure stimulation of an experimental fault”. In: *Earth and Planetary Science Letters* 477 (2017), pp. 84–96. DOI: `10.1016/J.EPSL.2017.08.009`.

[206] S. Secchi, L. Simoni, and B. A. Schrefler. “Mesh adaptation and transfer schemes for discrete fracture propagation in porous materials”. In: *International Journal for Numerical and Analytical Methods in Geomechanics* 31.2 (2007), pp. 331–345. DOI: `10.1002/nag.581`.

[207] J. M. Segura and I. Carol. “Coupled HM analysis using zero-thickness interface elements with double nodes. Part I: Theoretical model”. In: *International Journal for Numerical and Analytical Methods in Geomechanics* 32.18 (2008), pp. 2083–2101. DOI: `10.1002/nag.735`.

[208] J. M. Segura and I. Carol. “On zero-thickness interface elements for diffusion problems”. In: *International Journal for Numerical and Analytical Methods in Geomechanics* 28.9 (2004), pp. 947–962. DOI: `10.1002/nag.358`.

[209] A. Settari and D. A. Walters. “Advances in Coupled Geomechanical and Reservoir Modeling With Applications to Reservoir Compaction”. In: *SPE Journal* 6.03 (2007), pp. 334–342. DOI: `10.2118/74142-pa`.

[210] S. Shad and I. D. Gates. “Multiphase Flow in Fractures: Co-Current and Counter-Current Flow in a Fracture”. In: *Canadian International Petroleum Conference*. Petroleum Society of Canada, 2008, pp. 17–19. DOI: `10.2118/2008-147`.

[211] S. Shad, B. B. Maini, and I. D. Gates. “Effect of gap and flow orientation on two-phase flow in an oil-wet gap: Relative permeability curves and flow structures”. In: *International Journal of Multiphase Flow* 57 (2013), pp. 78–87. DOI: `10.1016/j.ijmultiphaseflow.2013.07.004`.

[212] A. V. Shenoy. “Non-Newtonian Fluid Heat Transfer in Porous Media”. In: *Advances in Heat Transfer* 24 (1994), pp. 101–190. DOI: `10.1016/S0065-2717(08)70233-8`.

[213] J. Y. Shih, D. J. Thompson, and A. Zervos. “The effect of boundary conditions, model size and damping models in the finite element modelling of a moving load on a track/ground system”. In: *Soil Dynamics and Earthquake Engineering* 89 (2016), pp. 12–27. DOI: `10.1016/J.SOILDYN.2016.07.004`.

[214] L. J. Sluys and R. de Borst. “Wave propagation and localization in a rate-dependent cracked medium-model formulation and one-dimensional examples”. In: *International Journal of Solids and Structures* 29.23 (1992), pp. 2945–2958. DOI: `10.1016/0020-7683(92)90151-I`.

[215] T. Sochi. “Non-Newtonian Rheology in Blood Circulation”. In: *physics.flu-dyn* (2013), pp. 1–26.

[216] T. Sochi and M. J. Blunt. “Pore-scale network modeling of Ellis and Herschel–Bulkley fluids”. In: *Journal of Petroleum Science and Engineering* 60.2 (2008), pp. 105–124. DOI: 10.1016/j.petrol.2007.05.009.

[217] D. A. Spence and P. Sharp. “Self-similar solutions for elastohydrodynamic cavity flow”. In: *Proceedings of the Royal Society of London. A. Mathematical and Physical Sciences* 400.1819 (1985), pp. 289–313. DOI: 10.1098/rspa.1985.0081.

[218] M. Spiegelman, D. A. May, and C. R. Wilson. “On the solvability of incompressible Stokes with viscoplastic rheologies in geodynamics”. In: *Geochemistry, Geophysics, Geosystems* 17.6 (2016), pp. 2213–2238. DOI: 10.1002/2015GC006228.

[219] V. R. Tagirova. “Hydraulic fracture crack propagation driven by a non-Newtonian fluid”. In: *Moscow University Mechanics Bulletin* 64.6 (2009), pp. 135–142. DOI: 10.3103/S0027133009060016.

[220] E. L. Templeton and J. R. Rice. “Off-fault plasticity and earthquake rupture dynamics: 1. Dry materials or neglect of fluid pressure changes”. In: *Journal of Geophysical Research: Solid Earth* 113.9 (2008), B09306. DOI: 10.1029/2007JB005529.

[221] T. K. Tokunaga and J. Wan. “Water film flow along fracture surfaces of porous rock”. In: *Water Resources Research* 33.6 (1997), pp. 1287–1295. DOI: 10.1029/97WR00473.

[222] A. Truty. “A Galerkin/least-squares finite element formulation for consolidation”. In: *International Journal for Numerical Methods in Engineering* 52.8 (2001), pp. 763–786. DOI: 10.1002/nme.224.

[223] A. Truty and T. Zimmermann. “Stabilized mixed finite element formulations for materially nonlinear partially saturated two-phase media”. In: *Computer Methods in Applied Mechanics and Engineering* 195.13-16 (2006), pp. 1517–1546. DOI: 10.1016/J.CMA.2005.05.044.

[224] G. U. Unnikrishnan, V. U. Unnikrishnan, and J. N. Reddy. “Tissue–fluid interface analysis using biphasic finite element method”. In: *Computer Methods in Biomechanics and Biomedical Engineering* 12.2 (2009), pp. 165–172. DOI: 10.1080/10255840802372045.

[225] P. H. Valvatne, M. Piri, X. Lopez, and M. J. Blunt. “Predictive Pore-Scale Modeling of Single and Multiphase Flow”. In: *Upscaling Multiphase Flow in Porous Media*. Vol. 58. Berlin/Heidelberg: Springer-Verlag, 2005, pp. 23–41. DOI: 10.1007/1-4020-3604-3.

[226] M. Vasilyeva, M. Babaei, E. T. Chung, and D. Spiridonov. “Multiscale modeling of heat and mass transfer in fractured media for enhanced geothermal systems applications”. In: *Applied Mathematical Modelling* 67 (2019), pp. 159–178. DOI: 10.1016/J.APM.2018.10.025.

[227] C. V. Verhoosel, M. A. Scott, R. de Borst, and T. J. R. Hughes. “An isogeometric approach to cohesive zone modeling”. In: *International Journal for Numerical Methods in Engineering* 87.1-5 (2011), pp. 336–360. DOI: 10.1002/nme.3061.

[228] A. Verruijt. *Theory and problems of poroelasticity*. Delft University of Technology, 2016.

[229] E. Veveakis, J. Sulem, and I. Stefanou. “Modeling of fault gouges with Cosserat Continuum Mechanics: Influence of thermal pressurization and chemical decomposition as coseismic weakening mechanisms”. In: *Journal of Structural Geology* 38 (2012), pp. 254–264. DOI: 10.1016/J.JSG.2011.09.012.

[230] R. C. Viesca and J. R. Rice. “Modeling slope instability as shear rupture propagation in a saturated porous medium”. In: *Submarine Mass Movements and Their Consequences - 4th International Symposium* (2010), pp. 215–225. DOI: 10.1007/978-90-481-3071-9_18.

[231] R. C. Viesca, E. L. Templeton, and J. R. Rice. “Off-fault plasticity and earthquake rupture dynamics: 2. Effects of fluid saturation”. In: *Journal of Geophysical Research* 113.B9 (2008), B09307. DOI: 10.1029/2007JB005530.

[232] J. Vignollet, S. May, and R. de Borst. “Isogeometric analysis of fluid-saturated porous media including flow in the cracks”. In: *International Journal for Numerical Methods in Engineering* 108.9 (2016), pp. 990–1006. DOI: 10.1002/nme.5242.

[233] J. Vignollet, L. Kaczmarczyk, and C. J. Pearce. “A Galerkin least-square stabilisation technique for hyperelastic biphasic soft tissue”. In: *Computers & Structures* 118 (2013), pp. 109–114. DOI: 10.1016/J.COMPSTRUC.2012.10.010.

[234] J. Vignollet, S. May, and R. de Borst. “On the numerical integration of isogeometric interface elements”. In: *International Journal for Numerical Methods in Engineering* 102.11 (2015), pp. 1733–1749. DOI: 10.1002/nme.4867.

[235] W. M. Wang, L. J. Sluys, and R. de Borst. “Viscoplasticity for instabilities due to strain softening and strain-rate softening”. In: *International Journal for Numerical Methods in Engineering* 40.20 (1997), pp. 3839–3864. DOI: 10.1002/(SICI)1097-0207(19971030)40:20<3839::AID-NME245>3.0.CO;2-6.

[236] E. W. Weisstein. *Geometric Series. From MathWorld–A Wolfram Web Resource. http://mathworld.wolfram.com/GeometricSeries.html.*

[237] X. Weng. “Modeling of complex hydraulic fractures in naturally fractured formation”. In: *Journal of Unconventional Oil and Gas Resources* 9 (2015), pp. 114–135. DOI: 10.1016/j.juogr.2014.07.001.

[238] P. A. Witherspoon, J. S. Y. Wang, K. Iwai, and J. E. Gale. “Validity of Cubic Law for fluid flow in a deformable rock fracture”. In: *Water Resources Research* 16.6 (1980), pp. 1016–1024. DOI: 10.1029/WR016i006p01016.

[239] Y.-S. Wu, B. Lai, J. L. Miskimins, P. Fakcharoenphol, and Y. Di. “Analysis of Multiphase Non-Darcy Flow in Porous Media”. In: *Transport in Porous Media* 88.2 (2011), pp. 205–223. DOI: 10.1007/s11242-011-9735-8.

[240] L. Xikui and O. C. Zienkiewicz. “Multiphase flow in deforming porous media and finite element solutions”. In: *Computers & Structures* 45.2 (1992), pp. 211–227. DOI: 10.1016/0045-7949(92)90405-O.

[241] P. Xu, S. Qiu, B. Yu, and Z. Jiang. “Prediction of relative permeability in unsaturated porous media with a fractal approach”. In: *International Journal of Heat and Mass Transfer* 64 (2013), pp. 829–837. DOI: 10.1016/j.ijheatmasstransfer.2013.05.003.

[242] X. P. Xu and A. Needleman. “Numerical simulations of fast crack growth in brittle solids”. In: *Journal of the Mechanics and Physics of Solids* (1994). DOI: 10.1016/0022-5096(94)90003-5.

[243] D. Zbinden, A. P. Rinaldi, L. Urpi, and S. Wiemer. “On the physics-based processes behind production-induced seismicity in natural gas fields”. In: *Journal of Geophysical Research: Solid Earth* 122.5 (2017), pp. 3792–3812. DOI: `10.1002/2017JB014003`.

[244] Y. Zhang, D. Zhong, B. Wu, T. Guan, P. Yue, and H. Wu. “3D Parametric Modeling of Complex Geological Structures for Geotechnical Engineering of Dam Foundation Based on T-Splines”. In: *Computer-Aided Civil and Infrastructure Engineering* 33.7 (2018), pp. 545–570. DOI: `10.1111/mice.12343`.

[245] Y. Zhang, D. M. Pedroso, and W. Ehlers. “One-dimensional dynamics of saturated incompressible porous media: analytical solutions and influence of inertia terms”. In: *International Journal for Numerical and Analytical Methods in Geomechanics* 40.18 (2016), pp. 2489–2513. DOI: `10.1002/nag.2541`.

[246] F. Zhou, A. Shi, and X. Wang. “An efficient finite difference model for multiphase flow in fractured reservoirs”. In: *Petroleum Exploration and Development* 41.2 (2014), pp. 262–266. DOI: `10.1016/S1876-3804(14)60031-8`.

[247] O. C. Zienkiewicz, A. H. C. Chan, M. Paston, B. A. Schrefler, and T. Shiomi. *Computational geomechanics-with special reference to earthquake engineering*. Chichester: John Wiley & Sons, 1999.

[248] O. C. Zienkiewicz, C. T. Chang, and P. Bettess. “Drained, undrained, consolidating and dynamic behaviour assumptions in soils”. In: *Géotechnique* 30.4 (1980), pp. 385–395. DOI: `10.1680/geot.1980.30.4.385`.

[249] G. Zimmermann and A. Reinicke. “Hydraulic stimulation of a deep sandstone reservoir to develop an Enhanced Geothermal System: Laboratory and field experiments”. In: *Geothermics* 39.1 (2010), pp. 70–77. DOI: `10.1016/J.GEOTHERMICS.2009.12.003`.